Doctoral Dissertation
博士論文

Photometric Observations of Tiny Near-Earth Asteroids during the Close Approaches

（極めて地球に近づく微小地球接近小惑星の測光観測）

A Dissertation Submitted for the Degree of Doctor of Philosophy
December 2023
令和 5 年 12 月博士（理学）申請

Department of Astronomy, Graduate School of Science,
The University of Tokyo
東京大学大学院理学系研究科天文学専攻

Jin Beniyama
紅山 仁

Photometric Observations of Tiny Near-Earth Asteroids during the Close Approaches

by

Jin Beniyama
Supervised by Dr. Shigeyuki Sako

A Dissertation Submitted for the Degree of Doctor of Philosophy
December 2023
Department of Astronomy, Graduate School of Science,
The University of Tokyo

TOMO-E GOZEN

THE UNIVERSITY OF TOKYO

Dissertation committee

Dr. Motohide Tamura (chair)	The University of Tokyo
Dr. Misato Fukagawa	National Astronomical Observatory of Japan
Dr. Takashi Miyata	The University of Tokyo
Dr. Masanao Abe	Japan Aerospace Exploration Agency
Dr. Kohei Kitazato	The University of Aizu

Acknowledgment

My five years of Ph.D. course research have been supported by a large number of people. Please forgive me for introducing a very small fraction below due to limitations of space.

First and foremost, I would like to express my greatest appreciation to my supervisor **Dr. Shigeyuki Sako**. His suggestions always make sense and definitely improved the discussion of my study. He is a man worthy of respect as both a supervisor and a human being, and I am glad to spend the first five years of my research life together. My appreciation can't be expressed in words. I sincerely thank **Dr. Ryou Ohsawa** for the comprehensive advice for my study. All comments and suggestions made my study more interesting. I was surprised by his wide range of research interests. I am looking forward to continuing to collaborate with him in the future.

I cannot forget to thank **Dr. Satoshi Takita** in the same laboratory. The coffee time with you made me relaxed every Thursday. When it comes to coffee, I enjoyed it made from beans by **Dr. Naoto Kobayashi**, who is my supervisor in the master's course. Their insightful comments always encouraged me.

I am greatly thankful to **Dr. Fumihiko Usui** for the discussion and his careful reading of my master's thesis and doctoral dissertation. I learned what a researcher should be from him. I deeply thank **Dr. Seitaro Urakawa**, **Dr. Tomohiko Sekiguchi**, **Dr. Masateru Ishiguro**, **Dr. Daisuke Kuroda**, and **Dr. Fumi Yoshida** for the precious suggestions about the small solar system bodies. I also acknowledge the endless contribution of **Dr. Katsuhito Ohtsuka** for the study of near-Earth asteroid pair. I am highly indebted to **Dr. Makoto Yoshikawa**, **Dr. Shin-ichiro Okumura**, and **Dr. Hidenori Sato** for the search of near-Earth asteroids. I give special thanks to **Mr. Yuto Kojima** for his technical assistance with the search of fast-moving objects. I would like to thank near-Earth asteroid observers around the world. This dissertation would never have been finished without their support.

I am thankful for support from the Tomo-e Gozen project team members including **Dr. Hidenori Takahashi**, **Dr. Sohei Kondo**, **Ms. Yuki Mori**, **Dr. Yuu Niino**, **Dr. Mamoru Doi**, **Dr. Toshikazu Shigeyama**, **Dr. Masaomi Tanaka**, **Dr. Nozomu Tominaga**, **Dr. Noriaki Arima**, **Dr. Ko Arimatsu**, **Dr. Toshihiro Kasuga**, and **Dr. Jun-ichi Watanabe**.

As a member of DESTINY$^+$ science team, I really enjoyed the study of one of the most interesting and attractive near-Earth asteroid (3200) Phaethon. I thank DESTINY$^+$ team members including **Dr. Tomoko Arai**, **Dr. Ko Ishibashi**, **Dr. Hiroki Senshu**, and **Dr. Takafumi Ootsubo**. I would like to express my gratitude toward **Ms. Jooyeon Geem** and **Dr. Yoonsoo P. Bach** for their support and private communications. I never forget the taste of sea squirts in Busan.

I would like to acknowledge **Dr. Chrysa Avdellidou**, **Dr. Kianhong Lee**, **Dr. Marin Ferrais**, and **Dr. Emmanuël Jehin** for their help in the study of the tiny asteroid 2015 RN_{35}.

I thank **Dr. Jun Takahashi**, **Dr. Seiko Takagi**, **Dr. Hiroaki Saito**, **Dr. Tatsuya Nakaoka**, **Dr. Tomoki Saito**, **Dr. Tomohito Ohshima**, **Mr. Ryo Imazawa**, and **Dr. Masato Kagitani** for their contribution to the study of the near-Earth asteroid pair 1998 WT_{24}–2010 XC_{15}.

It has been a pleasure getting to have the asteroid seminar with **Ms. Natsuho Maeda**, **Dr. Ryota Fukai**, **Dr. Yuuya Nagaashi**, **Ms. Asami Takumi**, **Mr. Ren Ikeya**, **Ms. Mitsuha Noma**, **Mr. Yosuke Kida**, **Mr. Tsubasa Kogin**, **Ms. Chihiro Senba**, **Mr. Ryo Matsuoka**, and **Mr. Yohei Moteki**. The seminar was not only scientifically interesting but also a relaxation for me. I thank all participants in the Solar System Minor Body Seminar at the National Astronomical Observatory of Japan.

My deepest appreciation goes to **Dr. Takafumi Kamizuka**, who is a guardian of our room. His hard work has been a positive influence on me. I am grateful to discuss future science cases using MIMIZUKU on The University of Tokyo Atacama Observatory 6.5 m telescope with **Dr. Takashi Miyata**. He is always kind to students. I would want to express my heartfelt gratitude to **Ms. Risa**

Tsutsuki. Her attitude toward research was a good influence on me. I will save a place in case she returns to the community. I owe my deepest gratitude to **Mr. Naruse C. Akira**. His unique way of thinking has brainstormed me every single day. I thank **Mr. Kengo Tachibana**, **Dr. Kentaro Motohara**, **Dr. Kentaro Asano**, **Dr. Kosuke Kushibiki**, **Ms. Aiko Masuhara**, **Ms. Natsuko Kato**, **Dr. Takashi Horiuchi**, **Dr. Yuki Hirao**, **Dr. Masataka Imai**, **Dr. Kosuke Namekata**, **Mr. Yohei Nishino**, **Mr. Keito Kurashima**, and **Mr. Sorato Wada** for the support of my research life in Mitaka.

I would like to offer my special thanks to the members of the NAOJ Astro-ph seminar: **Mr. Ikki Mitsuhashi**, **Mr. Shin-ichi W. Kinoshita**, **Mr. Raiga Kashiwagi**, and sometimes **Mr. Takaho Masai**. I was happy to be able to practice English and experience unfamiliar research topics. The dinner with you after the seminar is also an unforgettable memory for me.

I would like to thank all in Kiso Observatory. This research would not have been possible without their support. Life in Kiso was warmly supported by the delicious and much food made by **Ms. Noriko Nakaji**. The traditional food in the Kiso region is suitable for me. I would like to express the deepest appreciation to the legends of Kiso, **Mr. Tsutomu Aoki**, **Mr. Takao Soyano**, and **Mr. Ken-ichi Tarusawa**. My heartfelt appreciation goes to **Mr. Tsuyoshi Hashiguchi**, **Ms. Kumiko Akaiwa**, and **Ms. Toshiko Tachibana**. My life on the Mitaka campus was owing to their kind support. I also thank the staff in the University of Tokyo CO-OP NAOJ branch. The healthy lunch with high-cost performance gave me a strong motivation to study. I am deeply grateful to all in the Okayama Astronomical Observatory and the Kyoto University Okayama Observatory. I had a good time during observations thanks to their hospitality. Also, I want to thank a taxi driver **Kametaka-san** in Kamogata city. I don't know why but his nonstop talk calmed me down before and after observations of asteroids in Okayama.

I am beyond grateful to **Dr. Seiji Sugita**, **Dr. Masanori Kanamaru**, **Dr. Patrick Michel**, **Dr. Paolo Tanga**, and **Dr. Marco Delbo**. They helped me go to Nice, France, where my next research life will start. Nice is nice; nice is Nice.

Last but certainly not least, I thank my mother and brother. They are always by my side. I cannot finish this Ph.D. dissertation without their support from the bottom of their hearts.

I would like to express the gratitude to the Iwadare Scholarship Foundation, the Public Trust Iwai Hisao Memorial Tokyo Scholarship Fund, the JEES Mitsubishi Corporation Science Technology Student Scholarship, and Iue Memorial Foundation for the grants. I would like to thank for JST SPRING, Grant Number JPMJSP2108 and the UTEC UTokyo Scholarship. This research is partially supported by the Optical and Infrared Synergetic Telescopes for Education and Research (OISTER) program funded by the MEXT of Japan as well as a grant from the Hayakawa Satio Fund awarded by the Astronomical Society of Japan. I have been supported by the Japan Society for the Promotion of Science (JSPS) Grants-in-Aid for Scientific Research (KAKENHI) Grant Number 23KJ0640. I am grateful to the dissertation committee for helpful comments on the dissertation.

I would like to offer my special thanks to farmers in coffee plantations around the world. On average, I drink three cups of coffee every day. This means that I have drunk more than 5000 cups of coffee in my Ph.D. course, which corresponds to 800 L by volume and ¥500000 ($\sim$ \$3000 $\sim$ €3000) in terms of money. I cannot summarize this dissertation without the Apple products, which made me stay hungry and foolish for research activities.

Jin Beniyama
December 2023

Dedication

This dissertation is dedicated to my mother and brother who always encourage me to do whatever I like.

Jin Beniyama
December 2023

Abstract

Studying near-Earth asteroids (NEAs) is fundamental to understanding material transportation in our solar system and mitigating the hazard of asteroid impacts in terms of planetary defense as well as in situ exploration using spacecraft such as Hayabusa and Hayabusa2. Most of NEAs have their origins in the asteroid belt between the orbits of Mars and Jupiter called the main belt. Asteroidal fragments are thought to be generated from collisional events in the main belt and gradually drifted by the Yarkovsky effect, which is a thermal force caused by radiation from the Sun. After the asteroids are delivered to unstable orbital resonances with giant planets, their orbits evolve to those of NEAs in a few Myr. During the orbital evolution, the rotation states (i.e., rotation period and pole direction) of the object are changed by the Yarkovsky-O'Keefe-Radzievskii-Paddack (YORP) effect, which arises from the asymmetricity of scattered sunlight and thermal radiation from the surface. The change of the rotation state is important since rotation acceleration by YORP leads to deformation or rotation fission of the asteroid due to a strong centrifugal force. It is known that the YORP effect is a dominant mechanism to change the rotation states of km-sized or smaller asteroids. The orbital elements and rotation states are thus thought to be valuable tracers of their dynamical evolution, whereas recently mysterious results have been reported in various contexts. Therefore, the formation mechanism, dynamical evolution, and surface properties as well as interior structures of NEAs are not well understood.

One point that should be emphasized is the difference in environments between large and tiny (diameter less than 100 m) bodies. If the environment of tiny asteroids such as surface properties and internal structures are different from those of large asteroids, we could not use empirical relationships obtained in previous studies. We have to know the true nature of tiny asteroids to examine and test our knowledge about their dynamical histories. Moreover, the strength of the Yarkovsky and YORP effects increase with decreasing diameter, and smaller asteroids have experienced a larger change in the orbital and rotation states. Thus, the current states of tiny asteroids may be an important piece of information to understand the dynamical histories of the whole NEA population. Studying tiny asteroids is key to investigating the formation mechanism, dynamical evolution, and surface properties as well as interior structures of NEAs. Tiny asteroids in the main belt are too faint to characterize even using 8 m class telescopes. Only NEAs during the close approaches and a few spacecraft mission targets give us knowledge about tiny asteroids. However, it is not easy to characterize tiny NEAs; the number of targets is very limited for spacecraft missions, whereas ground-based observations are restricted by limited observational windows from hours to days, fast rotation sometimes less than a minute, and large apparent motion on the sky of about a few arcsec s^{-1} during the close approaches. Observations with exposure times sufficiently shorter than their rotation periods are essential to derive the short rotation period and suppress the trailing sensitivity loss effect. The previous surveys possibly undetected some very fast rotations due to a relatively long exposure time. Although characterizations of a handful of tiny NEAs have been conducted by campaign observations, most of tiny NEAs graze the Earth without being characterized even a little.

In this dissertation, we present the results of three observational studies of tiny asteroids, all of them stand alone. We have overcome the difficulties in observations of tiny asteroids by quick response or well-planned campaign observations using high-speed CMOS cameras. The objectives of this dissertation are to examine the formation mechanism, dynamical evolution, and surface properties as well as interior structures of NEAs.

First, we have obtained optical lightcurves of 108 tiny NEAs, and successfully derived the rotation periods and axial ratios of 52 tiny NEAs including 23 fast rotators with rotation periods less than 60 s. The fastest rotator found during our survey is 2020 HS_7 with a rotation period of 2.99 s. We statistically confirmed that there is a certain number of tiny fast rotators in the NEA population, which have been missed with any previous surveys. Moreover, we discovered the tentative critical rotation period of 10 s for tiny asteroids. The critical rotation period of 10 s could be explained by a nongravitational effect

considering the tangential YORP effect, which is caused by a recoil force parallel to the surface, although further observational and theoretical studies are needed to reach a conclusion.

Next, we have conducted optical multicolor photometry of the tiny NEA 2015 RN_{35} across a wide range of phase angles from 2° to 30° using two telescopes in Japan and Chile. We found that 2015 RN_{35} is a non-principle axis rotator with two characteristic periods of 1149.7 ± 0.3 s and 896.01 ± 0.01 s. We showed that a slope of a visible spectrum of 2015 RN_{35} is as red as asteroid (269) Justitia, one of the very red objects in the main belt, which indicates that 2015 RN_{35} can be classified as an A- or Z-type asteroid. In conjunction with the shallow slope of the phase curve, we suppose that 2015 RN_{35} is a high-albedo A-type asteroid. We demonstrated that the surface properties of tiny asteroids could be well constrained by intensive observations across a wide range of phase angles. 2015 RN_{35} is a possible mission accessible A-type NEA with a small Δv of 11.801 km s^{-1} in the launch window between 2030 and 2035. The other interpretation is that the shallow slope comes from the lack of fine grains on its surface due to the weak gravity and strong centrifugal force.

Finally, we have conducted optical multicolor photometry and polarimetry of the NEA pair candidate 2010 XC_{15} using four telescopes in Japan. The rotation period of 2010 XC_{15} is possibly a few to several dozen hours and color indices of 2010 XC_{15} are derived as $g-r = 0.435 \pm 0.008$, $r-i = 0.158 \pm 0.017$, and $r-z = 0.186 \pm 0.009$ in the Pan-STARRS system. The linear polarization degrees of 2010 XC_{15} are a few percent at the phase angle range of 58° to 114°. We found that 2010 XC_{15} is a rare E-type NEA on the basis of its photometric and polarimetric properties. Taking the similarity of not only physical properties but also dynamical integrals and the rarity of E-type NEAs into account, we suppose that 2010 XC_{15} and 1998 WT_{24} are of common origin (i.e., asteroid pair). These two NEAs are the sixth NEA pair and the first E-type NEA pair ever confirmed, possibly formed by rotation fission. We conjecture that the parent body of 2010 XC_{15} and 1998 WT_{24} was transported from the main belt through the ν_6 resonance or Hungaria region.

Combining the parts into a whole, we revealed the nature of tiny NEAs. As for surface properties of tiny NEAs, we found that the tiny fast-rotating NEA 2015 RN_{35} may lack the regolith on its surface. This is explained with the lack of fine grains on its surface due to the weak gravity and/or strong centrifugal force caused by the fast rotation. We showed that asteroid pairs share similar surface properties even in the small size range (100–400 m in diameter). The slightly bluer spectrum of 2010 XC_{15} is indicative of a lack of fine grains on the surface. Thus, we found direct evidence of the size dependence of the surface properties of NEAs; small NEAs may lack fine grains on the surface. Our conclusion, tiny NEAs lack fine regolith on the surface, is consistent with a recent study about histories of surface regolith considering both removal and production of them. As for interior structures, we succeeded in explaining the observed diameter and rotation period relation assuming the tiny NEAs are monolithic asteroids. This may imply that our assumption is correct; tiny asteroids are actually monolithic asteroids. In conjunction with the previous studies that imply some tiny asteroids are covered with fine grains or porous rocks, we suppose that the tiny asteroids might have porous structures. Throughout the dissertation, we conjecture that tiny asteroids are free from fine grains on the surface regardless of spin states, and possibly have porous interior structures.

The fact that tangential YORP is actually working on NEAs is an important implication to discuss the material transportation in our solar system. Our understanding of the formation mechanism of NEAs gives a strong constraint on the size frequency distribution of asteroids. Moreover, knowledge about the surface properties of tiny NEAs helps the understanding of the current mysterious results of tiny NEAs. The high porosity of tiny NEAs implies that they are more fragile than dense material. In terms of planetary defense, the effect of asteroid impact is qualitatively revised downward. Our conclusion that tiny bodies are porous monolithic rocks expands our knowledge of the origin of tiny bodies; the current tiny NEAs might be ejected from the surface of larger NEAs like Ryugu and Bennu by cratering events. Assuming that the tiny monolithic asteroids are remnants of planetesimals without differentiation, observations of tiny asteroids are in turn the observations of planetesimals. Measurements of bulk density,

porosity, and composition of tiny asteroids may inform us about planetesimals and planetary formation. Our understanding of the formation mechanism, dynamical evolution, and surface properties as well as interior structures of whole NEA population was dramatically expanded in the dissertation. The nature of tiny asteroids will be clearer in the next decade with the advent of such as the Rubin Observatory Legacy Survey of Space and Time, the Near Earth Object Surveyor, and the University of Tokyo Atacama Observatory as well as future spacecraft missions.

Keywords

minor planets, asteroids, near-Earth asteroids, photometry, multicolor photometry, polarimetry

Table of Contents

List of Figures

List of Tables

Copyright

Published works

- Chapter II: Video observations of tiny near-Earth objects with Tomo-e Gozen, PASJ, 74, 877–903. (Beniyama et al. 2022)
- Chapter III: Multicolor Photometry of Tiny Near-Earth Asteroid 2015 RN_{35} Across a Wide Range of Phase Angles: Possible Mission-accessible A-type Asteroid, AJ, 166, 229–241. (Beniyama et al. 2023a)
- Chapter IV: Photometry and Polarimetry of 2010 XC_{15}: Observational Confirmation of E-type Near-Earth Asteroid Pair, ApJ, 955, 143–158. (Beniyama et al. 2023b)

Abbreviations & Symbols

We summarize the abbreviations and symbols used in this dissertation in Tables A and B, respectively.

Table A. Abbreviations used in this dissertation

Abbreviation	
AO	adaptive optics
ASAS-SN	All-Sky Automated Survey for Supernovae
ATLAS	Asteroid Terrestrial-impact Last Alert System
CNEOS	Center for Near Earth Object Studies
CSS	Catalina Sky Survey
CYORP	crater-induced YORP
DAMIT	Database of Asteroid Models from Inversion Techniques
DART	Double Asteroid Redirection Test
DESTINY$^+$	Demonstration and Experiment of Space Technology for INterplanetary voYage, Phaethon fLyby and dUst Science
ECAS	Eight-Color Asteroid Survey
FWHM	full width at half maximum
HHO	Higashi-Hiroshima Observatory
HONIR	Hiroshima Optical and Near-InfraRed Camera
IFS	integral field spectrograph
IRAC	Infrared Array Camera
IRAS	Infrared Astronomical Satellite
IRTF	(NASA) Infrared Telescope Facility
JPL	(NASA) Jet Propulsion Laboratory
JT	Jupiter Trojan
JWST	James Webb Space Telescope
KMTNet	Korea Microlensing Telescope Network
KST	Kepler Space Telescope
LCDB	Asteroid Light Curve Database
LINEAR	Lincoln Near-Earth Asteroid Research
LONEOS	Lowell Observatory Near-Earth-Object Search
LSST	Legacy Survey of Space and Time
LWS	Long Wave Spectrometer
MANOS	Mission Accessible Near-Earth Objects Survey
MBA	main belt asteroid
MCCM	Monte Carlo using the Covariance Matrix
MIMIZUKU	Mid Infrared Multi-field Imager for gaZing at the UnKnown Universe
MMR	mean motion resonance
MOA	Microlensing Observations in Astrophysics
MSI	Multi-Spectral Imager
M4AST	Modeling for Asteroids

Table A. (Continued)

Abbreviation	
NEA	near-Earth asteroid
NEAR-Shoemaker	Near Earth Asteroid Rendezvous - Shoemaker
NEAT	Near-Earth Asteroid Tracking
NEO	near-Earth object
NEO Surveyor	Near-Earth Object Surveyor
NEOWISE	Near-Earth Objects Wide-field Infrared Survey Explorer
NHAO	Nishi-Harima Astronomical Observatory
NO	Nayoro Observatory
OSIRIS-APEX	OSIRIS-Apophis Explorer
OSIRIS-REx	Origins, Spectral Interpretation, Resource Identification, and Security–Regolith Explorer
Pan-STARRS	Panoramic Survey Telescope and Rapid Response System
PR	Poynting-Robertson
PSF	point spread function
SBDB	Small-Body Database
SDSS	Sloan Digital Sky Survey
SHARP (♯)	Small Hazardous Asteroid Reconnaissance Probe
SPHERE	Spectro-Polarimetric High-contrast Exoplanet REsearch
SR	secular resonance
SST	Spitzer Space Telescope
STM	Standard Thermal Model
SYORP	sublimation-driven YORP
TCO	temporarily-captured orbiter
TESS	Transiting Exoplanet Survey Satellite
TNO	trans-Neptunian object
TriCCS	TriColor CMOS Camera and Spectrograph
TYORP	tangential YORP
VLT	Very Large Telescope
VRO	very red object
WCS	World Coordinate System
WFGS2	Wide Field Grism Spectrograph 2
WISE	Wide-field Infrared Survey Explorer
YORP	Yarkovsky-O'Keefe-Radzievskii-Paddack
ZTF	Zwicky Transient Facility

Table B. Symbols used in this dissertation

Symbol	Description
G	slope parameter in the H-G model
G_1, G_2	slope parameters in the H-G_1-G_2 model
H	absolute magnitude
$H_{\rm V}$	absolute magnitude in V band
$p_{\rm V}$	geometric albedo in V band
m	mass
ρ	mass density
r, R	radius
D	diameter
S	area
V	volume (Note the confusion with V band magnitude.)
k	cohesion
ε	thermal emissivity
P	rotation period
Δm	lightcurve amplitude
a	semimajor axis
e	eccentricity
q	perihelion distance
Q	aphelion distance
i	inclination
Ω	longitude of ascending node
ω	argument of perihelion
M	mean anomaly
ν	true anomaly
α	solar phase angle
$r_{\rm h}$	heliocentric distance
Δ	observer-centric distance
$m_{\rm app}$	apparent magnitude
V	the Johnson V band (Note the confusion with volume.)
R	the Johnson R band
I	the Johnson I band
G	the Gaia G band
g	the Pan-STARRS g band
r	the Pan-STARRS r band
i	the Pan-STARRS i band
z	the Pan-STARRS z band

I'm convinced that the only thing that kept me going was that I loved what I did. You've got to find what you love. And that is as true for your work as it is for your lovers.
— Steve Jobs (1955–2011)

1. General Introduction

In this chapter, a comprehensive review of the scientific background and status of the research field as well as the scope of this dissertation are described.

1.1. Asteroids: treasure trove sometimes danger

In 1802, a German-born British astronomer Frederick William Herschel used the word "asteroid" combining "*aster (star)*" and "*-oid (like)*" to express *new stars* from their *asteroidical* appearance (Herschel 1802). Literally, they are like stars on astronomical images, but nonsidereally moving as time goes on due to their orbital motions unlike stars. Most asteroids are discovered in the main belt between the orbits of Mars and Jupiter. There are two main scenarios for the origin of the main belt (Raymond & Nesvorný 2022). Both two scenarios begin with many small bodies of 1 km size scales or larger called planetesimals. The classical view of the belt is that it was born with initial planetesimals equivalent with several Earth masses and later depleted (e.g., Kokubo & Ida 2000). On the other hand, a recent study proposed that very few planetesimals were in the belt and later implanted from inner and outer regions (Raymond & Izidoro 2017). In either case, the small asteroids are thought to be remnants or collisional fragments of planetesimals; asteroids smaller than 10–100 km have experienced collisional events in their life considering the collisional timescale (Bottke et al. 2005), whereas experienced no differentiation. Thus, they preserve crucial information about the early stage of planetary formation, and studying asteroids might be ultimately related to an understanding of the material transportation in the solar system and origins of water and/or organic materials (e.g., Meech & Raymond 2020). Circumstellar material possibly related to asteroids is also discovered outside our solar system as debris disks, which means that the asteroids are more like not a special population only in our system (e.g., Smith & Terrile 1984; Wyatt 2008). From a perspective of resources, asteroids are justified as a worthy field of study; a notable example is the NASA Psyche mission to the metallic asteroid (16) Psyche (Elkins-Tanton et al. 2014).

Asteroids in near-Earth space are called near-Earth asteroids, or NEAs. Recently, NEAs have been particularly of interest in many aspects. The composition of asteroids and their size dependence are affected by formation mechanism and dynamical evolution. Thus, the characterizations of NEAs in a wide size range are crucial to examine their dynamical histories. We could study tiny bodies as small as 1 m utilizing NEAs when they are bright in near-Earth space, which are too faint to be observed in their source region, the main belt. In terms of planetary defense, observations of NEAs are important to mitigate asteroid impacts such as the 10 km asteroid impact in the Gulf of Mexico–Caribbean region 66.5 Myr ago (Alvarez et al. 1980) and the 20 m asteroid impact near the Russian city of Chelyabinsk in 2013 (Popova et al. 2013). As a resource, temporarily-captured orbiter (TCO) may give a unique opportunity for asteroid mining (Jedicke et al. 2018); a low-cost mission is possible by utilizing a TCO. Several in situ investigations via space missions have been successful for decades such as the Near Earth Asteroid Rendezvous – Shoemaker (NEAR-Shoemaker, Veverka et al. 2001), Hayabusa mission (Fujiwara et al. 2006), Chang'e-2 (Huang et al. 2013), Hayabusa2 mission (Watanabe et al. 2019; Kitazato et al. 2019; Sugita et al. 2019), the Origins, Spectral Interpretation, Resource Identification, and Security–Regolith Explorer (OSIRIS-REx, Lauretta et al. 2017), and the Double Asteroid Redirection Test (DART, Rivkin et al. 2021).

Nevertheless, there are still many open questions regarding NEAs, these are, formation mechanism, dynamical evolution, and surface properties as well as interior structures of them. We will struggle to solve these problems throughout this dissertation.

1.2. Orbital population of asteroids

The small bodies in our solar system are divided into several subpopulations using orbital elements (Figure 1.1): main belt asteroids (MBAs), NEAs, Jupiter Trojans (JTs), and Trans-Neptunian Objects (TNOs). The spatial distributions of them as of 2023 October 3 are shown in Figure 1.2. Orbital elements are extracted from the Minor Planet Center Orbit Database file [1].

The MBAs are known to be the majority of small bodies with the number of discoveries of 1263507 as of 2023 October 3. After the discoveries of four large MBAs in the early 1800s, (1) Ceres in 1801, (2) Pallas in 1802, (3) Juno in 1804, and (4) Vesta in 1807, no asteroids were discovered for more than thirty years. From the late 1840s, a bunch of MBAs have been discovered. Although the definition of MBAs depends on references, they are located between the orbits of Mars and Jupiter with semimajor axes of about 2.0 to 3.5 au. The smallest size of the discovered MBAs is about 100 m even using an 8 m class ground-based telescope and a 6 m class space-borne telescope (Maeda et al. 2021; Müller et al. 2023).

The NEAs are small bodies with perihelion distances smaller than 1.3 au [2]. The first NEA, (433) Eros, was discovered in 1898. Since then, 32957 NEAs were discovered mainly by survey observations (see Section 1.3). We could discover tiny NEAs down to sub-m in diameter during the close approaches, when they are bright enough. By analysis of the recent discoveries of NEAs, the number of km-class and m-class NEAs are estimated to be 920 ± 10, and $(4 \pm 1) \times 10^8$, respectively (Tricarico 2017). The completeness of the discovery of m-class NEAs is less than 0.01%.

The JTs are located at L_4 and L_5 Lagrange points of Jupiter, and have stable orbits with semimajor axes of 5.05 to 5.40 au (Zellner et al. 1985a). Until now, 12925 JTs have been discovered. The TNOs are the small bodies with semimajor axes larger than a_N of 30.06 au, where a_N is a semimajor axis of Neptune. 4461 TNOs were discovered mainly from the deep images obtained with 4 to 8 m class telescopes (e.g., Bannister et al. 2018; Terai et al. 2018).

In this dissertation, we are especially focusing on NEAs. The NEAs have subpopulations depending on orbital elements (Figure 1.3): Amor-class, Apollo-class, Aten-class, Atira-class, and Vatira-class[3]. The Amor-class has $q > Q_E$, where Q_E is an aphelion distance of the Earth, 1.017 au. By definition, the Amor-class NEAs are always outside the Earth's orbit. The number of Amor-class NEAs is 11824. The Apollo-class has $a > a_E$ and $q < Q_E$, where a_E is a semimajor axis of the Earth, 1.0 au. The Apollo-class NEAs are mainly outside but sometimes inside the Earth's orbit. The number of Apollo-class NEAs is 18452. The Aten-class has $a < a_E$ au and $Q > q_E$, where q_E is a perihelion distance of the Earth, 0.983 au. The Aten-class NEAs are mainly inside but sometimes outside the Earth's orbit. The number of Aten-class NEAs is 2587. The Atira-class has $q_V < Q < q_E$[4], where q_V is a perihelion distance of Venus, 0.718 au. The Atira-class NEAs are always inside the Earth's orbit and outside Venus's orbit at some time. The number of Atira-class NEAs is 31. The Vatira-class has $Q < q_V$, which is always inside Venus's orbit. The existence of Vatiras is predicted by numerical simulations (Greenstreet et al. 2012), and the first Vatira-class NEA, 2020 AV_2, was finally discovered in 2020 (Popescu et al. 2020; Ip et al. 2022; Bolin et al. 2022).

[1] https://minorplanetcenter.net/iau/MPCORB/MPCORB.DAT

[2] This originates from the perihelion distances of asteroids close to the Earth discovered by the late 1970's are less than the minimum perihelion of Mars, 1.309 AU (Shoemaker & Helin 1978).

[3] The classes are named after prototypes: (1221) Amor, (1862) Apollo, (2062) Aten, and (163693) Atira. The Vatira is made up of "**V**enus" and "**Atira**".

[4] We use this definition rather than $Q < q_E$ to distinguish Atiras from Vatiras.

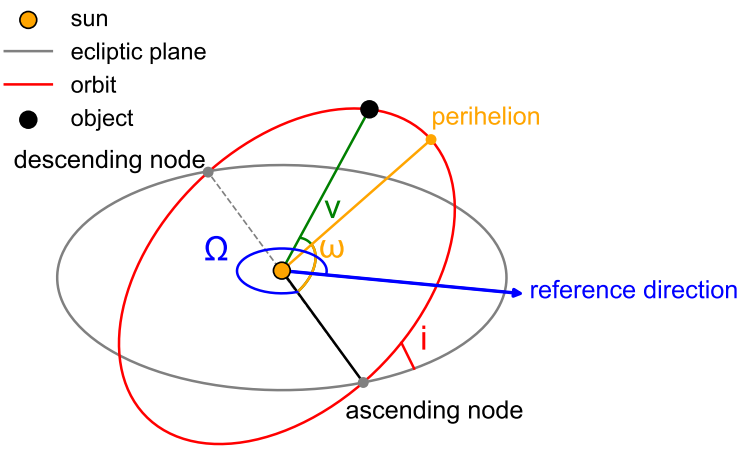

Figure 1.1. Orbital elements of the solar system bodies. The orbit of an object orbiting the Sun is shown with its inclination (i), argument of perihelion (ω), longitude of ascending node (Ω), and true anomaly (ν).

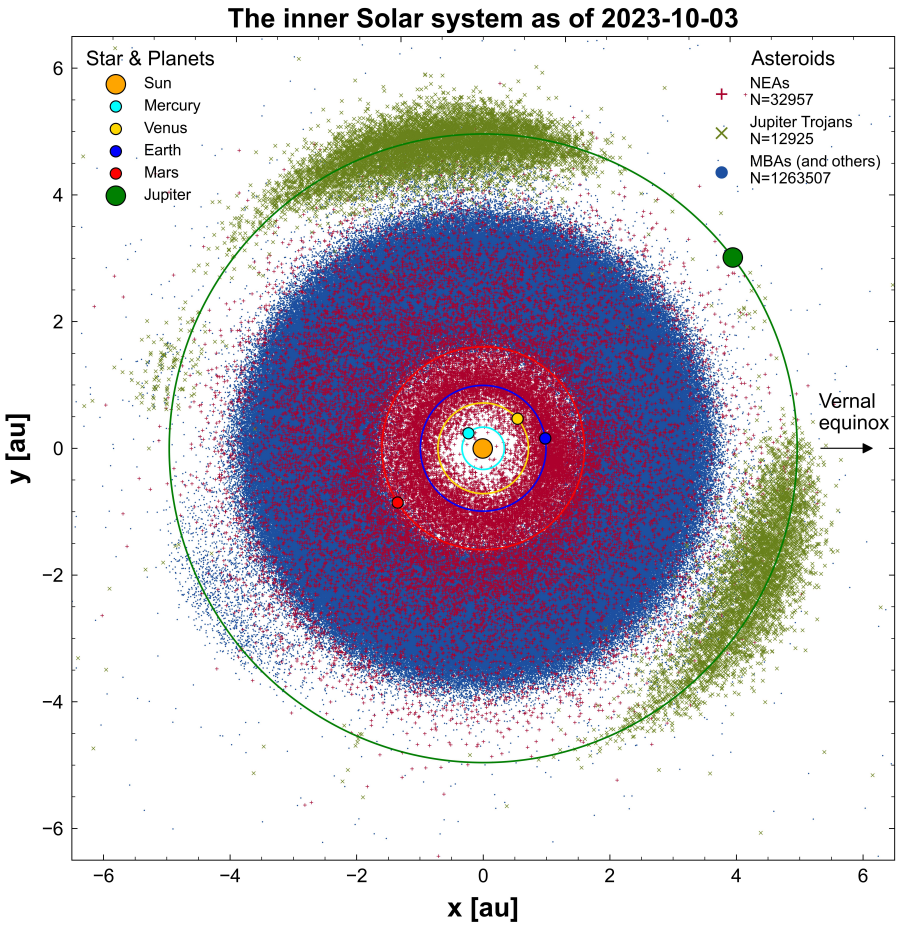

Figure 1.2. Spatial distribution of the small solar system bodies. NEAs, JTs, and the other populations including mainly MBAs are shown by plus signs, crosses, and dots, respectively. Orbital elements are extracted from the Minor Planet Center Orbit Database file as of 2023 October 3.

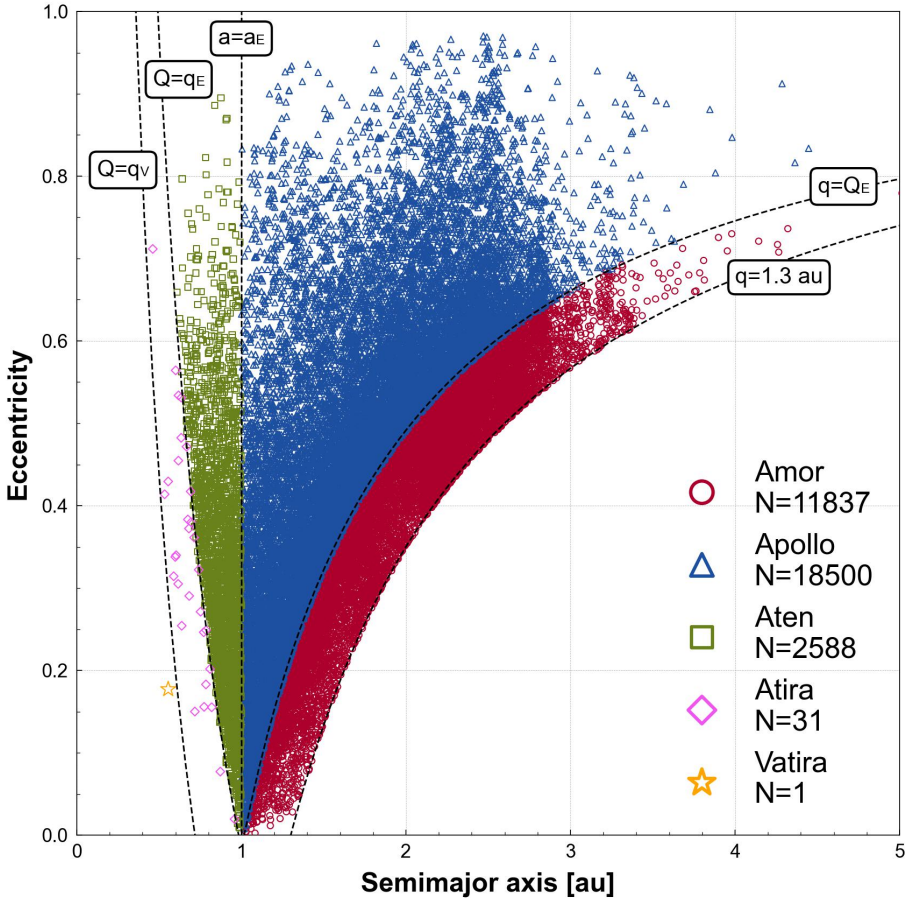

Figure 1.3. Semimajor axis versus eccentricity of NEAs. Amors, Apollos, Atens, Atiras, and Vatira are represented by circles, triangles, squares, diamonds, and star, respectively. Boundaries of each class are also shown. Orbital elements are extracted from the Minor Planet Center Orbit Database file as of 2023 October 3.

1.3. Discoveries of near-Earth asteroids

The 32957 NEAs have been discovered by wide-field photometric surveys such as Catalina Sky Survey (CSS, Drake et al. 2009), Panoramic Survey Telescope and Rapid Response System (Pan-STARRS, Chambers et al. 2016), and Asteroid Terrestrial-impact Last Alert System (ATLAS, Tonry et al. 2018; Tonry 2023). Astrometric measurements are the first step of the study of asteroids. The multiple (sometimes serendipitous) detections of a moving object turn out to be a discovery of a new asteroid. The number of discoveries of near-Earth objects (NEOs) [5] are shown in Figure 1.4. This figure is a reproduction of that in a website of Center for Near Earth Object Studies (CNEOS)[6]. We describe representative projects below.

The CSS is the survey project using three telescopes in US. The survey itself is performed using 1.5 m and 0.7 m telescopes on Mt. Lemon and Mt. Bigelow, respectively, whereas follow-up observations are performed using a 1.0 m telescope on Mt. Lemon. The Mt. Bigelow survey has been started in 1998 using a 0.7 m telescope. The CSS has discovered a large fraction of NEOs as shown in Figure 1.4.

The Pan-STARRS is a survey project using two 1.8 m telescopes Pan-STARRS1 and Pan-STARRS2 in Haleakala, Hawaii. The survey using Pan-STARRS1 and Pan-STARRS2 has started in 2010 and 2018, respectively (Wainscoat et al. 2022). The Pan-STRRS has also discovered a significant number of NEOs as CSS.

The ATLAS survey currently uses four 0.5 m telescopes to discover NEOs. The two are in Haleakala, Hawaii, one is in South Africa, the other is at El Sauce in Chile, and a fifth one is in preparation on Tenerife island in Spain (Tonry 2023). The survey in Hawaii has started in 2015.

The Lincoln Near-Earth Asteroid Research (LINEAR) is a survey project using two telescopes in New Mexico, US (Stokes et al. 2000). They used a 1.0 m telescope from 1996 to 2013, and a 3.5 m telescope from 2013 to 2017. The Near-Earth Asteroid Tracking (NEAT) is a survey using a 1.2 m Schmidt telescope on Mt. Palomar and 1 m telescope in Haleakala, Hawaii (Pravdo et al. 1999). The survey has been conducted from 1995 to 2007. The Spacewatch is a survey using two telescopes with diameters of 0.9 and 1.8 m in Arizona, US (McMillan & Spacewatch Team 2007). They started the survey in 1984 using a 0.9 m telescope. The Lowell Observatory Near-Earth-Object Search (LONEOS) has been conducted using a 0.6 m Schmidt telescope on Mt. Palomar from 1993 to 2008 (Koehn & Bowell 2000). The Wide-field Infrared Survey Explorer (WISE) was launched in 2009 (Wright et al. 2010). WISE conducted the infrared all-sky survey at 3.4 (W1 band), 4.6 (W2 band), 12 (W3 band), and 22 μm (W4 band). After the depletion of solid hydrogen in 2010, the mission was reactivated as the Near-Earth Objects Wide-field Infrared Survey Explorer (NEOWISE) using W1 and W2 bands (Mainzer et al. 2011; Masiero et al. 2021). The Zwicky Transient Facility (ZTF) is a survey project using a 1.2 m Schmidt telescope on Mt. Palomar (Bellm et al. 2019). They also performed a twilight survey to discover asteroids close to the Sun, and successfully discovered the first Vatira-class NEA 2020 AV_2 (Ye et al. 2020; Popescu et al. 2020; Ip et al. 2022; Bolin et al. 2022).

The number of discoveries of NEAs is increasing, especially small ones. As shown in upper panel of Figure 1.5, a number of small NEAs were discovered whereas few small MBAs were discovered. This is mainly because NEAs are relatively close to the Earth (observers) as shown in lower panel of Figure 1.5, and can be discovered by wide-field survey projects. Studying small NEAs is fundamental to understanding the formation mechanism and dynamical evolution of the whole NEA population, mitigating the hazard of asteroid impacts in terms of planetary defense, and in situ exploration using spacecrafts such as Hayabusa and Hayabusa2 if possible. Comprehensive studies of large asteroids have long been conducted, whereas only few studies focus on small asteroids due to observational difficulties caused by such as limited visibilities and large apparent motions of asteroids during their close approaches (see Subsection 1.7.2).

[5] The NEOs consist of not only near-Earth asteroids but also near-Earth comets.

[6] https://cneos.jpl.nasa.gov/stats/site_all.html

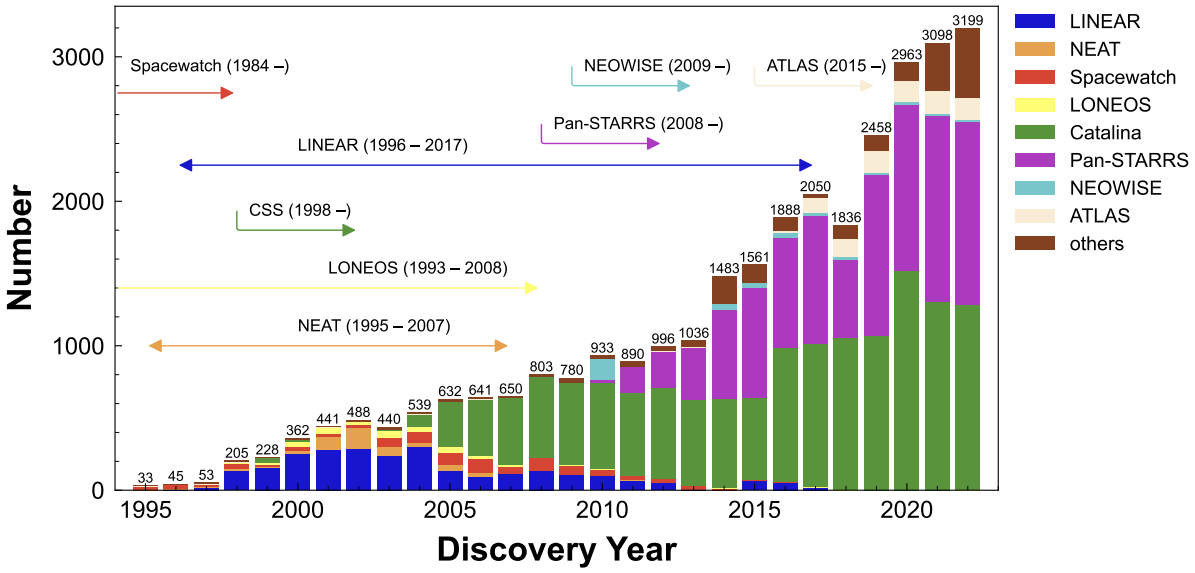

Figure 1.4. Discovery statistics of NEOs. The arrows indicate the period when projects are in operation. The number of discoveries in a year is shown on each bin. This figure is a reproduction of that on the website of CNEOS.

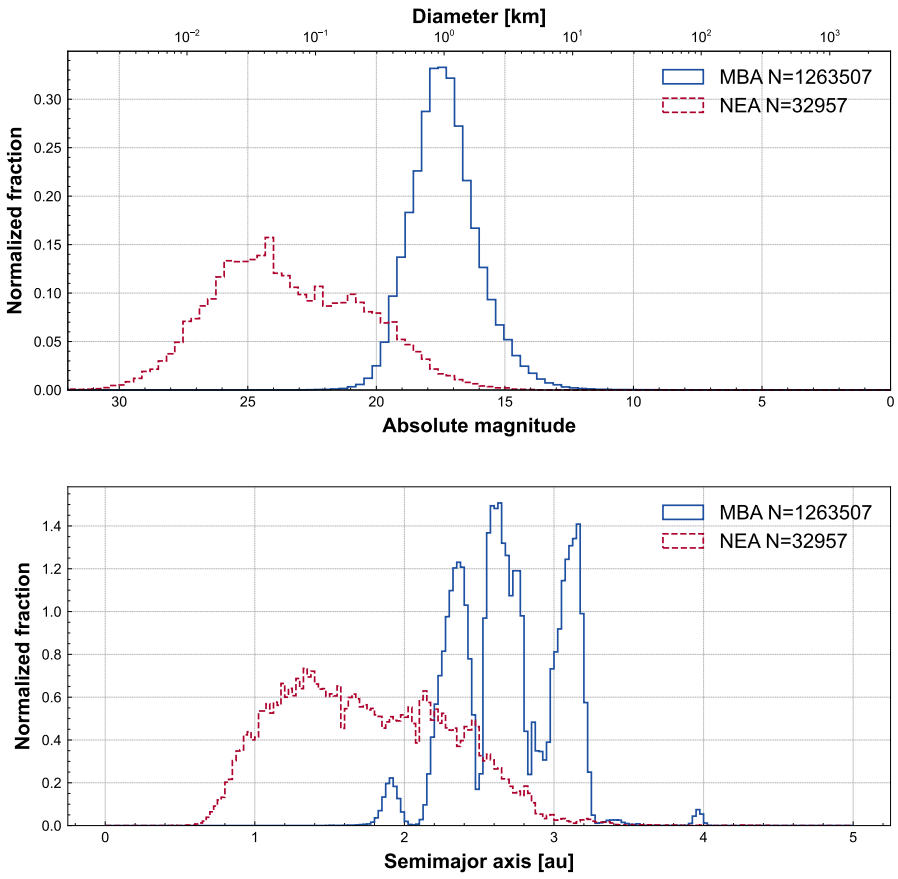

Figure 1.5. Size (upper) and semimajor axes (lower) of MBAs and NEAs. The absolute magnitude is converted to diameter using Equation 1.12 assuming a geometric albedo of 0.2. Orbital elements are extracted from the Minor Planet Center Orbit Database file as of 2023 October 3. The histograms are normalized so that each total area equals unity.

1.4. Dynamical histories of near-Earth asteroids

1.4.1. Change of orbits

The gravity is the most fundamental quantity to understand the evolution processes of asteroids. The gravities of giant planets such as Jupiter and Saturn play important roles in the dynamics of the asteroids. The "gaps" in the semimajor axes (not heliocentric distances) of MBAs, so-called Kirkwood gaps (Kirkwood 1867), are generated by the combination of mean-motion resonances (MMR) and secular resonances (SR). For instance, the asteroids with semimajor axes of 2.5 au are lacking due to the 3:1 MMR with Jupiter as seen in lower panel of Figure 1.5[7].

Nongravitational effects such as the radiation pressure, cometary activity, and Yarkovsky effect also contribute to the dynamical histories of the asteroids. The radiation pressure is caused by photons from the Sun in our solar system (Burns et al. 1979). The orbits of small dust particles are enlarged in a short time scale when the force caused by radiation pressure, $F_{\rm rad}$, is not negligible to the gravity, $F_{\rm grav}$. The condition is usually expressed using the $\beta = F_{\rm rad}/F_{\rm grav}$. When the $\beta \ll 1$, the orbit of the dust grain is not affected by the radiation pressure, whereas when the $\beta \gg 1$, the dust grain is pushed away from the Sun due to the radiation. A tangential component of radiation pressure is called the Poynting-Robertson (PR) effect named after two scientists (Poynting 1904; Robertson 1937). The PR effect works as a drag, and shrinks an orbit of a dust particle. Given their size (D) dependences of $F_{\rm rad}$ and $F_{\rm grav}$, or the fact that $\beta \sim 1$ when $D \sim 1$ μm, the radiation pressure including the PR effect is negligible in the scale of asteroids ($D \gg 1$ μm). Also, the nongravitational effect by cometary activity is not considered in the orbital evolution of rocky asteroids.

Therefore, the change of the orbital elements of asteroids due to the nongravitational effect is dominated by the Yarkovsky effect, which is caused by radiation from the Sun (e.g., Vokrouhlický 1998; Vokrouhlický et al. 2000; Bottke et al. 2006). The non-zero thermal inertia of the surface of the asteroid causes the momentum transfer, because the thermal emission from the asteroid has its peak in a direction a bit offset relative to the line of sight to the Sun as shown in Figure 1.6. The change of the orbit by the Yarkovsky effect is composed of two contributions (Vokrouhlický 1998): diurnal effect with a shorter timescale of its rotation and seasonal effect with a longer timescale of orbital revolution around the Sun. In panel (a) of Figure 1.6, the diurnal component can make a positive or negative change in the semimajor axis depending on its obliquity (i.e., pole orientation of the rotation axis). The diurnal effect has its maximum when the obliquity is 0° or 180° (i.e., the pole axis is perpendicular to its orbital plane). Meanwhile, the seasonal component always makes a negative change in the semimajor axis as shown in panel (b) of Figure 1.6. The seasonal effect has its maximum when the obliquity is 90° (i.e., the pole axis is parallel to its orbital plane).

It is known that the diurnal effect dominates the seasonal effects (Vokrouhlický et al. 2000; Vokrouhlický et al. 2015). The orbit-averaged drift rate in the semimajor axis by the diurnal effect is expressed as follows (Greenberg et al. 2017, 2020):

$$\frac{da}{dt} = \pm\xi \frac{3}{4\pi} \frac{1}{\sqrt{a}} \frac{1}{1-e^2} \frac{L_\odot}{c\sqrt{GM_\odot}} \frac{1}{D\rho}, \tag{1.1}$$

where ξ is the Yarkovsky efficiency, which expresses an efficiency considering the obliquity and phase lag, a is a semimajor axis, e is an eccentricity, $L_\odot$ is the luminosity of the Sun, c is the speed of light, G is the gravitational constant, $M_\odot$ is the mass of the Sun, D is a diameter of a body, and ρ is a mass density of a body. The Yarkovsky effect significantly changes the orbit of smaller asteroids at a rate da/dt proportional to $1/D$. As an example, the strength of the diurnal Yarkovsky effect of Icarus ($D \sim 1$ km) is estimated to be $(-4.84 \pm 0.44) \times 10^{-4}$ au Myr^{-1}[8] from astrometric measurements (Greenberg et al.

[7] $\frac{(T_{\rm J}/3)^2}{a^3} = \frac{T_{\rm J}^2}{a_{\rm J}^3}$ gives $a \sim 2.5$ au, whereby $T_{\rm J}$ and $a_{\rm J}$ are the orbital period and semimajor axis of Jupiter, respectively.

[8] The change equals ~ -70 m yr^{-1}.

2020).

1.4.2. Change of rotation states

Rotation states (i.e., rotation period and pole direction) of the object are known to be changed by the various mechanisms such as sublimation of volatile material, tidal torque, and the Yarkovsky-O'Keefe-Radzievskii-Paddack (YORP) effect, which arises from the asymmetricity of scattered sunlight and thermal radiation from the surface (e.g., Rubincam 2000; Vokrouhlický & Čapek 2002; Čapek & Vokrouhlický 2004; Bottke et al. 2006). The effect of the sublimation is called the sublimation-driven YORP (SYORP) effect (Steckloff & Jacobson 2016). The SYORP is a sublimation-driven analog to the YORP effect on icy bodies, and is not effective on rocky asteroids. The close encounters with terrestrial planets induce tidal torques (Scheeres et al. 2000; Vokrouhlický et al. 2004). The change of the rotation state of the small NEA (25143) Itokawa during the close approach with the Earth in June 2004 is negligible compared to the YORP effect (Ďurech et al. 2008a), whereas the rotation state change of the tiny NEA Duende in 2013 is possibly due to the close encounter with the Earth (Moskovitz et al. 2020; Benson et al. 2020). It has been reported that the YORP effect is a dominant mechanism for changing the rotation states of km-sized or smaller asteroids (Vokrouhlický & Čapek 2002). The rotation acceleration by YORP leads to deformation or rotation fission of the asteroid due to a strong centrifugal force (Walsh et al. 2008). Understanding the YORP effect is thus crucial to examining the origins and dynamical histories of asteroids.

The YORP torque is small but certainly changes the rotation state of the asteroids. For instance, the year-averaged YORP torque parallel to the spin pole of (162173) Ryugu ($D \sim 1$ km) is estimated to be -0.161 N m[9] (Kanamaru et al. 2021). A slightly modified rotation acceleration given by Rossi et al. (2009) is as follows:

$$\frac{d\omega}{dt} = C \frac{1}{a^2\sqrt{1-e^2}} \frac{1}{D^2\rho}, \tag{1.2}$$

where C is a coefficient related to its shape and moment of inertia. The rotation acceleration is proportional to D^{-2}, which is based on the fact that the torque N is proportional to $F \times D \propto D^2 \times D = D^3$, whereas the moment of inertia I is proportional to $m \times D^2 \propto D^5$.

Observationally, rotation accelerations of asteroids by YORP have been detected for twelve NEAs to date: (1862) Apollo (Kaasalainen et al. 2007; Ďurech et al. 2008a, 2023), (54509) YORP[10] (Lowry et al. 2007; Taylor et al. 2007), (1620) Geographos (Ďurech et al. 2008b, 2022b), Itokawa (Lowry et al. 2014), (3103) Eger, (Ďurech et al. 2012, 2018b), (161989) Cacus (Ďurech et al. 2018b, 2023), (101955) Bennu (Nolan et al. 2019; Hergenrother et al. 2019), (68346) 2001 KZ_{66} (Zegmott et al. 2021), (10115) 1992 SK (Ďurech et al. 2022b), (1685) Toro (Ďurech et al. 2022b; Tian et al. 2022), (2100) Ra-Shalom, and (138852) 2000 WN_{10} (Ďurech et al. 2023). The measured strength of the YORP effect of Bennu, with D of 482 m in NASA Jet Propulsion Laboratory (JPL) Small-Body Database (SBDB)[11], for instance, is estimated to be $3.63 \pm 0.52 \times 10^{-6}$ deg day^{-2} [12] from in situ observations by OSIRIS-REx (Hergenrother et al. 2019). Although the YORP torque is extremely sensitive to small-scale surface topography (Statler 2009), weak size dependence of the rotation change is seen in the previous twelve detections as shown in Figure 1.7.

In addition to them, a change of a rotation period is detected on the tumbling asteroid 2012 TC_4 (Lee et al. 2021). They explained the spin change is caused by the YORP. Recently, the spin acceleration of (3200) Phaethon has been reported (Marshall et al. 2022), although the rotation change could not be explained by the YORP considering its large size of about 5 km in diameter (Figure 1.7).

[9] The 0.161 N m is smaller than the torque necessary to open a plastic bottle cap, ~ 1 N m.
[10] "YORP" is named after the detection of the "YORP" effect.
[11] https://ssd.jpl.nasa.gov/tools/sbdb_lookup.html
[12] The change equals ~ 0.01 s yr^{-1}.

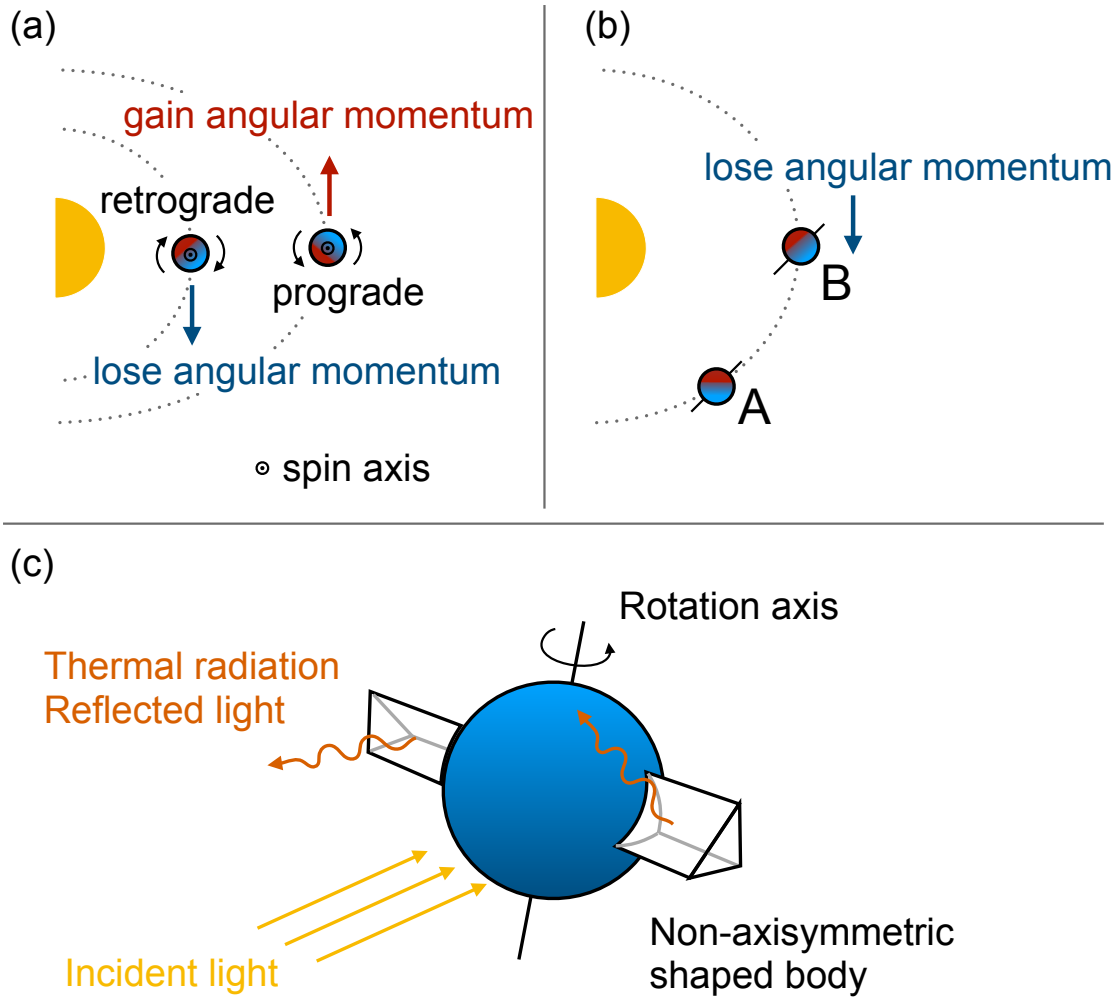

Figure 1.6. Schematic pictures of nongravitational effects. (a) Diurnal component of Yarkovsky effect. Prograde and retrograde rotators whose pole orientations are perpendicular to their orbital planes are shown. The hotter part is represented by redder color, whereas the cooler part is represented by bluer color. (b) Seasonal component of Yarkovsky effect. Object with pole axis parallel to its orbital plane at two different epochs is shown. The object is orbiting the Sun from A to B. The pole axis is shown by solid line. The hotter part is represented by redder color, whereas the cooler part is represented by bluer color. Leading part is always hotter than trailing part, and the object loses its angular momentum. (c) YORP effect. The net torque from total reflected light and thermal flux is not zero owing to the asymmetry arising from two wing components on the object.

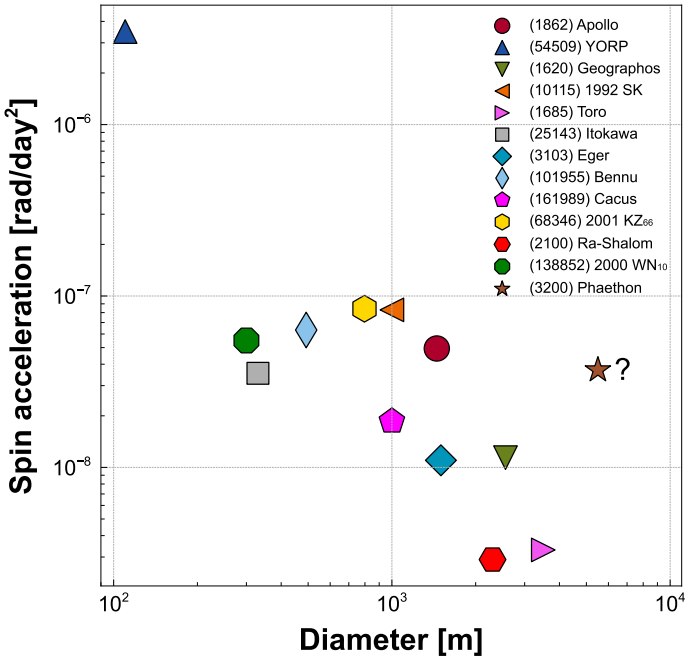

Figure 1.7. Diameter versus spin accelerations. Twelve asteroids of which spin accelerations by YORP are detected are plotted with Phaethon. Mechanism of the spin acceleration of Phaethon is still unclear.

1.4.3. Main belt to near-Earth space

Most of NEAs have their origins in the asteroid belt between the orbits of Mars and Jupiter. The established orbital evolution processes of NEAs are as follows (e.g., Gladman et al. 1997; Bottke et al. 2006). First, orbits of MBAs are gradually changed by the Yarkovsky effect, inward or outward depending on the pole orientation (see Equation 1.1). After the asteroids are delivered to unstable resonances with giant planets such as 3:1 and 5:2 MMRs with Jupiter at 2.5 au and 2.8 au, respectively, their orbits are strongly perturbed. The eccentricities and inclinations of asteroids are increased in a short time scale ($\leq$ 1 Myr) keeping the semimajor axes fixed. Then, some of them are scattered to near-Earth space in a few Myr (Gladman et al. 1997), whereas others are removed from the inner solar system. It is a widely held view that the orbits of NEAs are stable for about 10 Myr. After life as NEAs, some collide with the Sun, and some with the planets, and others escape the solar system (Granvik et al. 2018).

1.5. Observational characteristics of asteroids

In this section, observational characteristics of asteroids and related observation techniques are summarized.

1.5.1. Color and spectral type

The asteroids' compositions depend on where they are accumulated during the planetary formation. For instance, the water ice exists on the surface of TNOs, whereas it is rare in the inner main belt. Thus, compositions are valuable tracers of where they were born or where they came from. The first color measurements of asteroids might be for Ceres and Pallas (Herschel 1802). Herschel observed two large asteroids *by eye* with the seven feet reflector and wrote:

- *The colour of Ceres is ruddy, but not very deep.*
- *Ceres is much more ruddy than Pallas.*
- *Pallas is of a dusky whitish colour.*

Later, these statements were qualitatively confirmed by multicolor photometry and spectroscopy.

Multicolor photometry, photometry using broad-band filters to obtain flux within a certain wavelength range, enables us to obtain color indices (i.e., very low-resolution spectrum) of an asteroid. Spectroscopy can be said that high-resolution multicolor photometry, but we usually use a slit and spectrograph utilizing a prism, grating, or grism (grating prism). The detailed classifications of asteroids can be achieved by spectroscopy, whereas the targets are limited to bright ones compared to multicolor photometry since the light from the asteroid is more finely split. Spectral types are based on the shape of the reflectance spectra, which are controlled by the surface material (Bell et al. 1989). Thus, the spectral types are indicative of the surface composition of asteroids.

As an example, colors of asteroids observed by the Sloan Digital Sky Survey (SDSS) are shown in Figure 1.8. The SDSS is the large northern sky survey project, which performed photometric and spectroscopic observations at the Apache Point Observatory, New Mexico, US (York et al. 2000). Five broad-band filters in visible wavelengths, u', g', r', i', and z' are used in the photometric survey (Fukugita et al. 1996). Their main science targets are galaxies and quasars, whereas there are as many as millions of serendipitous detections of asteroids. In the latest catalog published in Sergeyev & Carry (2021), the probabilities of the asteroid complex are assigned for each asteroid. We extracted asteroids with 80% or higher probabilities to belong to a certain class except U, which indicates an unknown class, and calculated $g' - r'$, $r' - i'$, $i' - z'$, and a'. The a' is a quantity introduced in Ivezić et al. (2001):

$$a' = 0.89(g' - r') + 0.45(r' - i') - 0.57. \tag{1.3}$$

The a' passes between two prominent peaks in panel (a) of Figure 1.8, C and S-types, and asteroids with positive and negative a' are red and blue, respectively. In panel (b) of Figure 1.8, some types degenerating in panel (a) (i.e., only g, r, and i bands) are separated well using $i' - z'$ color. Multicolor photometry is informative for understanding the composition of asteroids.

The first taxonomy of asteroids was proposed by Chapman et al. (1975). They defined C and S-types, which correspond to carbonaceous and stony-metallic meteorites, respectively. Tholen (1984) made spectral templates by conducting the Arizona Eight-Color Asteroid Survey (ECAS, Zellner et al. 1985b). They observed 589 minor planets using eight broad-band filters in visible wavelengths from 0.34 to 1.04 μm. They divided asteroids into 14 classes based on their reflectance spectra taking albedo into account. Bus (1999) made new templates using asteroid spectra by spectroscopy in visible wavelength, and later it was expanded to near-infrared (DeMeo et al. 2009). Mahlke et al. (2022) proposed a new taxonomy considering geometric albedo. They newly introduced the Z-type, which are very red asteroids

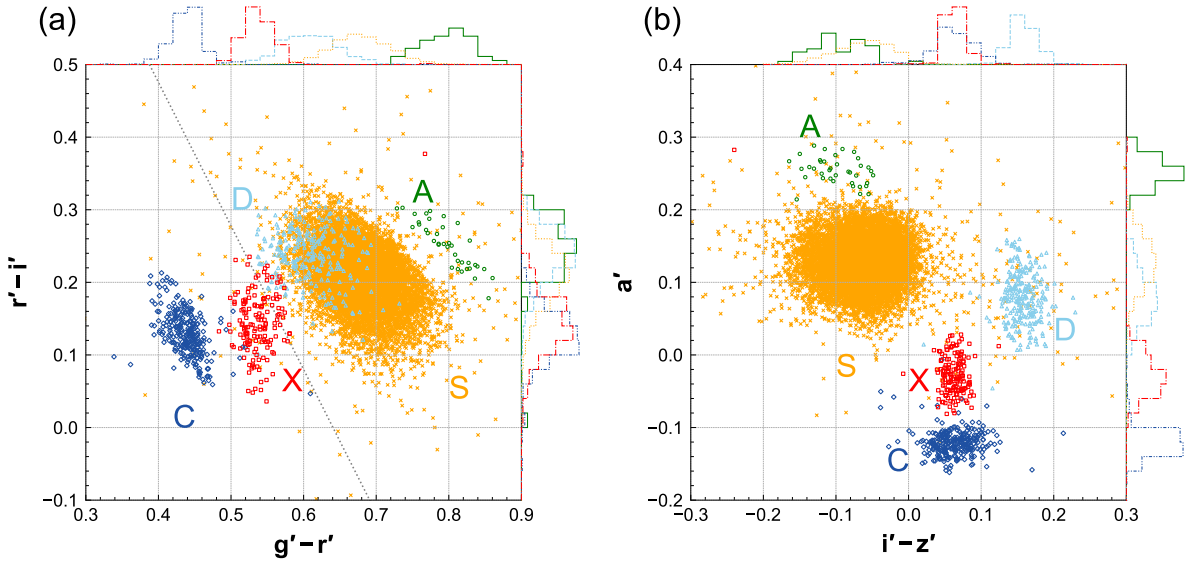

Figure 1.8. Color-color diagrams of asteroids. The magnitude system is the SDSS system. A-, D-, S-, C-, and X-types are presented by circles, squares, crosses, diamonds, and triangles, respectively. Only asteroids with a probability of a certain type larger than 80% are plotted in the catalog (Sergeyev & Carry 2021). Histograms in upper part and right side are normalized fractions of each class. A-, D-, S-, C-, and X-types are shown by solid, dashed, dotted, dotted–dashed, and double dotted–dashed lines, respectively. A diagonal dotted line in panel (a) is an isochrone of $a' = 0$.

recently reported. Examples of class templates of Bus-DeMeo taxonomy and Mahlke taxonomy are shown in Figure 1.9. We summarize representative types below.

S-types[13] are thought to be silicaceous bodies linked to ordinary chondrites. The relevant minerals are olivine and pyroxene (DeMeo et al. 2015). The absorption feature around 0.9 micron in the spectrum originates from transition metal ions such as Fe in the silicate material. An example of the S-type is Itokawa, explored by the Hayabusa mission (Fujiwara et al. 2006). The S-types are the dominant population of inner MBAs and NEAs (DeMeo & Carry 2013). Typical S-types have a middle geometric albedo of about 0.2 (DeMeo & Carry 2013).

C-types[14] are regarded as carbonaceous bodies linked to carbonaceous chondrites. The relevant minerals are opaques, carbon, and phyllosilicates (DeMeo et al. 2015). An example of the C-type is Ryugu, explored by the Hayabusa2 mission (Watanabe et al. 2019; Kitazato et al. 2019; Sugita et al. 2019). The C-types are the minority in inner MBs and NEAs, and the majority in outer MBs (DeMeo & Carry 2013). Typical C-types have a low geometric albedo of about 0.1 or less (DeMeo & Carry 2013).

V-types[15] are known to be differentiated asteroids as well as M-, E-, and A-types (Scott et al. 2015). V-types are believed to be basaltic asteroids possibly coming from the crust of differentiated bodies. A prototype is Vesta in the inner main belt. V-types have an average geometric albedo of about 0.35 (DeMeo & Carry 2013).

M-types[16] are possibly metallic asteroids, which come from the core of the differentiated bodies. The largest M-type asteroid is Psyche in the outer main belt, which will be visited by the NASA Psyche mission (Elkins-Tanton et al. 2014). M-types have an average geometric albedo of about 0.14 (DeMeo & Carry 2013).

[13]The letter S stems from silicaceous or stony.
[14]The letter C stems from carbonaceous.
[15]The letter V stems from a prototype asteroid Vesta.
[16]The letter M stems from metal.

E-types[17] (Mahlke taxonomy) or Xe-types (DeMeo taxonomy) are high-albedo asteroids with featureless reflectance spectra. E-types are thought to have mineralogical links to the enstatite achondrite meteorites (Aubrites) composed of almost iron-free enstatite (Zellner 1975; Zellner et al. 1977). A prototype is (44) Nysa in the inner main belt. With its complex shape and the similarity of its polarimetric properties to those of meteorites, Nysa has been thought to be the largest surviving mantle fragment of a differentiated parent body (Zellner et al. 1977). The E-types are plentiful in Hungaria (DeMeo & Carry 2013). Typical E-types have a high geometric albedo of about 0.5 (DeMeo & Carry 2013).

A-types[18] are thought to be olivine-rich asteroids and have similar spectra to those of silicate mineral olivine. A-types are thought to be a piece of differentiated planetesimal (Veeder et al. 1983; Cruikshank & Hartmann 1984; DeMeo et al. 2019), while other studies propose that some A-types may originate from the mantle of Mars (Polishook et al. 2017). The A-types may have an important role in investigating the formation of terrestrial planets. Typical A-types have a geometric albedo of about 0.3 (DeMeo & Carry 2013).

D-types[19] are associated with primitive material. The spectral slope in the visible to near-infrared range is very red as shown in Figure 1.9, which is explained by the existence of complex organic material (Barucci et al. 2018). The D-types are observed in outer solar system such as JTs and TNOs. Typical D-types have a low geometric albedo of about 0.1 (DeMeo & Carry 2013). Recently, the two very red objects (VROs), (203) Pompeja and (269) Justitia, were discovered in Hasegawa et al. (2021). Successively, Bourdelle de Micas et al. (2022) discovered the VRO (732) Tjilaki in the main belt. These VROs are classified as Z-types in the latest Mahlke taxonomy (Mahlke et al. 2022). The Z-types might have primitive organic materials on the surface as D-types.

1.5.2. Albedo

Two types of albedos are used to express the fraction of the reflected light to incident light: (bolometric) Bond albedo, A, and geometric albedo, p. The (bolometric) Bond albedo is a concept proposed by an American astronomer George Phillips Bond, which is defined as the ratio of bolometric incident light to bolometric reflected light, regardless of wavelength and direction. On the other hand, the geometric albedo is defined as the ratio of reflected light from the object at a phase angle of zero to that of a Lambertian disk of the same cross-section at the same distance[20]. The Lambertian disk has an ideal diffusely reflecting surface with equal intensity in all directions[21]. Considering a spherical asteroid with a radius of r and a Lambertian disk with a radius of r, which are Δ from us, p is derived as:

$$p = \frac{F_{\rm obj}(\alpha = 0, \Delta)}{F_{\rm Lambert}(\alpha = 0, \Delta)}, \tag{1.4}$$

where $F_{\rm obj}(\alpha = 0, \Delta)$ is a light flux from the object at a phase angle of zero and $F_{\rm Lambert}(\alpha = 0, \Delta)$ is a light flux from the Lambertian disk at a phase angle of zero (Pravec & Harris 2007). A geometric albedo in the visible wavelength, $p_{\rm V}$, is practically used since most observations of asteroids are performed in the visible wavelength.

In general, the albedo, the percentage of incoming solar light that the surface of the object reflects, is high for ordinary chondrite-like *bright* material, whereas low for carbonaceous chondrite-like *dark* material. The albedo depends on such as the surface grain size and roughness in addition to the composition, so the derivation of albedo is fundamental in examining the nature of asteroids.

[17] The letter E stems from enstatite.
[18] The letter A possibly stems from one of the prototypes (446) Aeternitas (Veeder et al. 1983).
[19] The letter D stems from dark.
[20] From these definitions, A is between 0 to 1, whereas p could be larger than the unity (e.g., 1.38 for Enceladus, Verbiscer et al. 2007).
[21] The brightness is proportional to $\cos\theta$, where θ is an angle between the line of sight and the normal to the surface.

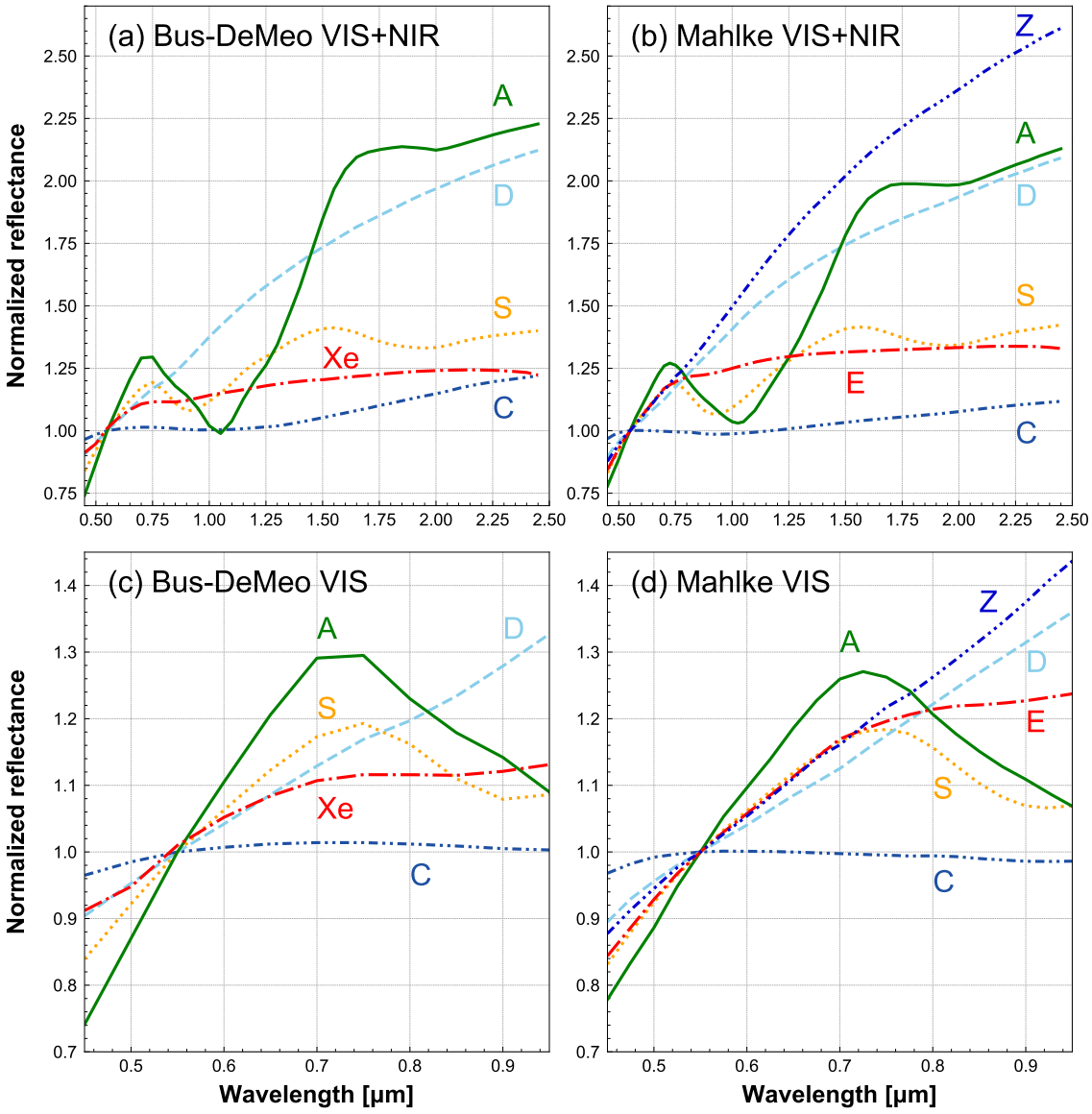

Figure 1.9. Spectral class templates of asteroids. All reflectance spectra are normalized at 0.55 μm. (a) Bus-DeMeo taxonomy in visible to near-infrared wavelength. Templates of A- (solid line), D- (dashed line), S- (dotted line), C- (dotted–dashed line), and Xe-types (double dotted–dashed line) are shown. (b) Mahlke taxonomy in visible to near-infrared wavelength. Templates of A- (solid line), D- (dashed line), S- (dotted line), C- (dotted–dashed line), E- (double dotted–dashed line), and Z-types (double dotted–dashed line) are shown. (c) Bus-DeMeo taxonomy in visible wavelength. Templates of A- (solid line), D- (dashed line), S- (dotted line), C- (dotted–dashed line), and Xe-types (double dotted–dashed line) are shown. (d) Mahlke taxonomy in visible wavelength. Templates of A- (solid line), D- (dashed line), S- (dotted line), C- (dotted–dashed line), E- (double dotted–dashed line), and Z-types (double dotted–dashed line) are shown.

Thermal observation is the most standard method to derive a geometric albedo of an asteroid breaking a degeneracy between diameter and albedo. A strong constraint on the diameter of the asteroid is obtained with thermal observation (see Subsection 1.5.5), and this leads to the albedo estimate when combined with measurements in visible wavelength. Several space-borne telescopes and a limited number of large ground-based telescopes have been used for thermal observations.

The Infrared Astronomical Satellite (IRAS) was launched in 1983 and conducted all-sky surveys at 12, 25, 60, and 100 μm (Neugebauer et al. 1984). The IRAS Minor Planet Survey observed 2228 asteroids multiple times (Tedesco et al. 2002). The Spitzer Space Telescope (SST) was launched in 2003 (Werner et al. 2004). The SST conducted three observation projects of NEAs using the Infrared Array Camera (IRAC) on the SST at 3.6 μm (and 4.5 μm for ExploreNEOs): ExploreNEOs (Trilling et al. 2010), NEOSurvey (Trilling et al. 2016), and NEOLegacy (Gustafsson et al. 2019). 2204 NEOs have been observed by the three major surveys[22]. The infrared astronomical satellite AKARI was launched in 2006 (Murakami et al. 2007). AKARI carried out the second infrared all-sky survey after IRAS, and diameters and albedos of 5120 asteroids were derived from mid-infrared measurements using S9W (6.7–11.6 μm) and L18W (13.9–25.6 μm) filters (Usui et al. 2011, 2013). As the third infrared all-sky survey, WISE and NEOWISE have been performing their all-sky survey as of 2023, and contributed to the estimate of diameters and albedos of more than 1845 NEAs. As for the outer solar system objects, *TNOs are cool* project determined albedo and diameters of more than a hundred TNOs using the Herschel Space Observatory (Müller et al. 2009). From the ground, such as Keck-I/Long Wave Spectrometer (LWS, Delbó et al. 2003) and UKIRT/Michelle (Takahashi et al. 2011) are used to study asteroids in the thermal infrared, although the measurements are limited to a certain wavelength range (e.g., N and Q bands), where atmospheric transparency is high.

Polarimetry is a kind of spectroscopy in a broad sense splitting the incident light into two orthogonally polarized beams, ordinary and extraordinary (e.g., Kawabata et al. 1999). Since the polarization degrees reflect the surface properties of asteroids such as geometric albedo, roughness, and grain size, polarimetry is one of the best techniques to examine the surface properties of asteroids. High-albedo asteroids have lower polarization degrees compared to low-albedo asteroids (Belskaya & Shevchenko 2000), which is the so-called Umov effect (Belskaya et al. 2015:for review). This is because the disk-integrated flux of high-albedo asteroids contains the contribution of multiple scattering, which cancels out the polarization, and vice versa.

The linear polarization degree depends on not only surface properties but also the solar phase angles. The phase angle dependence of an asteroid's linear polarization degree, the so-called polarization phase curve, informs about the surface properties of the asteroid. Asteroids have the maximum polarization degree at a phase angle of about 100° (e.g., Geake & Dollfus 1986; Hadamcik et al. 2023). Typical MBAs could be observable at a phase angle range of 0° to 30° from the Earth. Thus, the ground-based observations of asteroids at large phase angles ($\alpha \geq 30°$) can be achieved only for NEAs. In terms of phase angles, a latitude (l) of an observatory is also important. As described in Ishiguro et al. (2017), observatories at middle latitudes, $|l| \sim 45°$, have the superiority in observations at large phase angles utilizing the Earth as a natural coronagraph.

As shown in Figure 1.10, the number of polarimetric observations at large phase angles have been performed only for dozens of NEAs. The polarization degrees at large phase angles are indicative of their geometric albedo (e.g., Ishiguro et al. 2022; Kiselev et al. 2002; De Luise et al. 2007; Kuroda et al. 2021; Geem et al. 2023). High, middle, and low albedo asteroids have typical linear polarization degrees of about 2%, 5%, and 40%, respectively, at phase angles of about 80°.

[22] http://neareathobjects.nau.edu/spitzerneos.html, last accessed 2023 November 13.

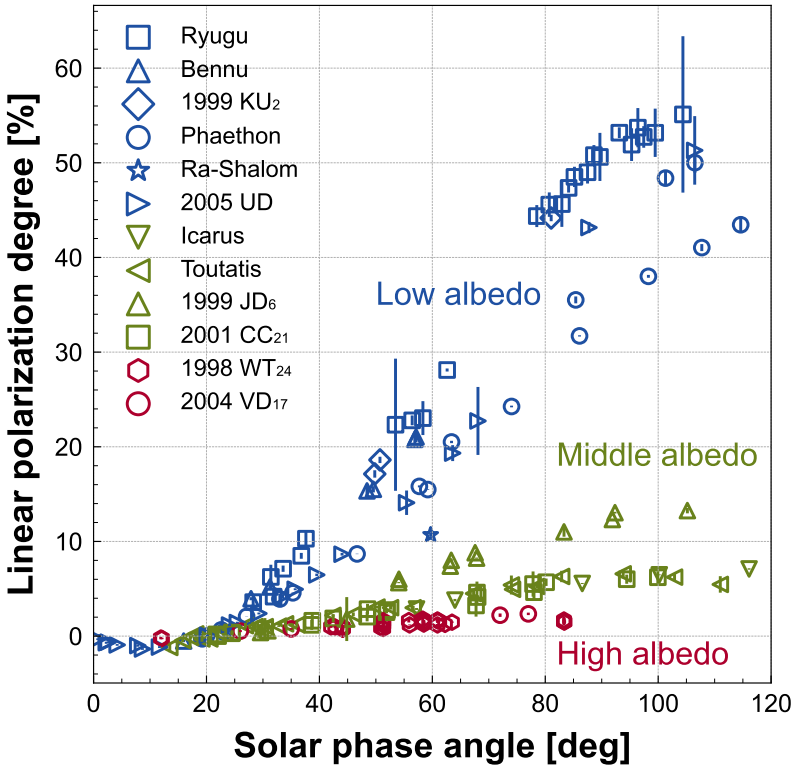

Figure 1.10. Phase angle dependence of linear polarization degree of asteroids (Kiselev et al. 2002; De Luise et al. 2007; Kuroda et al. 2021; Ishiguro et al. 2022; Geem et al. 2023).

1.5.3. Rotation state

A time-series brightness measurements of an asteroid is called a lightcurve. Lightcurves of asteroids in visible wavelength vary mainly by three factors: change of heliocentric distance (distance between the Sun and target, $r_{\rm h}$) and observer-centric distance (distance between the observer and target, Δ), change of solar phase angle (angle between the incident light onto an object and reflected light from the object, α), and change of the observing surface of the target (see Appendix A). The brightness variations in the lightcurve after the distance and phase corrections may reflect the change of the cross-section owing to the rotation of the asteroid. This is an inverse problem to derive the spin state and shape of the asteroid (see also Subsection 1.5.4).

The Asteroid Light Curve Database (LCDB, Warner et al. 2009) contains thousands of rotation periods of small bodies as shown in Figure 1.11. The LCDB includes the observational results of various projects such as the Mission Accessible Near-Earth Objects Survey (MANOS, Thirouin et al. 2016, 2018); the Formation of the Outer Solar System: An Icy Legacy Survey (FOSSIL, Chang et al. 2021, 2022; Ashton et al. 2023); and the ExploreNEOs, NEOSurvey, and NEOLegacy (Hora et al. 2018). Most asteroids larger than 200 m in diameter have rotation periods longer than two hours. This clear cutoff is called the cohesionless spin barrier and indicates most of the larger asteroids are rubble-piles (Pravec & Harris 2000). A power balance of a boulder on the surface of a rigid asteroid is expressed as follows:

$$G\frac{Mm}{r^2} = mr\omega^2, \tag{1.5}$$

where G is the gravitational constant, M is a mass of the asteroid, m is a mass of the boulder, r is a radius of the asteroid, and ω is an angular velocity of asteroid. Given the critical condition that the boulder is about to escape from the surface due to the centrifugal force, the critical rotation period, $P_{\rm cri}$, is obtained as:

$$P_{\rm cri} = \sqrt{\frac{3\pi}{G\rho}}, \tag{1.6}$$

where ρ is a mass density of the asteroid. By substituting a mass density of 2500 kg m^{-3} and 1000 kg m^{-3} into Equation 1.6, we obtain $P_{\rm cri}$ of about 2 hr and 3 hr, respectively.

In addition to targeted lightcurve observations, serendipitous detections are useful to constrain rotation states. Sparse photometry has been conducted by several projects using ground-based and space-borne telescopes such as Kepler Space Telescope (KST, Ryan et al. 2017; Szabó et al. 2016, 2017; Molnár et al. 2018; Szabó et al. 2020; Podlewska-Gaca et al. 2021; Kalup et al. 2021; Kecskeméthy et al. 2023), Transiting Exoplanet Survey Satellite (TESS, McNeill et al. 2019; Pál et al. 2020; Szabó et al. 2022; McNeill et al. 2023), Korea Microlensing Telescope Network (KMTNet, Erasmus et al. 2017, 2018), Pan-STARRS (Cibulková et al. 2018), All-Sky Automated Survey for Supernovae (ASAS-SN, Hanuš et al. 2021), Microlensing Observations in Astrophysics (MOA-II, Cordwell et al. 2022), WISE (Lam et al. 2023), and James Webb Space Telescope (JWST, Müller et al. 2023).

Radar observations are also a strong technique to constrain rotation states of asteroids (Benner et al. 2015; Margot et al. 2015), although the targets are limited to asteroids close to the Earth since the sensitivity is proportional to the fourth power of the distance between the target and the observer. The Arecibo Observatory and Goldstone Solar System Radar have been a great success (Virkki et al. 2022).

1.5.4. Shape

The lightcurve inversion method is practically used to make a shape model of an asteroid (Kaasalainen & Torppa 2001; Kaasalainen et al. 2001). Multiple dense lightcurves at different viewing geometry are helpful to construct a shape model. As of 2023 October 6, 16087 shape models are registered in the

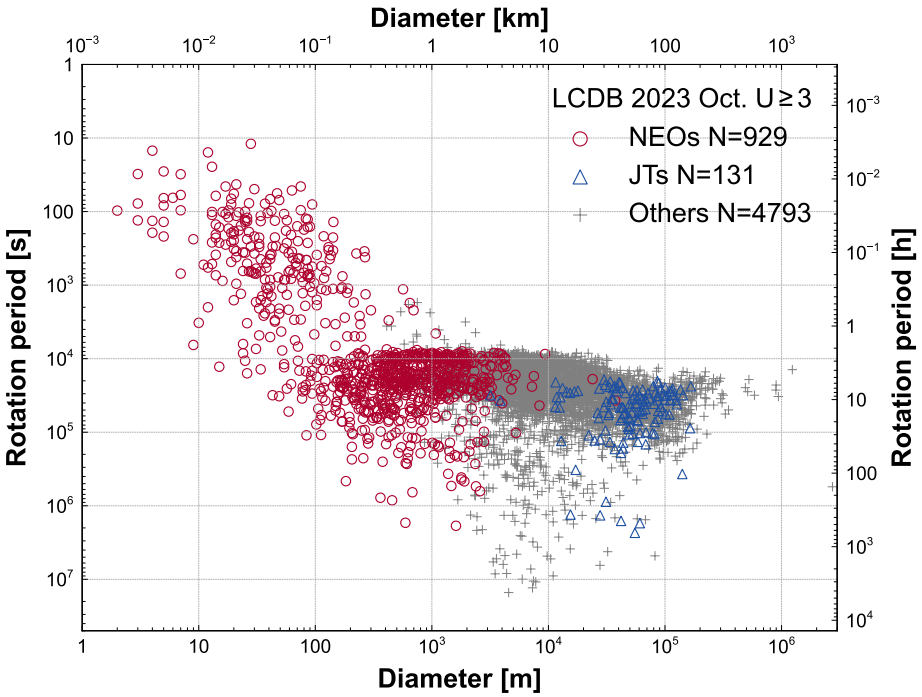

Figure 1.11. Diameter and rotation period relation. NEOs, JTs, and other objects (mainly MBAs) are presented in open circles, triangles, and plus signs, respectively.

Database of Asteroid Models from Inversion Techniques (DAMIT[23], Ďurech et al. 2010). Shape models were also made in a combination of dense lightcurves and sparse photometry (Hanuš et al. 2016a), or even only sparse photometry such as the Lowell photometry database (Ďurech et al. 2016), Gaia catalogs (Ďurech & Hanuš 2018, 2023), ATLAS photometry (Ďurech et al. 2020, 2022a), and combinations of these catalogs (Ďurech et al. 2019). In conjunction with occultation chords and mid-infrared observations, the size of the asteroids in addition to the shape models are derived (Ďurech et al. 2011, 2017, 2018a).

As in the case of the rotation state, radar observation is a strong technique to derive a shape of an asteroid. Especially, NEAs during the close approaches were intensively studied (Virkki et al. 2022).

The adaptive optics (AO) system on large telescopes such as Subaru telescope and Very Large Telescope (VLT) are necessary to achieve diffraction limited images from the ground. As seen in Figure 1.12, the targets are limited to a small fraction of a whole population even with direct imaging with the AO and large telescopes.

Recently, occultation observations of a number of asteroids were reported thanks to the high accuracy of the prediction with the advent of the Gaia satellite. Multiple chords are indicative of the projected shape of the asteroid (e.g., Devogèle et al. 2020; Yoshida et al. 2023).

1.5.5. Size

Thermal observation gives a strong constraint on the size of the asteroid because thermal flux weakly depends on albedo than visible flux (Lebofsky et al. 1986; Mainzer et al. 2011). Given an incoming solar flux density in visible wavelength, $F_{\odot,\nu}$, onto an asteroid, $F_{\odot,\nu}p_{\mathrm{V}}$ is reflected on the asteroidal surface and the left is absorbed and reemitted as a thermal flux, The flux density of the reflected light from an

[23] https://astro.troja.mff.cuni.cz/projects/damit/

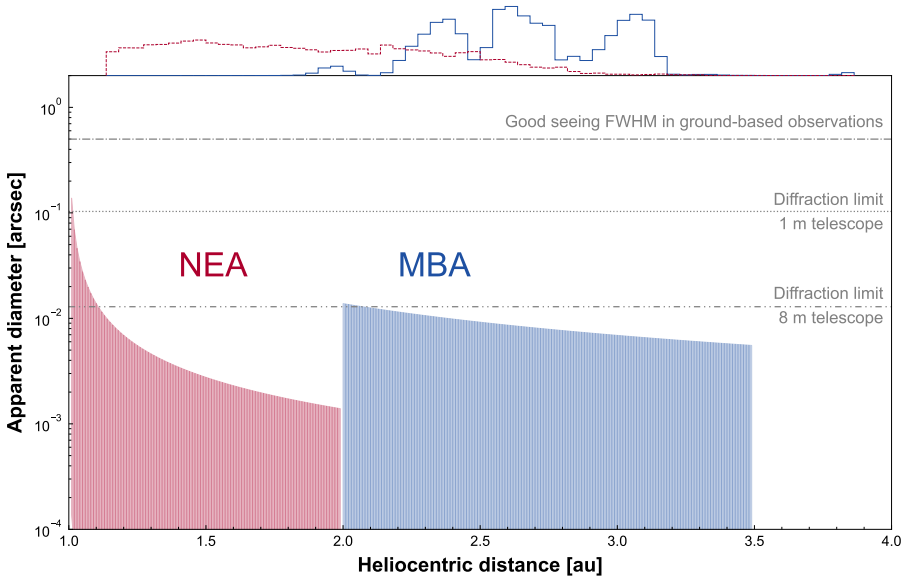

Figure 1.12. Distances of asteroids from the Earth versus apparent diameters. Hatched regions in left side and middle part are apparent diameters of NEAs ($D \leq 1$ km) and MBAs ($D \leq 10$ km), respectively. Histograms in upper part are normalized fractions of MBAs (solid line) and NEAs (dashed line) in each semimajor axis bin, not heliocentric distance. Good seeing full width at half maximum (FWHM) in ground-based observations, ~ 0.5 arcsec and diffraction limits in optical wavelengths using 1 and 8 m telescopes are shown by dotted–dashed, dotted, and double dotted–dashed lines, respectively.

asteroid with a cross-section of $S_{\rm ast}$ is thus written as:

$$F_{{\rm ref},\nu} = F_{\odot,\nu}\frac{S_{\rm ast}}{\Delta^2}p_{\rm V} \propto p_{\rm V}, \tag{1.7}$$

where

$$F_{\odot,\nu} = B_\nu(T_\odot)\frac{S_\odot}{r_{\rm h}^2}. \tag{1.8}$$

$B_\nu(T)$ is the Planck function, $T_\odot = 5772$ K is the temperature of the Sun, and $S_\odot$ is a cross-section of the Sun seen from the asteroid. Meanwhile, the flux density of the thermal emission from the asteroidal surface is written as follows:

$$F_{{\rm th},\nu} = \varepsilon B_\nu(T_{\rm eff})\frac{S_{\rm ast}}{\Delta^2}, \tag{1.9}$$

where ε is an emissivity and $T_{\rm eff}$ is an effective temperature of an asteroid's surface. An accurate determination of the surface temperature is not easy without knowledge of such as rotation, thermal inertia, and surface grain size of the asteroid. The temperature distribution is given as follows introducing sub-solar temperature, $T_{\rm ss}$ (Harris 1998):

$$T(\omega) = T_{\rm ss}\cos^{1/4}(\omega), \tag{1.10}$$

$$T_{\rm ss} = \sqrt[4]{\frac{(1-A)F_\odot}{\eta\varepsilon\sigma_{\rm SB}r_{\rm h}^2}}, \tag{1.11}$$

where ω is an angular distance from the sub-solar point, $F_\odot = 1366$ W m^{-2} is the solar constant, η is a beaming parameter, and $\sigma_{\rm SB}$ is the Stefan–Boltzmann constant. Since $T_{\rm eff} \sim T_{\rm ss} \propto (1-A)^{1/4} \propto$

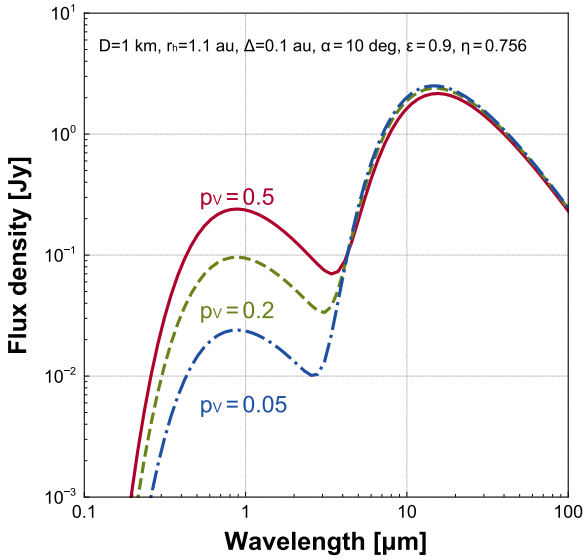

Figure 1.13. Spectral energy distributions for 1 km NEAs observed at a phase angle of 10° with visible geometric albedos of 0.5 (solid line), 0.2 (dashed line), and 0.05 (dotted-dashed line). Geocentric and heliocentric distances are 1.1 and 0.1 au, respectively. Emissivity of 0.9 and beaming parameter of 0.756 are assumed. Effective temperature of the asteroid is calculated with the Standard Thermal Model (STM, Lebofsky et al. 1986). Phase angle corrections in visible and infrared are performed using a simple exponential and linear model (Kaasalainen et al. 2001) and a linear model with a slope of 0.01 mag deg^{-1} (Lebofsky & Spencer 1989), respectively.

$(1 - qp_{\rm V})^{1/4}$, where q is a phase integral (Shevchenko et al. 2019), $F_{{\rm th},\nu}$ has a weak dependence on $p_{\rm V}$ rather than $F_{{\rm ref},\nu}$. We show three SEDs of asteroids with different albedos, $p_{\rm V}$ of 0.5, 0.2, and 0.05 in Figure 1.13. The SEDs are remarkably different in visible to near-infrared wavelengths ($\leq$ 3 μm), whereas almost the same in mid-infrared wavelengths ($\geq$ 5 μm). The thermal measurements are thus fundamental to estimating the diameter of asteroids owing to their weak dependence on $p_{\rm V}$.

The photometric measurements are also indicative of the diameters of asteroids. The diameter of an asteroid can be estimated with an absolute magnitude (brightness at a phase angle of zero, see Appendix B) and geometric albedo in the V band using the following equation (Fowler & Chillemi 1992; Pravec & Harris 2007):

$$D = \frac{1329}{\sqrt{p_{\rm V}}} \times 10^{-H_{\rm V}/5}. \tag{1.12}$$

The constant in the equation, 1329, is determined by the measurements of the absolute magnitude of the Sun in the V band(Pravec & Harris 2007), and the unit of diameter is in km. The observations with phase angles down to $< 10°$ are desired to accurately derive the absolute magnitude considering the opposition effect, which is a brightness surge at small phase angles (Belskaya & Shevchenko 2000). Otherwise, the estimated diameter depends on the model assumed. To determine the diameter D using Equation 1.12, we need to know $p_{\rm V}$ in addition to $H_{\rm V}$. When $p_{\rm V}$ is not available but its spectral type is determined, a typical albedo for each spectral type is usually assumed (e.g., Thomas et al. 2011; Usui et al. 2013).

Similar to the shape, direct imaging with a combination of the AO and large telescope as well as occultation observations is crucial to an accurate estimate of a diameter although the targets are very limited.

1.6. Open questions regarding near-Earth asteroids

Although the dynamical histories of NEAs have been studied for more than a hundred years as reviewed in Section 1.4, there are still several questions. Those are, for instance:

- What is the formation mechanism of NEAs?
- What is the dynamical evolution of NEAs?
- What are the surface properties and interior structures of NEAs?

Where and how NEAs are formed is an important open question since the origins of NEAs are closely related to the material transportation in our solar system. The formation mechanism of NEAs is still unclear, especially for small asteroids. Observationally, a number of binary NEAs are discovered by such as radar observations and lightcurve observations (e.g., Margot et al. 2015). And most of NEAs are thought to originate in the main belt (see Section 1.4). Are the current states of NEAs including binary systems not changed when they are in the main belt? Or did some mechanism such as the rotation fission (Walsh et al. 2008) change the population? A key to answering this question is asteroid pairs (Vokrouhlický & Nesvorný 2008). Unlike binaries, gravitationally unbound two asteroid components with common origin are called pairs. Asteroid pairs provide us insight into the formation mechanism of asteroids if they are genetically related. Some formation mechanisms have been proposed for the multiple asteroid systems, of which one of the leading formation mechanisms is the rotation fission (Walsh et al. 2008; Jacobson & Scheeres 2011; Jacobson et al. 2014, 2016). In the near-Earth region, only five asteroid pairs have been reported so far (Ohtsuka et al. 2006, 2007; Moskovitz et al. 2019; de la Fuente Marcos & de la Fuente Marcos 2019; Fatka et al. 2022). A large discrepancy in the number of discoveries of NEA binaries ($N = 60$[24], Pravec & Harris 2007) and pairs ($N = 5$) are possibly due to the chaotic behavior of their dynamical evolution. Frequent close encounters with inner planets change the orbits of NEAs in a shorter time scale compared to those of MBAs. Thus, the identification of NEA pairs using only current orbital elements is difficult. We lack the knowledge of the formation mechanism of NEAs.

How NEAs dynamically evolve is also a substantial question because it is directly relevant to material transportation as well as planetary defense. Recent studies posed questions about the dynamical evolution of NEAs. Seligman et al. (2023) reported unexpected large nongravitational accelerations for seven NEAs. They measured changes of orbits of NEAs by the Yarkovsky effect, and detected very large changes in the inactive six NEAs. One possibility is that some fractions of small NEAs are extinct comets in the near-Earth space (Seligman et al. 2023). Future characterizations are necessary to examine the dynamical evolution of NEAs. The study of NEA pair 2019 PR_2–2019 QR_6 (Fatka et al. 2022) may be consistent with the conclusion of Seligman et al. (2023); they explained the orbital evolution of the pair considering cometary activity. On the other hand, since the Yarkovsky effect is dependent on the pole orientation, evolution of the spin state is also crucial to investigate the orbital histories of NEAs. Golubov & Krugly (2012) and Zhou et al. (2022) introduced new types of YORP effect, tangential YORP (TYORP) and crater-induced YORP (CYORP), respectively. The spin and orbital evolution may be different whether we consider the TYORP or not (e.g., Kanamaru et al. 2021). However, the importance of TYORP is still under debate and our knowledge is very limited. Moreover, the spin state change of the NEA (3200) Phaethon is reported (Marshall et al. 2022). The acceleration is too large to explain by the YORP, and the key mechanism of the spin acceleration is poorly understood.

We emphasize that the surface properties and interior structures of NEAs are not completely understood, although it is significant to examine material transportation; how much water and organic materials could be delivered to the Earth? In terms of planetary defense, an understanding of the properties of NEAs such as composition, size, and strength is essential to evaluate and mitigate the damage of asteroid impacts. There are a handful of empirical relationships such as photometric phase slope–albedo relation

[24] https://www.asu.cas.cz/~asteroid/binastdata.htm, 2019-01-06 version.

(e.g., Belskaya & Shevchenko 2000), polarimetric phase slope–albedo relation (e.g., Geake & Dollfus 1986; Cellino et al. 2015), and a tight correlation between spectral type and albedo. These empirical relationships were established using observational data of mainly large MBAs ($D \geq 1$ km), which are bright and relatively easily observed. Nevertheless, the photometric phase slope–albedo relationship is also valid for some small NEAs, e.g., Ryugu (Ishiguro et al. 2014). Meanwhile, a recent study showed that the interpretation of the slope of the phase curve is difficult; we might not be able to use the empirical relation between the photometric phase slope and albedo (Arcoverde et al. 2023). One possible explanation is that the difference in size between observed MBAs and NEAs. As seen in Figure 1.11, smaller asteroids are rotating faster. The weak surface gravity and strong centrifugal force due to the fast rotation may remove fine grains on the surface of relatively small NEAs, and then different surface properties may be expected. Results of recent spectroscopic surveys also indicate that the spectral distribution of NEAs is different from that of MBAs (Devogèle et al. 2019; Marsset et al. 2022; Michimani et al. 2023). Special care should be taken to investigate the surface properties of NEAs.

1.7. Tiny near-Earth asteroids

In this dissertation, we particularly focus on tiny NEAs to attempt to solve open questions introduced in the previous section since we could put an end to the size dependence of the formation mechanism, dynamical evolution, and surface properties as well as interior structures of NEAs by utilizing such extremely small bodies. The uniqueness and challenges in observations as well as recently reported fascinating studies of tiny NEAs are summarized in this section.

1.7.1. What tiny near-Earth asteroids tell us

Tiny (diameter less than 100 m)[25] asteroids are the smallest limit among asteroids, and they are worthy of interest to investigate the formation mechanism, dynamical evolution, and surface properties as well as interior structures of the whole NEA population in a wide size range. Given the fact that tiny MBAs are too faint to be discovered even using 8 m class ground-based telescopes as shown in upper panel of Figure 1.5, only NEAs and a limited number of spacecraft mission targets give us knowledge about tiny asteroids. We could investigate the nature of tiny bodies utilizing tiny NEAs. Moreover, thanks to their changeabilities of orbits and rotation states by the Yarkovsky (Equation 1.1) and YORP effect (Equation 1.2), respectively, smaller asteroids have experienced larger changes in both the orbital and rotation states (Figure 1.7). Thus, the current orbital and rotation states of tiny asteroids may have important pieces of information to understand their dynamical histories. Since the Yarkovsky and YORP strengths are also dependent on physical properties such as shape and thermal conductivity, the orbits and rotation period distribution of tiny objects probably give knowledge of the physical properties of tiny bodies as well. Therefore, tiny asteroids are valuable targetfor understanding the formation mechanism and dynamical evolution of the whole NEA population as well as investigation of the nature of NEAs such as surface properties and internal structures.

1.7.2. Challenges in observations of tiny near-Earth asteroids

The increase in the number of discoveries of NEAs implies that the chance of characterization of NEAs is also increasing. However, we have to conduct quick response observations to characterize tiny NEAs soon after discoveries. As an example, an ephemeris of a tiny NEA 2020 EO is shown in Figure 1.14. The tiny asteroid 2020 EO was discovered by Jin Beniyama from the survey observation using the wide-field CMOS camera Tomo-e Gozen (Sako et al. 2018) at Kiso Observatory, Japan on March 12, 2020 around UT 11:00. 2020 EO is an Apollo-class NEA, and its absolute magnitude in the V band is 25.9 in NASA JPL SBDB. A diameter of 2020 EO is estimated to be $\sim$ 20 m with the $H_{\rm V}$ of 25.9 assuming its geometric albedo of 0.20, which is actually too small to be observed in the main belt.

In the top panel of Figure 1.14, the apparent V band magnitude of 2020 EO is about 16.5 at the time of the discovery and brighter than 18 until March 16, when the NEA was observed around the world. As shown in the second to top panel of Figure 1.14, the elevation of 2020 EO from Kiso Observatory has never reached larger than 30° after March 15. Although the target was observed outside Japan after March 15, the observing window to characterize the tiny asteroid using 1–2 m class telescopes is typically limited to less than a week in terms of visibility. The phase angles of 2020 EO are always larger than $\sim$ 25° in 2020 apparition as seen in the second to bottom panel of Figure 1.14. This means that the observations of NEAs are sometimes limited to a certain range of phase angles. The empirical relations such as phase slope–albedo relation (Shevchenko 1996; Belskaya & Shevchenko 2000) are hardly applicable to those NEAs to derive their physical properties. The velocities of 2020 EO are shown in the bottom panel of Figure 1.14. The apparent motions on the sky are as large as a few arcsec $\rm s^{-1}$ during the close approach.

Finally, we emphasize the necessity of follow-up observations of tiny asteroids soon after the discovery in Figure 1.15. 2020 EO never becomes brighter than 24 in the V band in the next 30 years except for the

[25] We define tiny asteroids as asteroids smaller than 100 m in diameter throughout this dissertation.

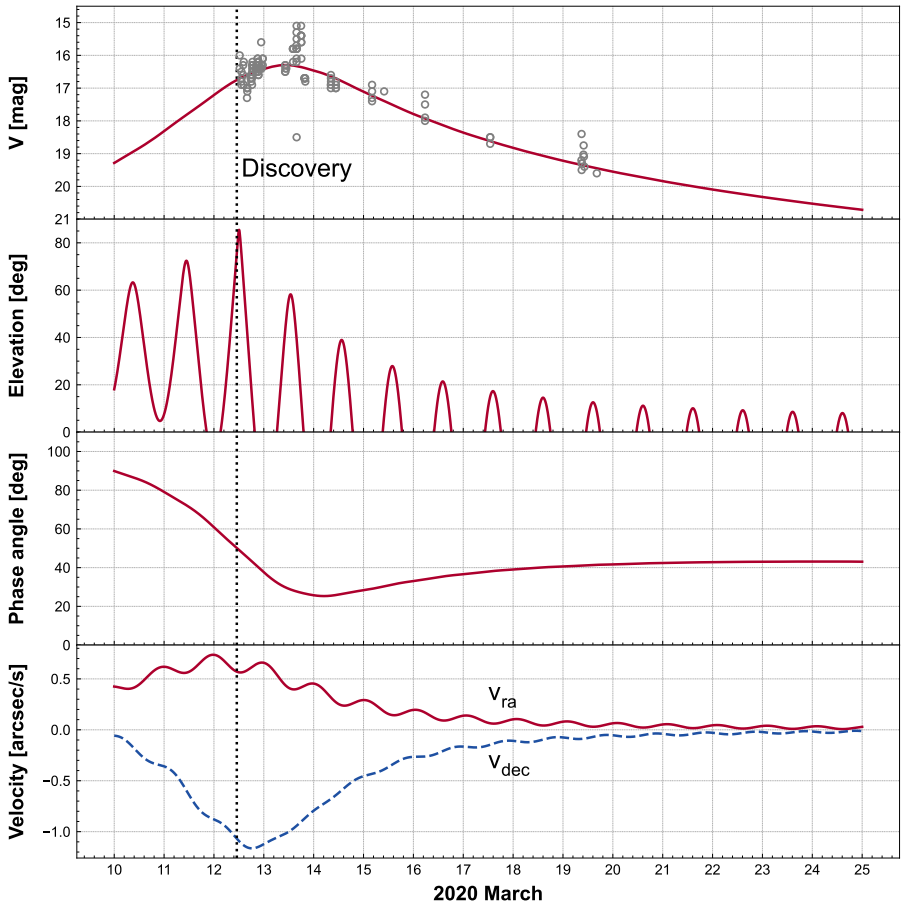

Figure 1.14. Short ephemeris of a tiny NEA 2020 EO before and after its discovery from Kiso Observatory, Japan. The ephemeris is referenced from the NASA JPL HORIZONS. The time of discovery is indicated by a horizontal dotted line. (top panel) Predicted V band magnitude. Observations registered in the MPC database are represented by circles. (second to top panel) Elevation. (second to bottom panel) Solar phase angle. (bottom panel) Velocities along RA (solid line) and Dec (dashed line) directions.

2020 apparition (upper panel of Figure 1.15). As shown in middle panel of Figure 1.15, the positional uncertainties are gradually increasing and as large as 1000 arcsec in three years, which is comparable to the field of view of most ground-based telescopes. Characterizations of tiny NEAs are thus *once-in-a-lifetime opportunities*. Actually, for instance, the fraction of NEOs whose spectral type are estimated are $\sim 1/3$, $\sim 1/10$, and $\sim 1/100$ for km-class, 0.3–1 km-class , and less than 300 m-class bodies, respectively (Perna et al. 2018).

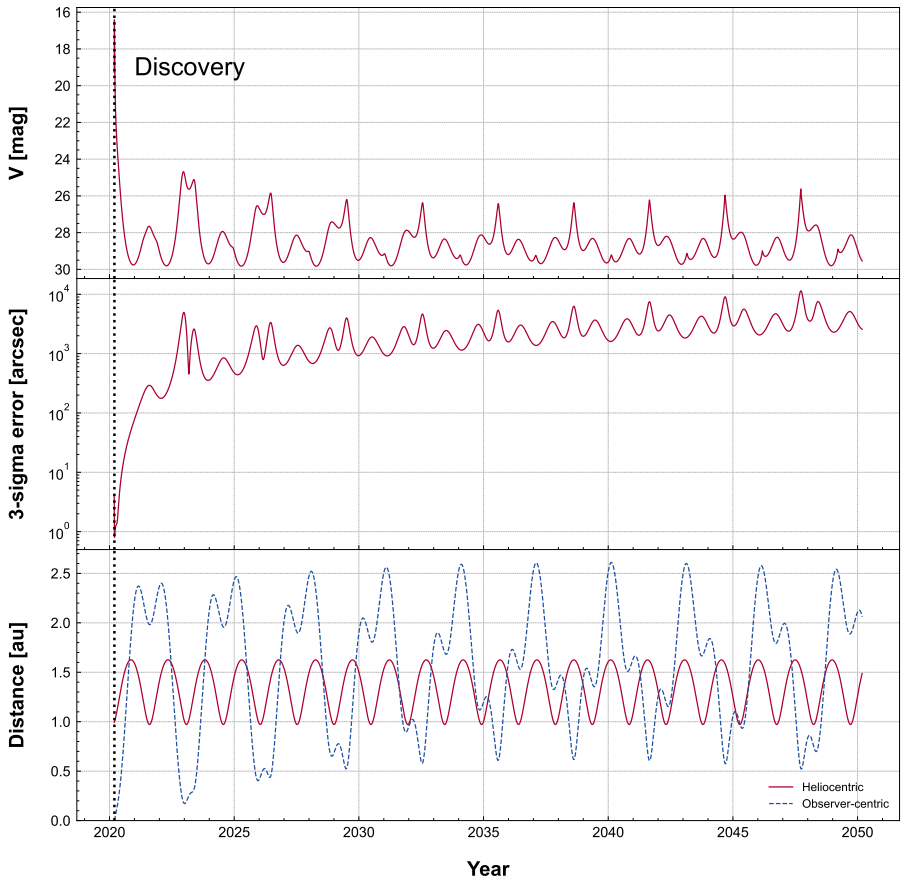

Figure 1.15. Long ephemeris of a tiny NEA 2020 EO for 30 years from Kiso Observatory, Japan. The ephemeris is referenced from the NASA JPL HORIZONS. The time of discovery is indicated by a horizontal dotted line. (top panel) Predicted V band magnitude. (middle panel) 3-sigma orbital uncertainty. (bottom panel) Heliocentric and observer-centric distances.

1.7.3. Surprising and mysterious properties of tiny asteroids

Recent observational studies focusing on tiny asteroids are often surprising and mysterious. They have revealed the need for further investigation of tiny asteroids.

Six out of the seven NEAs with large nongravitational accelerations reported in Seligman et al. (2023) are tiny NEAs: 2006 RH_{120}, 1998 KY_{26}, 2005 VL_1, 2016 NJ_{33}, 2010 VL_{65}, and 2010 RF_{12}. They include two fast-rotating asteroids 1998 KY_{26} (Ostro et al. 1999) and 2016 RH_{120} (Granvik et al. 2012). This may imply that we lack the knowledge of surface properties of tiny and/or fast-rotating asteroids.

Terai et al. (2013) observed the tiny L-type NEA (367943) Duende across a wide phase angle range from 19° to 42°. They derived the slope parameter in the H-G model, G, as $0.44^{+0.06}_{-0.08}$, which is larger than the typical value of L-types. The tiny asteroid Duende has a shallow slope in the phase curve. They interpreted the large slope parameter or shallow slope with the difference of surface environment due to the lack of the fine regolith or high geometric albedo. Small gravity on tiny asteroids might lead to the lack of the fine regolith on its surface. The shadow-hiding effect is weak when the fine regolith is deficient, and the slope of the phase curve would be shallow. Other recent studies showed that there is almost no correlation between albedo and slope parameters using the phase curves obtained in the framework of the IMPACTON project and the ATLAS survey (Rondón et al. 2019; Arcoverde et al. 2023). They interpreted this is due to the difference in diameters between NEAs and MBAs. These studies on phase curves of NEAs suggest that we might not be able to use the empirical relation between the photometric phase slope and albedo, especially for tiny NEAs.

Licandro et al. (2023) found that a visible spectrum of the tiny fast-rotating asteroid 2022 AB ($D \sim 65$ m and rotation period $P \sim 3$ minutes) shows an upturn over the 0.4 to 0.6 μm, which does not fit with any known asteroid spectrum. Based on recent spectroscopic surveys, the small NEAs might have a different distribution from large asteroids such as overabundances of D- and A-types (Perna et al. 2018; Devogèle et al. 2019; Marsset et al. 2022; Michimani et al. 2023). The overabundance of D- and A-types in small NEAs may imply the fragility of carbonaceous and olivine-rich materials, respectively (Michimani et al. 2023). Moreover, the overabundance of D-types is interpreted due to the space weathering effect from D- to C- or P-types (Marsset et al. 2022). More and more characterizations are desired to clarify the idea of a non-homogeneous NEO population (Michimani et al. 2023). Reddy et al. (2016) conducted radar, lightcurve, and spectroscopic observations of the tiny E-type NEA 2015 TC_{25} ($D \sim 2$ m). They concluded that 2015 TC_{25} is a fragment possibly ejected from the E-type main belt asteroid Nysa. One of the interesting properties of 2015 TC_{25} is its bluer spectrum compared to a typical E-type. They explained the bluer slope of 2015 TC_{25} in the visible wavelength with a lack of fine regolith on the surface due to a combination of weak gravity and fast rotation.

Using the IRAC on the SST, Mommert et al. (2014a,b) conducted infrared observations of the tiny NEAs 2011 MD ($D \sim 10$ m) and 2009 BD ($D \leq 5$ m). According to these observations, asteroid 2009 BD has an inconclusive surface nature which could be either covered by fine regolith or composed of a collection of bare rocks, while the bulk density of 2011 MD is estimated to be $1.1^{+0.7}_{-0.5} \times 10^3$ kg m^{-3}, indicating a porous structure. The results are consistent with direct detections of radiation pressure on the two NEAs (Micheli et al. 2012, 2014). Recently, Fenucci et al. (2021, 2023) found that the tiny superfast rotators (499998) 2011 PT ($D \sim 35$ m and $P \sim 10$ minutes) and 2016 GE_1 ($D \sim 12$ m and $P \sim 34$ s) have small thermal conductivities of $K \leq 0.1$ W m^{-1} K^{-1} and $K \leq 0.001$ W m^{-1} K^{-1}, respectively. Such small conductivities imply that these two tiny asteroids are covered with fine regolith or highly porous rocks (Avdellidou et al. 2020; Cambioni et al. 2021).

The above results by photometry, spectroscopy, and thermal observations might suggest the difference in surface properties as well as internal structures between large and tiny asteroids, or be indicative of the nature of tiny bodies. However, the interpretations are still inconclusive.

1.8. Scope of this dissertation

The scope of this dissertation is depicted in Figure 1.16. In this dissertation, we present the results of three comprehensive observational studies of tiny NEAs. We have overcome the difficulties in observations of tiny asteroids by quick response or well-planned campaign observations using high-speed CMOS cameras. The objectives of this dissertation are to examine the formation mechanism, dynamical evolution, and surface properties as well as interior structures of NEAs.

The dissertation is organized as follows. The Chapter 2 to Chapter 4 are summarized to stand alone. In Chapter 2, we describe video observations of more than a hundred tiny NEAs. The rotation period distribution is a valuable tracer to investigate not only the YORP effect, but also the surface properties and interior structures of tiny bodies. We have obtained 2 fps optical lightcurves of 108 tiny NEAs. In Chapter 3, we present the results of observations of the tiny NEA 2015 RN_{35}. We have conducted optical multicolor photometry of the tiny NEA 2015 RN_{35} ($D \sim 40$ m) across a wide range of phase angles from 2° to 30° using two telescopes. We use a dense phase curve of the tiny asteroid 2015 RN_{35} to investigate the surface properties of the tiny asteroid. In Chapter 4, we focus on a member of the possible NEA pair, 2010 XC_{15}. We have conducted optical multicolor photometry and polarimetry of the NEA pair candidate 2010 XC_{15} ($D \sim 100$ m) using four telescopes. We investigate the formation mechanism of the small NEA 2010 XC_{15} through optical multicolor photometry and polarimetry as well as orbital integration. Finally, we discuss the formation mechanism, dynamical history, and surface properties as well as interior structures of NEAs in Chapter 5 combining the parts into a whole.

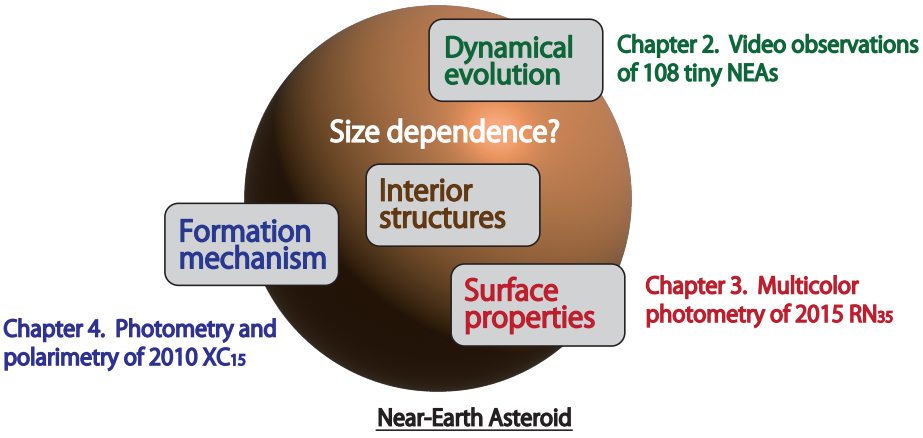

Figure 1.16. Scope of this dissertation.

So keep looking until you find it. Don't settle.
— Steve Jobs (1955–2011)

2. *Video Observations of Tiny Near-Earth Asteroids*

In this chapter, we report the results of video observations of tiny NEOs with Tomo-e Gozen on the Kiso 1.05 m Schmidt telescope. A rotation period of a tiny asteroid reflects its dynamical history and physical properties since smaller objects are sensitive to the YORP effect. We carried out video observations of 108 tiny NEOs at 2 fps from 2018 to 2023 and successfully derived the rotation periods and axial ratios of 52 NEOs including 23 fast rotators with rotation periods less than 60 s. The fastest rotator found during our survey is 2020 HS_7 with a rotation period of 2.99 s. We statistically confirmed that there is a certain number of tiny fast rotators in the NEO population, which have been missed with any previous surveys. We have discovered that the distribution of the tiny NEOs in a diameter and rotation period (D-P) diagram is truncated around a period of 10 s. The truncation with a flat-top shape is not explained well either by a realistic tensile strength of NEOs or suppression of YORP by meteoroid impacts. We propose that the dependence of the tangential YORP effect on the rotation period potentially explains the observed pattern in the D-P diagram.

A part of contents of this chapter has been published in Beniyama et al. (2022).

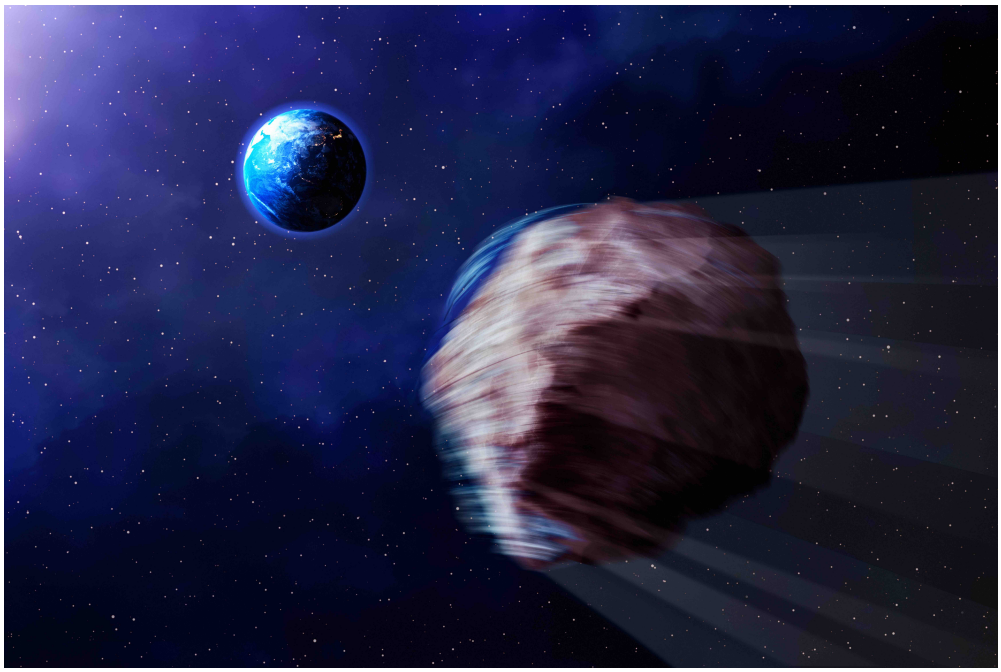

Figure 2.1. Illustration of fast-rotating tiny NEO during the close approach.
Credit: Kiso Observatory

2.1. Introduction

As of March 2022, 28527 NEOs have been discovered by wide-field monitoring surveys such as CSS (Drake et al. 2009), Pan-STARRS (Chambers et al. 2016), and ATLAS (Tonry et al. 2018; Tonry 2023). Most NEOs have their origins in the main belt (e.g., Bottke et al. 2000; Granvik et al. 2018). Asteroidal fragments are generated from collisional events in the main belt and their orbital elements are gradually changed by the Yarkovsky effect, which is a thermal force caused by radiation from the Sun (e.g., Vokrouhlický 1998; Vokrouhlický et al. 2000; Bottke et al. 2006). When the asteroids enter into orbital resonances with giant bodies, their orbits evolve to those of NEOs in a few Myr (e.g., Gladman et al. 1997; Bottke et al. 2006). During the orbital evolution, the rotation states (i.e., rotation period and pole direction) of the object are changed by the YORP effect, which arises from asymmetricity of scattered sunlight and thermal radiation from its surface (e.g., Rubincam 2000; Vokrouhlický & Čapek 2002; Čapek & Vokrouhlický 2004; Bottke et al. 2006). The YORP effect caused by a recoil force normal to the surface, NYORP, is investigated intensively in previous studies. Recently, the tangential YORP (TYORP) effect, which is caused by a recoil force parallel to the surface, was proposed by Golubov & Krugly (2012).

Since the strength of the YORP effect increases with decreasing diameter, smaller asteroids would experience a larger change in the rotation states. Thus, YORP is a dominant mechanism to change the rotation states of km-sized or smaller asteroids (Vokrouhlický & Čapek 2002). The rotation acceleration by YORP leads to deformation or rotation fission of the asteroid due to a strong centrifugal force. Because the YORP strength is also dependent on physical properties such as shape and thermal conductivity, the rotation period distribution of smaller objects probably reflects the dynamical history and physical properties.

In general, it is difficult to constrain the rotation states of tiny asteroids due to limited observational windows (hours to days), fast rotation (less than a minute), and large apparent motion on the sky (a few arcsec s^{-1}). Observations with exposure times sufficiently shorter than their rotation periods are required. The shorter exposure times are effective to suppress the trailing sensitivity loss effect, which is the degradation of a surface brightness of a moving object on an image (Zhai et al. 2014).

The LCDB (Warner et al. 2009) contains thousands of rotation periods of minor planets. The diameter and rotation period relation (hereinafter referred to as D-P relation) is shown in Figure 2.2. As of June 2023, rotation periods of 5853 objects are estimated with high accuracy (the quality code U in Warner et al. (2009) is 3 or 3-, see Table 2.1). For asteroids larger than 200 m in diameter, the rotation period distribution is truncated around two hours. This clear structure is called the cohesionless spin barrier and indicates most of the larger asteroids are rubble-piles (Pravec & Harris 2000). It is possible to constrain the physical properties of asteroids smaller than 200 m in diameter from the D-P relation as same as the larger asteroids. However, there is a smaller number of smaller asteroids for which the rotation period has been reported so far.

The LCDB has the observational results of MANOS, which obtained more than 300 lightcurves of small NEOs with the mean absolute magnitude of about 24 using large and medium aperture telescopes (Thirouin et al. 2016, 2018). Although MANOS successfully derived the rotation periods of NEOs with high accuracy, the main motivation of the survey is not to detect fast rotators, but to characterize mission-accessible NEOs. Due to a relatively long exposure time (1–300 s), the survey possibly undetected the very fast rotations. Systematic high-speed observations are required to correctly derive shorter rotation periods and obtain an unbiased D-P relation of tiny NEOs.

In this chapter, we report the results of imaging observations at 2 fps of 108 tiny NEOs with the wide-field CMOS camera Tomo-e Gozen. The observed NEOs are smaller than 100 m in diameter and their mean diameter is 15 m. The aims of this study are to obtain an unbiased D-P relation by video observations and to reveal dynamical histories and physical properties of tiny NEOs. Observations and data reduction are described in Section 2.2. The results are compared with previous studies in Section

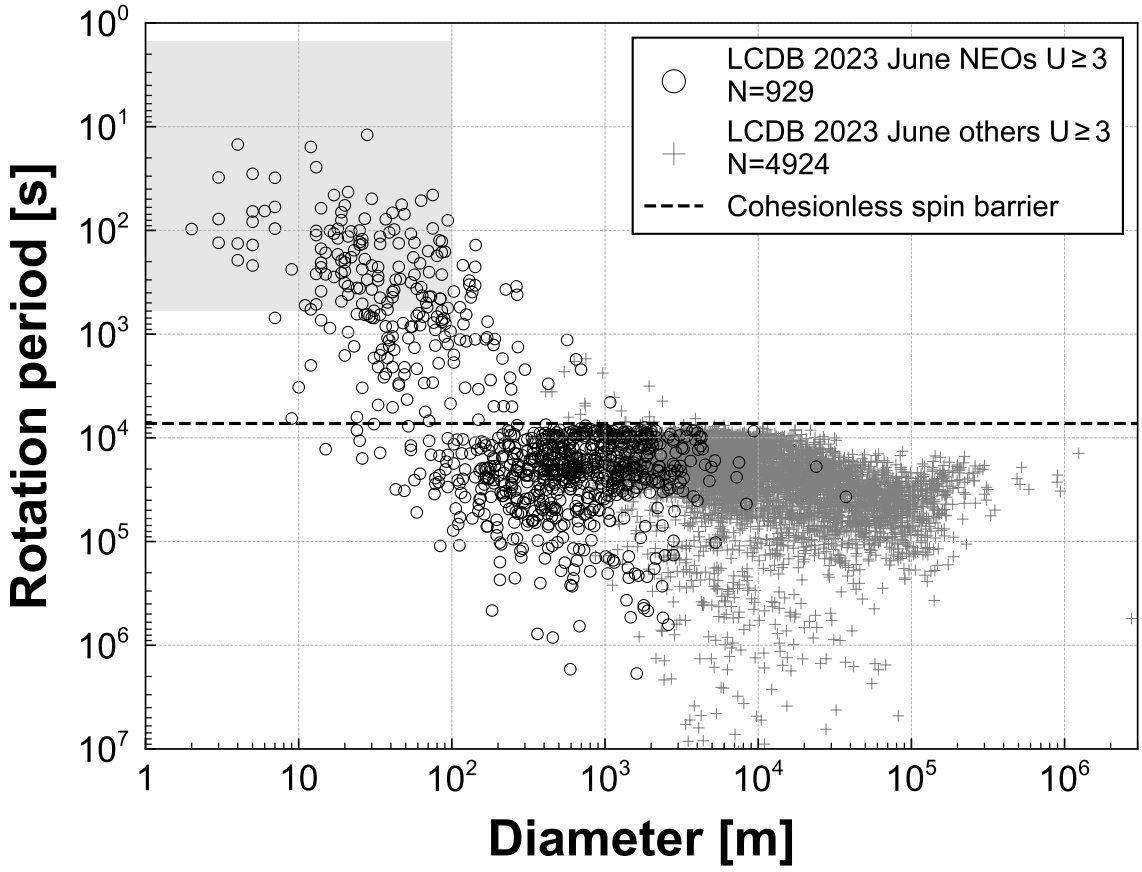

Figure 2.2. Diameter and rotation period relation of the objects in the LCDB (Warner et al. 2009) as of 2023 October. NEOs and other objects (main belt and trans-Neptunian objects) are presented in filled circles and plus signs, respectively. A cohesionless spin barrier assuming a typical density of S-type asteroids of 2.67 g cm^{-3} (Yeomans et al. 2000) is shown by a dashed line. Tiny ($D \leq 100$ m) and fast ($P \leq 10$ minutes) biased region is shown as a gray shaded area.

Table 2.1. Quality code of lightcurves in the LCDB (Warner et al. 2009)

U	Meaning
0	Result later proven incorrect. This appears only on records of individual observations.
1, 1-, 1+	Result based on fragmentary lightcurve(s), may be completely wrong.
2, 2-, 2+	Result based on less than full coverage, so that the period may be wrong by 30% or so. Also, a quality of 2 is used to note results where an ambiguity exists as to the number of extrema per cycle or the number of elapsed cycles between lightcurves. Hence the result may be wrong by an integer ratio.
3, 3-	Denotes a secure result with no ambiguity and full lightcurve coverage.

Note. — In some cases, the numerical quality code may be followed by a plus or minus sign, indicating that the reliability is judged somewhat better (+) or worse (−) than implied by an un-signed number alone. This refinement in scale has been only recently added, and not yet retroactively, so most entries do not have signs, even in those cases where they would be appropriate.

2.3. In Section 2.4, the D-P relation of the tiny NEOs obtained in this study is discussed taking into account the spin acceleration by YORP.

2.2. Observations and data reduction

2.2.1. Observations

We conducted photometric observations at 2 fps with the wide-field CMOS camera Tomo-e Gozen (Sako et al. 2018). Tomo-e Gozen is a wide-field high-speed camera mounted on the 1.05 m Schmidt telescope at Kiso Observatory (Minor Planet Center code 381) in Nagano, Japan. The field of view is 20.7 square degrees covered by 84 chips of CMOS sensors without photometric filters. A timestamp of each image data is GPS-synchronized and has a time accuracy of 0.2 milliseconds. We have performed 2 fps all-sky survey observations with Tomo-e Gozen since 2019. Data accumulated each night amounts to 30 TB, from which various types of transients such as supernovae and tiny NEOs are searched for. Tomo-e Gozen has discovered 49 NEOs from the survey data in real time from March 2019 to November 2023 with the fast-moving object pipeline using the machine-learning technique (Ohsawa et al. in prep.). The algorithms used in the pipeline are partly described in Ohsawa (2022).

We have obtained lightcurves of 108 NEOs from May 2018 to October 2023. Nominal criteria for target selection are that a V band apparent magnitude (V) is smaller than 17 and an absolute magnitude (H) is larger than 22.5. We referred V and H from the website of the International Astronomical Union Minor Planet Center[1] to make observation plans. We call our selected samples hereinafter the Tomo-e NEOs, which are listed in Table 2.2. The observation specifications are referenced from NASA JPL HORIZONS with using the `Python` package `astroquery` (Ginsburg et al. 2019). The Tomo-e NEOs consist of 72 NEOs discovered by other facilities and 36 NEOs discovered by Tomo-e Gozen itself. The V band magnitude of 17 corresponds to a 5σ limiting magnitude in 2 fps video observations with Tomo-e Gozen. An asteroid diameter (D) in Table 2.2 is derived from H using Equation 1.12 (Fowler & Chillemi 1992; Pravec & Harris 2007).

[1] https://minorplanetcenter.net/

In this study, we assume that p_V is 0.20, which is a typical value for S-type asteroids, as used in LCDB. The absolute magnitude of 22.5 corresponds to 94 m in diameter. Since a median rotation period of NEOs in LCDB satisfying the quality code U of 3 or 3- and H smaller than 22.5 is about 9 minutes, we set a nominal duration of observation as 20 minutes. A mean absolute magnitude of our samples is 26.6 corresponding to 14 m in diameter. As shown in Figure 2.3, the peak of the distribution ($H \sim 26$) is smaller than the peak of the targets observed by MANOS ($H \sim 24$), hereinafter referred to as the MANOS NEOs.

The Tomo-e NEOs were typically located at a few lunar distances from Earth when observed. A typical angular velocity was about a few arcsec s^{-1}. Most of the Tomo-e NEOs were discovered a few hours or a few days before our observations, except for 2010 WC_9, 2011 DW, 2017 WJ_{16}, 2017 WN_{13}, and 2015 RN_{35}. TMG0042, TMG0049, and TMG0061 are NEO candidates discovered by Tomo-e Gozen. Due to the limited number of follow-up observations, provisional designations for the two objects were not served from the Minor Planet Center.

To obtain the lightcurve of the NEO, we used a single sensor of Tomo-e Gozen with a field of view of $39.7' \times 22.4'$ and a pixel scale of 1.189 arcsec. Sidereal tracking and re-pointing were performed to follow the fast-moving NEOs. All of the Tomo-e NEOs except for 2018 LV_3 were observed at 2 fps. The lightcurve of 2018 LV_3 was obtained at 0.2 fps as an experimental observation.

2.2.2. Data reduction

Photometry

Observations are composed of a series of video data, that were typically a minute in length. The video data were compiled into cube FITS files. After bias and dark subtraction and flat-field correction, standard circle aperture photometry was performed on a target and reference stars in each frame using the SExtractor-based python package `sep` (Bertin & Arnouts 1996; Barbary et al. 2015). Since the elongations of the NEOs were negligible, we applied the standard aperture photometry method. The aperture radius was set to 2 to 3 times larger than the FWHM of the point spread function (PSF) of reference stars, which was typically 3 to 5 arcsec. We determined the FWHM of the stellar PSF in the first frame of the cube, and then conducted the photometry of the objects in each frame. Sometimes the target was too faint to be detected possibly by the brightness variation of the target. In such cases, we set the aperture at the expected positions interpolated from the positions in adjacent frames and performed forced photometry.

We used the G band magnitude of Gaia DR2 catalog as brightness references since the spectral response of Tomo-e Gozen (350 to 950 nm, Kojima et al. 2018). is similar to that of the G band of Gaia (330 to 1050 nm, Gaia Collaboration et al. 2018). The difference in the spectral responses may affect the mean apparent magnitudes of the NEOs, but the rotation period is not affected by the spectral response and the effect on the amplitudes is negligible. The discussion in this study is not affected.

The G band magnitude of a NEO, m_G, on each frame was derived as follows:

$$m_G = -2.5 \log_{10} F + Z, \tag{2.1}$$

where F is a total flux in the aperture and Z is the magnitude zero point of the frame. Stars with G band magnitudes $10 < m_G < 15$ and broad-band colors $-1 < G_{\rm BP} - G_{\rm BP} < 1$, typically 20–30, were used to calculate the magnitude zero points and the median value of the zero points was used as Z. An uncertainty of Z was estimated from the median absolute deviation of the zero points. The photometric error of the NEO consists of the background noise, the Poisson noise, and the uncertainty of Z.

The observed G band magnitudes were converted to reduced magnitudes with the distance between the Sun and NEO (r) and NEO and observer (Δ) at the time of observations. The phase angle correction and the light-travel time correction were done to obtain the corrected lightcurves.

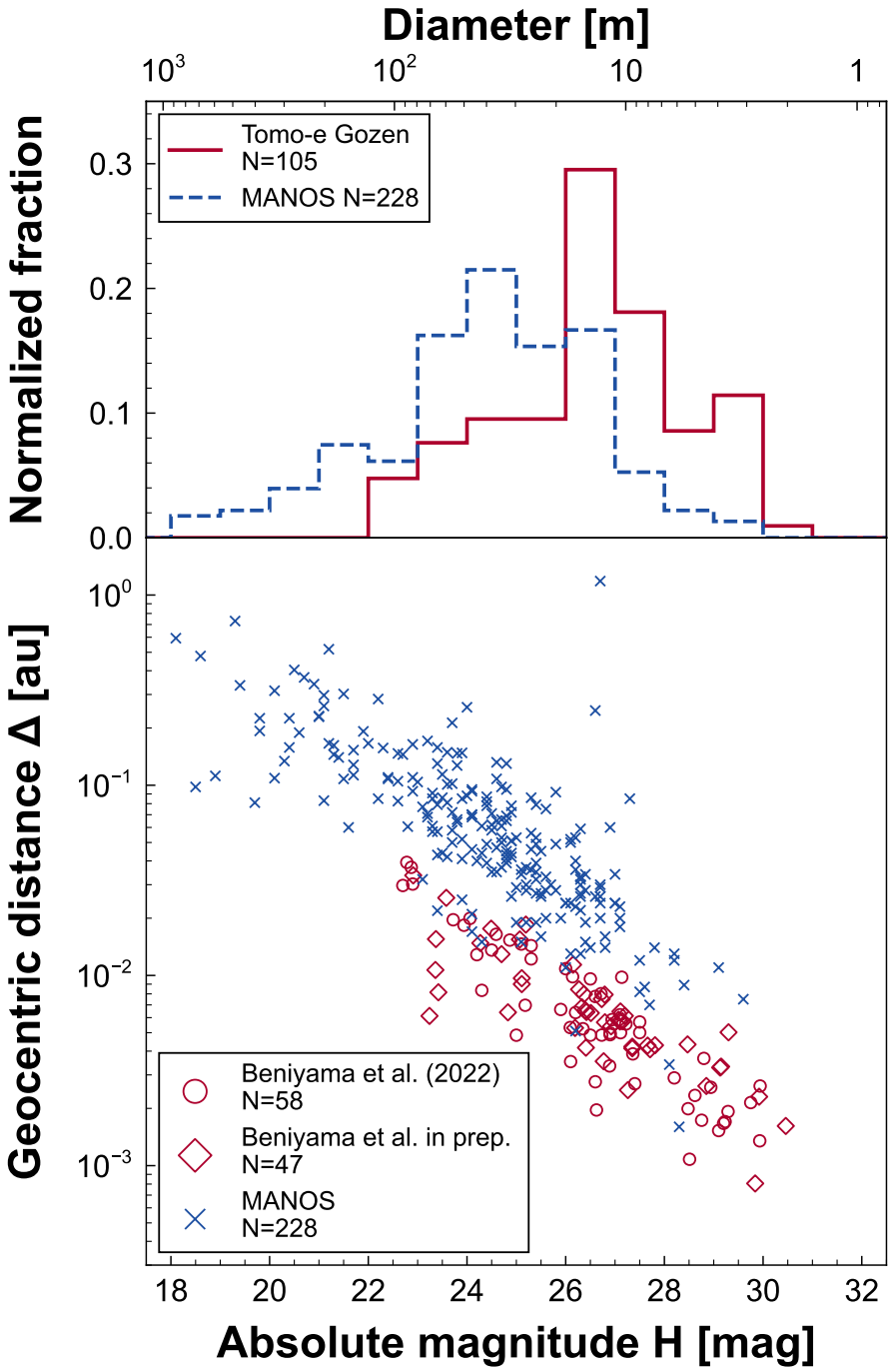

Figure 2.3. (upper panel) Fractional distribution of absolute magnitudes. Tomo-e NEOs and MANOS NEOs are illustrated by solid and dashed lines, respectively. (lower panel) Absolute magnitude versus geocentric distance of the Tomo-e NEOs and the MANOS NEOs at the observation times. Tomo-e NEOs in Beniyama et al. (2022) and new samples are represented by open circles and diamonds, respectively, whereas MANOS NEOs are represented by crosses. The absolute magnitude is converted to diameter using Equation 1.12 assuming a geometric albedo of 0.2. The absolute magnitude and the geocentric distances of Tomo-e NEOs in Beniyama et al. (2022) and new samples are referenced from NASA JPL HORIZONS as of 2021-12-27 (UTC) and 2023-11-05 (UTC), respectively. NEO candidates, TMG0042, TMG0049, and TMG0061, are not included in this figure.

Table 2.2. Summary of the observations

Object	Dyn. Class	H (mag)	$D^{\dagger}$ (m)	Obs. Date (UTC)	T (minutes)	V (mag)	Vel. (arcsec s^{-1})	α (°)	Δ (au)	r (au)	Note
2010 WC_9	Apollo	23.5	59	2018-05-15 12:19:01	14.0	12.3	2.3	28.0	0.0033	1.0138	
2011 DW	Aten	22.9	79	2021-02-28 15:15:36	20.0	16.4	0.5	10.0	0.0370	1.0271	
2017 WJ_{16}	Aten	24.5	37	2020-11-23 17:42:48	16.0	16.7	0.4	37.1	0.0136	0.9982	
				2020-11-25 13:30:59	60.0	16.7	0.3	34.9	0.0141	0.9986	
2018 LV_3	Apollo	26.5	15	2018-06-13 15:18:08	100.0	17.9	0.4	33.6	0.0096	1.0236	5 s exposure
2018 UD_3	Apollo	26.2	17	2018-11-01 13:47:46	36.5	17.1	1.0	50.3	0.0064	0.9966	
2019 BE_5	Aten	25.1	28	2019-02-01 09:58:47	114.0	17.5	0.7	39.1	0.0146	0.9967	
2020 EO	Apollo	25.9	20	2020-03-13 10:47:05	13.0	16.3	1.1	29.6	0.0066	0.9998	
2020 FA_2	Apollo	27.5	9	2020-03-18 16:53:30	44.0	17.4	1.3	22.5	0.0057	1.0008	
2020 FL_2	Apollo	26.1	18	2020-03-22 13:28:48	14.0	14.5	2.1	11.7	0.0035	1.0001	
2020 GY_1	Apollo	26.6	14	2020-04-05 17:16:28	14.0	14.9	1.3	24.0	0.0028	1.0032	
2020 HK_3	Apollo	24.2	43	2020-04-30 13:41:54	13.0	17.2	1.6	69.2	0.0129	1.0120	
2020 HS_7	Apollo	29.1	4	2020-04-28 14:36:31	14.0	16.0	3.0	19.1	0.0015	1.0085	
				2020-04-28 16:24:41	9.0	15.1	8.4	25.7	0.0009	1.0079	
2020 HT_7	Apollo	26.9	12	2020-04-27 16:40:37	13.0	16.9	1.1	39.5	0.0049	1.0105	
2020 HU_3	Apollo	26.0	19	2020-04-21 16:23:06	6.0	17.6	1.3	32.0	0.0109	1.0144	
2020 PW_2	Apollo	28.8	5	2020-08-14 16:46:48	24.0	17.8	2.0	24.8	0.0037	1.0162	crowded field
2020 PY_2	Apollo	26.5	15	2020-08-20 12:50:56	23.0	15.7	2.3	12.1	0.0049	1.0165	
2020 QW	Apollo	25.3	26	2020-08-17 16:10:51	20.0	18.3	0.9	73.4	0.0122	1.0158	crowded field
2020 TD_8	Apollo	26.9	12	2020-10-26 16:59:35	17.0	17.2	1.0	48.3	0.0050	0.9972	
2020 TE_6	Apollo	27.4	10	2020-10-18 10:30:50	19.0	16.8	3.2	62.9	0.0027	0.9975	
2020 TS_1	Aten	29.2	4	2020-10-12 10:13:04	9.0	16.8	3.6	37.4	0.0017	0.9993	
2020 UQ_6	Apollo	22.7	86	2020-10-28 17:30:35	17.0	16.0	0.4	16.0	0.0297	1.0219	
2020 VF_4	Apollo	26.6	14	2020-11-13 16:56:23	20.0	17.0	2.0	18.5	0.0078	0.9968	
2020 VH_5	Apollo	29.2	4	2020-11-13 17:33:04	21.0	15.9	5.4	7.7	0.0017	0.9912	
2020 VJ_1	Apollo	26.7	13	2020-11-09 15:23:30	20.0	16.6	3.1	34.1	0.0049	0.9944	
2020 VR_1	Apollo	28.9	5	2020-11-09 15:44:37	16.0	17.5	6.4	36.1	0.0026	0.9925	
2020 VZ_6	Apollo	25.0	30	2020-12-02 14:07:02	14.0	14.7	1.1	31.0	0.0049	0.9900	
2020 XH	Apollo	24.6	36	2020-12-05 16:35:39	17.0	16.8	0.6	24.2	0.0165	1.0004	crowded field
2020 XH_1	Apollo	22.9	78	2020-12-08 12:56:09	20.0	16.7	0.4	30.9	0.0302	1.0108	
2020 XQ_2	Apollo	22.8	83	2020-12-09 15:00:39	20.0	16.6	0.8	15.0	0.0393	1.0228	
2020 XX_3	Apollo	28.5	6	2020-12-17 14:09:52	18.0	16.5	1.0	38.0	0.0020	0.9856	
2020 XY_4	Aten	26.9	12	2020-12-20 11:10:51	20.0	17.3	2.1	40.3	0.0059	0.9883	thin cloud
2020 YJ_2	Apollo	27.4	10	2020-12-21 14:09:09	20.0	16.7	2.3	35.7	0.0039	0.9869	crowded field
2021 AT_5	Apollo	27.5	9	2021-01-13 13:40:09	10.0	16.9	1.8	17.9	0.0050	0.9884	crowded field
2021 BC	Aten	24.3	41	2021-01-21 10:55:35	18.0	15.9	1.8	55.7	0.0083	0.9888	
2021 CA_6	Apollo	28.5	6	2021-02-13 16:03:04	22.0	16.0	8.1	66.3	0.0011	0.9879	
2021 CC_7	Apollo	29.8	3	2021-02-12 18:06:58	11.0	17.1	2.6	11.5	0.0021	0.9894	
2021 CG	Apollo	26.1	18	2021-02-06 15:18:41	20.0	17.0	1.1	16.7	0.0098	0.9957	
2021 CO	Apollo	25.3	26	2021-02-09 12:12:05	21.0	16.6	0.2	7.3	0.0143	1.0009	
2021 DW_1	Apollo	25.2	27	2021-03-02 11:14:22	2.0	16.2	0.5	49.2	0.0070	0.9957	crowded field
2021 EM_4	Apollo	27.1	11	2021-03-18 16:04:37	20.0	16.8	1.5	26.6	0.0050	0.9999	
2021 EQ_3	Apollo	26.1	18	2021-03-15 11:07:03	14.0	16.6	1.0	49.6	0.0053	0.9980	
2021 ET_4	Apollo	23.9	48	2021-03-16 14:20:17	18.0	17.0	0.7	45.1	0.0184	1.0078	
2021 EX_1	Apollo	24.9	32	2021-03-08 12:53:11	20.0	16.9	0.5	22.3	0.0153	1.0069	
2021 FH	Apollo	26.7	13	2021-03-22 13:13:51	20.0	17.3	0.3	21.5	0.0080	1.0040	thin cloud
2021 GD_5	Aten	27.1	11	2021-04-08 15:38:36	20.0	18.2	2.7	24.3	0.0098	1.0104	
2021 GQ_{10}	Apollo	26.6	14	2021-04-14 16:03:02	20.0	15.4	2.8	65.7	0.0020	1.0040	
2021 GT_3	Apollo	26.4	16	2021-04-10 13:03:32	20.0	15.7	2.1	11.5	0.0052	1.0071	
2021 JB_6	Apollo	28.8	5	2021-05-13 15:11:10	20.0	16.8	2.7	47.3	0.0017	1.0118	
2021 KN_2	Apollo	28.6	6	2021-05-30 16:53:29	14.0	17.1	2.3	41.2	0.0023	1.0156	
2021 KQ_2	Aten	29.9	3	2021-05-31 16:27:10	20.0	17.2	2.9	39.1	0.0014	1.0150	
2021 RB_1	Amor	24.1	46	2021-09-06 13:16:10	20.0	16.8	1.1	26.5	0.0199	1.0258	
2021 RX_5	Apollo	23.7	54	2021-09-15 15:25:56	7.0	16.6	0.5	33.2	0.0196	1.0219	
2021 TG_1	Apollo	28.2	7	2021-10-03 13:22:32	20.0	17.1	2.5	39.4	0.0029	1.0028	
2021 TL_{14}	Apollo	26.9	12	2021-10-14 14:45:00	21.0	15.7	2.4	27.8	0.0033	1.0004	
2021 TQ_3	Atira	27.1	11	2021-10-06 16:25:11	20.0	17.1	1.4	21.3	0.0062	1.0055	
2021 TQ_4	Apollo	29.9	3	2021-10-06 16:54:27	3.0	17.3	3.1	2.4	0.0026	1.0023	
2021 TY_{14}	Apollo	27.2	11	2021-10-15 11:56:39	20.0	17.0	1.8	22.2	0.0056	1.0023	
2021 UF_{12}	Apollo	29.3	4	2021-10-29 14:46:18	8.0	16.5	9.2	14.0	0.0019	0.9951	
TMG0042	Apollo‡	28.5‡	6	2021-04-10 16:16:17	20.0	-	-	-	-	-	NEO candidate
TMG0049	Apollo‡	30.0‡	3	2021-05-30 15:30:09	16.0	-	-	-	-	-	NEO candidate

Table 2.2. (Continued)

Object	Dyn. Class	H (mag)	$D^{\dagger}$ (m)	Obs. Date (UTC)	T (minutes)	V (mag)	Vel. (arcsec s^{-1})	α (°)	Δ (au)	r (au)	Note
2021 VH_1	Aten	26.4	15	2021-11-04 16:05:36	14.0	17.4	1.8	52.3	0.0064	0.9957	crowded field
2021 VK_3	Apollo	30.5	2	2021-11-07 12:20:45	20.0	17.0	4.3	6.5	0.0016	0.9926	
2021 VV_3	Apollo	23.6	57	2021-11-07 12:59:34	14.0	17.0	0.9	32.5	0.0256	1.0125	
2021 WK_1	Apollo	26.3	17	2021-12-01 15:02:45	8.0	17.0	0.8	23.3	0.0084	0.9939	crowded field
TMG0061	Apollo‡	28.3‡	7	2021-12-11 14:11:08	20.0	-	-	-	-	-	
2021 XA_6	Aten	24.8	32	2021-12-13 12:09:37	17.0	16.4	0.5	72.6	0.0064	0.9864	
2021 YK	Apollo	27.4	10	2022-01-01 15:23:46	7.0	16.9	0.7	36.9	0.0042	0.9868	
2022 AB_1	Apollo	28.5	6	2022-01-06 15:19:51	10.0	17.2	1.6	7.6	0.0043	0.9877	crowded field
2022 AR_2	Apollo	27.7	9	2022-01-07 15:02:32	16.0	16.6	3.7	14.1	0.0043	0.9875	crowded field
2022 BB	Apollo	27.1	11	2022-01-26 14:45:54	18.0	17.1	1.6	25.1	0.0057	0.9899	
2022 BH_3	Apollo	26.3	16	2022-01-28 15:31:50	19.0	17.1	0.8	41.3	0.0068	0.9900	
2022 BU_4	Aten	27.2	11	2022-01-30 15:01:40	20.0	16.9	1.6	15.0	0.0061	0.9911	
2022 CG	Apollo	26.2	17	2022-02-03 15:27:51	20.0	16.7	0.8	52.3	0.0053	0.9890	
2022 CW	Apollo	26.9	12	2022-02-08 12:07:45	20.0	16.9	1.3	32.1	0.0054	0.9910	
2022 CV_5	Apollo	27.7	9	2022-02-11 15:19:11	20.0	16.9	1.2	26.1	0.0041	0.9907	
2022 DC_4	Apollo	27.1	11	2022-02-28 15:27:32	20.0	17.0	1.4	23.7	0.0057	0.9959	
2022 EZ	Apollo	29.3	4	2022-03-02 16:07:07	20.0	18.3	2.3	7.4	0.0050	0.9961	
2022 EV_3	Apollo	29.8	3	2022-03-09 11:36:04	16.0	15.5	11.0	23.6	0.0008	0.9936	
2017 WN_{13}	Apollo	22.9	78	2022-04-01 13:06:35	14.0	16.9	0.4	28.8	0.0336	1.0286	
2022 GN_1	Apollo	27.8	8	2022-04-05 15:31:42	20.0	17.0	1.0	19.9	0.0043	1.0045	
2022 HC	Apollo	25.1	28	2022-04-19 14:56:56	16.0	16.8	1.9	45.6	0.0097	1.0111	
2022 JL	Apollo	23.4	63	2022-05-03 14:01:54	20.0	16.3	0.9	51.1	0.0155	1.0178	
2022 JK	Apollo	26.7	13	2022-05-03 14:54:03	18.0	17.1	1.5	19.6	0.0075	1.0152	
2022 KK_5	Apollo	25.1	28	2022-05-29 15:13:24	20.0	16.9	1.2	55.2	0.0090	1.0187	
2022 KD_2	Amor	24.5	38	2022-06-01 13:52:28	15.0	16.3	0.5	7.9	0.0176	1.0315	
2022 QX_4	Aten	24.7	34	2022-08-28 13:22:46	5.0	16.1	0.9	13.2	0.0129	1.0228	
2022 RW	Aten	23.4	62	2022-09-05 10:57:03	20.0	16.0	1.8	86.5	0.0082	1.0087	
2022 UG_2	Apollo	27.1	11	2022-10-20 13:44:05	19.0	17.2	1.5	19.9	0.0065	1.0019	
2022 UQ_6	Apollo	29.1	4	2022-10-20 16:46:37	7.0	18.1	3.2	32.5	0.0033	0.9986	
2022 UC_1	Apollo	26.4	16	2022-10-21 09:50:36	20.0	15.8	1.9	30.8	0.0042	0.9992	
2022 UY_5	Apollo	27.3	10	2022-10-22 10:53:04	19.0	16.8	2.6	74.0	0.0025	0.9960	crowded field
2022 UL_{11}	Aten	29.1	4	2022-10-26 14:02:14	20.0	17.7	3.6	18.5	0.0033	0.9973	
2022 UB_{13}	Apollo	29.9	3	2022-10-27 14:44:24	16.0	17.6	3.7	17.7	0.0023	0.9961	
2022 UA_{13}	Aten	26.4	16	2022-10-27 16:44:21	6.0	16.8	1.2	18.4	0.0080	1.0015	
2022 UW_{10}	Apollo	26.1	17	2022-10-30 12:35:31	18.0	17.1	0.7	11.0	0.0114	1.0043	
2022 WA	Apollo	26.8	13	2022-11-17 12:07:45	19.0	16.8	1.2	7.6	0.0079	0.9967	
2022 WS_9	Apollo	25.1	29	2022-11-30 13:15:32	17.0	16.8	1.2	13.4	0.0155	1.0013	
2022 XA	Apollo	27.4	10	2022-12-02 12:04:58	20.0	16.9	2.9	36.6	0.0041	0.9893	
2015 RN_{35}	Apollo	23.2	67	2022-12-16 13:13:47	17.0	13.6	0.9	36.1	0.0061	0.9892	
2022 YG_2	Apollo	28.9	5	2022-12-22 10:57:49	20.0	17.2	2.6	28.2	0.0026	0.9861	
2022 YF_6	Apollo	26.5	15	2022-12-27 14:50:47	12.0	16.8	4.2	29.2	0.0063	0.9891	
2023 CG_2	Apollo	27.1	11	2023-02-16 10:32:56	20.0	17.0	2.7	24.8	0.0058	0.9932	
2023 ES	Apollo	26.4	16	2023-03-13 11:34:01	19.0	16.8	1.2	29.1	0.0066	0.9995	
2023 DZ_2	Apollo	24.3	42	2023-03-22 10:12:08	20.0	17.3	0.0	60.9	0.0148	1.0034	
2023 GG	Apollo	23.4	63	2023-04-10 10:48:35	20.0	15.7	1.3	61.8	0.0107	1.0067	
2023 HU_4	Apollo	26.8	13	2023-04-27 13:22:12	16.0	15.8	2.9	27.6	0.0035	1.0096	
2023 UW_1	Apollo	26.8	13	2023-10-19 12:09:57	20.0	16.5	1.6	18.3	0.0057	1.0016	
2023 UH_5	Apollo	25.2	27	2023-10-24 13:42:38	17.0	16.9	0.8	3.1	0.0185	1.0132	

Note. — Dynamical class (Dyn. Class) and absolute magnitude (H) are from NASA JPL HORIZONS as of 2023-11-5 (UTC). Observation starting time in UTC (Obs. Date) and duration time of observation (T) for each object are listed. V-band apparent magnitude (V), angular rate of change in apparent RA and DEC (Vel.), phase angle (α), distance between NEO and observer (Δ), and distance between the Sun and NEO (r) at the observation time are also from NASA JPL HORIZONS as of 2023-11-5 (UTC). † Diameter (D) is derived from H assuming geometric albedo in V-band of 0.20. ‡ Dyn. Class and H of the NEO candidates are derived from orbits determined with the Tomo-e Gozen data using Find_Orb (https://www.projectpluto.com/fo.htm).

Periodic analysis

We used the Lomb-Scargle technique to estimate rotation periods from non-evenly sampled data (Lomb 1976; Scargle 1982; VanderPlas 2018). Fitting models are given in the following form:

$$y_{\rm model}(f,t) = c_0 + \sum_{i=1}^{n}\{S_i \sin(2\pi i f t) + C_i \cos(2\pi i f t)\}, \tag{2.2}$$

where f is a frequency, c_0 denotes the average brightness, n is the number of harmonics, and S_i and C_i are the Fourier coefficients of the i-th harmonics. The normalized residual χ^2 was calculated as

$$\chi^2(f) = \sum_{j=1}^{n_{\rm obs}} \left(\frac{y_{\rm model}(f,t_j) - y_{{\rm obs},j}}{y_{{\rm err},j}} \right)^2, \tag{2.3}$$

where $n_{\rm obs}$ is the number of observation data, t_j is an observation time of the j-th sample, $y_{{\rm obs},j}$ and $y_{{\rm err},j}$ are the j-th measured brightness and its uncertainty, respectively. We calculated the Lomb-Scargle periodogram $P_{\rm LS}$ as

$$P_{\rm LS}(f) = \frac{\chi_0^2 - \chi^2(f)}{2}, \tag{2.4}$$

where χ_0^2 is a $\chi^2(f)$ for a constant fitting model where S_i and C_i are set to zero for all i.

The significance of a peak in a periodogram is evaluated by calculating a confidence level against the null hypothesis. Assuming that the data consists of pure Gaussian noise, $2P_{\rm LS}$ follows a χ^2 distribution with two degrees of freedom when $n = 1$. Thus,

$$p_{\rm single}(z) = 1 - e^{-z} \tag{2.5}$$

expresses a cumulative probability that $P_{\rm LS}$ is less than z at each frequency. We assumed that the frequencies are independent of each other and defined an effective number of frequencies as

$$N_{\rm eff} = f_{\rm max} T, \tag{2.6}$$

where $f_{\rm max}$ is a maximum frequency to be considered. A false alarm probability, $FAP(z)$, is calculated as follows:

$$FAP(z) = 1 - p_{\rm single}(z)^{N_{\rm eff}}. \tag{2.7}$$

We calculated a 99.9% confidence level in each periodogram. We derived a candidate of a rotation period from the highest peak of $P_{\rm LS}$ larger than 99.9% confidence level.

For optimal determination of the number of harmonics n, we used the Akaike Information Criterion (AIC, Akaike 1974). AIC indicates the trade-off between the goodness of fit and the simplicity of the model. AIC is calculated as

$$\begin{aligned} AIC &= -\ln L + 2(2n+1) \\ &= \frac{1}{2}\sum_{j=1}^{n_{\rm obs}} \left(\frac{y_{\rm model}(f,t_j) - y_{{\rm obs},j}}{y_{{\rm err},j}} \right)^2 \\ &+ \ln \prod_{j=1}^{n_{\rm obs}} y_{{\rm err},j} + \frac{n_{\rm obs}}{2} \ln 2\pi + 2(2n+1), \end{aligned} \tag{2.8}$$

where L is the likelihood of the parameters. We adopted n of each NEO for which AIC value is the minimum.

The uncertainty of the rotation period and the lightcurve amplitude were estimated using the Monte Carlo method. We created 3000 lightcurves for each NEO by randomly resampling the data assuming

each observed data follows a normal distribution whose standard deviation is a photometric error. We performed the same analyses above for 3000 lightcurves and obtained 3000 sets of Fourier coefficients in Equation 2.2. We calculated the 3000 periods and the 3000 amplitude with the corresponding peak frequencies for each lightcurve. As an example, an analysis result of 2021 CG is shown in Figure 2.4. We adopted the standard deviations as the uncertainties of the period and the amplitude. If the estimated standard deviation was larger than 5 % of the rotation period, we judged the derived rotation period was suspicious and the correct rotation period was not derived. We used the Fourier coefficients of which the rotation period and the lightcurve amplitude are the closest to the average values to plot a typical model curve.

There are several candidates of non-principal axis rotators (i.e., tumblers) in the Tomo-e NEOs. The tumbler is in an excited state and its lightcurve is complicated (e.g., Paolicchi et al. 2002; Pravec et al. 2005). Therefore, the periodograms of the tumblers show additional peaks which are not aliases of the highest peak. We defined such objects with multiple peaks as tumbler candidates in this study.

2.3. Results

We successfully derived the rotation periods of 52 NEOs. Results of the analysis are summarized in Table 2.3. The rotation periods of 20 are reported in previous studies: 2019 BE_5 (Warner et al. 2009), 2020 TD_8, 2020 UQ_6, 2020 VZ_6, 2020 XX_3 (Birtwhistle 2021a), 2021 EX_1, 2021 FH (Birtwhistle 2021b), 2021 KN_2, 2021 JB_6, 2021 GQ_{10} (Birtwhistle 2021c), 2021 DW_1 (Kwiatkowski et al. 2021), 2021 YK (Ondrejov Asteroid Photometry Project[2]), 2022 HC, 2022 JL (Birtwhistle 2022a), 2022 KK_5 (Birtwhistle 2022a; Sonka et al. 2022), 2022 QX_4 (Birtwhistle 2023a), 2023 DZ_2 (Popescu et al. 2023; Bacci & Maestripieri 2023; Sioulas 2023), 2022 CV_5 (Birtwhistle 2022b), 2015 RN_{35} (Franco et al. 2023; Colazo et al. 2023; Koleńczuk et al. 2023; Beniyama et al. 2023a), and 2023 HU_4 (Birtwhistle 2023b).

The periodogram of 2021 FH has a prominent peak but its significance level is lower than 99.9%. We considere that the peak of 2021 FH to be reliable since the peak frequency corresponds to the rotation period (63.4 s) reported by Birtwhistle (2021b). We did not derive rotation periods of 2021 YK and 2022 QX_4 using our short lightcurve for seven and five minutes, respectively. Our results of the others are consistent with previous studies [3].

The rotation periods of 43 objects were not derived due to small amplitudes. These objects may have axisymmetric shapes, rotation periods longer than the duration of observation, rotation periods shorter than the exposure time, or rotation axes parallel to the line of sight. When a lightcurve shows a clear brightness variation but whole cycles of rotation are not obtained, we adopted the duration times of the observations as lower limits of rotation periods.

We found 13 candidates of tumbler: 2010 WC_9, 2017 WJ_{16}, 2020 TE_6, 2021 CO, 2020 EO, 2021 KN_2, 2021 KQ_2, 2021 TG_1, 2021 TL_{14}, 2021 TQ_4, 2022 CV_5, 2015 RN_{35}, and 2023 HU_4. Physical modeling of these candidates will be presented elsewhere.

2.3.1. Lightcurves and periodograms

As an example, we presented the lightcurve and periodogram of 2021 CG in Figures 2.5 and 2.6, respectively. The rotation period and the lightcurve amplitude of 2021 CG were estimated to be 15.296 ± 0.002 s and 0.27 ± 0.02 mag, respectively, using the Monte Carlo method as shown in Figure 2.4. The lightcurve folded by the rotation period (hereinafter referred to as phased lightcurve) is shown in Figure 2.7. Thanks to the video observations at 2 fps, we can estimate such a short period of rotation with high

[2] https://www.asu.cas.cz/~ppravec/newres.txt

[3] The result of 2021 DW_1 was updated from Beniyama et al. (2022) after the reanalysis.

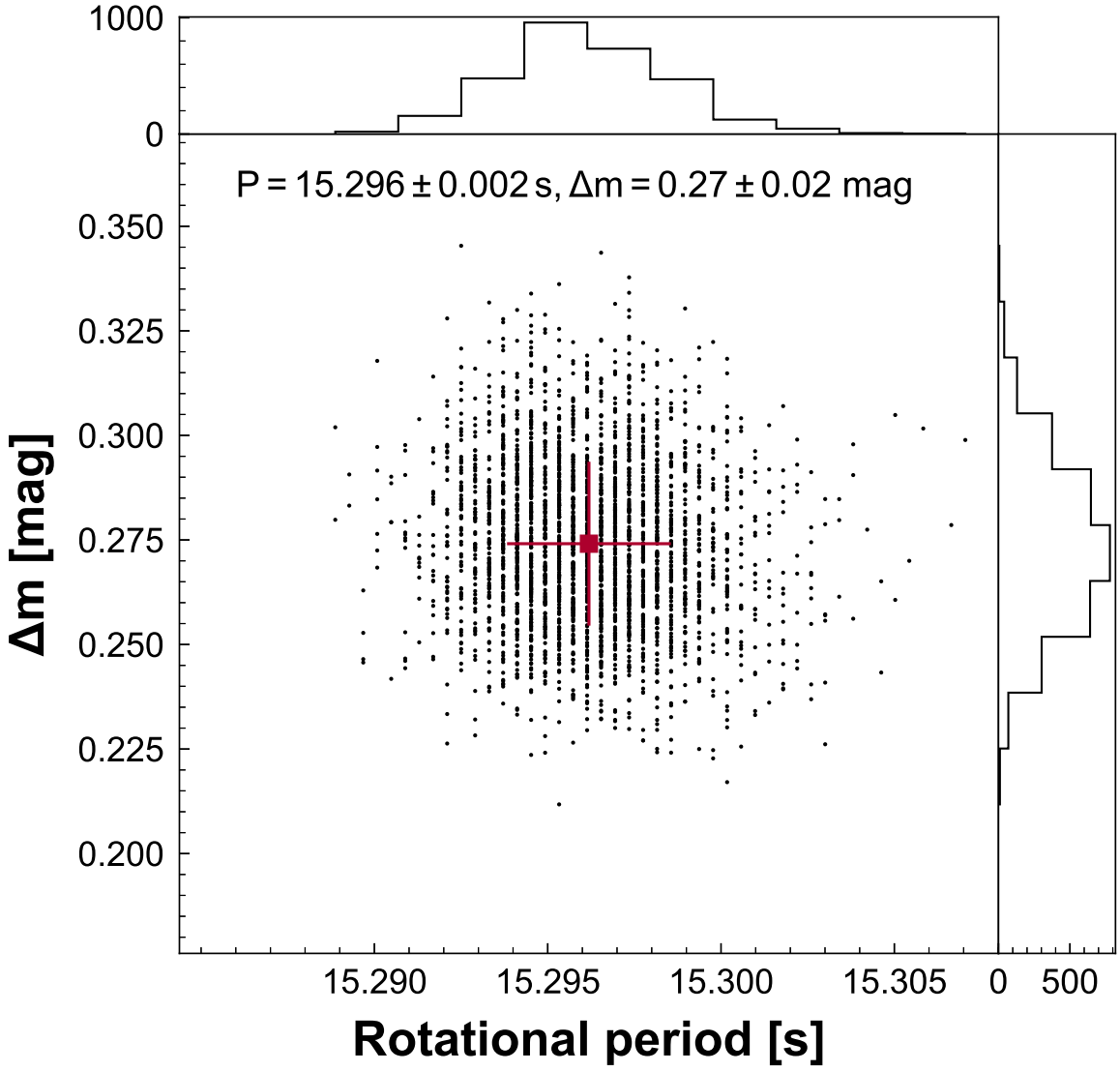

Figure 2.4. Scatter plot of the rotation periods and the lightcurve amplitudes of 3000 model curves of 2021 CG. Histograms present the marginal distributions of the periods and the amplitudes, respectively. The derived period and amplitude are presented by a square symbol with a cross that indicates the standard deviations of the period and the amplitude.

Table 2.3. Summary of the observational results

Object	H (mag)	D (m)	$N_{\rm obs}$	n	P (s)	Δm (mag)	a/b	Note
2010 WC_9	23.5	59	670	-	-	-	-	known tumbler
2011 DW	22.9	79	2099	-	>1320	>1320	-	
2017 WJ_{16}	24.5	37	135	-	-	-	-	tumbler
			2114	-	-	-	-	tumbler
2018 LV_3	26.5	15	700	3	415.9 ± 0.4	0.46 ± 0.03	≥1.24	5 s exposure
2018 UD_3	26.2	17	3977	12	29.720 ± 0.003	0.55 ± 0.02	≥1.22	
2019 BE_5	25.1	28	1125	4	11.97902 ± 0.00009	0.80 ± 0.04	≥1.40	
2020 EO	25.9	20	1483	-	-	-	-	tumbler
2020 FA_2	27.5	9	4930	6	150.67 ± 0.02	0.26 ± 0.01	≥1.15	
2020 FL_2	26.1	18	1557	9	325.1 ± 0.8	0.102 ± 0.005	≥1.07	
2020 GY_1	26.6	14	1474	6	303 ± 3	0.17 ± 0.02	≥1.10	
2020 HK_3	24.2	43	1476	-	>780	>780	-	
2020 HS_7	29.1	4	1365	1	2.9945 ± 0.0002	0.069 ± 0.006	≥1.04	
			896	2	2.9938 ± 0.0002	0.075 ± 0.006	≥1.04	
2020 HT_7	26.9	12	1411	6	45.8 ± 0.01	0.38 ± 0.02	≥1.17	
2020 HU_3	26.0	19	666	-	>360	>360	-	
2020 PW_2	28.8	5	1198	8	87.6 ± 0.6	0.54 ± 0.06	≥1.33	
2020 PY_2	26.5	15	1815	6	19.835 ± 0.002	0.28 ± 0.01	≥1.21	
2020 QW	25.3	26	1102	-	>1200	>1200	-	
2020 TD_8	26.9	12	434	5	29.53 ± 0.01	1.19 ± 0.04	≥1.56	
2020 TE_6	27.4	10	1537	-	-	-	-	tumbler
2020 TS_1	29.2	4	793	-	>540	>540	-	
2020 UQ_6	22.7	86	1730	13	162.82 ± 0.03	0.819 ± 0.009	≥1.66	
2020 VF_4	26.6	14	1808	-	>1200	>1200	-	
2020 VH_5	29.2	4	2098	7	157.6 ± 0.4	0.15 ± 0.01	≥1.12	
2020 VJ_1	26.7	13	938	13	241 ± 1	0.64 ± 0.05	≥1.34	
2020 VR_1	28.9	5	677	-	>1200	>1200	-	
2020 VZ_6	25.0	30	1622	10	353.4 ± 0.2	1.06 ± 0.02	≥1.66	
2020 XH	24.6	36	208	-	>1020	>1020	-	
2020 XH_1	22.9	78	1912	-	>1200	>1200	-	
2020 XQ_2	22.8	83	244	-	>1200	>1200	-	
2020 XX_3	28.5	6	1664	13	136.22 ± 0.05	0.98 ± 0.02	≥1.52	
2020 XY_4	26.9	12	2020	3	324 ± 6	0.15 ± 0.01	≥1.06	
2020 YJ_2	27.4	10	182	-	>1200	>1200	-	
2021 AT_5	27.5	9	458	-	>600	>600	-	
2021 BC	24.3	41	1382	-	>1200	>1200	-	
2021 CA_6	28.5	6	2219	6	14.3159 ± 0.0004	0.694 ± 0.008	≥1.24	
2021 CC_7	29.8	3	1109	4	13.514 ± 0.008	0.24 ± 0.02	≥1.18	
2021 CG	26.1	18	1857	9	15.296 ± 0.002	0.27 ± 0.02	≥1.18	
2021 CO	25.3	26	1603	-	-	-	-	known tumbler
2021 DW_1	25.2	27	146	6	47.5 ± 0.4	0.73 ± 0.08	≥1.31	
2021 EM_4	27.1	11	1438	8	99.5 ± 0.4	0.26 ± 0.03	≥1.14	
2021 EQ_3	26.1	18	1376	11	119.41 ± 0.02	0.71 ± 0.02	≥1.30	
2021 ET_4	23.9	48	1703	4	87.8 ± 0.2	0.21 ± 0.02	≥1.09	
2021 EX_1	24.9	32	2227	4	410 ± 1	0.222 ± 0.009	≥1.13	
2021 FH	26.7	13	1632	3	63.5 ± 0.6	0.16 ± 0.02	≥1.09	
2021 GD_5	27.1	11	2240	-	>1200	>1200	-	
2021 GQ_{10}	26.6	14	1167	3	19.308 ± 0.003	0.192 ± 0.007	≥1.06	
2021 GT_3	26.4	16	2013	10	155.1 ± 0.2	0.149 ± 0.009	≥1.11	
2021 JB_6	28.8	5	2212	2	65.64 ± 0.02	0.55 ± 0.01	≥1.23	
2021 KN_2	28.6	6	1244	-	-	-	-	known tumbler
2021 KQ_2	29.9	3	1829	-	-	-	-	tumbler
2021 RB_1	24.1	46	1931	-	>1200	>1200	-	
2021 RX_5	23.7	54	528	-	>420	>420	-	
2021 TG_1	28.2	7	780	-	-	-	-	tumbler
2021 TL_{14}	26.9	12	1626	-	-	-	-	tumbler
2021 TQ_3	27.1	11	1897	-	>1200	>1200	-	
2021 TQ_4	29.9	3	424	-	-	-	-	tumbler
2021 TY_{14}	27.2	11	2051	4	15.292 ± 0.002	0.61 ± 0.02	≥1.40	
2021 UF_{12}	29.3	4	423	1	14.86 ± 0.004	0.51 ± 0.02	≥1.39	
TMG0042	28.5	6	1937	20	314.4 ± 0.3	1.00 ± 0.04	≥2.51	
TMG0049	30.0	3	1538	-	>1080	>1080	-	

Table 2.3. (Continued)

Object	H (mag)	D (m)	$N_{\rm obs}$	n	P (s)			Δm (mag)			a/b	Note
2021 VH_1	26.4	15	417	-		>1200			>1200		-	
2021 VK_3	30.5	2	2026	1	35.12	±	0.01	0.3	±	0.01	≥1.26	
2021 VV_3	23.6	57	646	-		>960			>960		-	
2021 WK_1	26.3	17	313	-		>1200			>1200		-	
TMG0061	28.3	7	2108	5	20.528	±	0.001	0.459	±	0.009	≥1.53	
2021 XA_6	24.8	32	1605	-		>1200			>1200		-	
2021 YK	27.4	10	369	-		>720			>720		-	
2022 AB_1	28.5	6	377	-		>720			>720		-	
2022 AR_2	27.7	9	375	-		>1080			>1080		-	
2022 BB	27.1	11	1665	6	281	±	2	0.49	±	0.03	≥1.29	
2022 BH_3	26.3	16	1882	5	484	±	1	0.62	±	0.02	≥1.29	
2022 BU_4	27.2	11	1735	1	112.19	±	0.04	0.68	±	0.01	≥1.54	
2022 CG	26.2	17	2149	-		>1200			>1200		-	
2022 CW	26.9	12	2019	-		>1200			>1200		-	
2022 CV_5	27.7	9	2123	-		-			-		-	known tumbler
2022 DC_4	27.1	11	2129	12	261.4	±	0.5	0.51	±	0.02	≥1.32	
2022 EZ	29.3	4	2077	-		>1200			>1200		-	
2022 EV_3	29.8	3	1437	5	5.12381	±	8e-05	0.542	±	0.009	≥1.34	
2017 WN_{13}	22.9	78	1380	-		>1200			>1200		-	
2022 GN_1	27.8	8	2071	-		>1200			>1200		-	
2022 HC	25.1	28	1565	4	51.25	±	0.05	0.42	±	0.03	≥1.18	
2022 JL	23.4	63	1991	7	51.643	±	0.007	0.49	±	0.01	≥1.20	
2022 JK	26.7	13	2025	5	198.7	±	0.9	0.15	±	0.01	≥1.09	
2022 KK_5	25.1	28	2210	7	299.1	±	0.3	1.03	±	0.03	≥1.43	
2022 KD_2	24.5	38	1253	-		>1080			>1080		-	
2022 QX_4	24.7	34	565	-		>240			>240		-	$P \sim 320$ s in Birtwhistle (2023a)
2022 RW	23.4	62	1562	-		>1200			>1200		-	
2022 UG_2	27.1	11	1873	-		>1140			>1140		-	
2022 UQ_6	29.1	4	655	4	24.59	±	0.04	0.46	±	0.04	≥1.24	
2022 UC_1	26.4	16	2134	10	632	±	1	0.51	±	0.01	≥1.28	
2022 UY_5	27.3	10	530	12	60.07	±	0.01	1.18	±	0.04	≥1.40	
2022 UL_{11}	29.1	4	1946	8	106	±	2	0.35	±	0.04	≥1.23	
2022 UB_{13}	29.9	3	1738	5	53.76	±	0.03	0.48	±	0.02	≥1.33	
2022 UA_{13}	26.4	16	720	-		>420			>420		-	
2022 UW_{10}	26.1	17	1671	-		>1200			>1200		-	
2022 WA	26.8	13	1543	4	17.897	±	0.006	0.2	±	0.02	≥1.16	
2022 WS_9	25.1	29	1152	-		>1200			>1200		-	
2022 XA	27.4	10	932	4	16.689	±	0.002	0.84	±	0.04	≥1.45	
2015 RN_{35}	23.2	67	1167	-		-			-		-	known tumbler
2022 YG_2	28.9	5	1297	-		>1200			>1200		-	
2022 YF_6	26.5	15	615	-		>1200			>1200		-	
2023 CG_2	27.1	11	1906	-		>1200			>1200		-	
2023 ES	26.4	16	2280	-		>1140			>1140		-	
2023 DZ_2	24.3	42	2400	11	373.7	±	0.8	0.55	±	0.02	≥1.20	
2023 GG	23.4	63	2145	-		>1200			>1200		-	
2023 HU_4	26.8	13	1419	-		-			-		-	known tumbler
2023 UW_1	26.8	13	2003	9	182.9	±	0.2	0.27	±	0.01	≥1.17	
2023 UH_5	25.2	27	1420	-		>1200			>1200		-	

Note. — $N_{\rm obs}$ is the number of frames. n is the number of harmonics of the model curve. P is a rotational period. Δm is a light curve amplitude. a/b is an axial ratio of the asteroid derived from Δm.

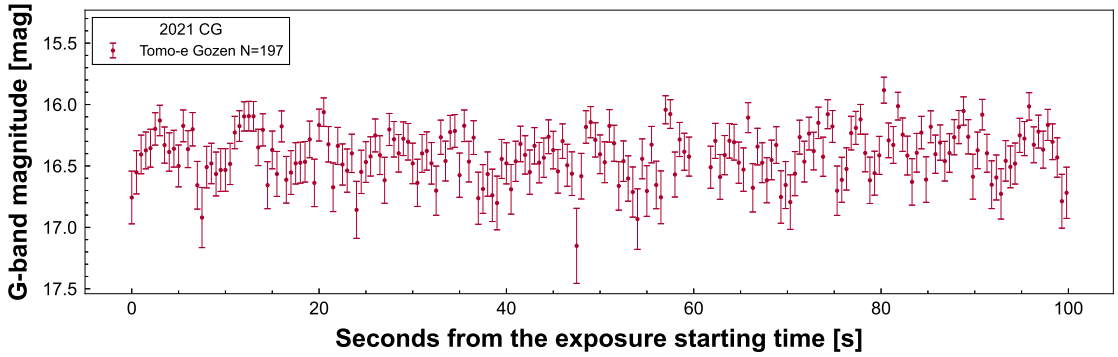

Figure 2.5. Lightcurve of 2021 CG. The first 100 s part of the whole 20 minutes lightcurve are plotted. Bars indicate the 1σ uncertainties (see text for details).

reliability. The lightcurves, periodograms of 108 NEOs, and phased lightcurves of NEOs whose rotation periods were estimated are attached in Figures C.1–D.3, see Appendix.

2.3.2. D-P relation

The D-P relation of the Tomo-e NEOs and the NEOs in LCDB is shown in Figure 2.8. The Tomo-e NEOs are distributed in a range of 3 to 100 m in diameter and 3 to 632 s in rotation period. We found 23 NEOs with rotation periods less than 60 s.

We create cumulative histograms of rotation periods of the Tomo-e NEOs and the NEOs in LCDB (Figure 2.9). The D-P relation of the Tomo-e NEOs looks different from that of the NEOs in LCDB. We performed the Kolmogorov-Smirnov(KS) test to check the null hypothesis that the two D-P relations are the same. We chose the NEOs satisfying the criteria that the absolute magnitude is larger than 22.5, the rotation period is shorter than 632 s corresponding to the longest rotation period of the Tomo-e NEOs. The NEOs whose quality code is 3 or 3- are used as the NEOs in LCDB. The deduced KS statistics and the p-value are 0.00009 and 0.366, respectively. This tentatively implies that rotation periods of some fast rotators have not been able to be estimated due to long exposure times and other factors in the previous studies.

2.3.3. Axial ratios

We defined a lightcurve amplitude Δm by a difference between the maximum and minimum values of the model curve. We assumed the asteroid is a triaxial ellipsoid with axial lengths of a, b, and c ($a > b > c$) and the aspect angle of 90°. A lower limit of axial ratio a/b is estimated as follows:

$$\frac{a}{b} \geq 10^{0.4\Delta m(\alpha)/(1+s\alpha)}, \tag{2.9}$$

where $\Delta m(\alpha)$ is the lightcurve amplitude at a phase angle of α and s is a slope depending on the taxonomic type of the asteroid (Bowell et al. 1989). We assumed that s is 0.030, a typical value of S-type asteroids (Zappala et al. 1990).

A relation between the absolute magnitudes H and the lower limits of axial ratios a/b of the Tomo-e NEOs and the MANOS NEOs with rotation periods shorter than 600 s are shown in Figure 2.10. A relation between the rotation period P and a/b of the Tomo-e NEOs and the MANOS NEOs with $P \leq 600$ s are shown in Figure 2.11. The mean of a/b for each range of H and P is also presented. The range is determined based on the Sturges' rule. No strong correlation is seen in both Figures 2.10 and 2.11. The present results are consistent with Hatch & Wiegert (2015) and Thirouin et al. (2016).

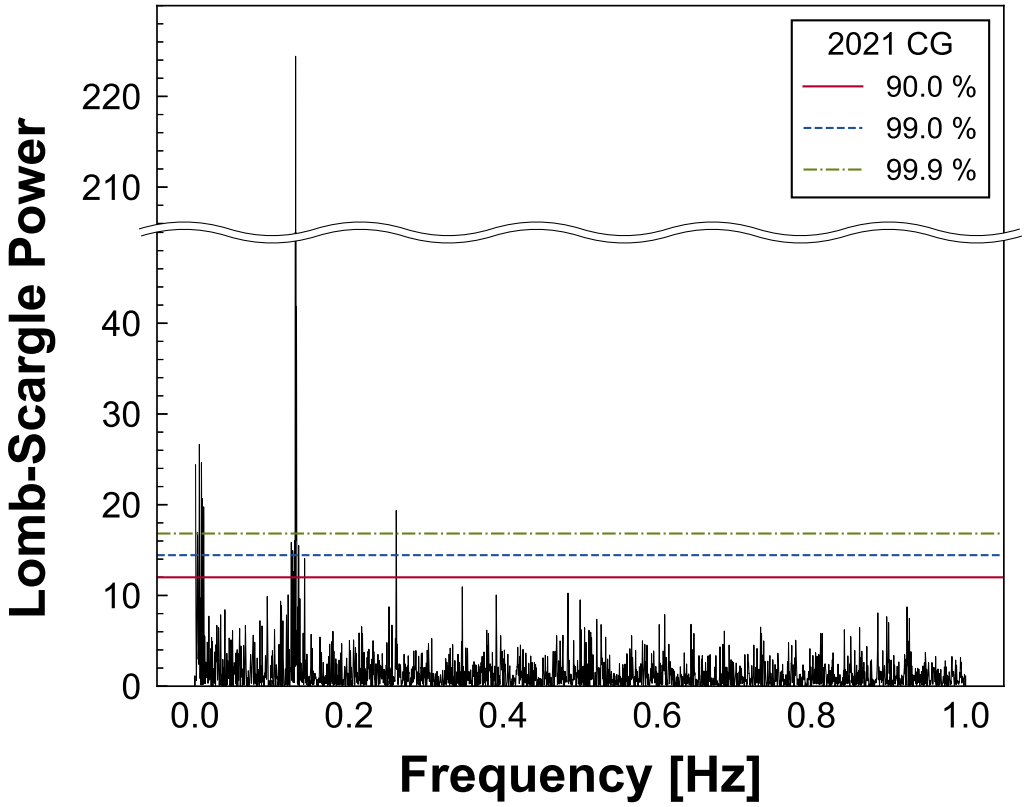

Figure 2.6. Lomb-Scargle periodogram of 2021 CG. The number of harmonics is unity. Solid, dashed, and dot-dashed horizontal lines show 90.0, 99.0, and 99.9% confidence levels, respectively.

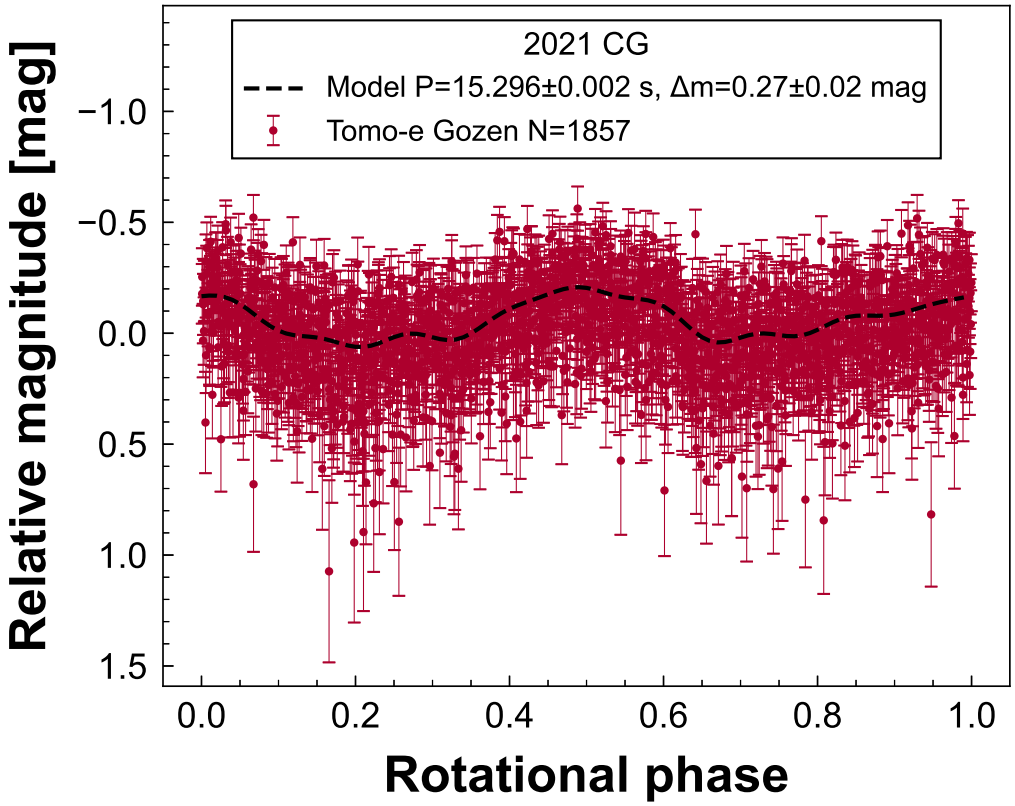

Figure 2.7. Phased lightcurve of 2021 CG. A model curve with a period of 15.296 s and a lightcurve amplitude of 0.27 mag is shown by a dashed line. Photometric errors are the same as in Figure 2.5.

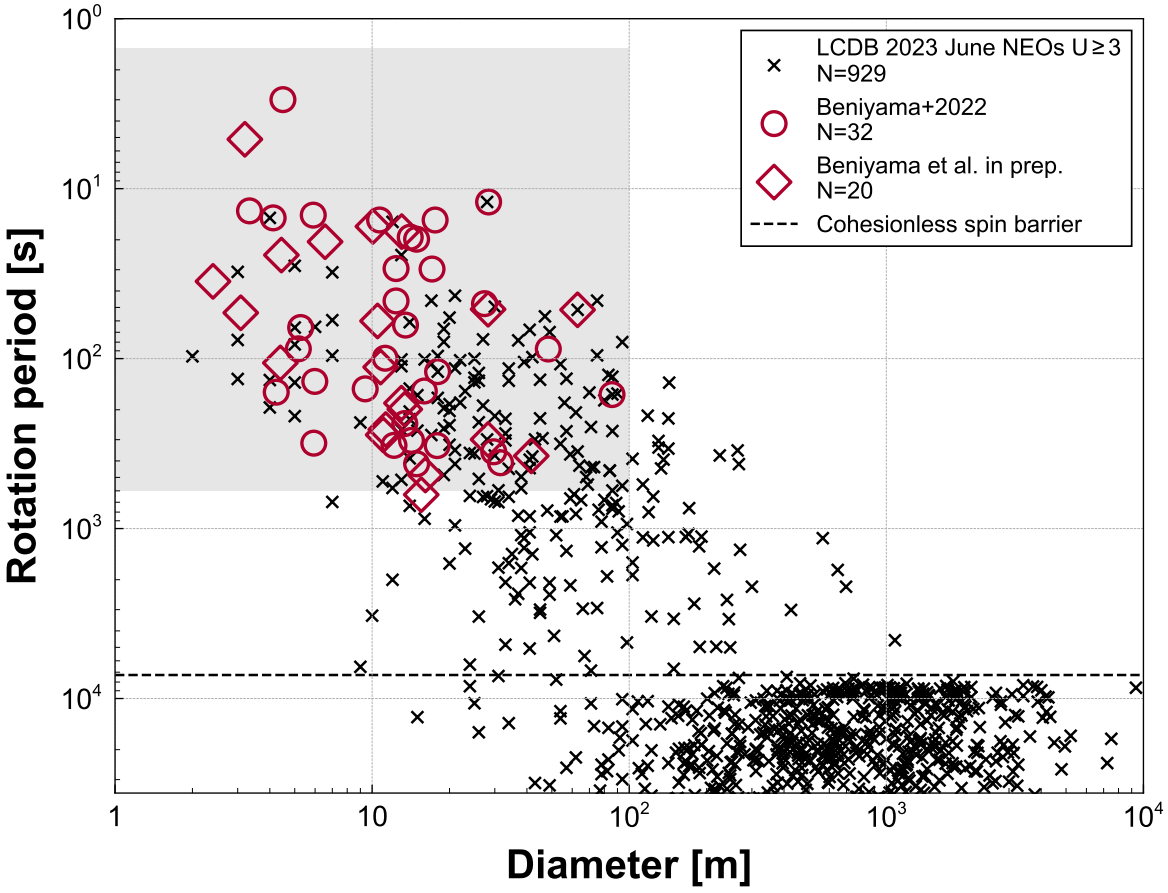

Figure 2.8. D-P relations of the Tomo-e NEOs and the NEOs in LCDB. Tomo-e NEOs in Beniyama et al. (2022) and new samples are represented by open circles and diamonds, respectively. NEOs in LCDB are represented by crosses. A cohesionless spin barrier assuming a typical density of S-type asteroids of 2.67 g cm^{-3} (Yeomans et al. 2000) is shown by a dashed line. The range of detectable rotation period of our targets ($D \leq 100$ m), 1.5 s to 10 minutes, in typical observations at 2 fps for 20 minutes with Tomo-e Gozen is shown as a gray shaded area.

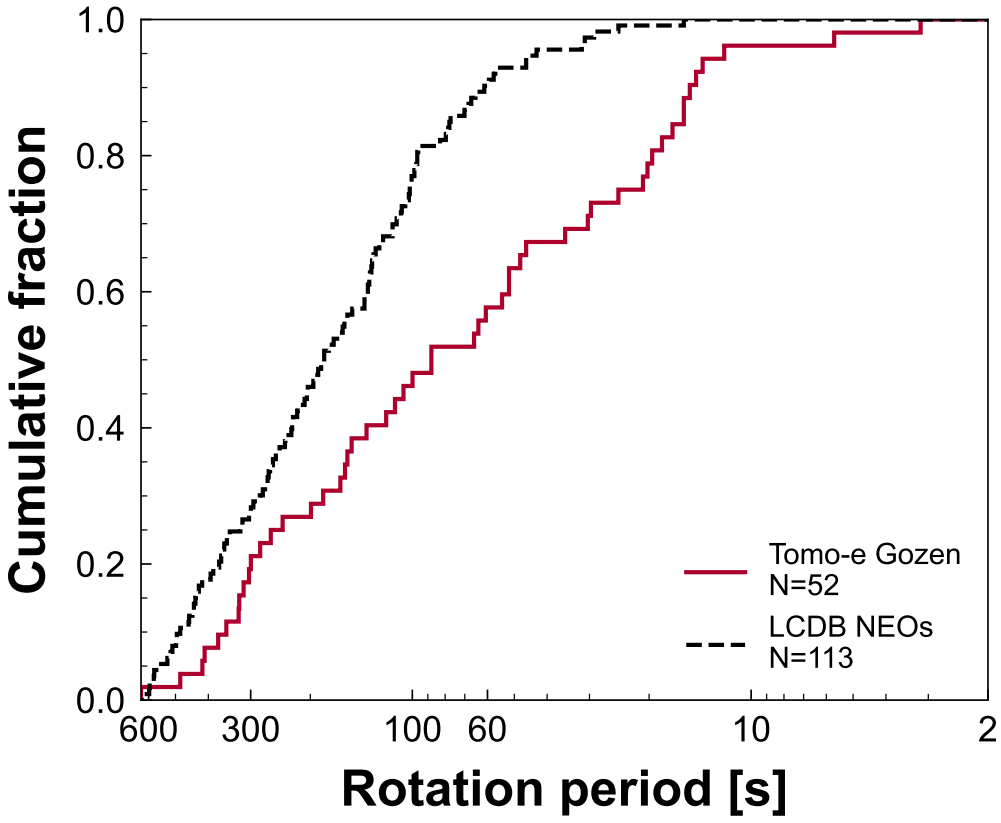

Figure 2.9. Cumulative histograms of rotation periods of the Tomo-e Gozen NEOs (solid line) and the NEOs in LCDB (dashed line) with absolute magnitudes larger than 22.5 and rotation periods shorter than 632 s.

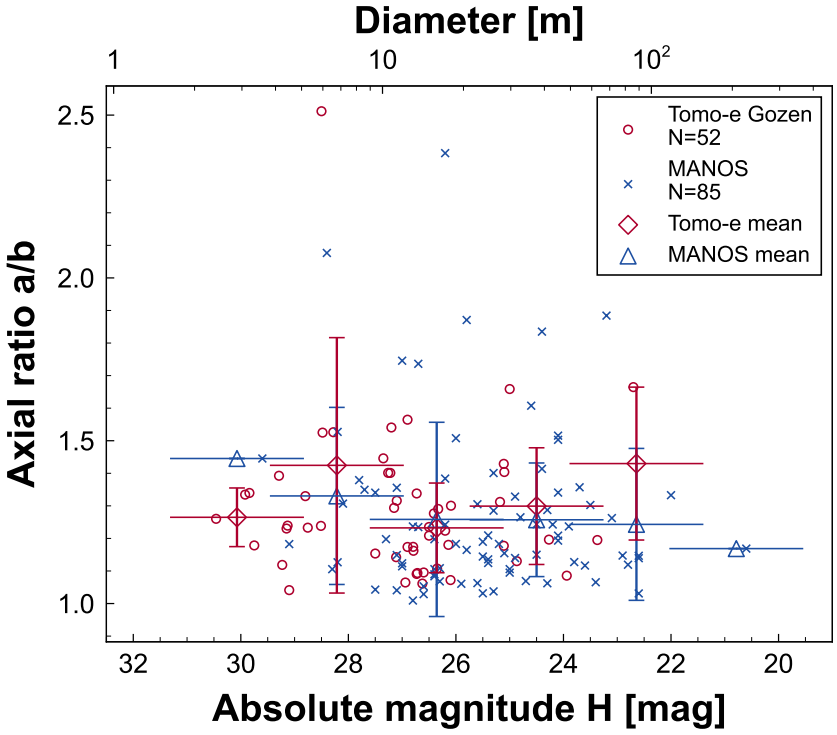

Figure 2.10. Absolute magnitude versus lower limits of axial ratios of the Tomo-e (open circles) and the MANOS NEOs (crosses) with rotation periods shorter than 600 s. The absolute magnitude is converted to diameter using Equation 1.12 assuming a geometric albedo of 0.2. The mean value in each range is presented by a diamond and a triangle for the Tomo-e NEOs and the MANOS NEOs, respectively. Vertical bars indicate standard deviations.

The difference in mean axial ratios between the Tomo-e NEOs ($\sim$ 1.29) and the MANOS NEOs ($\sim$ 1.27) is about 0.02. We performed a bootstrap test to check the null hypothesis that the mean axial ratios of the two samples are the same. We generated 10000 differences in the mean axial ratios by resampling the Tomo-e and MANOS NEOs as shown in Figure 2.12. The 95% confidence interval is from -0.05 to 0.11. Thus, the null hypothesis is not rejected at the 5% significance level.

Figure 2.13 shows measured a/b of various sources: the average of the sum of the Tomo-e NEOs and the MANOS NEOs, the average of fast-rotating asteroids (FRAs) with diameters less than 200 m and a rotation period less than an hour (Michikami et al. 2010), and the averages of boulders on the surfaces of asteroids Itokawa (Michikami et al. 2010) and Ryugu (Michikami et al. 2019).

Michikami et al. (2010) mention that the lower limits of a/b of FRAs and the a/b of boulders are similar to those of laboratory experiments ($\sim$ 1.4), although the aspect angles of asteroids are unknown. The lower limits of a/b of asteroids are lower in the case of recent observational results such as Tomo-e Gozen ($\sim$ 1.29) and MANOS ($\sim$ 1.27). It is important not only to increase the number of lightcurve observations, but also to determine pole directions to discuss a relation with fragments of laboratory experiments and boulders (e.g., Kwiatkowski et al. 2021).

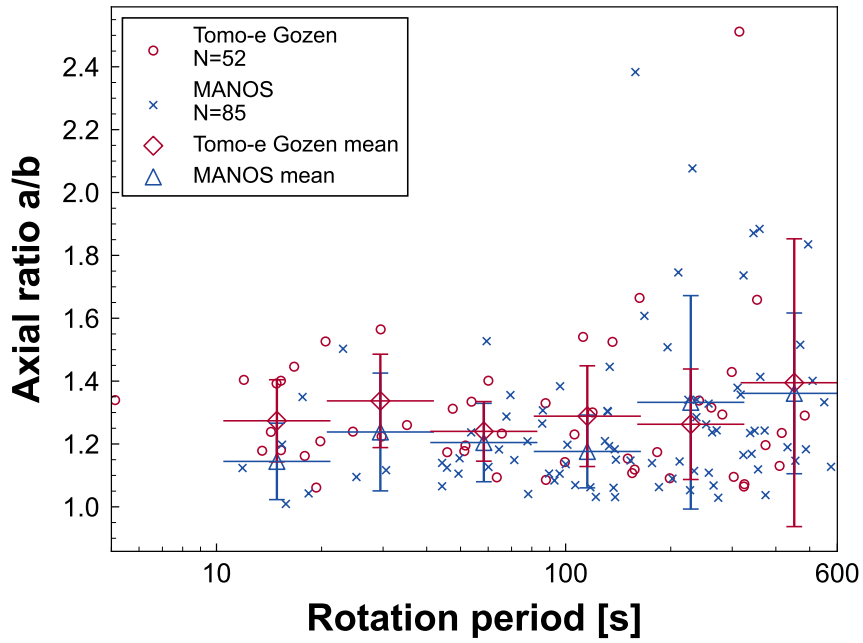

Figure 2.11. Rotation periods versus lower limits of axial ratios of the Tomo-e (open circles) and the MANOS NEOs (crosses) with rotation periods shorter than 600 s. The mean value in each range is presented by a diamond and a triangle for the Tomo-e NEOs and the MANOS NEOs, respectively. Vertical bars indicate standard deviations.

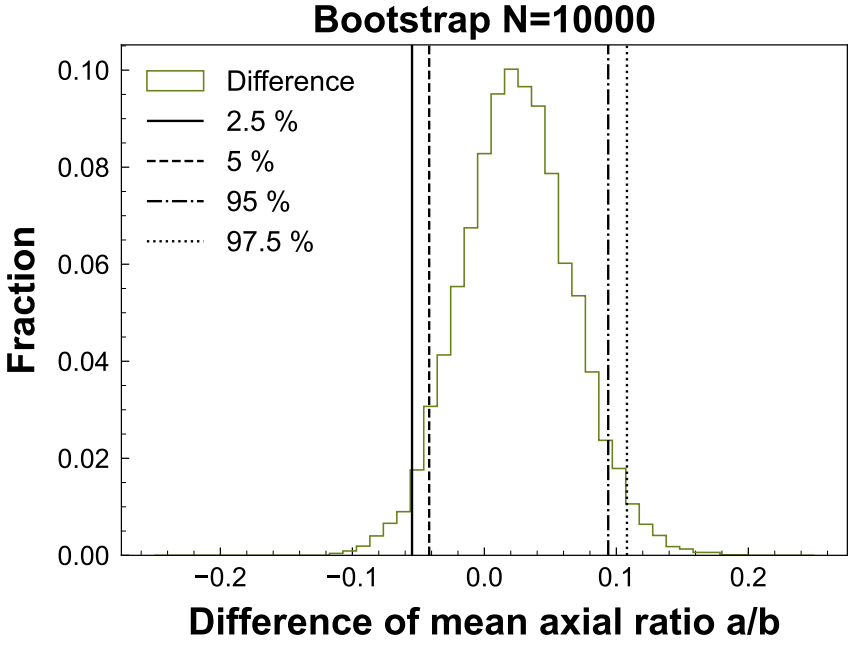

Figure 2.12. Difference of mean axial ratio a/b in bootstrap sampling.

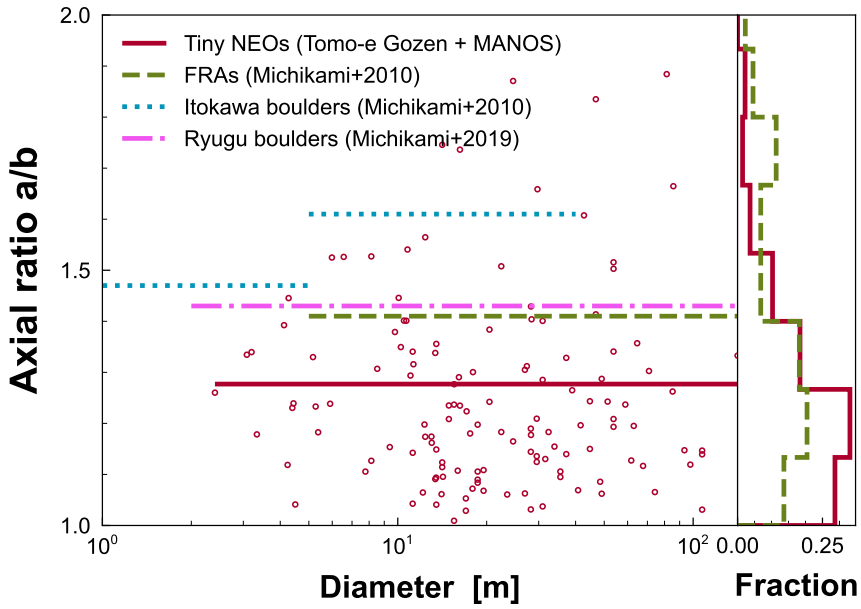

Figure 2.13. Diameter versus lower limits of axial ratios of tiny NEOs, fast-rotating asteroids (FRAs), and apparent axis ratios of boulders on Itokawa and Ryugu. Mean values of tiny NEOs and FRAs are presented as solid and dashed lines, respectively. Typical values of boulders on Itokawa and Ryugu are presented as dotted and dash-dot lines, respectively. Fractions of each range of axial ratio for tiny NEOs and FRAs are shown as histograms in right panel. NEOs with axial ratios larger than 2.0 are not shown in Figures but are used in calculations.

Table 2.4. Periodic analysis results of pseudo lightcurves

Object	$N_{\rm det}$	$P_{\rm det}$ (s)		
pseudo 2020 HT_7	1411	1.30906	$\pm$	0.0002
pseudo 2020 PY_2	1815	1.32235	$\pm$	0.00002
pseudo 2020 TD_8	434	1.2302	$\pm$	0.0001
pseudo 2021 CA_6	2219	1.31436	$\pm$	0.000007
pseudo 2021 CC_7	1109	1.501	$\pm$	0.001
pseudo 2021 CG	1857	1.3906	$\pm$	0.0002
pseudo 2021 GQ_{10}	1167	1.20683	$\pm$	0.00004
pseudo 2021 TY_{14}	2051	1.27431	$\pm$	0.00006

Note. — $P_{\rm det}$ is the detectable rotational period of the object with the same observational conditions in this paper.

2.4. Discussion

2.4.1. Detectable rotation period

Sparse sampling and finite exposure time may lead to underestimating the light curve amplitude and misidentifying periodicity (Pravec & Harris 2000; Thirouin et al. 2018; Birtwhistle 2021c). We examine detection limits in rotation periods ($P_{\rm det}$) in our observations to verify the deficiency of asteroids rotating faster than 10 s. We simulate lightcurves if an asteroid is rotating faster than it is, and then the lightcurves are analyzed in the same manner. We selected 8 NEOs such that their rotation periods are short ($P \leq 60$ s), and the durations of the observations are typical ($10 \leq T \leq 30$ minutes). We excluded 2020 HS_7 in this examination since the exposure time is not sufficiently shorter than the rotation period and the observed lightcurve can be underestimated (Birtwhistle 2021c). Their model lightcurves are used as templates. The rotation period of a hypothetical asteroid $P_{\rm pseudo}$ is set to $P_{\rm pseudo} = P/2, P/3, P/4, ...$, where P is the original rotation period in Section 3. Then, the hypothetical asteroid is virtually observed to generate a pseudo lightcurve. The number of measurements ($N_{\rm obs}$) and the timestamps are the same as the actual observation. The pseudo lightcurve is perturbed to match the noise level with the original observation. The criterion of the periodicity identification is the same as in Sub-subsection 2.2.2.

The results of the periodic analysis are summarized in Table 2.4. The detectable rotation periods are less than 2 s for all the eight asteroids. Although our observations are unevenly sampled because of intervals between frames, large fractions of the data are evenly sampled at 2 fps. The periodograms of the pseudo lightcurves can be affected by aliases when the frequency gets closer to the Nyquist limit $f_{\rm Ny} = 2/2 = 1$ Hz. However, the peaks by the aliases become weaker than the genuine peaks due to the uneven sampling. Thus, it is natural that we detect shorter rotation periods than the Nyquist limit ($P = 2$ s assuming typical double-peak lightcurves). We conservatively set the detectable rotation period to 1.5 s in our systematic 20 minutes video observations at 2 fps. Therefore, it is inevitable that there are only two fast rotators whose rotation periods are shorter than 10 s in our 108 NEOs.

2.4.2. Deficiency of fast rotators

We found no NEOs with rotation periods shorter than 10 s other than 2020 HS_7 and 2022 EV_3. The distribution of the Tomo-e NEOs in the D-P relation is truncated around 10 s in the rotation period as shown in Figures 2.8. To interpret this flat-top distribution, we consider the evolution of rotation periods of the NEOs.

Since smaller asteroids experience a stronger Yarkovsky effect and their semimajor axes are changed, parts of them drift to the resonances with giant planets in the main belt in a short time scale ($\sim$ a few Myr) and then are scattered into the near-Earth region (Bottke et al. 2006). The orbits of the scattered asteroids evolve to those of NEOs over a few Myr (Gladman et al. 1997). Therefore, typical NEOs are considered a few to 10 Myr old. This timescale (hereinafter referred to as NEO age) is consistent with a typical cosmic ray exposure age of meteorites (Eugster et al. 2006).

Since YORP gradually changes the rotation states of NEOs during the orbital evolution, the distribution of the rotation periods reflects the NEO age. Although YORP also decelerates the rotation, here we consider only the acceleration. The decelerated tiny asteroids shortly enter tumbling states once spinning down starts (Vokrouhlický et al. 2007; Breiter et al. 2011) and it is difficult to predict their evolution accurately. In this study, we estimate reachable rotation periods of NEOs by the YORP acceleration. For the sake of simplicity, we do not take into account the time evolution of the orbital elements, resulting in a constant acceleration.

We use two assumptions as follows. A tiny asteroid is a fragment of a collisional event and its initial rotation period, $P_{\rm init}$, is given by an extrapolation of the diameter and rotation period relation for mm-sized fragments in a collisional experiment (Kadono et al. 2009):

$$P_{\rm init} = 10 \left(\frac{D}{1\,{\rm m}} \right) \ {\rm s}. \tag{2.10}$$

The YORP acceleration follows a scaling law and is derived from the YORP strength of the near-Earth object Bennu (Vokrouhlický et al. 2004; Hergenrother et al. 2019):

$$\frac{d\omega}{dt} = 8.5 \times 10^{-18} \times \left(\frac{a_{\rm Bennu}^2 \sqrt{1-e_{\rm Bennu}^2}}{a_{\rm ast}^2 \sqrt{1-e_{\rm ast}^2}} \right) \left(\frac{D_{\rm Bennu}}{D} \right)^2 \ {\rm rad\,s^{-2}}, \tag{2.11}$$

where ω is the angular velocity of the asteroid, $D_{\rm Bennu}$ is the diameter of Bennu, $a_{\rm Bennu}$ and $a_{\rm ast}$ are the semimajor axes of Bennu and the asteroid, and $e_{\rm Bennu}$ and $e_{\rm ast}$ are the orbital eccentricities of Bennu and the asteroid. We adopt that $D_{\rm Bennu}$ is 482 m, $a_{\rm Bennu}$ is 1.126 au, and $e_{\rm Bennu}$ is 0.204[4]. We set $a_{\rm ast}$ to 2 au and $e_{\rm ast}$ to zero since most of NEOs have come from the inner main belt (Granvik et al. 2018).

We assume a linear acceleration of a rotation period by YORP and obtain the ω in time t as follows:

$$\omega = \frac{d\omega}{dt} t + \omega_0 \ {\rm rad\,s^{-1}}, \tag{2.12}$$

where ω_0 is the initial angular velocity of the asteroid. We calculate the NEO age, $\tau_{\rm YORP}$, as follows by solving Equation 2.12 for t with Equations 2.10 and 2.11:

$$\tau_{\rm YORP} = 3.7 \times 10^3 \left(\frac{a_{\rm ast}^2 \sqrt{1-e_{\rm ast}^2}}{a_{\rm Bennu}^2 \sqrt{1-e_{\rm Bennu}^2}} \right) \tag{2.13}$$

$$\times \left(\frac{D}{D_{\rm Bennu}} \right)^2 \left(\frac{1}{P} - \frac{1}{10D} \right) \ {\rm Myr}. \tag{2.14}$$

[4] https://ssd.jpl.nasa.gov/tools/sbdb_lookup.html#/, last accessed 2021 December 20.

Figure 2.14 shows isochrones for t = 0.1, 1, 10, 100, and 1,000 Myr. Based on the isochrones, tiny NEOs with diameters less than 10 m and ages older than 10 Myr, corresponding to the typical dynamical evolution timescale of the NEOs, rotates faster than about 10 s. However, such fast rotators are not found other than 2020 HS_7. The observed truncation is not produced by the constant acceleration model.

The densities and surface properties of NEOs depend on their sizes (Carry 2012). However, the density difference of NEOs is a factor of a few at most and does not suppress the acceleration of rotation sufficiently. The thermal inertia also has little effect on the rotation period (Čapek & Vokrouhlický 2004; Golubov et al. 2021). Therefore, other dynamical mechanisms are required to explain the flat-top distribution.

Tensile strength

We discuss the possibility that fast-rotating tiny asteroids are destroyed by the centrifugal force. The critical rotation period for keeping the shape against the centrifugal force, $P_{\rm cri}$, is expressed as follows (see Appendix E for the details):

$$P_{\rm cri} = 0.42 (C_{\rm shape})^{-1} \left(\frac{\rho}{2500\,{\rm kg\,m^{-3}}} \right)^{1/2} \times \left(\frac{\kappa}{10^5\,{\rm N\,m^{-3/2}}} \right)^{-1/2} \left(\frac{D}{1\,{\rm m}} \right)^{5/4} {\rm s}, \tag{2.15}$$

where ρ is a bulk density and κ is a tensile strength coefficient (Holsapple 2007; Kwiatkowski et al. 2010). $C_{\rm shape}$ is the coefficient indicating the shape of the asteroid defined as

$$C_{\rm shape} = (C_1 C_2)^{1/3} \sqrt{\frac{5(3C_{\rm fric}(1+C_2^2) - \sqrt{3(1-C_2^2+C_2^4)})}{3{C_{\rm fric}}^2(1+C_2^2)^2 - 1 + C_2^2 - C_2^4}}, \tag{2.16}$$

where C_1 and C_2 are the axial ratios of c/a and b/a, respectively, and $C_{\rm fric}$ is a friction coefficient (Holsapple 2007). We adopt that C_1 is 0.7, C_2 is 0.7, and $C_{\rm fric}$ is 0.31 corresponding to a friction angle of 40°. Then, the shape coefficient $C_{\rm shape}$ equals 1.8.

We present two lines indicating $P_{\rm cri}$ with tensile strength of typical stony meteorites ($\kappa = 10^5\,{\rm N\,m^{-3/2}}$, Kwiatkowski et al. 2010) and weak material ($\kappa = 10^3\,{\rm N\,m^{-3/2}}$), respectively, in panel (b) of Figure 2.14. We use a typical density of S-type asteroids ($\rho = 2500\,{\rm kg\,m^{-3}}$). In the case of weak material, we can explain the deficiency of NEOs with $D \leq 10\,{\rm m}$ and $P \leq 10\,{\rm s}$. However, the flat-top shape of the distribution is not reproduced because $P_{\rm cri}$ is proportional to $D^{5/4}$.

Suppression of YORP by meteoroid impacts

The YORP acceleration can be suppressed by meteoroid impacts onto an asteroid's surface (Farinella et al. 1998; Wiegert 2015). We investigate the evolution of the rotation period taking into account possible effects of meteoroid impacts. We discuss two effects related to meteoroid impacts: angular momentum transfer and cratering.

Angular momentum transfer The absolute angular momentum of an asteroid is written as $L = I\omega$, where I is a moment of inertia of the asteroid. A change of the angular momentum caused by a collision of a meteoroid is expressed as $\delta L = \beta |m\vec{v}_{\rm imp} \times \vec{R}|$, where β is a dimensionless momentum multiplication factor, m is the mass of the meteoroid, $\vec{v}_{\rm imp}$ is the impact velocity vector of the meteoroid, and $\vec{R}$ is the position vector from the center of the asteroid. Assuming the angle between $\vec{v}_{\rm imp}$ and $\vec{R}$ is 90°, a relative angular momentum change in a single collision is written as

$$\frac{\delta L}{L} = \frac{\beta m v_{\rm imp} R}{\frac{2}{5} M R^2 \frac{2\pi}{P}} = \frac{15 \beta m v_{\rm imp} P}{16 \pi^2 \rho R^4}, \tag{2.17}$$

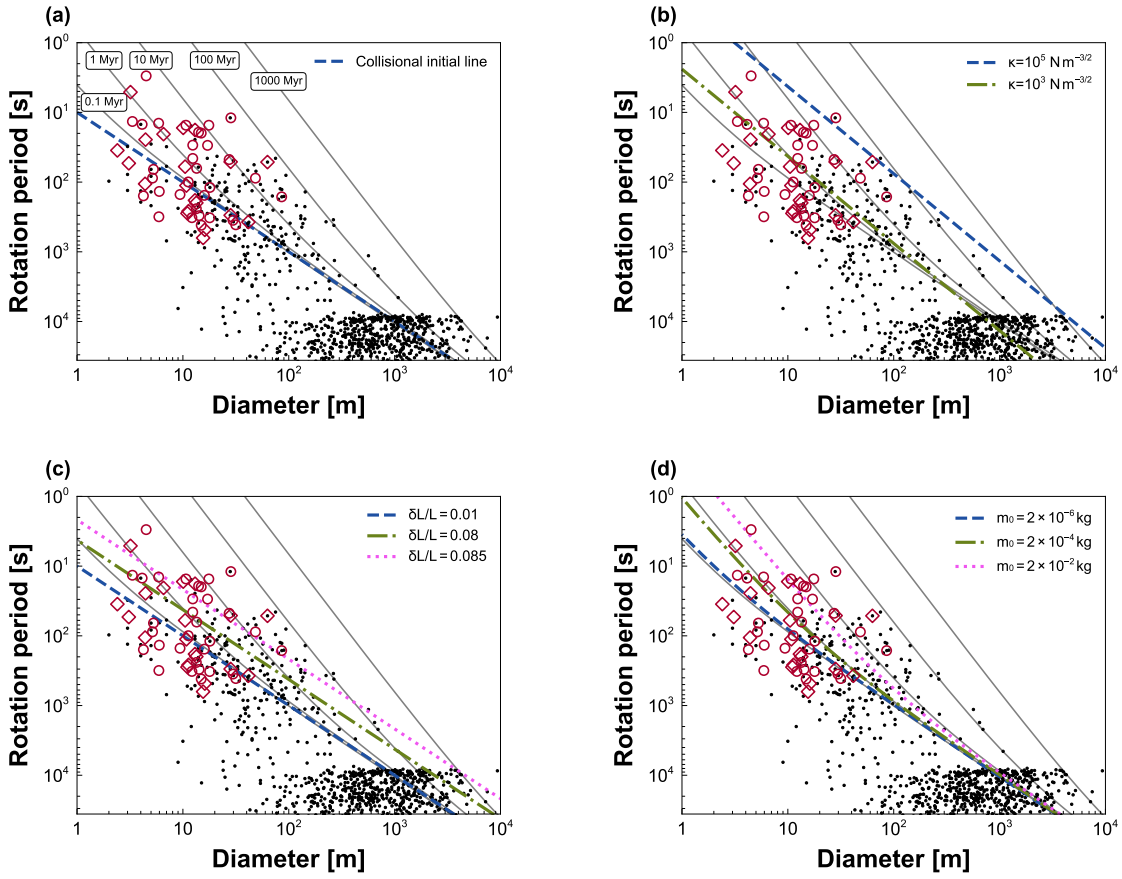

Figure 2.14. D-P relations of NEOs with the isochrones (solid lines). The Tomo-e NEOs in Beniyama et al. (2022) and new samples are represented by open circles and diamonds, respectively. NEOs in LCDB are represented by filled circles. (a) D-P relation with the collisional initial line (dashed line). (b) D-P relation with lines of critical rotation periods when asteroids have tensile strength of a typical meteorite (dashed line) and weak material (dot-dashed line). (c) D-P relation with lower limits by angular momentum transfers due to meteoroid impacts with $\delta L/L = 0.01$ (dashed-line), 0.08 (dot-dashed line), and 0.085 (dotted line). (d) D-P relation with lower limits by cratering due to meteoroid impacts with m_0 of 2×10^{-6} kg (dashed-line), 2×10^{-4} kg (dot-dashed line), and 2×10^{-2} kg (dotted line). See text for details.

where M and ρ are the mass and the bulk density of the asteroid, respectively (Wiegert 2015). When a collision with a large $\delta L/L$ occurs, the spin axis of the asteroid can be tilted. heading to a ceasing of the YORP acceleration. Therefore, a timescale of such a critical collision, $\tau_{\rm L}$, corresponds to the duration of the YORP acceleration,

Campbell-Brown & Braid (2011) estimated a flux of meteoroids from observations of sporadic meteors as

$$N(>m) = 5 \times 10^{-11} \left(\frac{m}{2 \times 10^{-6}\,\mathrm{kg}} \right)^{-1} \mathrm{m}^{-2}\mathrm{s}^{-1}. \tag{2.18}$$

A typical timescale that a meteoroid with a mass larger than m collides with the asteroid with the radius of R is written as follows:

$$\begin{aligned} \tau_{\rm L} &= \frac{1}{N(>m) \times \pi R^2} \\ &= 1.1 \left(\frac{\delta L}{L} \right) \left(\frac{\beta}{20} \right)^{-1} \left(\frac{v_{\rm imp}}{3 \times 10^4\,\mathrm{m\,s^{-1}}} \right)^{-1} \\ &\times \left(\frac{\rho}{2500\,\mathrm{kg\,m^{-3}}} \right) \left(\frac{D}{1\,\mathrm{m}} \right)^{2} \left(\frac{P}{1\,\mathrm{s}} \right)^{-1} \mathrm{Myr}. \end{aligned} \tag{2.19}$$

We adopt that β is 20, $v_{\rm imp}$ is $3 \times 10^4\,\mathrm{m\,s^{-1}}$, and ρ is $2500\,\mathrm{kg\,m^{-3}}$ as typical quantities. A timescale $\tau_{\rm L}$ provides the possible fastest rotation period accelerated by YORP. We present three limiting lines for different $\delta L/L$ values in panel (c) of Figure 2.14. The YORP acceleration of smaller asteroids is more suppressed by the angular momentum transfer. However, the flat-top shape of the distribution is not reproduced because the reachable periods are proportional to D.

Cratering When a sufficiently large fraction of the asteroid's surface is covered with the craters, the continuous YORP acceleration is not an appropriate assumption since YORP is sensitive to small structures (Statler 2009). To discuss the cratering effect of meteoroid impacts, we use the crater scaling law in Holsapple (1993):

$$\frac{\rho V_{\rm crater}}{m} = K_2 \left(\frac{Y}{\rho v_{\rm imp}^2} \right)^{-3\mu/2}, \tag{2.20}$$

where $V_{\rm crater}$ is the volume of the crater, Y is the tensile strength of the target, and both K_2 and slope μ are constants depending on the taxonomic type of the target. We refer to the material strength in Holsapple (2020):

$$Y = 1.5 \times 10^7 \left(\frac{D}{10^{-1}\,\mathrm{m}} \right)^{1/4} \mathrm{Pa}. \tag{2.21}$$

The radius of the crater $R_{\rm crater}$ is written as follows:

$$R_{\rm crater} = K_R V_{\rm crater}^{1/3}\ \mathrm{m}, \tag{2.22}$$

where K_R is a constant that depends on the crater shape.

From Equations 2.20–2.22, a surface area of a single crater, $S_{\rm crater}$, is written as follows assuming a bowl-like crater:

$$S_{\rm crater} \sim \pi R_{\rm crater}^2 = \pi K_R^2 \left(\frac{K_2}{\rho} \right)^{2/3} \left(\frac{Y}{\rho v_{\rm imp}^2} \right)^{-\mu} m^{2/3}\ \mathrm{m}^2. \tag{2.23}$$

From Equation 2.18, the flux density of the meteoroids colliding with the target, n, is expressed as a function of the mass of the impactor, m, and the radius of the target, R, as follows:

$$n = 10^{-16} m^{-2} \cdot 4\pi R^2\ \mathrm{kg}^{-1}\,\mathrm{s}^{-1}. \tag{2.24}$$

We can estimate the total surface of the cratering area by meteoroids per unit time, $S^{\rm total}_{\rm crater}$, as follows:

$$S^{\rm total}_{\rm crater} = \int_{m0}^{m1} S_{\rm crater} n dm = 12\pi^2 \times 10^{-16} \times (m_0^{-1/3} - m_1^{-1/3}) R^2 K_R^2 \left(\frac{K_2}{\rho}\right)^{2/3} \left(\frac{Y}{\rho v_{\rm imp}^2}\right)^{-\mu} \ {\rm m^2\,s^{-1}}, \tag{2.25}$$

where m_0 and m_1 are minimum and maximum masses of the meteoroids, respectively. We set $m_1 \to \inf$ and m_0 as a free parameter.

We assume that no further YORP acceleration works once the craters cover a certain fraction of the target surface, $\delta S/S$. The timescale covering $\delta S/S$ of the surface with craters, $\tau_{\rm crater}$, is expressed as

$$\tau_{\rm crater} = \left(\frac{\delta S}{S}\right) \frac{10^{16}}{3\pi K_R^2} \left(\frac{\rho}{K_2}\right)^{2/3} \left(\frac{Y}{\rho v_{\rm imp}^2}\right)^{\mu} m_0^{1/3} \ {\rm Myr}, \tag{2.26}$$

where S is the entire surface area of the target.

We adopt that K_2 is 1 and μ is 0.55, typical values for S-type asteroids. Assuming a bowl-like crater, we set K_R to 1.3 (Holsapple 1993, 2020). The timescale for S-type asteroids, $\tau_{\rm crater,S}$, is given by

$$\tau_{\rm crater,S} = 0.13 \left(\frac{\rho}{2500\,{\rm kg\,m^{-3}}}\right)^{2/3-0.55} \left(\frac{v_{\rm imp}}{3\times10^4\,{\rm m\,s^{-1}}}\right)^{-1.1} \times \left(\frac{D}{1\,{\rm m}}\right)^{0.55/4} \left(\frac{m_0}{2\times10^{-6}\,{\rm kg}}\right)^{1/3} \left(\frac{\delta S}{S}\right) \ {\rm Myr}. \tag{2.27}$$

We adopt ρ of $2500\,{\rm kg\,m^{-3}}$, $v_{\rm imp}$ of $3\times10^4\,{\rm m\,s^{-1}}$. The possible fastest rotation periods are presented over a wide range of m_0 values in panel (d) of Figure 2.14. The possible fastest rotation period is approximately proportional to D. Therefore, we cannot explain the truncated distribution with the suppression of YORP by cratering.

Tangential YORP effect

We have considered only the normal YORP (NYORP) disregarding tangential YORP (TYORP). TYORP depends on the rotation period and thermal properties of the asteroid as with NYORP. In most cases, TYORP contributes to the acceleration of the rotation unlike NYORP, which decelerates the rotation as well (Golubov & Krugly 2012; Golubov et al. 2014).

By taking both NYORP and TYORP into consideration, the YORP acceleration is expressed as follows:

$$\frac{d\omega}{dt} = 8.5\times10^{-18} \left(\frac{a^2_{\rm Bennu}\sqrt{1-e^2_{\rm Bennu}}}{a^2_{\rm ast}\sqrt{1-e^2_{\rm ast}}}\right) \times \left(\frac{D_{\rm Bennu}}{D}\right)^2 (\gamma + (1-\gamma)\eta(\theta)) \ {\rm rad\,s^{-2}}, \tag{2.28}$$

where γ is a fraction of the NYORP contribution to the total YORP strength, $\eta(\theta)$ is an efficiency function of TYORP, and θ is a thermal parameter corresponding to a ratio of two characteristic scales related to thermal conductivity: a thermal conductivity length $L_{\rm cond}$ and a length of heat conductivity wave $L_{\rm wave}$ (Golubov & Kruguly Golubov2012).

The thermal conductivity length is defined as

$$L_{\rm cond} = \frac{\lambda}{((1-A)^3\Phi^3\varepsilon\sigma_{\rm SB})^{1/4}} \ {\rm m}, \tag{2.29}$$

where λ is the heat conductivity of the asteroid, ε and A are the thermal emissivity and the Bond albedo of the surface, respectively, Φ is the solar energy flux, and $\sigma_{\rm SB}$ is Stefan-Boltzmann's constant. $L_{\rm cond}$ is a typical scale of how far the heat conduction takes place. The length of the heat conductivity wave is defined as

$$L_{\rm wave} = \left(\frac{\lambda}{C\rho\omega}\right)^{1/2} \ {\rm m}, \tag{2.30}$$

where C is the heat capacity of the asteroid. $L_{\rm wave}$ is a typical scale how far the heat is transferred when considering a time variation against a heat source.

Therefore, θ is written as follows:

$$\theta(\omega) = \frac{L_{\rm cond}}{L_{\rm wave}} = \frac{(C\rho\lambda\omega)^{1/2}}{((1-A)^3\Phi^3\varepsilon\sigma_{\rm SB})^{1/4}}. \tag{2.31}$$

The parameter θ characterizes the temperature condition of the surface and is a function of a rotation period.

Numerical simulations show that the TYORP effect is significant for $\theta \sim 1$ (Golubov & Krugly 2012; Golubov et al. 2014). We simplify the efficiency of TYORP as follows:

$$\eta(\theta) = \begin{cases} 1 & \theta_{\rm min} < \theta < \theta_{\rm max}, \\ 0 & \text{otherwise}, \end{cases} \tag{2.32}$$

where $\theta_{\rm min}$ and $\theta_{\rm max}$ are free parameters. We show an example of θ and η assuming $\theta_{\rm min}$ of 0.1 and $\theta_{\rm max}$ of 5 in Figure 2.15.

The isochrones considering TYORP are shown in panel (a) of Figure 2.16. We adopt γ equals 0.1 and 0.5 since TYORP is thought to be as strong as or stronger than NYORP (Golubov & Krugly 2012; Golubov et al. 2014). Previous studies suggest that parts of tiny NEOs have fine particles on the surface (Mommert et al. 2014a; Fenucci et al. 2021). We assume that the asteroid's surface is covered by regolith with $\lambda = 0.0015\,{\rm W\,m^{-1}\,K^{-1}}$, $C = 680\,{\rm J\,kg^{-1}\,K^{-1}}$, and $\rho = 2500\,{\rm kg\,m^{-3}}$. We set $\varepsilon = 0.7$ and $a = 2.0\,{\rm au}$ corresponding to typical values for NEOs. We adopt that $A = 0.084$, which is derived with typical properties of moderate albedo asteroids: p_V of 0.2 and a phase integral q of 0.42 (Shevchenko et al. 2019). As of November 2021, the change in the rotation periods of 10 asteroids have been confirmed (Ďurech et al. (2022b), and references therein). The range of θ among the 10 asteroids is calculated to be 0.26 to 1.3. Since all the 10 asteroids are accelerated, not decelerated, we assume that TYORP is effective for all of them. Thus, we set $\theta_{\rm min}$ and $\theta_{\rm max}$ to 0.1 and 5, respectively. The YORP acceleration considering TYORP successfully leads to flat-top shapes around $D \sim 100\,{\rm m}$ and $P \sim 300\,{\rm s}$ since the YORP acceleration becomes weaker at $\theta = \theta_{\rm max} = 5$. However, they do not match the truncated distribution around $D \sim 10\,{\rm m}$ and $P \sim 10\,{\rm s}$ seen in the D-P relation diagram. In the case of $\theta_{\rm max} = 30$, the isochrones become similar to the observed distribution as shown in Figure 2.16 (b). The larger θ value means that much more asteroids experience TYORP acceleration than theoretical predictions. The fact that TYORP acts up to $\theta = 30$ under assumptions above is rephrased as the asteroids are illuminated by stronger radiation or thermal parameters such as C and λ are smaller. Most of Tomo-e NEOs have smaller perihelion distances ($r \sim 1\,{\rm au}$) than $2\,{\rm au}$ at the time of observations. Thus, in the case of C or λ is an order of magnitude less, θ changes by the factor $(2^2)^{3/4} \times (10)^{1/2} \sim 9$. The observed truncation around 10 s in the rotation period may be produced by the TYORP effect.

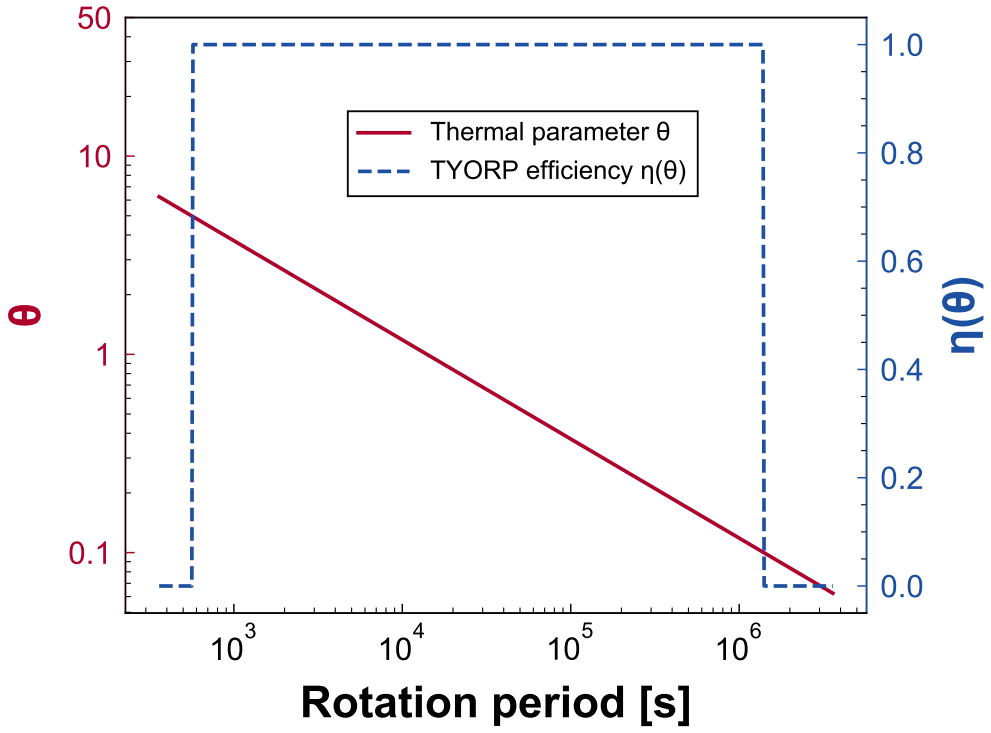

Figure 2.15. Visualization of thermal parameter and the efficiency of TYORP. $\theta_{\rm min}$ of 0.1 and $\theta_{\rm max}$ of 5 are assumed.

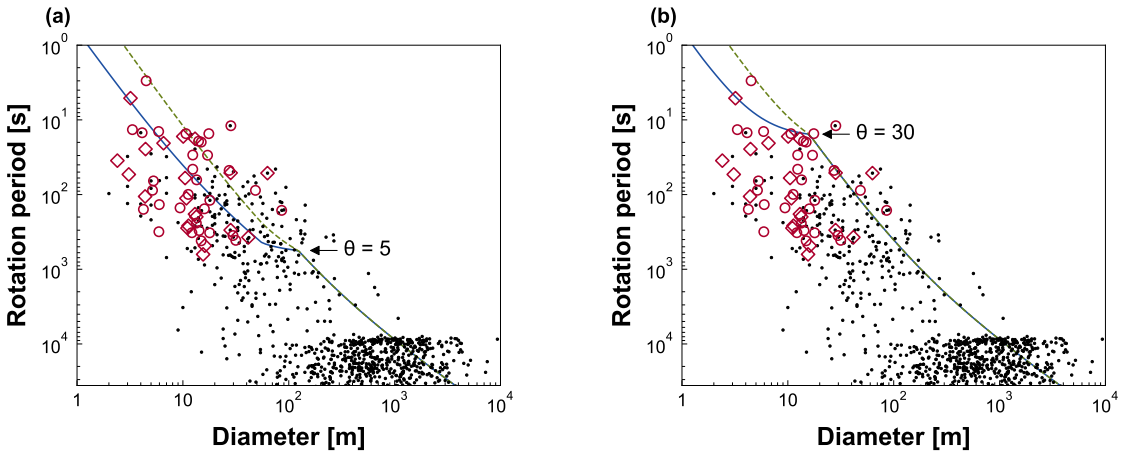

Figure 2.16. D-P relations of NEOs with isochrones considering the TYORP effect. The Tomo-e NEOs in Beniyama et al. (2022) and new samples are represented by open circles and diamonds, respectively. NEOs in LCDB are represented by filled circles. (a) Case with $\theta_{\rm max}$ of 5. (b) Case with $\theta_{\rm max}$ of 30. Isochrones of 10 My old with γ of 0.1 and 0.5 are shown with solid and dashed lines, respectively. Arrows indicate positions where θ reaches $\theta_{\rm max}$.

2.5. Summary of this chapter

A rotation period of an asteroid reflects its dynamical history and physical properties. We have obtained the lightcurves of 108 tiny NEOs with the wide-field CMOS camera Tomo-e Gozen. We successfully derived the rotation periods and axial ratios of 52 samples owing to the video observations at 2 fps. We found 23 objects with rotation periods less than 60 s. Compared with the literature, the distribution of the rotation periods of 52 objects shows a potential excess in shorter periods. This result suggests that previous studies missed some populations of fast-rotating asteroids due to long exposure time observations.

We discovered that the distribution of the tiny NEOs in the D-P diagram is truncated around a period of 10 s. We performed model calculations taking into account the YORP effect. A NEO smaller than 10 m is expected to rotate with a period shorter than 10 s assuming a constant acceleration by YORP, which is not consistent with the present results. The truncated distribution is not well explained by either the realistic tensile strength of NEOs or the suppression of YORP by meteoroid impacts. We found that the tangential YORP effect is a possible mechanism to produce the truncated distribution, although further observational and theoretical studies as well as high-speed lightcurve observations of NEOs are necessary to reach a conclusion.

Quality is more important than quantity. One home run is much better than two doubles.
— Steve Jobs (1955–2011)

3. *Multicolor Photometry of Tiny Near-Earth Asteroid 2015 RN_{35}*

In this chapter, we report the results of multicolor photometry of the tiny near-Earth asteroid 2015 RN_{35} using the 3.8 m Seimei telescope in Japan and the TRAPPIST-South telescope in Chile over twelve nights in 2022 December and 2023 January. We observed 2015 RN_{35} across a wide range of phase angles from 2° to 30° in the g, r, i, and z bands in the Pan-STARRS system. These lightcurves show that 2015 RN_{35} is in a non-principal axis spin state with two characteristic periods of 1149.7 ± 0.3 s and 896.01 ± 0.01 s. We found that a slope of a visible spectrum of 2015 RN_{35} is as red as asteroid Justitia, one of the very red objects in the main belt, which indicates that 2015 RN_{35} can be classified as an A- or Z-type asteroid. In conjunction with the shallow slope of the phase curve, we suppose that 2015 RN_{35} is a high-albedo A-type asteroid. We demonstrated that the surface properties of tiny asteroids could be well constrained by intensive observations across a wide range of phase angles. 2015 RN_{35} is a possible mission accessible A-type near-Earth asteroid with a small Δv of 11.801 km s^{-1} in the launch window between 2030 and 2035.

The contents of this chapter have been published in Beniyama et al. (2023a).

3.1. Introduction

It is now well established that the first stage of the planetary formation process is the accretion of the so-called planetesimals from the solids in our protoplanetary disk. Theoretical and observational studies have shown that the planetesimals were formed at large sizes, diameters (D) larger than 50 to 100 km (Delbo' et al. 2017). The small bodies of our solar system are remnants of that era. However, not all the current asteroids are survivors from primordial times. Collisions between this original planetesimal population produced clusters of fragments of smaller sizes, the so-called asteroid families. A nongravitational effect—the Yarkovsky effect—slowly changes the orbital semimajor axis a of asteroids at a rate da/dt proportional to $1/D$ (Vokrouhlický 1998). Asteroids in the prograde rotation have da/d$t > 0$ and migrate towards larger heliocentric distances, whereas those in retrograde rotation with da/d$t < 0$ migrate towards the Sun. Another effect that is also caused by solar radiation, the YORP effect (Rubincam 2000), can change the spin state of asteroids affecting the rate of the drift due to Yarkovsky. Both the Yarkovsky and YORP effects depend on the surface properties of the asteroids and their internal structure. The migration of small main belt asteroids can lead the smaller ones to reach the dynamical routes (resonances with planets) that can bring them to near-Earth space, hence sampling several regions (as well as asteroid families) of the main belt. Studying NEAs is therefore crucial to understanding the material transportation from the main belt to near-Earth space as well as to mitigate the hazard of an asteroid's impact to the Earth.

Tiny asteroids having diameters less than 100 m could be characterized during their close approaches to the Earth using ground-based and space-borne telescopes. Comprehensive studies of large asteroids have been conducted, whereas only a few studies focus on tiny asteroids due to observational difficulties caused by limited visibilities and large apparent motions of asteroids during their close approaches.

Reddy et al. (2016) conducted radar, lightcurve, and spectroscopic observations of the tiny E-type NEA 2015 TC_{25} ($D \sim 2$ m). They concluded that 2015 TC_{25} is a fragment possibly ejected from the E-type main belt asteroid (44) Nysa. One of the interesting properties of 2015 TC_{25} is its bluer spectrum

compared to a typical E-type. They explained the bluer slope of 2015 TC_{25} in the visible wavelength with a lack of fine regolith on the surface due to a combination of weak gravity and fast rotation. Recently, Licandro et al. (2023) found that a visible spectrum of the tiny fast-rotating asteroid 2022 AB ($D \sim 65$ m and $P \sim 3$ minutes) shows an upturn over the 0.4 to 0.6 μm, which does not fit with any known asteroid spectrum [1].

The phase angle dependence of an asteroid's brightness, the so-called phase curve, informs about the surface properties of the asteroid (see, e.g., Bowell et al. 1989; Belskaya & Shevchenko 2000). High-albedo asteroids have shallower slopes in their phase curves since the contribution of the shadow-hiding decreases as albedo increases (Belskaya & Shevchenko 2000), whereas low-albedo asteroids have steeper slopes. Apart from the albedo, other properties are related to the phase curve such as the surface grain size and roughness. An important consideration in studying phase curves of asteroids is the rotation correction (see, e.g., Harris & Lupishko 1989). Homogeneous sets of the typical brightness such as the maximum and mean of the lightcurves at certain phase angles are necessary to accurately derive the related quantities, otherwise, the brightness variation caused by the rotation leads to a misunderstanding of observational results. Thus, the tiny asteroids, which are often fast-rotating (Thirouin et al. 2016, 2018; Beniyama et al. 2022) and do not require a long time to obtain a mean brightness across a rotation phase, are appropriate targets to investigate phase curves.

Well-sampled phase curves of small asteroids are less commonly obtained since their observation opportunities are limited. Reddy et al. (2015) characterized the small NEA 2004 BL_{86} ($D \sim 300$ m) at a wide phase angle range from 1.5° to 49.6°. The visible geometric albedo of about 0.4 derived from the slope of the phase curve is consistent with the near-infrared spectrum of 2004 BL_{86}, which implies that 2004 BL_{86} is a typical high-albedo V-type asteroid. Recently, several dozens of phase curves of NEAs have been studied in the framework of the IMPACTON project (Rondón et al. 2019, 2022; Ieva et al. 2022; Arcoverde et al. 2023). They made a database with phase curves of 30 NEAs using three 1 m-class telescopes in Brazil and Italy (Arcoverde et al. 2023). Their sample includes only one tiny NEA, 2017 DC_{38}, with the absolute magnitude H of 24.22, that was successfully observed at a very small phase angle of 1.1°. However, its rotation period was not obtained and thus no rotation correction has been performed in the analysis of the phase curve of 2017 DC_{38}.

In this chapter, we present the results of multicolor photometry of the tiny NEA 2015 RN_{35} over twelve nights in Japan and Chile. The target asteroid 2015 RN_{35} was discovered by the Pan-STARRS 1 survey (Chambers et al. 2016) on 2015 September 9. 2015 RN_{35} is an Apollo-class NEA, and its absolute magnitude in the V band is 23.24 in NASA JPL SBDB as of 2023 August 10. The trajectories of 2015 RN_{35} were well studied and possible collisions with Earth were discussed (Petrov et al. 2018). 2015 RN_{35} had a close approach in 2022 December. 2015 RN_{35} was observable at phase angles from 30° to 0.6 ° from 2022 December to 2023 January, which is a rare opportunity to obtain a well-sampled phase curve of a tiny asteroid. The chapter is organized as follows. In Section 3.2, we summarize our observations and data reduction. The physical properties of 2015 RN_{35} are summarized in Section 3.3. The surface properties of the tiny asteroid 2015 RN_{35} and possible exploration by spacecraft mission are discussed in Section 3.4.

3.2. Observations and data reduction

We conducted photometric observations at two observatories in Japan and Chile. The observing conditions are summarized in Table 3.1. The predicted V band magnitudes, phase angles, distances between 2015 RN_{35} and observer, and distances between 2015 RN_{35} and the Sun in Table 3.1 were obtained from NASA JPL HORIZONS using the `Python` package `astroquery` (Ginsburg et al. 2019).

[1] We note that the spectrum is similar to that of the Martian Trojan (121514) 1998 UJ_7 (Borisov et al. 2018).

3.2.1. Seimei telescope

We obtained 12 lightcurves of 2015 RN_{35} using the TriColor CMOS Camera and Spectrograph (TriCCS) on the 3.8 m Seimei telescope (Kurita et al. 2020) from 2022 December 23 to 2023 January 21. We simultaneously took three-band images in the Pan-STARRS (g, r, i) and (g, r, z) filter (Chambers et al. 2016). The field of view is 12.6 $\times$ 7.5 with a pixel scale of 0.350 arcsec/pixel.

Nonsidereal tracking was performed during the observations of 2015 RN_{35}. The exposure times were 5 or 60 s according to the brightness of 2015 RN_{35}. The signal-to-noise ratios of 2015 RN_{35} in the data taken in 2023 January are too low to detect 2015 RN_{35} in a single exposure. We took multiple images with short exposures rather than a single image with long exposures in our observations in order to avoid having elongated photometric reference stars and also to eliminate the cosmic rays.

We performed standard image reduction including bias subtraction, dark subtraction, and flat-fielding. The astrometry of reference sources from the Gaia Data Release 2 was performed using the `astrometry.net` software (Lang et al. 2010). For the data taken in 2023 January, we performed stacking of images before photometry to avoid the elongations of the images of 2015 RN_{35} as shown in upper panels of Figure 3.1 (hereinafter referred to as the nonsidereally stacked image). We stacked 20 successive images with exposure times of 60 s. Since a typical readout time of the CMOS sensors on TriCCS is 0.4 milliseconds, the total integration time is about 1200 s, which corresponds to one of the characteristic periods of 2015 RN_{35} (see Section 3.3.1). We also stacked images using the World Coordinate System (WCS) of images corrected with the surrounding sources to suppress the elongations of the images of reference stars as shown in lower panels of Figure 3.1 (hereinafter referred to as the sidereally stacked image).

We derived colors and magnitudes of 2015 RN_{35} following the same procedure described in Appendix F (Beniyama et al. 2023c). Cosmic rays were removed with the `Python` package `astroscrappy` (McCully et al. 2018) using the Pieter van Dokkum's `L.A.Cosmic` algorithm (van Dokkum 2001). The circular aperture photometry was performed for 2015 RN_{35} and the reference stars using the SExtractor-based `Python` package `sep` (Bertin & Arnouts 1996; Barbary et al. 2017). The aperture radii were set to twice as large as the FWHMs of the PSFs of the reference stars in the sidereally stacked images. The photometric results of 2015 RN_{35} and reference stars were obtained from the nonsidereal and sidereal stacked images, respectively.

3.2.2. TRAPPIST-South telescope

We obtained five lightcurves of 2015 RN_{35} using the robotic telescope TRAPPIST-South (the Minor Planet Center code I40; Jehin et al. 2011) of the University of Liège between 2022 December 19 and 26. TRAPPIST-South is a 0.6-m Ritchey-Chrétien telescope operating at f/8 and equipped with a CCD camera FLI ProLine 3041-BB. The field of view is 22 $\times$ 22 with an un-binned pixel scale of 0.64 arcsec/pixel.

We obtained images in the sidereal tracking mode with the wide Exo-filter, whose wavelength coverage roughly corresponds to the r to y bands in the Pan-STARRS system (Jehin et al. 2011). We set the exposure time to 40 s on December 19, 20, 21, and 22 using the 2 $\times$ 2 binning mode, and to 120 s on December 26 while using no binning.

The raw images were processed using standard bias, dark, and flat field frames. The photometry was performed using the `PHOTOMETRYPIPELINE` (Mommert 2017) to derive the r band magnitudes in the Pan-STARRS system. This pipeline allows zero-point calibration by matching field stars with online catalogs. Typically 100 stars with solar-like colors (i.e. stars with $g - r$ and $r - i$ colors closer than 0.2 magnitudes to that of the Sun) were used in each image for the magnitude calibration. Aperture radii were set to 4 pixels for the binned observations and to 8 pixels for the un-binned mode.

Table 3.1. Summary of the observations

Obs. Date (UTC)		Tel.	Filter	$t_{\rm exp}$ (s)	$N_{\rm img}$	V (mag)	α (deg)	Δ (au)	$r_{\rm h}$ (au)	Air Mass	Weather
2022 Dec 19	05:05:40–08:40:18	TRAPPIST-S	Exo	40	233	15.3	31.1	0.014	0.996	1.24–1.48	Clear
2022 Dec 20	02:46:27–04:00:16	TRAPPIST-S	Exo	40	83	15.7	31.3	0.017	0.998	1.71–2.64	Clear
2022 Dec 21	07:13:33–08:34:49	TRAPPIST-S	Exo	40	91	16.1	31.1	0.021	1.002	1.32–1.51	Clear
2022 Dec 22	06:02:40–08:40:00	TRAPPIST-S	Exo	40	171	16.5	30.7	0.024	1.004	1.33–1.55	Clear
2022 Dec 23	16:32:56–17:14:41	Seimei	g, r, i	5	394	16.8	30.0	0.029	1.008	1.07–1.09	Clear
2022 Dec 23	19:03:49–19:45:32	Seimei	g, r, z	5	275	16.9	29.9	0.029	1.009	1.20–1.33	Clear
2022 Dec 26	05:04:08–08:39:14	TRAPPIST-S	Exo	120	100	17.4	28.1	0.037	1.016	1.39–1.64	Clear
2022 Dec 26	18:09:43–18:35:49	Seimei	g, r, i	30	53	17.5	27.7	0.039	1.018	1.10–1.14	Clear
2023 Jan 12	12:15:06–12:35:09	Seimei	g, r, i	1200	2	19.1	10.9	0.100	1.082	1.52–1.66	Cirrus
2023 Jan 16	14:54:23	Seimei	g, r, i	1200	1	19.3	6.7	0.117	1.100	1.06–1.06	Clear
2023 Jan 17	12:11:24	Seimei	g, r, i	1200	1	19.3	5.8	0.121	1.104	1.53–1.53	Cirrus
2023 Jan 18	14:07:50–14:30:15	Seimei	g, r, i	1200	2	19.4	4.7	0.125	1.109	1.08–1.11	Clear
2023 Jan 18	14:51:09	Seimei	g, r, z	1200	1	19.4	4.7	0.126	1.109	1.06–1.06	Clear
2023 Jan 20	14:04:41	Seimei	g, r, i	1200	1	19.4	2.8	0.134	1.118	1.10–1.10	Clear
2023 Jan 20	14:25:34	Seimei	g, r, z	1200	1	19.4	2.8	0.134	1.118	1.07–1.07	Clear
2023 Jan 21	14:03:12	Seimei	g, r, i	1200	1	19.4	1.9	0.139	1.123	1.10–1.10	Clear
2023 Jan 21	14:27:02–14:47:05	Seimei	g, r, z	1200	2	19.4	1.9	0.139	1.123	1.05–1.07	Clear

Note. — Observation time in UT in midtime of exposure (Obs. Date), telescope (Tel.), filters (Filters), total exposure time per frame ($t_{\rm exp}$), the number of images ($N_{\rm img}$), and weather condition (Weather) are listed. Predicted V band apparent magnitude (V), phase angle (α), distance between 2015 RN_{35} and observer (Δ), and distance between 2015 RN_{35} and Sun ($r_{\rm h}$) at the observation starting time are referred to NASA Jet Propulsion Laboratory (JPL) HORIZONS as of 2023 August 19 (UTC). Elevations of 2015 RN_{35} to calculate air mass range (Air Mass) are also referred to NASA JPL HORIZONS.

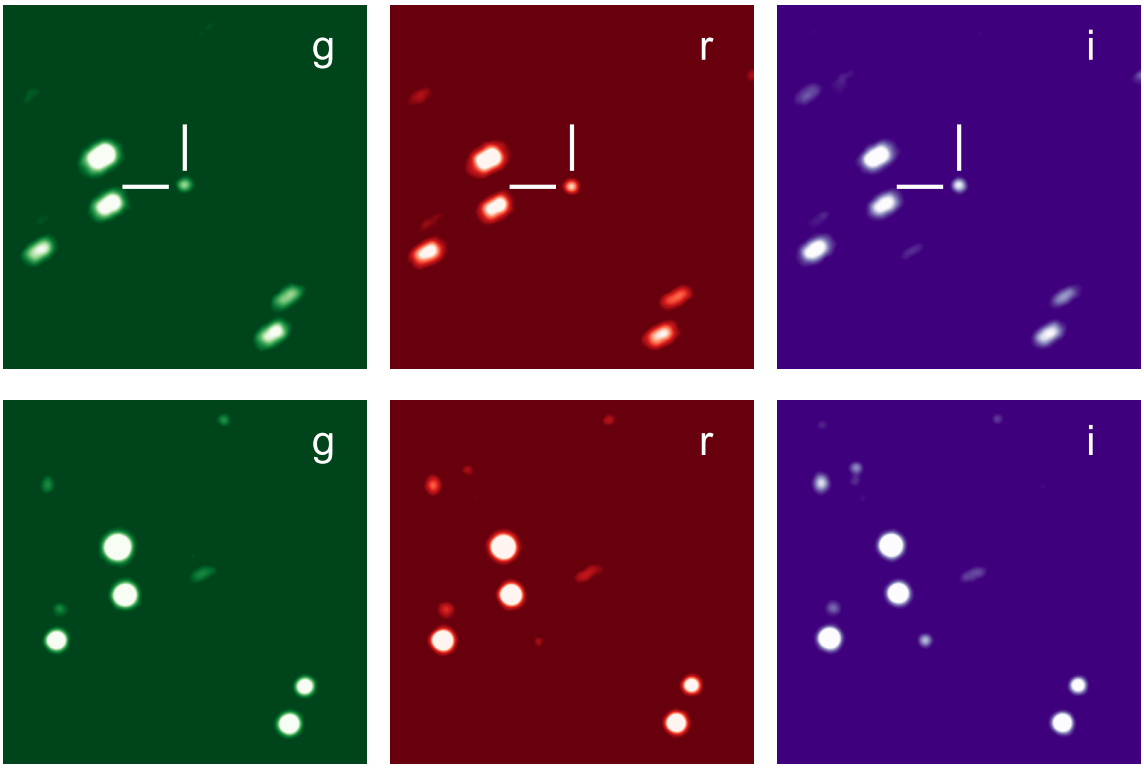

Figure 3.1. Stacked images of 2015 RN_{35} in g, r, and i bands with a total integration time of 1200 s in 2023 January 16. Nonsidereally stacked images (top) and sidereally stacked images (bottom) are shown. Horizontal and vertical bars indicate 2015 RN_{35}. Field of view covers 1.75×1.75. North is to the top and East is to the left.

3.3. Results

3.3.1. Lightcurves and rotation period

The light-travel time was corrected to obtain the time-series colors and magnitudes of 2015 RN_{35} (Harris & Lupishko 1989). The eight lightcurves of 2015 RN_{35} taken on 2022 December are shown in Figure 3.2. A brightness variation of about 0.7 mag is seen in each lightcurve. The lightcurves show non-perfect periodic signals, implying that 2015 RN_{35} is a non-principal axis rotator in a complex rotation state (i.e., a tumbler; Pravec et al. 2005).

We performed the periodic analysis using the Lomb–Scargle technique (Lomb 1976; Scargle 1982; VanderPlas 2018) with three long lightcurves obtained with the TRAPPIST-South telescope on 2022 December 19, 22, and 26. The Lomb–Scargle periodograms with a period range between 500 to 2000 s are shown in Figure 3.3, where four peak frequencies, f_a, f_b, f_c, and f_d, are indicated. We focused on the two strongest frequencies, f_b and f_d, based on the powers of periodograms. The f_d appears to be the first overtone of f_b: $2f_bf_d$. We regarded that f_b corresponds to a period of 2015 RN_{35}, P_1, since folded lightcurves with f_b^{-1} are typical double-peaked lightcurves. The uncertainty of P_1 was estimated with the Monte Carlo technique following the previous work (Beniyama et al. 2022). We obtained 1000 lightcurves by randomly resampling the data assuming each observed data point follows a normal distribution whose standard deviation is a photometric error. We calculated the 1000 periods corresponding to P_1 and derived it with the uncertainty each night as 1149.7 ± 0.4 s (Dec. 19), 1149.6 ± 0.5 s (Dec. 22), and 1149.9 ± 0.5 s (Dec. 26). We adopted the error-weighted average of these three periods, 1149.7 ± 0.3, as P_1.

Figure 3.4 shows the eight r band lightcurves of 2015 RN_{35} folded with the period of 1149.7 s. The folded lightcurves seem to be double-peaked but do not perfectly overlap each other in the rotation phase, probably due to the non-principal axis rotation. The model curve with the period of 1149.7 s is also shown in Figure 3.4. The root mean square of residual (RMS) is calculated as follows:

$$\mathrm{RMS} = \sqrt{\sum_i^{n_{\mathrm{obs}}} \frac{[y_{\mathrm{obs}}(t_i) - y_{\mathrm{model}}(t_i)]^2}{n_{\mathrm{obs}}}} \tag{3.1}$$

where n_{obs} is the number of observation data, t_i is the observation time of the i-th sample, $y_{\mathrm{obs}}(t_i)$ is i-th observed brightness at t_i, and $y_{\mathrm{model}}(t_i)$ is the model brightness at t_i. The RMS is calculated as 0.104.

Franco et al. (2023) derived the rotation period of 2015 RN_{35} to be 0.3193 ± 0.0001 hr ~ 1149 s using lightcurves obtained on 2022 December 18 and 19. Koleńczuk et al. (2023) found the rotation period of 19.1692 ± 0.0069 minutes ~ 1150 s from the intensive observation campaign during 2022 December. These reported periods are close to P_1 and corresponding to f_b in Figure 3.3. On the other hand, Colazo et al. (2023) derived the rotation period of 2015 RN_{35} to be 0.478 ± 0.008 hr ~ 1721 s using lightcurves obtained on 2022 December 16, which corresponds to f_a in Figure 3.3. Since the phased lightcurves in Colazo et al. (2023) appear as not double-peaked unlike others, the rotation period of ~ 1150 s is highly likely.

We continue the periodic analysis for the three lightcurves obtained with the TRAPPIST-South telescope on 2022 December 19, 22, and 26 following procedures in previous studies (Pravec et al. 2005, 2014; Lee et al. 2017, 2022). The purpose of the successive analysis is to derive the other period P_2 characterizing the non-principal axis rotation of 2015 RN_{35}. Searching for the P_2 is performed against all five lightcurves obtained with the TRAPPIST-South telescope. We fit the lightcurves with

two-dimensional Fourier series keeping P_1 fixed:

$$y_{\rm model}(t) = C_0 + \sum_{j=1}^{m}\left[C_{j0}\cos\left(\frac{2\pi j}{P_1}t\right) + S_{j0}\sin\left(\frac{2\pi j}{P_1}t\right)\right] + \sum_{k=1}^{m}\sum_{j=-m}^{m}\left[C_{jk}\cos\left(\frac{2\pi j}{P_1}t + \frac{2\pi k}{P_2}t\right) + S_{jk}\sin\left(\frac{2\pi j}{P_1}t + \frac{2\pi k}{P_2}t\right)\right], \quad (3.2)$$

where t is time, m is the order of Fourier series, C_0, C_{jk} and S_{jk} are the Fourier coefficients. We set P_2 and Fourier coefficients as free parameters and searched P_2 from 100 s to 10000 s with a step of 1 s. The RMS residual between observed and model lightcurves of 2015 RN_{35} is calculated in each step. The results of the search of P_2 are shown in Figure 3.5. We plotted the results of the grid search of P_2 in cases with m of 3 and 4. Five periods with smaller RMSs in the two cases, P_a = 896 s, P_b = 1603 s, P_c = 2688 s, P_d = 4062 s, and P_e = 8123 s, are indicated in Figure 3.5. The five periods might be linear combinations of the two basic periods. These appear to be related to each other: $P_b^{-1}P_c^{-1} + P_d^{-1}$, $P_c = 3P_a$, $2P_d 9P_a$, and $P_e 2P_d$. Thus, we regard the shortest period P_a as P_2, which is a period independent from P_1. This P_2 corresponds to the third strongest peak, f_c, in Figure 3.3. We also estimated the uncertainty of P_2 with the Monte Carlo technique as that of P_1. We derived P_2 as 896.01 ± 0.01 s with randomly resampled 1000 lightcurves.

The model curves with P_1 of 1149.7 s and P_2 of 896.01 s are shown in Figure 3.6 with the observed lightcurves. The RMS is calculated as 0.069. The model and observed lightcurves well overlap each other, which indicates that P_1 and P_2 are periods characterizing the rotation state of 2015 RN_{35}. We note that P_1 and P_2 may not necessarily correspond to rotation and precession (or precession and rotation) periods, respectively. Determination of the rotation and precession periods needs detailed physical modeling, which is out of the scope of this chapter.

3.3.2. Colors and reflectance spectrum

The time-series of colors of 2015 RN_{35} in 2022 December are shown in Figure 3.7. The error-weighted averages of those colors are derived as $g-r$ =0.714 ± 0.008, $r-i$ =0.245 ± 0.009, and $r-z$ =0.255 ± 0.020. The systematic errors in color determination with TriCCS are considered as in Beniyama et al. (2023c). The error-weighted average colors correspond to each other within the measurement errors when we consider the results on 2023 January (see panel (b) of Figure 3.9).

The reflectance spectrum of 2015 RN_{35} in Figure 3.8 was calculated with the derived colors and the solar colors with the same method in Beniyama et al. (2023b). The reflectances at the central wavelength of the r, i, and z bands, R_r, R_i, and R_z, were calculated as (DeMeo et al. 2009):

$$R_r = 10^{-0.4[(r-g)_{\rm RN_{35}} - (r-g)_\odot]}, \quad (3.3)$$

$$R_i = 10^{-0.4[(i-g)_{\rm RN_{35}} - (i-g)_\odot]}, \quad (3.4)$$

$$R_z = 10^{-0.4[(z-g)_{\rm RN_{35}} - (z-g)_\odot]}, \quad (3.5)$$

where $(r-g)_{\rm RN_{35}}$, $(i-g)_{\rm RN_{35}}$, and $(z-g)_{\rm RN_{35}}$ are the colors of 2015 RN_{35}, whereas $(r-g)_\odot$, $(i-g)_\odot$, and $(z-g)_\odot$ are the colors of the Sun in the Pan-STARRS system. We referred to the absolute magnitude of the Sun in the Pan-STARRS system as g = 5.03, r = 4.64, i = 4.52, and z = 4.51 (Willmer 2018). We set the uncertainties of the magnitudes of the Sun as 0.02.

The reflectance spectra in Figure 3.8 are normalized at the center of the g band in the Pan-STARRS system, 0.481 μm (Tonry et al. 2012). The horizontal bars in the 2015 RN_{35}'s spectrum indicate the filter bandwidths. The reflectance spectra except 2015 RN_{35} are originally normalized at 0.55 μm. We renormalize those spectra at 0.481 μm as follows:

$$R'(\lambda) = \frac{R(\lambda)}{R(0.481\,\mu m)}, \quad (3.6)$$

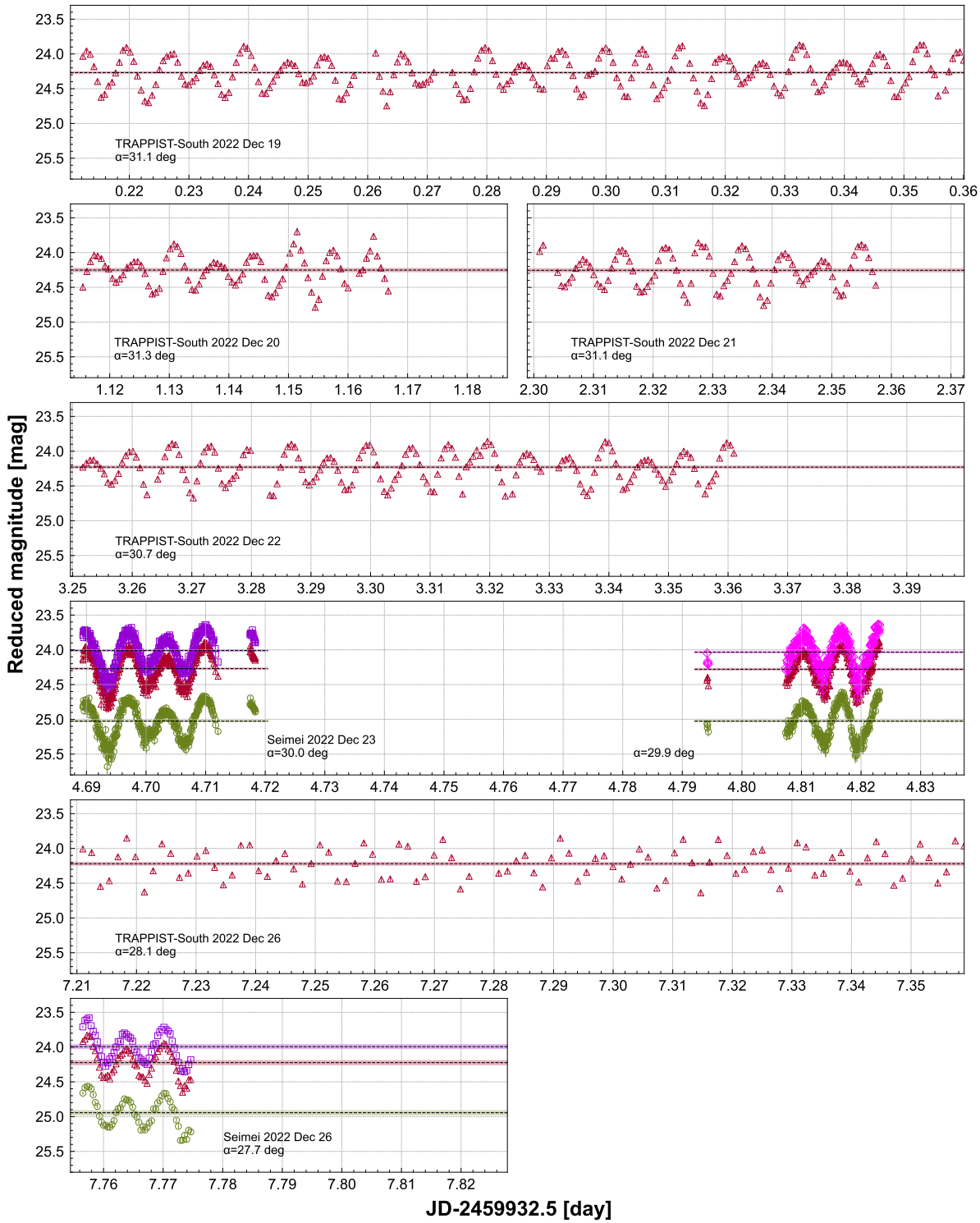

Figure 3.2. Lightcurves of 2015 RN_{35}. The reduced g, r, i, and z band magnitudes are presented as circles, triangles, squares, and diamonds, respectively. Bars indicate the 1σ uncertainties. Error-weighted average of magnitude in each lightcurve is presented with a dashed line. Shaded areas indicate the standard errors of the weighted averaged magnitudes.

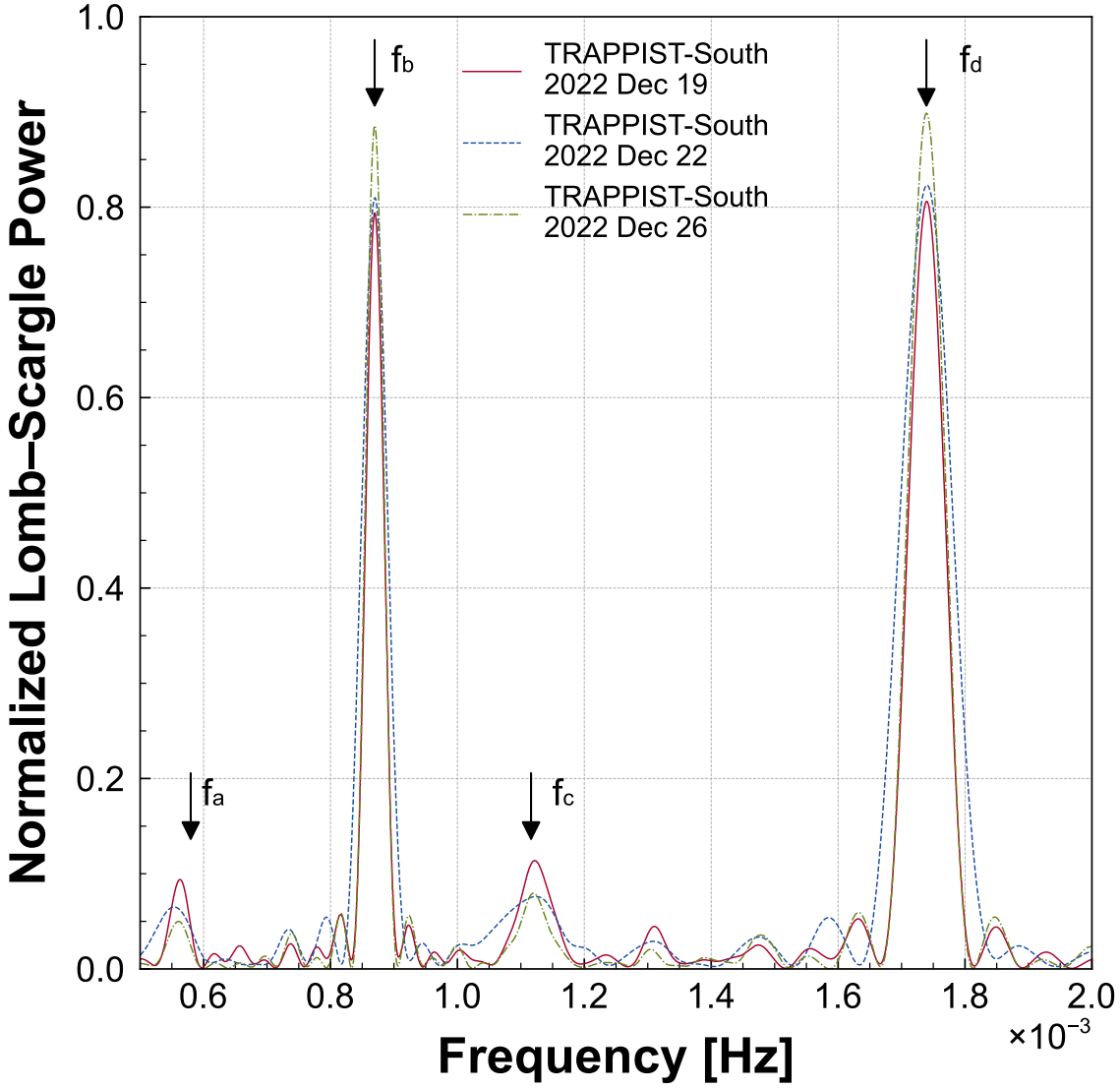

Figure 3.3. Lomb–Scargle periodogram of 2015 RN_{35}. The number of harmonics is two. The three periodograms were created using lightcurves obtained with the TRAPPIST-South telescope on 2022 December 19, 22, and 26. Four peak frequencies in either case are indicated.

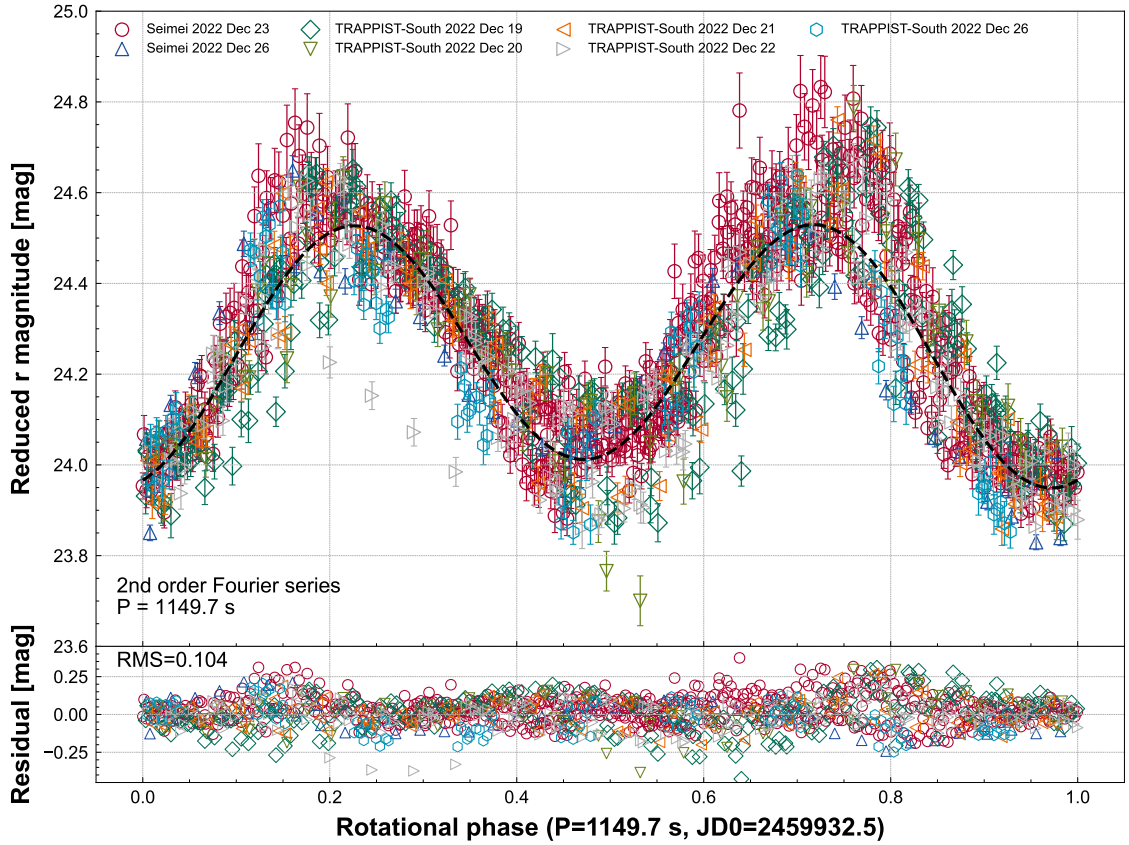

Figure 3.4. Phased lightcurves of 2015 RN_{35}. All lightcurves in reduced r magnitude are folded with a period of 1149.7 s. Phase zero is set to JD 2459932.5. Bars indicate the 1σ uncertainties of measurements. Model curve fitted to lightcurves is shown by dashed line.

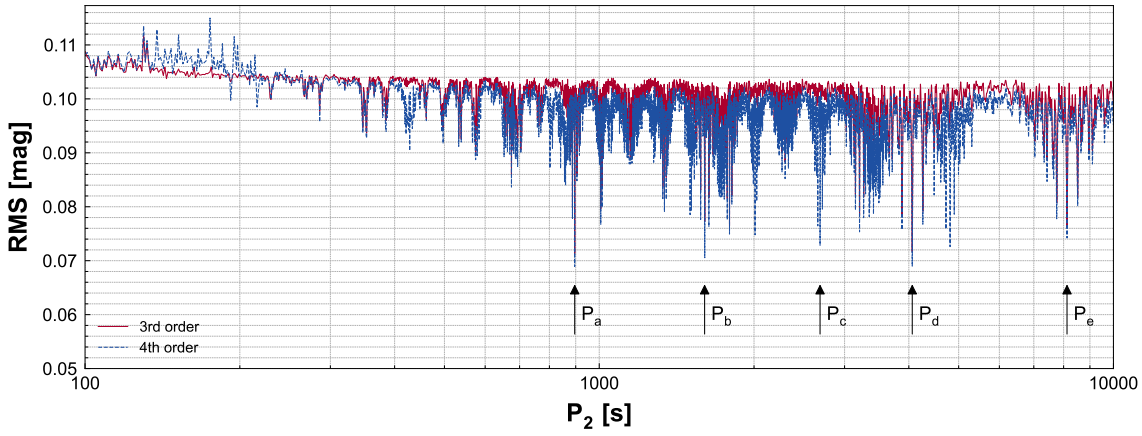

Figure 3.5. RMS residuals between observed and model lightcurves of 2015 RN_{35} fixing P_1 of 1149.7 s. Residuals using two-dimensional Fourier series with m of 3 and m of 4 are shown by solid and dashed lines, respectively. Five periods with smaller RMS in either case are indicated.

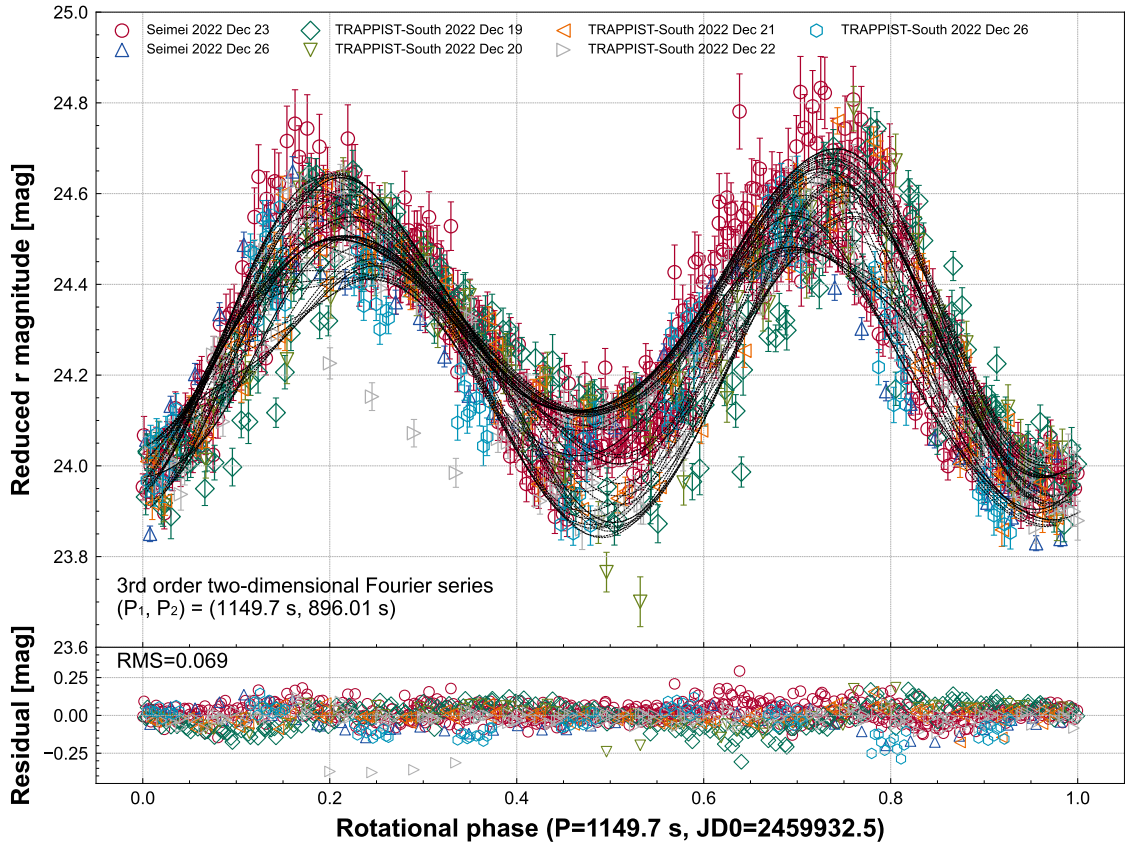

Figure 3.6. Phased lightcurves of 2015 RN_{35} with two-dimensional Fourier series. All lightcurves in reduced r magnitude are folded with P_1 of 1149.7 s and P_2 of 896.01 s. Phase zero is set to JD 2459932.5. Bars indicate the 1σ uncertainties. Model curves fitted to lightcurves are shown by dashed lines.

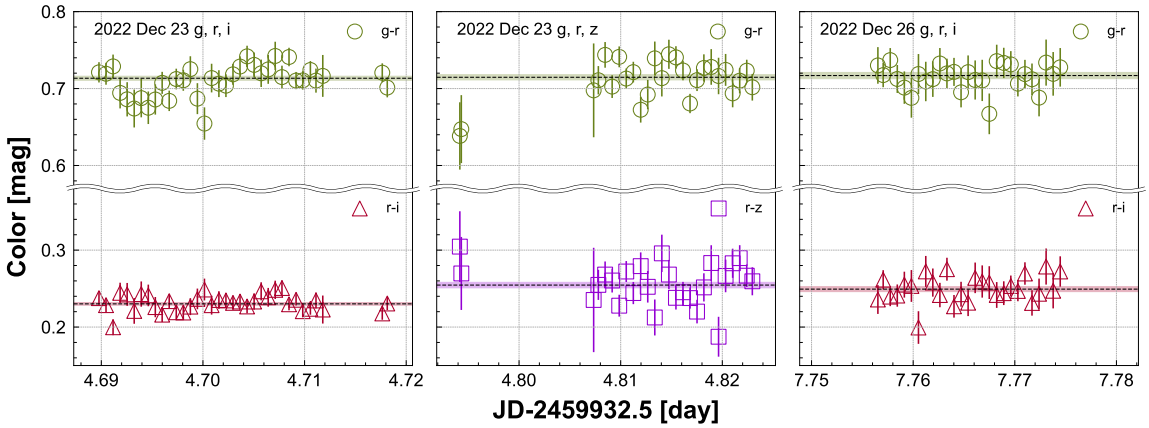

Figure 3.7. Time-series colors of 2015 RN$_{35}$. The $g-r$, $r-i$, and $i-z$ colors are shown by circles, triangles, and squares, respectively. Binning of 60 s is performed for all colors. Bars indicate the 1σ uncertainties. Weighted mean and its error are indicated by dashed lines and shaded areas, respectively.

where $R'(\lambda)$ is a renormalized reflectance at a wavelength of λ, $R(\lambda)$ is an original reflectance at a wavelength of λ, and $R(0.481\,\mu m)$ is an original reflectance at a wavelength of 0.481 μm.

3.3.3. Phase curves

We observed 2015 RN$_{35}$ across a wide range of phase angles from 2° to 30°, which provides us with a well-sampled phase curve as shown in Figure 3.9. We converted the g and r band magnitudes in the Pan-STARRS system to the V band magnitude in the Johnson system using the equations in Tonry et al. (2012). We stacked 20 images obtained in 2023 January to make a decent detection of 2015 RN$_{35}$ for photometry as shown in upper panels of Figure 3.1. The total integration time, 1200 s, is compatible with one of the characteristic periods of 2015 RN$_{35}$, P_1 of 1149.7 s. Thus, the rotation effects have been corrected in the phase curves of 2015 RN$_{35}$.

We derived an absolute magnitude in the V band, H, and slope parameters, G_1 and G_2, with the H-G_1-G_2 model (Muinonen et al. 2010:, see the appendix B). The uncertainty of H, G_1, and G_2 were estimated with the Monte Carlo technique. We made 1000 phase curves by randomly resampling the data assuming each observed data follows a normal distribution whose standard deviation is a standard error of weighted mean magnitude. We derived H of 23.9±0.2, G_1 of -0.10 ± 0.08, and G_2 of 0.8 ± 0.1. The absolute magnitude and slope parameters in the g, r, and i bands are also derived in Figure 3.9 for convenience.

3.4. Discussion

3.4.1. Possible classification of 2015 RN$_{35}$

The visible spectrum of 2015 RN$_{35}$ suggests that 2015 RN$_{35}$ is a VRO in the near-Earth region. We compare the spectrum with the class templates from Mahlke et al. (2022) in Figure 3.8. We also show the spectra of the A-type MBA (246) Asporina and the VRO in the main belt Justitia. These two spectra were obtained with SpeX (Rayner et al. 2003) on the NASA Infrared Telescope Facility (IRTF). We obtained the two spectra via the M4AST online tool (Modeling for Asteroids; Popescu et al. 2012). Justitia is known to have a very red slope like the trans-Neptunian objects (TNOs; Hasegawa et al. 2021), and is classified as Z-type in the latest Mahlke taxonomy (Mahlke et al. 2022). We note that the spectrum of Justitia seems to be out of the range of the Z-type template in the visible wavelength in Figure 3.8. This is

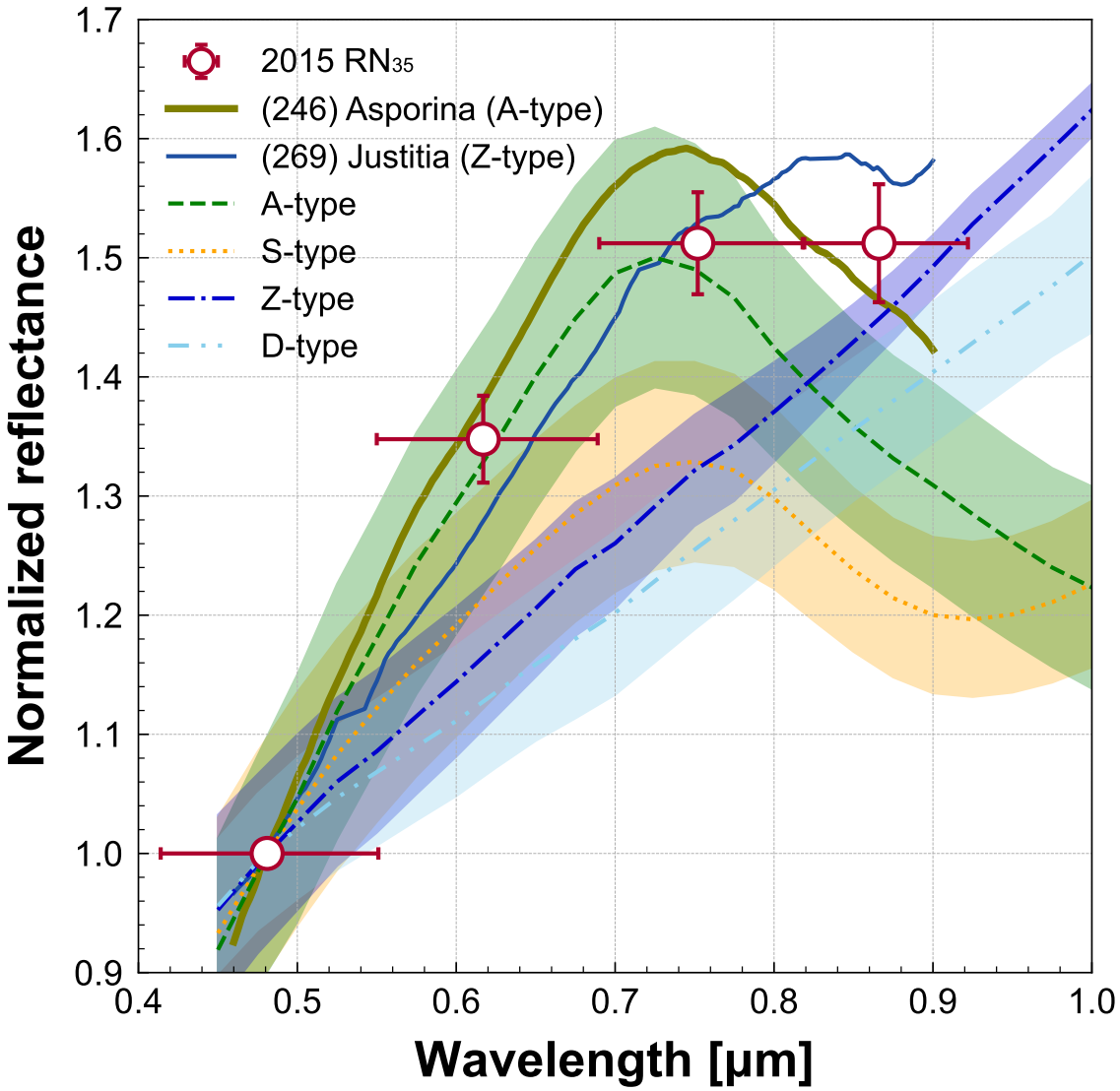

Figure 3.8. Reflectance spectrum of 2015 RN_{35} (circles). Vertical bars indicate the 1σ uncertainties. Horizontal bars indicate the filter bandwidths. Template spectra of A- (dashed line), S- (dotted line), Z- (dot-dashed line), and D-types (dot-dot-dashed line) are shown (Mahlke et al. 2022). Shaded areas indicate the standard deviations of the template spectra. Visible spectra of the A-type asteroid Asporina (thick solid line) and the Z-type asteroid Justitia (thin solid line) are shown. The reflectance spectra are normalized at 0.481 μm.

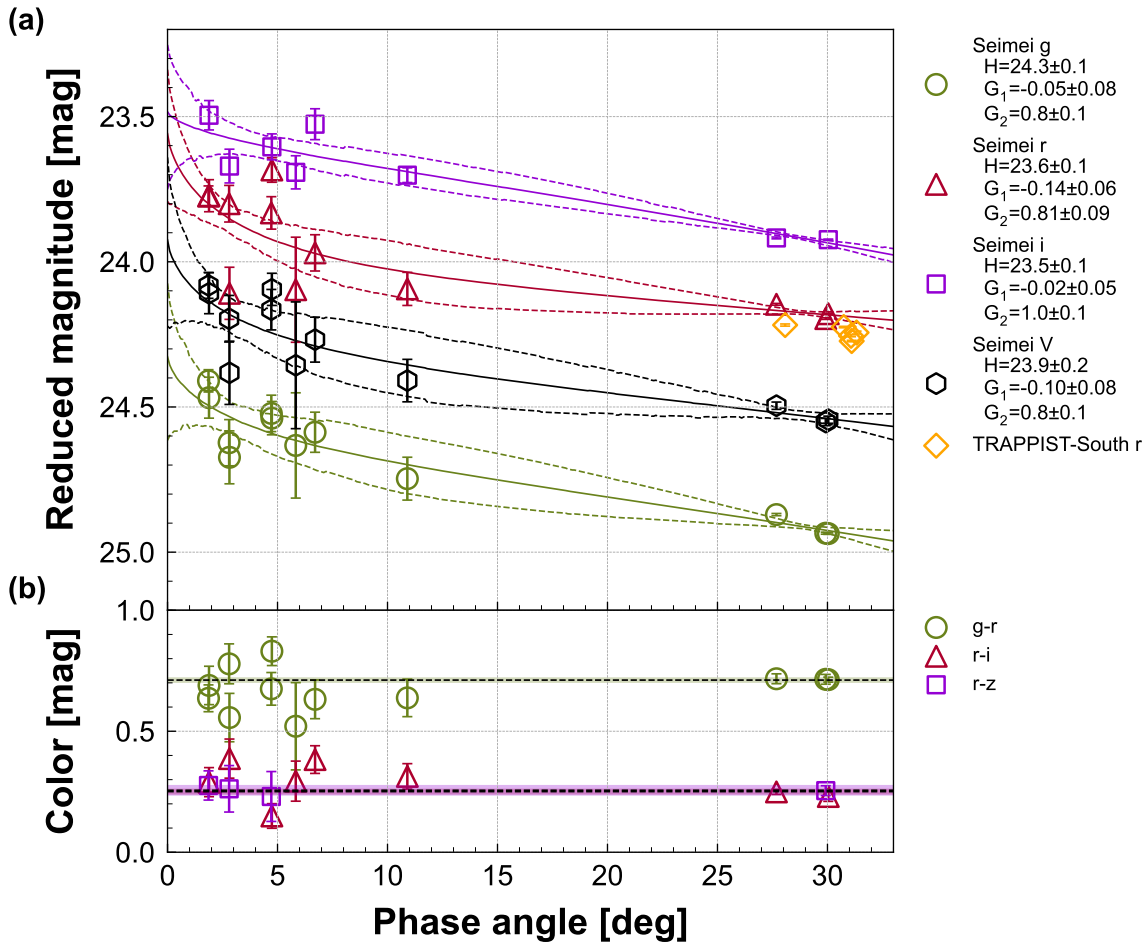

Figure 3.9. Phase-angle dependence of magnitude and colors of 2015 RN_{35}. (a) Mean reduced g, r, i, z, and V band magnitudes (Seimei) are presented as circles, triangles, squares, diamonds, and hexagons, respectively. Mean reduced r-band magnitudes (TRAPPIST-South) are presented as diamonds. Bars indicate the 1σ uncertainties. The medians (50th percentile) of fitting model curves with the H–G_1–G_2 model are presented as solid lines. Uncertainty envelopes representing the 95 % highest density interval values are shown by dashed lines. (b) Weighted mean $g-r$, $r-i$, and $r-z$ colors and their errors on each day are presented as circles, triangles, and squares, respectively. Bars indicate the 1σ uncertainties. Global weighted mean colors and their standard errors are indicated by dashed lines and shaded areas, respectively, although they are small and hard to see due to scale effects.

because Justitia is classified as Z-type in Mahlke et al. (2022) using both visible and near-infrared spectra. Thus, Justitia is a bit redder than the typical Z-types. The Z-types have featureless and extremely redder spectra than the D-types.

We evaluate the goodness-of-fit between the spectrum of 2015 RN_{35} and templates using the following quantity:

$$\delta^2 = \frac{1}{N}\sum_j (R_{\mathrm{obs},j} - R_{\mathrm{model},j})^2, \tag{3.7}$$

where N is the number of reflectance values, $R_{\mathrm{obs},j}$ is a reflectance of 2015 RN_{35} at jth wavelength, and $R_{\mathrm{model},j}$ is a reflectance of a template spectrum at the wavelength. We found that the spectrum of 2015 RN_{35} seems like those of A-types ($\delta^2 = 0.008$) and Z-types ($\delta^2 = 0.018$), whereas the spectrum does not fit well with S-types ($\delta^2 = 0.034$) and D-types ($\delta^2 = 0.033$). We note that only visible colors are often not enough to determine the spectral types of asteroids. For instance, half of all objects classified as A-types based on spectra in the visible wavelength are not A-types in the near-infrared (DeMeo et al. 2019).

We classified 2015 RN_{35} as an A- or Z-type in this study, where both types represent rare populations (Mahlke et al. 2022). The A-type asteroids are olivine-rich and have similar spectra to those of silicate mineral olivine and are thought to be a piece of differentiated planetesimal (DeMeo et al. 2019), while other studies propose that some A-types may originate from the mantle of Mars (Polishook et al. 2017). Thus, the A-types may have an important role in investigating the formation of terrestrial planets. Recently, the two VROs, Pompeja and Justitia, were discovered in Hasegawa et al. (2021). Bourdelle de Micas et al. (2022) discovered the VRO Tjilaki in the main belt. These VROs are classified as Z-types in the latest Mahlke taxonomy (Mahlke et al. 2022). In total, 23 asteroids including one NEA, (141670) 2002 JS_{100}, are classified as Z-type in Mahlke et al. (2022). The Z-types might have primitive organic materials on the surface as D-types (Barucci et al. 2018). Justitia is selected as the rendezvous target of the Emirates Mission to Explore the Asteroid Belt (Alhameli et al. 2023).

It is known that the slope parameters G_1 and G_2 have a tight correlation with the geometric albedo (Muinonen et al. 2010; Shevchenko et al. 2016). We show typical G_1 and G_2 values of A-, E-, S-, C- and D-types in Figure 3.10 (Shevchenko et al. 2016; Mahlke et al. 2021). We also plot the G_1 and G_2 of the A-type MBA Asporina derived using the sparse photometric observations from Gaia Data Release 2 (Martikainen et al. 2021). The smaller G_1 and larger G_2, by definition, mean that the slope of the phase curve is shallower. The slopes of high-albedo asteroids are shallower since the contribution of the shadow-hiding effect decreases as albedo increases (e.g., Belskaya & Shevchenko 2000), whereas those of low-albedo asteroids are steeper on the contrary. Thus, the small G_1 and large G_2 of 2015 RN_{35} are indicative of a high geometric albedo.

The G_1 and G_2 of 2015 RN_{35} seem a bit far from the typical values of A-types in Figure 3.10. But, the typical values are slightly different from each other by about 0.1–0.2 on the G_1–G_2 plane depending on the references. Thus, the discrepancy between the slope parameters of 2015 RN_{35} and typical values does not necessarily indicate that 2015 RN_{35} is an outlier. Therefore we concluded that 2015 RN_{35} is an A-type asteroid in conjunction with the colors and slope parameters in the visible wavelength. We demonstrated that only photometry in the visible wavelength is sufficient to determine the spectral type of asteroids if it is across a wide range of phase angles.

Finally, we discuss other interpretations of the shallow phase slope of 2015 RN_{35}. The environments such as self-gravity and rotation period are different between small and large asteroids. Small asteroids may have different surface properties compared with large asteroids. Terai et al. (2013) observed the tiny L-type NEA Duende (also known as 2012 DA_{14}) across a wide phase angle range from 19° to 42°. They derived the slope parameter in the H-G model, G, as $0.44^{+0.06}_{-0.08}$, which is larger than the typical value of L-types. The tiny asteroid Duende has a shallow slope in the phase curve. They interpreted the large slope parameter or shallow slope with the difference of surface environment due to the lack of the fine regolith or high geometric albedo. Small gravity on tiny asteroids might lead to the lack of the fine regolith on its

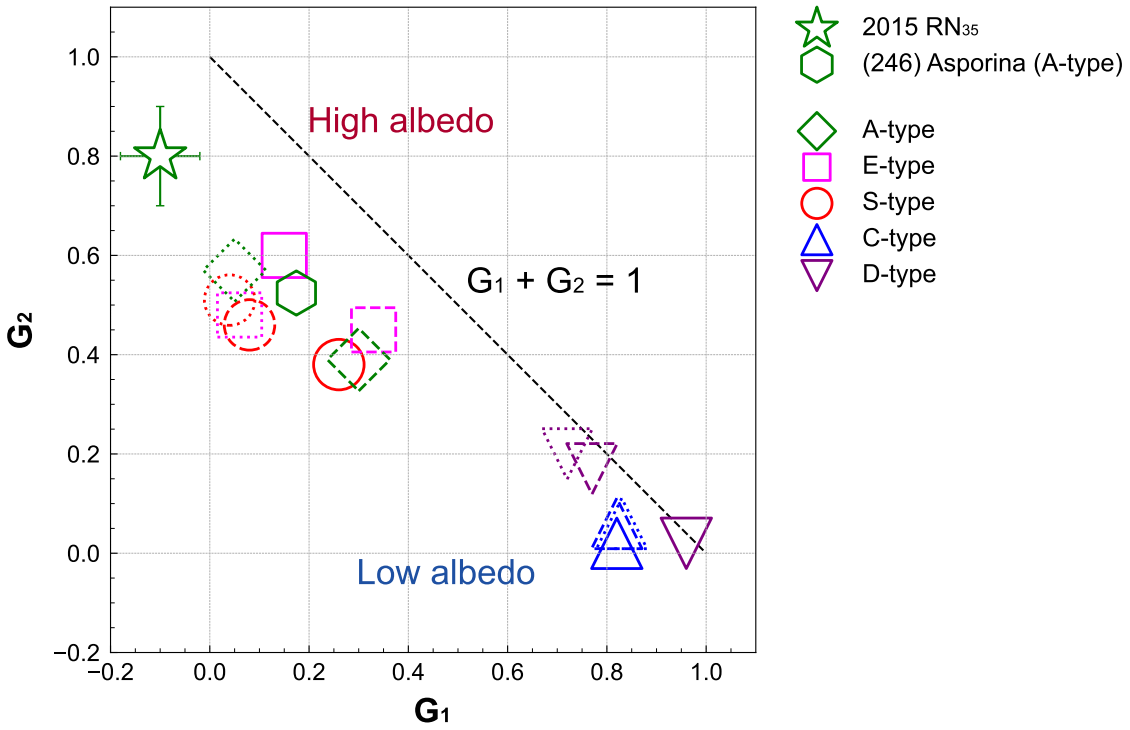

Figure 3.10. G_1 and G_2 of 2015 RN$_{35}$ in the V band (star). Bars indicate the 1σ uncertainties. G_1 and G_2 of the A-type asteroid Asporina is shown by hexagon (Martikainen et al. 2021). Typical G_1 and G_2 values of A-, E-, S-, C-, and D-types are shown by diamonds, squares, circles, triangles, and inverted triangles, respectively. Markers are enclosed by solid lines (Shevchenko et al. 2016), dashed lines (cyan band; Mahlke et al. 2021), and dotted lines (orange band; Mahlke et al. 2021). Isochrone for $G_1 + G_2 = 1$ is plotted by the dashed line for convenience.

surface. The shadow-hiding effect is weak when the fine regolith is deficient and the slope of the phase curve is shallow. As for 2015 RN$_{35}$, in addition to the small gravity, the fast rotation of about 20 minutes also supports the hypothesis of the lack of fine regolith. Other recent studies showed that there is almost no correlation between albedo and slope parameters using the phase curves obtained in the framework of the IMPACTON project and the ATLAS survey (Rondón et al. 2019; Arcoverde et al. 2023). They interpreted that this is due to the difference in diameters between NEAs and MBAs. The trend is not clear since the number of samples is limited due to the observational difficulties. A comprehensive research of phase parameters is desired to reach a conclusion.

Various observations such as near-infrared spectroscopy and polarimetry are crucial in forthcoming approaches of 2015 RN$_{35}$ to put an end to the spectral type. The next two opportunities are in 2031 September and 2056 December, where 2015 RN$_{35}$ will be brightened up to 21 mag and 16 mag in the V band, respectively.

3.4.2. Diameter estimation of tiny asteroids

Estimation of asteroid sizes is important not only to evaluate the risk of impact to the Earth but also to plan exploration missions. However, small NEAs are often observed only at a few apparitions at relatively large phase angles compared to MBAs and TNOs. Thus, the absolute magnitude of the asteroid is often not well constrained. The absolute magnitude could be uncertain by ~ 0.3 depending on whether the opposition

surge exists (see, e.g., Belskaya et al. 2003). Jurić et al. (2002) and Pravec et al. (2012) independently estimated that there is a systematic uncertainty of H of about 0.4. In addition to the uncertainty of H, the geometric albedo is not well estimated for small bodies since observing opportunities are limited to only a short period, as in this study.

We estimated the absolute magnitude of 2015 RN_{35} with high accuracy as 23.9±0.2 through observations across a wide range of phase angles down to 2°. The surface colors as well as the slope of the phase curve indicate that 2015 RN_{35} is a very red asteroid, probably classified as an A-type asteroid. The typical geometric albedo of A-types is estimated as 0.282 ± 0.101 and 0.28 ± 0.09 in Usui et al. (2013) and DeMeo et al. (2019), respectively. We assume the geometric albedo of 2015 RN_{35} as p_V of 0.28 ± 0.10. The diameter of an asteroid can be estimated with H and p_V using Equation 1.12 (Fowler & Chillemi 1992; Pravec & Harris 2007). The diameter of 2015 RN_{35} is estimated to be 41 ± 8 m. We updated the absolute magnitude of 2015 RN_{35} by about 0.7 compared to H of 23.24 in JPL SBDB. Our study demonstrated that it is crucial to observe the asteroid in multibands at multi-epochs including where the phase angles are low to derive H and D accurately. Observations at very low phase angles are not possible for all NEAs. Detailed planning of observations is crucial for the diameter estimation of tiny asteroids.

3.4.3. Mission accessibility

One of the important parameters to plan the spacecraft mission is the delta-v (Δv), which is the required impulse per unit of spacecraft mass to change the status of the spacecraft. We refer to the total Δv [2] as the sum of (i) the maneuver required to depart a notional 400 km altitude circular Earth parking orbit, (ii) the Δv required to match the NEA's velocity at arrival, (iii) the Δv required to depart the NEA, and (iv) the Δv (if any) required to control atmospheric entry speed at Earth return. We queried the Δv of NEAs for the Near-Earth Object Human Space Flight Accessible Targets Study (NHATS; Abell et al. 2012) [3]. The Δv of 2015 RN_{35} is estimated as 11.801 km s^{-1} in the launch window between 2030 and 2035, which is smaller than the limit of NHATS, 12 km s^{-1}. In terms of the engineering aspect, 2015 RN_{35} is a good candidate for a future spacecraft mission. From a scientific point of view, 2015 RN_{35}, either it is an A- or a Z-type NEA, is a great candidate for a future mission. Specifically, there are no planned future spacecraft missions to A-type asteroids.

3.5. Summary of this chapter

We conducted multicolor photometry of the tiny NEA 2015 RN_{35} over twelve nights in 2022 December and 2023 January. We observed 2015 RN_{35} across a wide range of phase angles from 2° to 30° in the g, r, i, and z bands in the Pan-STARRS system. We found that 2015 RN_{35} is in a non-principal axis spin state with two characteristic periods of 1149.7 ± 0.3 s and 896.01 ± 0.01 s. The visible spectrum of 2015 RN_{35} is as red as Justitia, one of the VROs in the main belt, which indicates that 2015 RN_{35} can be classified as an A- or Z-type asteroid. Together with the shallow slope of the phase curve, we suppose 2015 RN_{35} is a high-albedo A-type asteroid.

Various observations such as near-infrared spectroscopy and polarimetry are encouraged during the forthcoming approaches of 2015 RN_{35}. The next opportunity is in September 2031, where 2015 RN_{35} will be brightened up to 21 mag. Though additional follow-up observations are required to reach a conclusion, 2015 RN_{35} is a possible mission accessible A-type NEA with small Δv of 11.801 km s^{-1} in a launch window between 2030 and 2035.

[2] https://cneos.jpl.nasa.gov/nhats/
[3] https://ssd-api.jpl.nasa.gov/doc/nhats.html, last accessed 2023 August 10.

Remembering that you are going to die is the best way I know to avoid the trap of thinking you have something to lose.
— Steve Jobs (1955–2011)

4. Photometry and Polarimetry of Small Near-Earth Asteroid 2010 XC_{15}

In this chapter, we present a series of optical photometric and polarimetric observations of a small NEA 2010 XC_{15} in 2022 December to investigate its surface properties. The rotation period of 2010 XC_{15} is possibly a few to several dozen hours and color indices of 2010 XC_{15} are derived as $g-r = 0.435 \pm 0.008$, $r-i = 0.158 \pm 0.017$, and $r-z = 0.186 \pm 0.009$ in the Pan-STARRS system. The linear polarization degrees of 2010 XC_{15} are a few percent at the phase angle range of 58° to 114°. We found that 2010 XC_{15} is a rare E-type NEA on the basis of its photometric and polarimetric properties. Taking the similarity of not only physical properties but also dynamical integrals and the rarity of E-type NEAs into account, we suppose that 2010 XC_{15} and 1998 WT_{24} are of common origin (i.e., asteroid pair). These two NEAs are the sixth NEA pair and the first E-type NEA pair ever confirmed, possibly formed by rotation fission. We conjecture that the parent body of 2010 XC_{15} and 1998 WT_{24} was transported from the main belt through the ν_6 resonance or Hungaria region.

The contents of this chapter have been published in Beniyama et al. (2023b).

4.1. Introduction

Gravitationally bound multiple systems in the asteroids have an important role in studying the solar system; they provide us with rare opportunities to understand the physical properties, such as density and mass of the asteroids (e.g., Merline et al. 2002; Margot et al. 2015; Walsh & Jacobson 2015:for reviews). The usefulness of the binary system has been demonstrated by the planetary defense mission DART (Rivkin et al. 2021). The spacecraft changed the orbital period of Dimorphos (secondary) around Didymos (primary) by approximately 33 minutes (Thomas et al. 2023), which indicates a large momentum transfer efficiency. Additional characterizations will be performed by Hera, a European Space Agency rendezvous mission (Michel et al. 2022). The DART mission provided never-before-heard-of science cases by comparing the observational results pre- and post-DART impact (e.g., Bagnulo et al. 2023; Gray et al. 2023).

The first satellite of asteroids was discovered around the MBA (243) Ida by the Galileo spacecraft (Chapman et al. 1995; Belton et al. 1995). Later, lots of binaries were identified by lightcurve observations (e.g., Pravec & Harris 2007) and direct imaging (e.g., Rojo & Margot 2011; Brož et al. 2022). A number of binary systems have been reported in the near-Earth region as well. Binary asteroids are not a rare population in NEAs (Pravec et al. 2006; Scheirich & Pravec 2009). The lightcurve observations are, in principle, biased towards the detection of close binaries while radar observations are biased towards the detection of binaries with large separations (Margot et al. 2002; Ostro et al. 2006). Homogeneous spectra of binaries have been reported by the simultaneous spectroscopic and photometric observations (Polishook et al. 2009). Besides binary systems, Marchis et al. (2005) reported the MBA (87) Sylvia as the first triple system observed using the AO system on the VLT. Recently, Berdeu et al. (2022) discovered the third satellite around the MBA (130) Elektra using the Spectro-Polarimetric High-contrast Exoplanet REsearch (SPHERE) adaptive optics system and coronagraphic facility and an integral field spectrograph (IFS) on the VLT, making Elektra the first quadruple asteroid.

Gravitationally unbound two asteroid components with a common origin in the asteroids are called

pairs. Asteroid pairs were first reported by Vokrouhlický & Nesvorný (2008). The formation time of the pairs (i.e., ages) was estimated with differences in mean anomaly ΔM and semimajor axis separation Δa of cluster members (Vokrouhlický & Nesvorný 2008). As with the binaries, lots of lightcurve (Pravec et al. 2019) and spectroscopic observations (Duddy et al. 2013; Polishook et al. 2014a,b) have been carried out. Most asteroid pairs have similar spectra (Polishook et al. 2014a,b) while the pair (17198) Gorjup and (229056) 2004 FC_{126} have slightly different spectra (Duddy et al. 2013). Asteroid pairs are mainly studied for MBAs since in the near-Earth region, only five asteroid pairs have currently been reported.

The first NEA pair[1], (3200) Phaethon and (155140) 2005 UD, was discovered by Ohtsuka et al. (2006). They performed backward and forward orbital integrations of both NEAs and found that their same orbital evolutionary phase has been shifted by 4600 years, which indicates they are of common origin. The similarity of the visible spectra of Phaethon and 2005 UD classified as B-types supports the hypothesis of common origin. Their similar polarimetric properties also support this hypothesis (Devogèle et al. 2020; Ishiguro et al. 2022); however, their near-infrared spectra are different (Kareta et al. 2021).

Ohtsuka et al. (2008) reported that another NEA (225416) 1999 YC is dynamically related to Phaethon and 2005 UD. The visible color measurements of 1999 YC indicate that the NEA is classified as a C-type taxonomy, not a B-type one (Kasuga & Jewitt 2008). Ohtsuka et al. (2007) found the second NEA pair, (1566) Icarus–2007 MK_6, using the same method as Ohtsuka et al. (2006). As written in Ohtsuka et al. (2007), the determination of additional physical parameters of both Icarus and 2007 MK_6 is crucial to further investigate their common origin. After more than ten years, de la Fuente Marcos & de la Fuente Marcos (2019) reported the discovery of a third NEA pair 2017 SN_{16}–2018 RY_7. The orbits of the pair asteroids are stable owing to the 3:5 mean motion resonance (MMR) with Venus, avoiding close encounters with it. Moskovitz et al. (2019) found that 2017 SN_{16} and 2018 RY_7 have similar visible spectra, which supports that they are of common origin. Moskovitz et al. (2019) also found that the visible spectra of the two NEAs 2015 EE_7 and 2015 FP_{124} resemble each other and concluded that they are a pair candidate. Recently, Fatka et al. (2022) discovered a very young NEA pair 2019 PR_2–2019 QR_6. The visible spectra of 2019 RP_2 and 2019 QR_6 are similar to primitive D-types, which is a rare type in the near-Earth region. The D-types have similar colors with cometary nuclei (e.g., Capaccioni et al. 2015). Their backward orbital integrations did not show the close encounters of the two NEAs (i.e., break up event) without cometary-like nongravitational force. They concluded that the separation time is approximately 300 years ago with the cometary-like nongravitational model, which implies that 2019 PR_2–2019 QR_6 is the youngest pair known to date.

The leading formation mechanism of the multiple asteroid systems such as binaries and pairs is the rotation fission (Walsh et al. 2008; Jacobson & Scheeres 2011; Jacobson et al. 2014, 2016). [2] Walsh et al. (2008) found that satellites are formed by mass shedding events after a spin-up by the YORP effect, which arises from the asymmetry of scattered sunlight and thermal radiation from its surface (Rubincam 2000). The rotation fission is consistent with the observational fact that many primaries of binary and pair systems are fast-rotating asteroids (Pravec et al. 2010, 2019). As for the NEA pairs, the fast rotation of the primary Icarus approximately 2.3 hr leverages the rotation fission hypothesis. In general, however, the dynamical environments of MBAs and NEAs are different; MBAs are relatively stable in terms of dynamics, whereas NEAs are chaotic in nature due to frequent close encounters with the planets. Confirmed NEA pairs are relatively free from close approaches with the inner planets owing to such as large eccentricity, large inclination, and MMR. Thus, the formation mechanisms of NEA pairs are still unclear, and other formation mechanisms such as tidal interaction with the planets are under consideration (Richardson et al. 1998; Walsh & Richardson 2006; Scheeres et al. 2000). Additional observations of multiple systems are essential to reach a consensus regarding the origins of binary and pair systems.

The target NEA of this chapter, 2010 XC_{15}, was discovered by the CSS (Drake et al. 2009) with a

[1] We use the term NEA pair regardless of whether the age of the pair is estimated or not.

[2] We use the term rotation fission in this chapter instead of rotational breakup or rotational disruption.

0.7 m Schmidt telescope on Mt. Bigelow on 2010 December 5. Assuming an absolute magnitude H of 21.70 and a geometric albedo p_V of $0.350^{+0.176}_{-0.151}$, derived from thermal observations using the IRAC on the SST in 2017 as part of the NEO Legacy project [3], the diameter of 2010 XC_{15} was derived to be approximately 100 m. The orbital elements of 2010 XC_{15} resemble those of (33342) 1998 WT_{24}, which is a well-characterized E-type NEA (Kiselev et al. 2002; Harris et al. 2007; Busch et al. 2008). 1998 WT_{24} has an effective diameter of 415 ± 40 m (Busch et al. 2008). E-types are thought to have mineralogical links to the enstatite achondrite meteorites (Aubrites) composed of almost iron-free enstatite (Zellner 1975; Zellner et al. 1977). The orbital similarity criterion, D_{SH} (Southworth & Hawkins 1963) between two orbits, is as small as 0.04 presently, which is comparable to the well-established Phaethon–Geminid meteor stream relation. This value is smaller than the empirical cutoff for significance, ∼0.20 (Drummond 1991), and indicates the orbital similarity of 2010 XC_{15} and 1998 WT_{24}. The apparent magnitude of 2010 XC_{15} in the V band was brightened up to 13 mag in 2022 December, which allowed us to constrain the surface properties of a small asteroid. We conducted a one-week observation campaign of 2010 XC_{15} with multiple telescopes in 2022 December. In Section 4.2, we describe our methods: photometry, polarimetry, and orbital integrations. The results are presented in Section 4.3. The surface properties of 2010 XC_{15} are investigated in Section 4.4. The possible dynamical history and origin of 2010 XC_{15} and 1998 WT_{24} are also discussed.

4.2. Methods

4.2.1. Photometric observations

We performed multicolor photometry of 2010 XC_{15} using TriCCS on the Seimei 3.8 m telescope (Kurita et al. 2020) at the Kyoto University Okayama Observatory (133.5967°E, 34.5769°N, and 355 m in altitude). The details of the photometry are presented in Table 4.1. The single exposure time was set to 5.0 s, and the telescope was operated in the non-sidereal tracking mode. The data simultaneously obtained with g, r, and i or z band in the Pan-STARRS system (Chambers et al. 2016) were analyzed following the same procedure described in Appendix F (Beniyama et al. 2023c).

After bias subtraction, dark subtraction, and flat-fielding, the astrometry of all the reduced images was performed using `astrometry.net` software (Lang et al. 2010). Cosmic ray related signals were removed using the `Python` package `Astro-SCRAPPY` (McCully et al. 2018) based on Pieter van Dokkum's `L.A.Cosmic` algorithm (van Dokkum 2001). The circular aperture photometry was performed on 2010 XC_{15} and reference stars in each frame with the SExtractor-based `Python` package `SEP` (Bertin & Arnouts 1996; Barbary et al. 2015). The aperture radii were set to twice the size of the FWHMs of the PSFs of reference stars. The light-travel time of the target asteroid was corrected to obtain the time-series colors and magnitudes (Harris & Lupishko 1989).

Reference stars meeting any of the criteria below were not used in the determination of colors and magnitudes: uncertainties in g, r, i, or z band magnitudes in Pan-STARRS Data Release 2 (DR2, Flewelling et al. 2020) are larger than 0.05, $(g-r)_{PS} > 1.1$, $(g-r)_{PS} < 0.0$, $(r-i)_{PS} > 0.8$, or $(r-i)_{PS} < 0.0$, where $(g-r)_{PS}$ and $(r-i)_{PS}$ are colors in Pan-STARRS system. We discarded the sources close to the edges of the image frame (100 pixels from the edge) or with any other sources within the aperture. Objects categorized as extended sources, possible quasars, and variable stars were removed with the `objinfoflag` and `objfilterflag` in Pan-STARRS DR2. After deriving the colors and magnitudes of 2010 XC_{15} in the Pan-STARRS system for each frame, we used a binning of 60 s for all magnitudes and colors.

[3] http://nearearthobjects.nau.edu/spitzerneos.html

Table 4.1. Summary of photometric observations

Obs. Date (UT)	Filters	$T_{\rm exp}$ (s)	$N_{\rm exp}$	V (mag)	α (deg)	Δ (au)	$r_{\rm h}$ (au)	Air Mass	Weather
2022 Dec 22 16:25:41–18:11:52	g, r, i	5	478	15.9	58.5	0.030	0.999	1.24–1.52	Cirrus
2022 Dec 23 16:14:26–21:11:10	g, r, i	5	1699	15.5	59.2	0.024	0.996	1.20–1.57	Clear
2022 Dec 23 18:35:51–19:00:50	g, r, z	5	172	15.5	59.2	0.024	0.996	1.20–1.21	Clear
2022 Dec 24 15:45:24–21:08:32	g, r, i	5	1230	14.9	60.9	0.018	0.992	1.17–1.80	Clear
2022 Dec 25 18:18:53–21:04:21	g, r, z	5	821	14.2	65.0	0.012	0.989	1.13–1.22	Clear

Note. — Observation time in UT in mid-time of exposure (Obs. Date), filters (Filters), exposure time ($T_{\rm exp}$), the number of exposures ($N_{\rm exp}$), and weather condition (Weather) are listed. Predicted V-band apparent magnitude (V), phase angle (α), distance between 2010 XC_{15} and observer (Δ), and distance between 2010 XC_{15} and the Sun ($r_{\rm h}$) at the observation starting time are from NASA JPL HORIZONS as of 2023 May 11 (UTC). Elevations to calculate air mass range (Air Mass) are also from NASA JPL HORIZONS.

4.2.2. Polarimetric observations

We conducted polarimetric observations at three sites in Japan; Nayoro Observatory (142.4830°E, 44.3736°N, and 151 m in altitude, the Minor Planet Center code Q33, hereinafter referred to as NO), Nishi-Harima Astronomical Observatory (134.3356°E, 35.0253°N, and 449 m in altitude, hereinafter referred to as NHAO), and Higashi-Hiroshima Observatory (132.7767°E, 34.3775°N, and 511.2 m in altitude, hereinafter referred to as HHO). The observing specifications of polarimetry are summarized in Table 4.2. We used the Multi-Spectral Imager (MSI, Watanabe et al. 2012) mounted on 1.6 m Pirka Telescope at NO, the Wide Field Grism Spectrograph 2 (WFGS2, Uehara et al. 2004; Kawakami et al. 2021) mounted on 2.0 m Nayuta Telescope at NHAO, and the Hiroshima Optical and Near-InfraRed Camera (HONIR, Akitaya et al. 2014) mounted on 1.5 m Kanata telescope at HHO. Wollaston prisms and rotatable half-wave plates are installed in all three instruments; thus, data obtained at the three sites were analyzed in the same standard reduction procedure (e.g., Kawabata et al. 1999; Ishiguro et al. 2017). We used the SExtractor-based `Python` package `SEP` for the circular aperture photometry. We derived linear polarization degrees relative to the perpendicular to the scattering plane, $P_{\rm r}$, and position angles of polarization, $\theta_{\rm r}$. Additionally, we observed a polarimetric standard star HD 19820 (Schmidt et al. 1992) to verify the consistency of our measurements (Appendix H). We considered the deviations between the polarimetric parameters in the literature and those derived here as systematic uncertainties in the measurements of the polarimetric parameters of 2010 XC_{15}.

4.2.3. Orbital integrations

Orbits of 2010 XC_{15} and a well-characterized E-type NEA 1998 WT_{24} resemble each other with a small $D_{\rm SH}$ of 0.04. The geometric albedos of these two NEAs derived in previous studies are in agreement (Kiselev et al. 2002). This suggests that the two NEAs could be of common origin and it makes sense to investigate the orbital history of these two NEAs.

To investigate the dynamical link and origins of 2010 XC_{15} and 1998 WT_{24}, we performed backward orbital integrations using `Mercury 6`, a general-purpose software package for problems in solar system dynamics (Chambers & Migliorini 1997). We computed close encounters accurately with the general Bulirsch-Stoer algorithm available in `Mercury 6`. We also performed orbital integrations with the hybrid of symplectic and Bulirsch-Stoer integrator in `Mercury 6` and confirmed the results of our integrations do not significantly change.

Table 4.2. Summary of polarimetric observations

Obs. Date (UT)	Inst.	Filter	$T_{\rm exp}$ (s)	$N_{\rm exp}$	V (mag)	α (°)	ϕ (°)	$P_{\rm r}$ (%)	$\theta_{\rm r}$ (°)	Air Mass
2022 Dec 20 15:30:37–16:29:49	WFGS2	$R_{\rm C}$	300	8	16.7	58.2	298.2	1.61 ± 0.44	-7.43 ± 7.85	1.51–1.91
2022 Dec 21 15:46:40–16:37:10	MSI	$R_{\rm C}$	180	12	16.3	58.2	297.9	1.69 ± 0.56	-2.00 ± 8.51	1.57–1.79
2022 Dec 24 20:36:51–20:55:13	HONIR	$R_{\rm C}$	115	8	14.9	61.0	294.9	1.36 ± 0.20	1.09 ± 4.09	1.25–1.29
2022 Dec 25 16:57:21–21:12:51	HONIR	$R_{\rm C}$	115	16	14.2	64.9	292.7	1.27 ± 0.17	4.26 ± 3.56	1.13–1.42
2022 Dec 26 17:40:04–18:49:09	HONIR	$R_{\rm C}$	115	16	13.5	75.8	291.0	1.74 ± 0.08	1.44 ± 1.85	1.17–1.38
2022 Dec 27 19:36:23–20:57:28	WFGS2	$R_{\rm C}$	60	32	14.4	113.1	316.7	1.85 ± 0.25	-7.41 ± 2.57	1.36–1.78
2022 Dec 27 20:20:18–21:30:02	HONIR	$R_{\rm C}$	115	8	14.4	114.2	318.1	1.82 ± 0.15	-0.43 ± 2.45	1.28–1.56

Note. — Observation time in UT in mid-time of exposure (Obs. Date), instrument (Inst.), filter (Filter), exposure time ($T_{\rm exp}$), and the number of exposures ($N_{\rm exp}$) are listed. Predicted V-band apparent magnitude (V), phase angle (α), and the position angle of the scattering plane (ϕ) are from NASA JPL HORIZONS as of 2023 May 11 (UTC). Elevations to calculate air mass range (Air Mass) are also from NASA JPL HORIZONS.

The nominal orbital elements of asteroids, their uncertainties, and the covariance data were referred to NASA JPL SBDB. The coordinates and velocities of the Sun and eight planets were obtained from NASA JPL HORIZONS. The nongravitational transverse acceleration parameters, A_2 (Farnocchia et al. 2013), are given for both 2010 XC_{15} and 1998 WT_{24} in NASA JPL SBDB. The semimajor axes of these two asteroids have shrunk, possibly due to the Yarkovsky effect (e.g., Vokrouhlický 1998; Vokrouhlický et al. 2000; Bottke et al. 2006). Thus, we also considered the nongravitational transverse acceleration by setting A_2 parameters in the integrations. We investigated the time evolutions of the asteroids under the gravity of the Sun and eight planets in the solar system. The first time step was set to 0.1 days in all integrations. The coordinates and velocities of asteroids were output every 300 days. We converted coordinates and velocities to orbital elements using `element6`, a program in `Mercury 6`.

Orbital evolution of NEAs often turns chaotic after a short period ($\sim$ 100 yr) of integration due to frequent close encounters with planets (Yoshikawa et al. 2000). We generated clones utilizing the classical Monte Carlo using the Covariance Matrix (MCCM, Avdyushev & Banshchikova 2007; de la Fuente Marcos & de la Fuente Marcos 2015) approach to check this chaotic behavior. Each clone had initial orbital elements slightly different from the nominal ones. In total, we generated 1000 clones considering the uncertainties of eccentricity (e) , perihelion distance (q), time of perihelion passage (τ), longitude of ascending node (Ω), argument of perihelion (ω), and inclination (i). The 1000 clones were generated with random numbers made with the `np.random.randn` function in the `Python` package `NumPy` (Oliphant 2015; Harris et al. 2020). We set the seed of the random number as 0. The semimajor axis (a) was calculated as $a = q/(1 - e)$ after the orbital integrations. The epochs of orbital elements of 2010 XC_{15} and 1998 WT_{24} were 2018 January 1 UT, JD 2458119.5, and 2016 April 16 UT, JD 2457494.5, respectively.

To discuss whether or not the asteroids are of common origin, we used the following three integrals of motion of the asteroids in the circular restricted three-body problem (Lidov 1962) in the von Zeipel-Lidov-Kozai (vZLK) oscillation (Lidov 1962; Kozai 1962; Ito & Ohtsuka 2019):

$$C_0 = \frac{1}{a} \equiv \text{const}, \tag{4.1}$$

$$C_1 = (1 - e^2)\cos^2 i \equiv \text{const}, \tag{4.2}$$

$$C_2 = e^2(0.4 - \sin^2 i \sin^2 \omega) \equiv \text{const}. \tag{4.3}$$

When an asteroid breaks up into multiple bodies by catastrophic impacts or rotation fission, the fragments have slightly different orbital elements at that time. In the orbital evolutions of NEAs, their orbital parameters could be drastically changed due to close encounters with planets. On the other hand, the

integrals of C_0, C_1, and C_2 are kept constant for a longer time. Thus, these integrals should be good indicators to determine whether the asteroids are an NEA pair (Ohtsuka et al. 2006, 2007).

4.3. Results

4.3.1. Lightcurves and rotation period

For periodic analysis, we calculated reduced magnitudes from observed magnitudes as:

$$m_{\mathrm{red},n}(\alpha) = m_{\mathrm{obs},n}(\alpha) - 5\log_{10}(\Delta r_{\mathrm{h}}), \tag{4.4}$$

where n is the index of the band, $m_{\mathrm{red},n}(\alpha)$ is a reduced magnitude in the n band, $m_{\mathrm{obs},n}(\alpha)$ is an observed magnitude in the n band, Δ is a distance between 2010 XC_{15} and the Earth, and r_{h} is a distance between 2010 XC_{15} and the Sun. We performed the phase angle correction since the phase angle of 2010 XC_{15} changed significantly during our observations, $\sim 6.5^{\circ}$ (Table 4.1). In general, an empirical relation, such as the H-G model (Bowell et al. 1989), which is originally applied for photometric data taken at phase angles smaller than $\sim 30^{\circ}$, is used for the phase correction. The phase angles of 2010 XC_{15} in our observations are as large as 60°, where the brightness dependence on the solar phase angle, phase curve, is still poorly understood. We assumed the phase curve in linear form as follows:

$$m_{\mathrm{red},n}(\alpha) = H_n + b\alpha, \tag{4.5}$$

where H_n is an absolute magnitude in n band, and b is a linear slope of the phase curve. We converted the reduced magnitudes to absolute magnitudes using Equation 4.5. Carefully checking the corrected lightcurves while setting $b = 0.010, 0.015, 0.020, 0.025, 0.030$, and 0.035 mag/deg, we finally adopted $b = 0.030$ mag deg^{-1} for the corrected lightcurves, as shown in Figure 4.1. The clear variations with amplitudes of approximately 0.1 mag are seen in the corrected lightcurves.

A rotation period of 2010 XC_{15} has been reported in the Asteroid Lightcurve Database (LCDB, Warner et al. 2009). The period derived as 2.673 ± 0.001 hr with two days of optical photometry in 2022 December by Petr Pravec [4] is a possible solution with a quality code U in the LCDB of 2-. Another period has been derived from the radar observations using the Goldstone Radar at DSS-14 [5]. Assuming that the effective diameter of 2010 XC_{15} is approximately 150 m, they concluded that the Doppler broadening approximately 1.3 Hz at a wavelength of 3.5 cm corresponds to a rotation period of approximately 11.5 hr. The rotation period is constrained using the relation given by $B = (4\pi D)/(\lambda P_{\mathrm{rot}})\sin\beta$, where B is a measured bandwidth, D is a diameter, λ is a transmitted wavelength, P_{rot} is a rotation period, and β is the angle between the line of sight and a spin vector of the object (Ostro et al. 1988). The 11.5 hr can be derived assuming $\sin\beta$ of 1. Thus, the 11.5 hr is an upper limit of the rotation period since the pole orientation of 2010 XC_{15} is unknown.

We performed a periodic analysis with g band lightcurves using the Lomb-Scargle method limiting the period range to between 0.16 and 11.5 hr, as shown in Figure 4.2. We found no significant peak in the Lomb-Scargle periodogram. Figure 4.3 shows the phased lightcurves folded by a rotation period of 2.673 hr reported in the LCDB. We checked other phased lightcurves but it is difficult to conclude which peak to prefer over the others as our lightcurve coverage is insufficient and a lightcurve amplitude of 2010 XC_{15} is small at approximately 0.1 mag. The small lightcurve amplitude implies that 2010 XC_{15} has a nearly spherical shape or its rotation axis is parallel to the line of sight. Lightcurves with small amplitudes sometimes show more than two maxima in a single rotation (Harris et al. 2014). For example, (5404) Uemura shows six maxima (Harris et al. 2014), and Bennu shows three maxima (Hergenrother et al. 2013) in a single rotation. Additional observations are necessary for more constraint on the rotation state of 2010 XC_{15}. Furthermore, we cannot rule out the possibility that 2010 XC_{15} is a non-principal axis rotator (i.e., tumbler, Paolicchi et al. 2002; Pravec et al. 2005).

[4] https://www.asu.cas.cz/~ppravec/newres.txt
[5] https://echo.jpl.nasa.gov/asteroids/2010XC15/2010XC15.2022.goldstone.planning.html

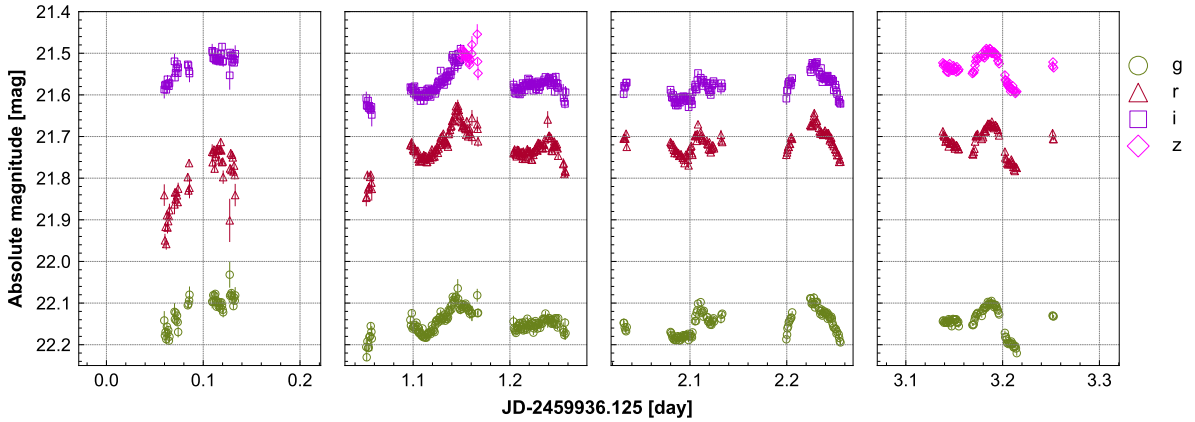

Figure 4.1. Phase corrected lightcurves of 2010 XC_{15}. Phase corrected lightcurves in the g (circles), r (triangles), i (squares), and z bands (diamonds) are presented. Time zero is set to JD 2459936.125 (2022 December 22 15:00:00 UT). Bars indicate the 1σ uncertainties.

4.3.2. Colors and reflectance spectrum

We presented the colors of 2010 XC_{15} in Figure 4.4. We estimated the systematic uncertainties of $g-r$, $r-i$, and $r-z$ colors in our observations, δ_{g-r}, δ_{r-i}, and δ_{r-z}, on the basis of the photometric measurements of reference stars (Beniyama et al. 2023c): $\delta_{g-r} = 0.03$ and $\delta_{r-i} = 0.03$ in the observations with g, r, and i band filters on December 23, $\delta_{g-r} = 0.02$ and $\delta_{r-z} = 0.02$ in the observations with g, r, and z band filters on December 23, $\delta_{g-r} = 0.02$ and $\delta_{r-i} = 0.02$ in the observations with g, r, and i band filters on December 24, whereas $\delta_{g-r} = 0.01$ and $\delta_{r-z} = 0.01$ for the observations with g, r, and z band filters on December 25. The weighted average colors of 2010 XC_{15}, except for the first night when the condition of the sky was not ideal, were derived as $g - r = 0.435 \pm 0.008$, $r - i = 0.158 \pm 0.017$, and $r - z = 0.186 \pm 0.009$. The colors correspond to $V - R = 0.41 \pm 0.02$ and $R - I = 0.39 \pm 0.03$ in the Johnson system (Tonry et al. 2012). We could not find notable rotational spectral variations when assuming the rotation periods to be 2.673 hr.

The reflectance spectrum of 2010 XC_{15} in Figure 4.5 was calculated with the derived colors and the solar colors as Chapter 3. The reflectance spectra in Figure 4.5 are normalized at the band center of r band in the Pan-STARRS system, 0.617 μm (Tonry et al. 2012). Horizontal bars in 2010 XC_{15}'s spectrum indicate filter bandwidths (Tonry et al. 2012). The reflectance spectra other than 2010 XC_{15} are originally normalized at 0.55 μm. We renormalize the spectra at 0.617 μm as follows:

$$R(\lambda)' = \frac{R(\lambda)}{R(0.617\,\mu m)}, \tag{4.6}$$

where $R(\lambda)'$ is a renormalized reflectance at wavelength of λ, $R(\lambda)$ is an original reflectance at wavelength of λ, and $R(0.617\,\mu m)$ is an original reflectance at wavelength of 0.617 μm. We normalized spectra after smoothing every 0.03 μm.

4.3.3. Linear polarization degrees

The derived linear polarization degrees and position angles of 2010 XC_{15} are listed in Table 4.2. Figure 4.6 shows the observed phase angle dependence of the linear polarization degrees of 2010 XC_{15}. The derived polarization degrees are a few percent at the phase angle range of 58° to 114°. The small linear polarization degrees combined with the spectrum imply that 2010 XC_{15} is an E-type asteroid with a high geometric albedo. This is consistent with the p_V of $0.350^{+0.176}_{-0.151}$ derived from thermal observations using the IRAC on SST.

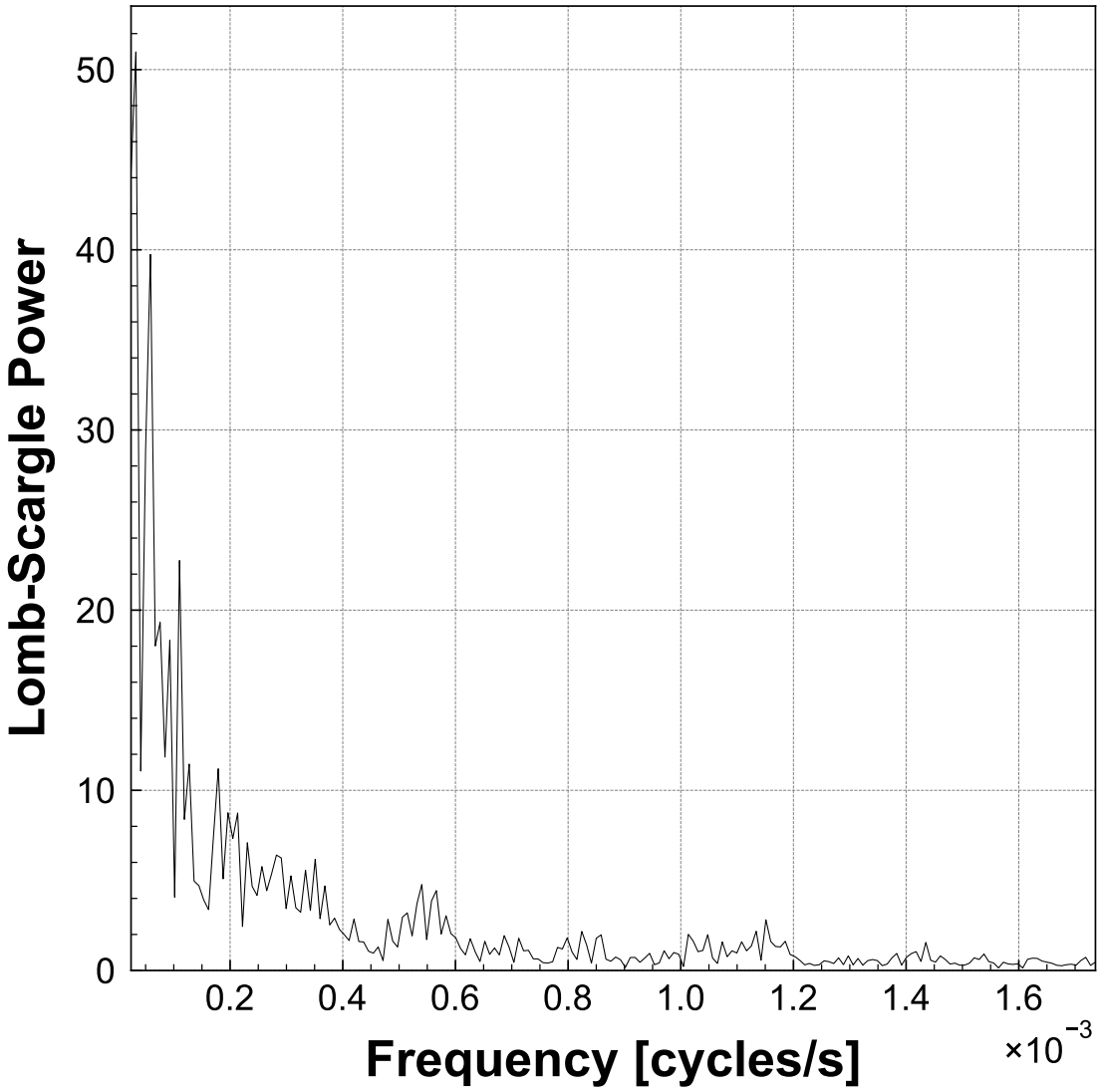

Figure 4.2. Lomb-Scargle periodogram of 2010 XC_{15}. The number of harmonics of the model curve is five.

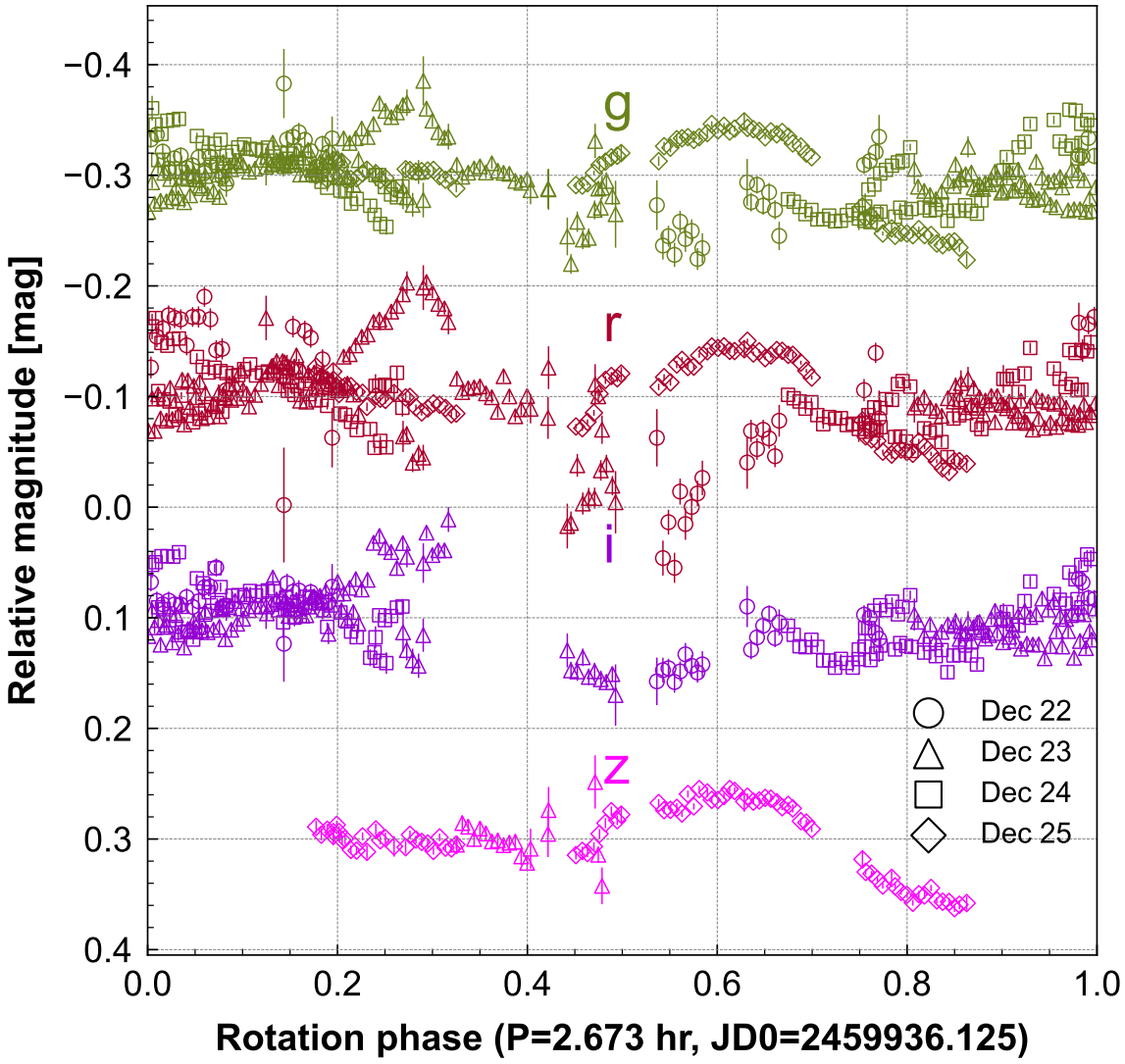

Figure 4.3. Phased lightcurves of 2010 XC_{15}. From top to bottom, g, r, i, and z bands lightcurves are presented. Lightcurves are folded by the derived period of 2.673 hr. Phase zero is set to JD 2459936.125 (2022 December 22 15:00:00 UT). Lightcurves in each band are horizontally offset by 0.2 mag for the sake of clarity. Bars indicate the 1σ uncertainties.

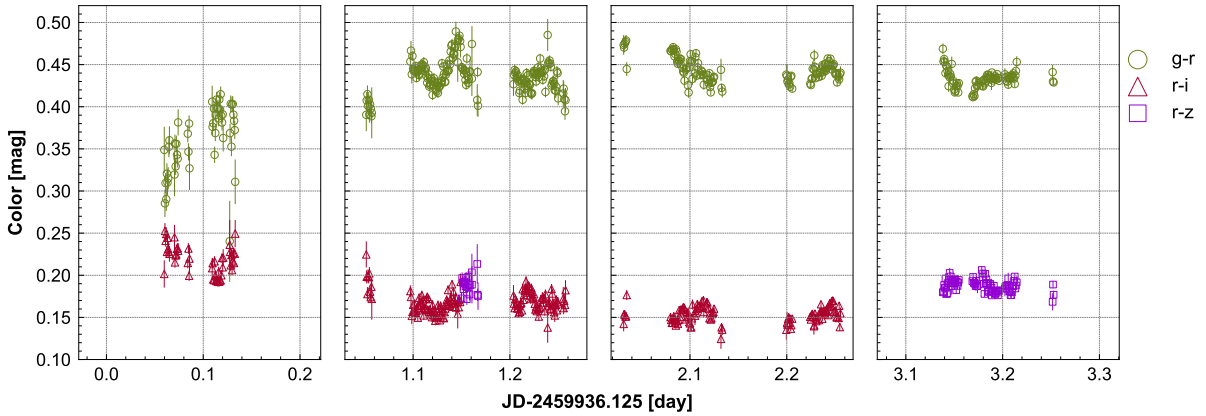

Figure 4.4. Time variations of colors of 2010 XC_{15}. $g-r$ (circles), $r-i$ (triangles), and $r-z$ (squares) colors are presented. Time zero is set to JD 2459936.125 (2022 December 22 15:00:00 UT). Bars indicate the 1σ uncertainties.

We fit the linear polarization degrees of 2010 XC_{15} using an empirical model curve as follows:

$$P_{\rm r}(\alpha) = b \sin^{c_1}(\alpha) \cos^{c_2}\left(\frac{\alpha}{2}\right) \sin(\alpha - \alpha_0), \tag{4.7}$$

where b, c_1, c_2, and α_0 are free parameters (Lumme & Muinonen 1993; Penttilä et al. 2005). We used the `curve_fit` function in the `Python` package `SciPy` (Virtanen et al. 2020). The `curve_fit` routine determines the best-fit parameters using the Levenberg–Marquardt algorithm. Our polarimetric measurements were obtained at the phase angle range of 58° to 114°. The free parameters were not constrained well with only our measurements since our phase angle coverage was insufficient. It is known that asteroids that belong to the same spectral class show a similar phase angle dependence of linear polarization (Belskaya et al. 2017). As for E-types, polarimetric measurements at phase angles larger than 50° have been reported for two NEAs: 1998 WT_{24} (Kiselev et al. 2002) and (144898) 2004 VD_{17} (De Luise et al. 2007). In Figure 4.6, we plot the polarization degrees of these two asteroids. These two asteroids were also not observed at small phase angles. We plotted the polarization degrees of the prototype E-type MBA Nysa (Zellner & Gradie 1976). We adopted the polarization degrees determined using the R band or 678 nm filter for 1998 WT24, and those determined using the R-band filter for Nysa as our observations of 2010 XC_{15} were conducted in the R band. We note that 2004 VD_{17} was observed with the V-filter. A good match was found between phase angle dependences of linear polarization degrees of 2010 XC_{15} and 1998 WT_{24}, whereas the linear polarization degrees of 2004 VD_{17} indicated a different trend. Therefore, we combined and fit the linear polarization degrees of 2010 XC_{15} and 1998 WT_{24} with the empirical model curve above. There is a good match between the model curve and linear polarization degrees of Nysa.

We generated 3000 polarization data sets by randomly resampling the measured data assuming each polarization degree follows a normal distribution with a standard deviation of its uncertainty. We obtained 3000 sets of fitting parameters from the generated data sets. The maximum polarization degree of 2010 XC_{15} was derived as approximately 2 % at α of approximately 100°.

4.3.4. Dynamical evolution

The time evolutions of the orbital elements of 2010 XC_{15} and 1998 WT_{24} during the last 1000 years are presented in Figure 4.7. The orbital elements of 2010 XC_{15} and 1998 WT_{24} can be successfully traced for approximately 200 and 250 years, respectively. The orbital elements of clones become scattered, and chaotic behaviors can be seen.

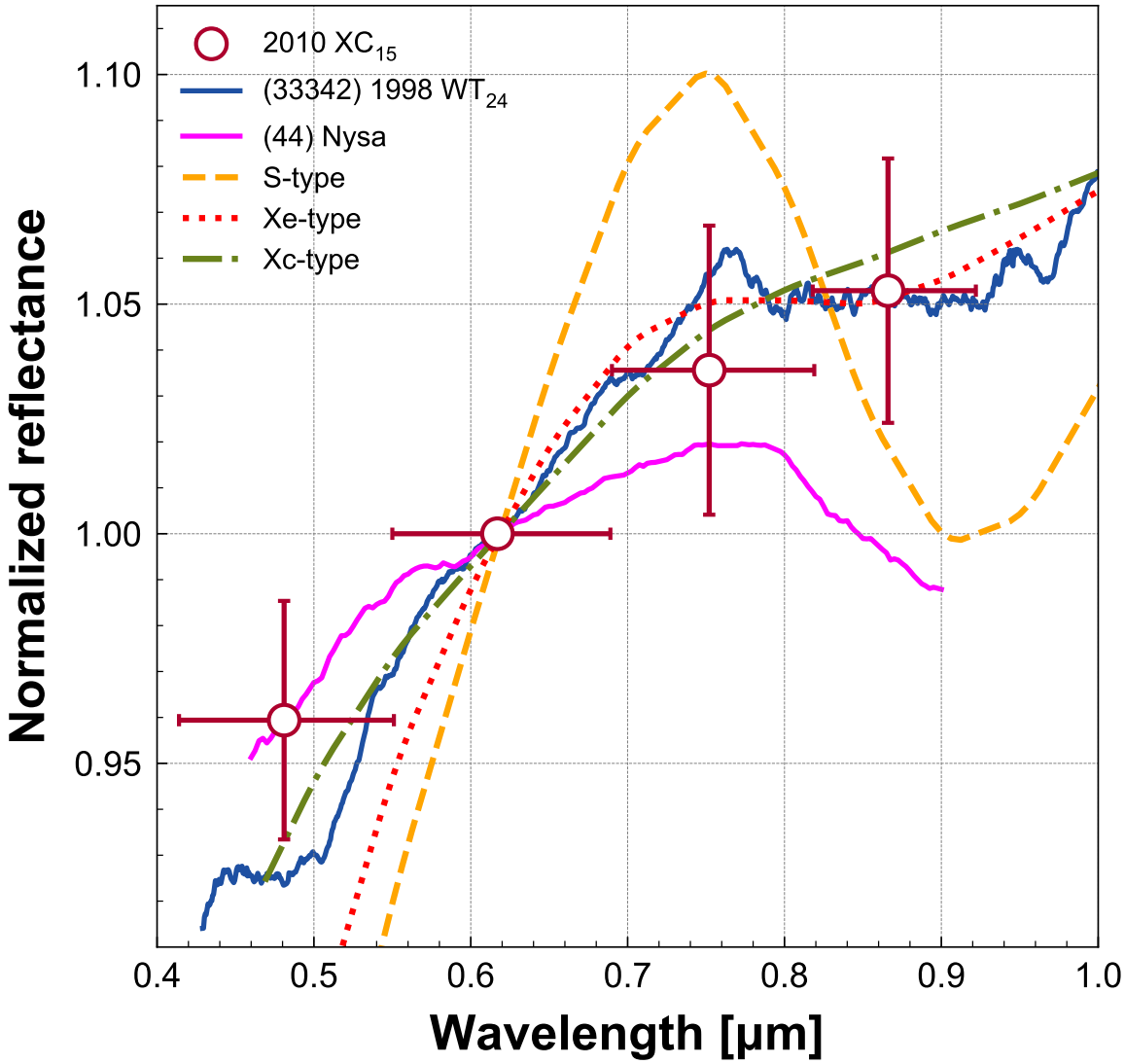

Figure 4.5. Reflectance spectrum of 2010 XC_{15} (circles). Vertical bars indicate the 1σ uncertainties. Horizontal bars indicate the filter bandwidths. Visible spectra of other E-types are shown: 1998 WT_{24} (upper solid line on the right side, Lazzarin et al. 2004) and Nysa (lower solid line on the right side, Bus & Binzel 2002). Template spectra of S- (dashed line), Xe- (dotted line), and Xc-types (dot-dashed line) are shown (Bus & Binzel 2002; DeMeo & Carry 2013). The reflectance spectra are normalized at 0.617 μm.

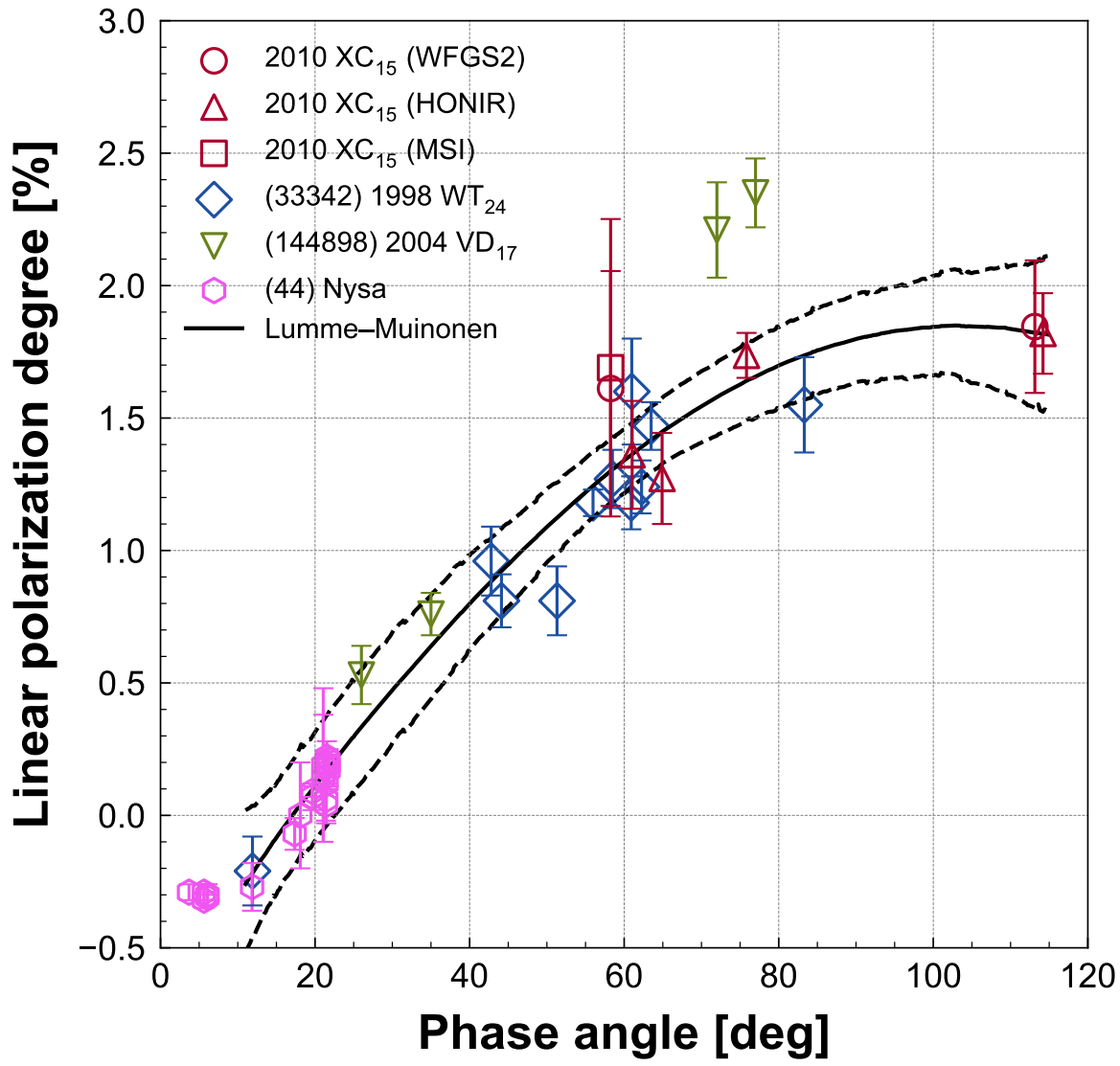

Figure 4.6. Phase angle dependences of linear polarization degrees of 2010 XC_{15} and E-type asteroids. Polarization degrees of 2010 XC_{15} are presented by circles (WFGS2) triangles (HONIR), and a square (MSI). Polarization degrees of E-types are shown: 1998 WT_{24} (diamonds, Kiselev et al. 2002), 2004 VD_{17} (inverted triangles, De Luise et al. 2007), and Nysa (hexagons, Zellner & Gradie 1976). Bars indicate the 1σ uncertainties. The polarization phase curve of 1998 WT_{24} and 2010 XC_{15} fitted with the empirical function (Lumme & Muinonen 1993; Penttilä et al. 2005) is indicated by a solid line. Uncertainty envelopes representing the 95 % highest density interval (HDI) values are indicated by dashed lines.

We checked the distance between the inner planets and both 2010 XC_{15} and 1998 WT_{24}, outputting the coordinates and velocities of asteroids every 0.1 days. The close approaches at a few lunar distances from the Earth-Moon system had strong influences on the orbital evolution of both 1998 WT_{24} and 2010 XC_{15}. The three integrals of motion, $C_0(= 1/a)$, C_1, and C_2 have been stable for 1000 years. The C_0 of 2010 XC_{15} and 1998 WT_{24} are within the ranges of 1.350 to 1.361 and 1.391 to 1.398, respectively; the C_1 of them are within the ranges of 0.809 to 0.813 and 0.809 to 0.812, respectively; the C_2 of them are within the ranges of 0.067 to 0.069 and 0.069 to 0.071, respectively.

4.4. Discussion

4.4.1. Observational confirmation of E-type NEA pair 1998 WT_{24}–2010 XC_{15}

In Figure 4.5, we show the template spectra of S-, Xe-, and Xc- types (Bus-DeMeo taxonomy, Bus & Binzel 2002; DeMeo & Carry 2013) [6], spectrum of the E- (Tholen taxonomy) and Xc-type (Bus-DeMeo taxonomy) MBA Nysa (Bus & Binzel 2002), and the E-type NEA 1998 WT_{24} (Lazzarin et al. 2004). The latter two were obtained via the M4AST online tool (Popescu et al. 2012). We confirm the similarity between spectra of 2010 XC_{15} and 1998 WT_{24}.

We check the difference of phase angles at the observations as it is known that the slope of the visible spectrum changes depending on solar phase angles, also known as the phase reddening effect (Sanchez et al. 2012). Phase angles, specific dates and times of observations of 1998 WT_{24} are not described in Lazzarin et al. (2004). We carefully combine the available information in Lazzarin et al. (2004): their observations were performed on 2000 October 26–28 or 2001 November 17–20 and V band magnitude of 1998 WT_{24} was 16.0 mag at the observations. According to the ephemerides provided by NASA JPL HORIZONS, the V band magnitude are approximately 20 mag and 16 mag on 2000 October 26–28 and 2001 November 17–20, respectively. The V band magnitude indicates that the observations were conducted in the latter period. The phase angles of 1998 WT_{24} in 2001 November 17–20 were 73–77°, which is not far from those of our 2010 XC_{15}'s observations, 58–65°. Therefore, we ignore the phase reddening effect.

We derived the linear polarization degrees of 2010 XC_{15} are a few percent at the phase angles across wide ranges. The linear polarization degrees of 2010 XC_{15} and 1998 WT_{24} at phase angles around 60° match well. The $P_{\max}$ of 2010 XC_{15} is about 2 %. This is almost equivalent to the $P_{\max}$ of 1998 WT_{24}, 1.6–1.8, derived in Kiselev et al. (2002), although it must be noted that the $P_{\max}$ of 2010 XC_{15} was derived with the polarization degrees of 1998 WT_{24}. We further note that the $P_{\max}$ of 1998 WT_{24} in Kiselev et al. (2002) was derived with the polarization degrees of other E-types, Nysa and (64) Angelina.

The physical properties and orbital elements of 2010 XC_{15} and 1998 WT_{24} are summarized in Table 4.3. On the basis of the photometric and polarimetric properties described above, the surface properties of two E-type asteroids 2010 XC_{15} and 1998 WT_{24} resemble each other. The recent spectroscopic survey of NEAs show E-types comprise only a few percent of the total NEA population (Marsset et al. 2022). Taking the similarity of not only physical properties but also dynamical integrals and the rarity of E-types in the near-Earth region into account, we suppose that 2010 XC_{15} and 1998 WT_{24} are fragments from the same parent body (i.e., asteroid pair). They are the sixth NEA pair and the first E-type NEA pair ever confirmed. The next close approaches of 2010 XC_{15} and 1998 WT_{24} will take place in 2027 December with $V \leq 17$ mag and in 2029 December with $V \leq 14$ mag, respectively. Additional spectroscopic observations in wide wavelength coverage are encouraged to investigate the common origin of the two NEAs.

[6] http://smass.mit.edu/busdemeoclass.html

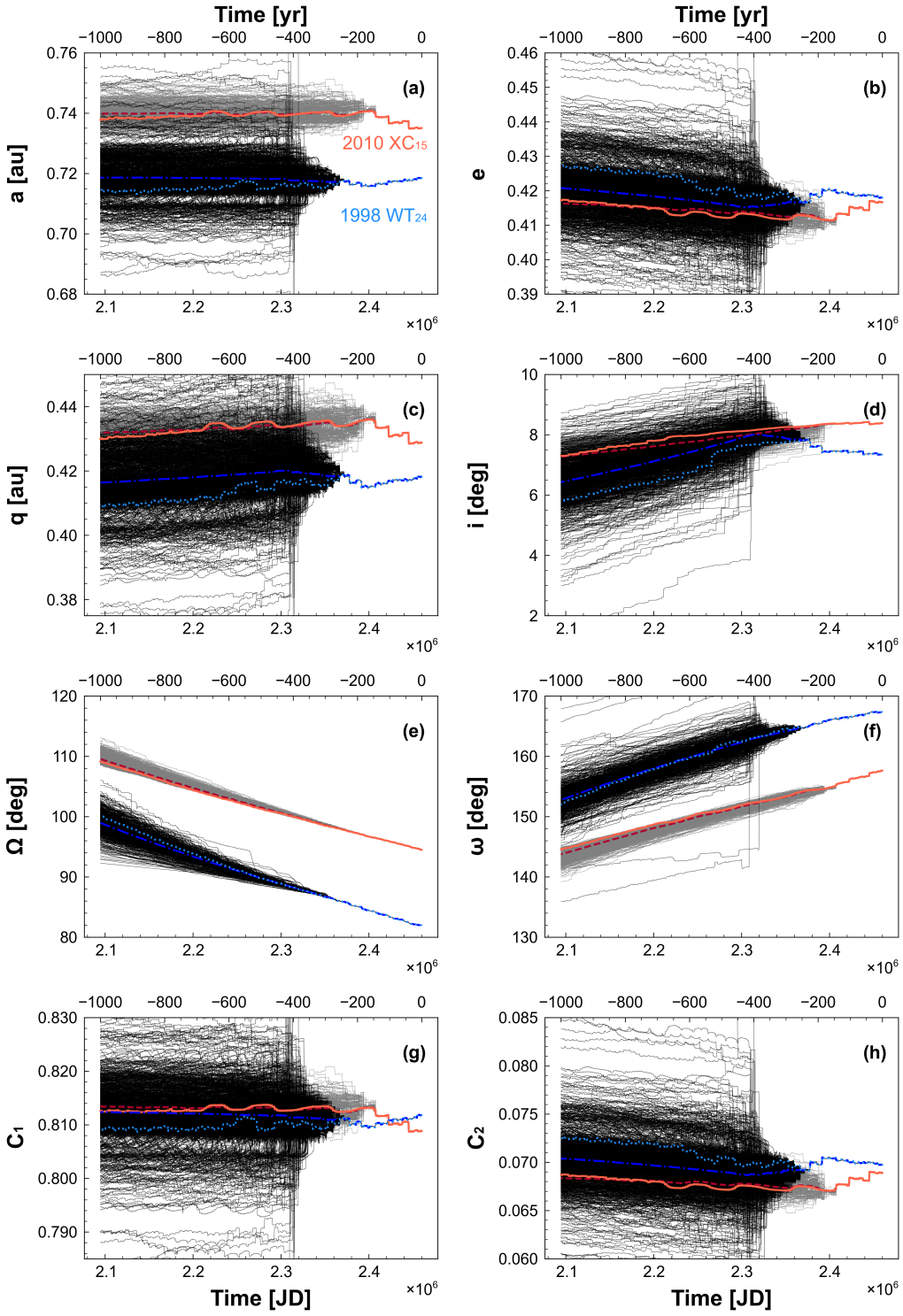

Figure 4.7. Time evolution of orbital elements and integrals of 2010 XC_{15} and 1998 WT_{24} during 1000 years backward integration: (a) semimajor axis, (b) eccentricity, (c) perihelion distance, (d) inclination, (e) longitude of ascending node, (f) argument of perihelion, (g) C_1 integral, and (h) C_2 integral. Time evolution of nominal and averaged values for 2010 XC_{15} are presented by solid and dashed lines, respectively. Time evolution of nominal and averaged values for 1998 WT_{24} are presented by dotted and dot-dashed lines, respectively. Time evolution of other clones for 2010 XC_{15} and 1998 WT_{24} are shown by gray and black lines, respectively.

Table 4.3. Comparison of physical properties and orbital elements of 2010 XC_{15} and 1998 WT_{24}

	2010 XC_{15}	1998 WT_{24}	References
Absolute magnitude, H (mag)	21.70	18.69 ± 0.3	1, 2
Geometric albedo, p_V	$0.350^{+0.176}_{-0.151}$	0.34 ± 0.20, 0.56 ± 0.2	1, 2, 3
Rotation period (hr)	a few to several dozen	3.6970 ± 0.0002	This study, 2
Volume equivalent diameter (m)	102^{+30}_{-17}	415 ± 40	1, 2
Maximum polarization degree, P_{max} (%)	~ 2	1.6–1.8	This study, 4
Shape	nearly spherical	nearly spherical	This study, 2
Semimajor axis, a (au)	0.732375383(0.000000015)	0.7187740919(0.0000000027)	5
Eccentricity, e	0.419862999(0.000000040)	0.4176018439(0.0000000098)	5
Inclination, i (°)	8.2392588(0.0000060)	7.3675902(0.0000019)	5
Longitude of ascending node, Ω (°)	94.4069555(0.0000035)	81.6663922(0.0000021)	5
Argument of perihelion, ω (°)	158.1007878(0.0000069)	167.5262827(0.0000028)	5
Mean anormaly, M (°)	323.063632(0.000012)	136.978426(0.000022)	5

Note. — (1) NEO Legacy (2) Busch et al. (2008) (3) Best-fit values from thermal-infrared observations in Harris et al. (2007) (4) Kiselev et al. (2002) (5) The orbital elements of 2010 XC_{15} are referred to epoch Julian Day 2460000.5 (2023 February 25.0) TDB (Barycentric Dynamical Time, J2000.0 ecliptic and equinox). It is based on 279 observations with a data-arc span of 4406 days (solution date, 2023 February 14 15:10:21). The orbital elements of 1998 WT_{24} are referred to epoch Julian Day 2460000.5 (2023 February 25.0) TDB. It is based on 1842 observations with a data-arc span of 8489 days (solution date, 2023 March 1 06:14:53). Information above together with orbital elements are extracted from NASA JPL SBDB. Values in the parentheses are 1σ uncertainties of orbital elements.

4.4.2. Dynamical history and origin of E-type NEA pair

The six confirmed NEA pairs are presented on an a–e_{min} or $1/C_0$–e_{min} plane in Figure 4.8: Phaethon–2005 UD (Ohtsuka et al. 2006), Icarus–2007 MK_6 (Ohtsuka et al. 2007), 2017 SN_{16}–2018 RY_7 (de la Fuente Marcos & de la Fuente Marcos 2019; Moskovitz et al. 2019), 2015 EE_7–2015 FP_{124} (Moskovitz et al. 2019), 2019 PR_2–2019 QR_6 (Fatka et al. 2022), and 1998 WT_{24}–2010 XC_{15}. The e_{min} is a minimum value of the orbital eccentricity over one period of ω (Gronchi & Milani 2001). The orbital elements were extracted from the NEA element catalogs of NEODyS-2[7] as of 2023 May 1. The C_1 and C_2 of 2010 XC_{15}, 1998 WT_{24}, and other NEA pairs are plotted on the Lidov diagram in Figure 4.9 (Lidov 1962; Ito & Ohtsuka 2019). The Lidov diagram helps us understand the dynamical characteristics of the system. The orbital elements used to calculate C_1 and C_2 were extracted from the Minor Planet Center Orbit Database file[8] as of 2023 May 1. The separations of 2010 XC_{15} and 1998 WT_{24} on Figures 4.8 and 4.9 are as small as the other NEA pairs as summarized in Table 4.4. This supports the idea that the two asteroids are of common origin as these integrals are useful indicators to confirm NEA pairs (Ohtsuka et al. 2006, 2007). As shown in Figure 4.7, the orbital elements of 2010 XC_{15} and 1998 WT_{24} become scattered after backward integrations of 200 and 250 years, respectively. Thus, we could not determine the exact time of the breaking-up event.

It is worth mentioning that the mass ratio of 1998 WT_{24}–2010 XC_{15} as well as Phaethon–2005 UD and Icarus–2007 MK6 is close to 0.25. The rotation period of the primary 1998 WT_{24} is 3.6970 hr (Busch et al. 2008), which is also close to that of another primary Phaethon. Busch et al. (2008) revealed that the shape of 1998 WT_{24} looks like a spherical body with three basins. They interpreted that the basins may be impact craters or a relic of past dynamical disruption. The overall shape of 1998 WT_{24} resembles top-shaped asteroids such as 2008 EV_5 and 2000 DP_{107} on which rotation fissions may have occurred

[7] https://newton.spacedys.com/neodys/
[8] https://minorplanetcenter.net/iau/MPCORB/NEA.txt

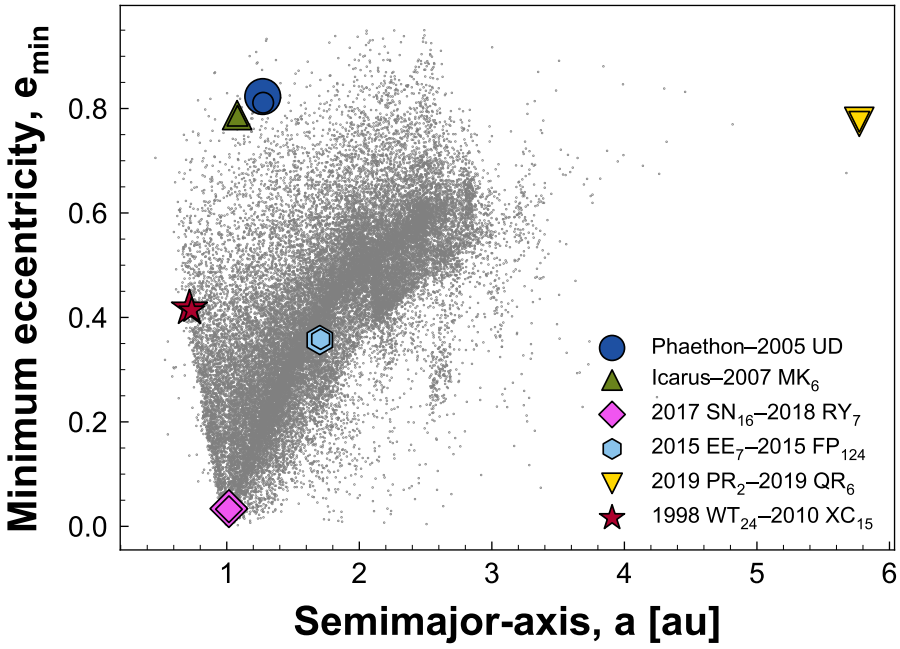

Figure 4.8. Semimajor-axis (a) versus minimum eccentricity ($e_{\min}$) of NEAs. Larger (primary) asteroids are plotted with larger markers than smaller (secondary) asteroids for all pairs. Orbital elements are extracted from the NEODyS-2 as of 2023 May 1.

(Tardivel et al. 2018). The mass ratio and rotation period are consistent with the theory of rotation fission (Scheeres 2007; Pravec et al. 2010). This is also the case for the Phaethon–2005 UD pair (Hanuš et al. 2016b). Therefore, the rotation fission is favored as the formation mechanism of the 1998 WT_{24}–2010 XC_{15} pair. Considering the diameter of the parent body of 1998 WT_{24}–2010 XC_{15} is almost equivalent to that of 1998 WT_{24} at approximately 400 m, the YORP spin-up might play an important role in rotation fission since it strongly changes the rotation state of such small bodies (Rubincam 2000). In terms of the spherical shape of the primary 1998 WT_{24}, rotation fission is preferred instead of tidal disruption, which typically expects elongated primaries (Walsh & Richardson 2006).

There are some escape regions from MBAs to NEAs (Granvik et al. 2018). One is the ν_6 resonance at the inner edge of the main belt with a semimajor axis of approximately 2.1 au. Nysa is located at the inner main belt with a semimajor axis of approximately 2.4 au. Reddy et al. (2016) characterized a tiny ($D \sim 2$ m) E-type NEA 2015 TC_{25} in radar, optical lightcurves, and near-infrared spectroscopic observations. They combined the spectral and dynamical properties of 2015 TC_{25} and concluded that it was a fragment possibly ejected from Nysa. Another representative escape region for E-types is the Hungaria region with a semimajor axis of approximately 1.9 au and an inclination of about 20°. It is known that the fraction of NEAs from the Hungaria region is smaller than those from the inner main belt through the ν_6 resonance (Granvik et al. 2018). On the other hand, considering the relative fractions of E-types in different regions of the main belt, the probability of them originating from the Hungaria region is higher than from the ν_6 resonance or comparable within uncertainties (Binzel et al. 2019). Thus, the source region of 2010 XC_{15}, 1998 WT_{24}, and their parent body cannot be clearly determined.

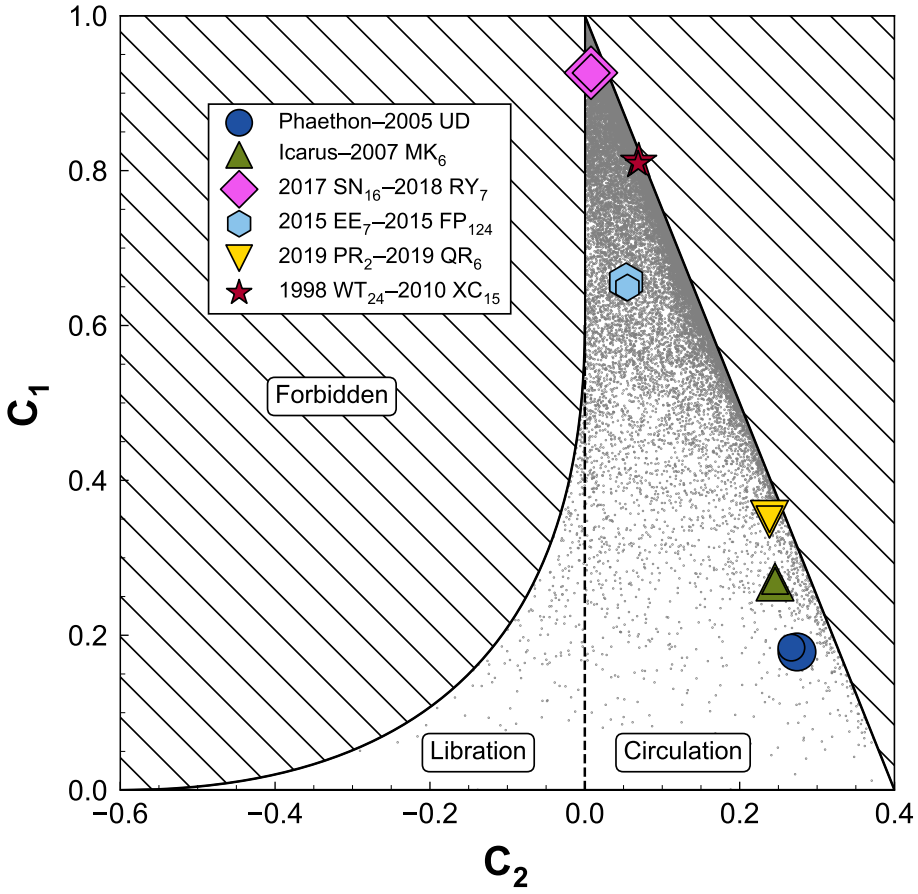

Figure 4.9. Lidov diagram with C_1 and C_2 of NEAs. Larger asteroids (primary) are plotted with larger markers than smaller asteroids (secondary) for all pairs. The area to the left of the separatrix (dashed line) is libration mode (argument of perihelion librates), and the area to the right is circulation mode (argument of perihelion circulates). The forbidden region is hatched. Orbital elements used to calculate C_1 and C_2 are extracted from the Minor Planet Center Orbit Database file as of 2023 May 1.

Table 4.4. Proper orbital elements and integrals of NEA pairs

	a	$e_{\min}$	C_0	C_1	C_2
Phaethon	1.2713	0.8229	0.78661	0.17842	0.27397
2005 UD	1.2748	0.8111	0.78444	0.18403	0.26681
difference	0.0035	0.0118	0.00218	0.00561	0.00716
Icarus	1.0779	0.7875	0.92770	0.26871	0.24558
2007 MK_6	1.0808	0.7862	0.92521	0.27029	0.24572
difference	0.0029	0.0012	0.00248	0.00158	0.00015
2017 SN_{16}	1.0161	0.0339	0.98417	0.92635	0.00797
2018 RY_7	1.0162	0.0328	0.98403	0.92618	0.00813
difference	0.0001	0.0012	0.00015	0.00017	0.00016
2015 EE_7	1.7017	0.3567	0.58765	0.65636	0.05328
2015 FP_{124}	1.7084	0.3584	0.58533	0.64897	0.05501
difference	0.0067	0.0017	0.00232	0.00738	0.00172
2019 PR_2	5.7721	0.7744	0.17325	0.34974	0.23851
2019 QR_6	5.7727	0.7745	0.17323	0.34972	0.23857
difference	0.0006	0.0001	0.00002	0.00001	0.00006
1998 WT_{24}	0.7185	0.4179	1.39183	0.81205	0.06962
2010 XC_{15}	0.7349	0.4135	1.36073	0.80887	0.06889
difference	0.0164	0.0043	0.03110	0.00318	0.00073

Note. — Seminajor axis, a, minimum eccentricity, $e_{\min}$, C_0, C_1, and C_2 of NEA pairs. The absolute differences of five parameters for each pair are listed for each pair. The $a(\equiv 1/C_0)$ and $e_{\min}$ are extracted from the NEA element catalogs of NEODyS-2 as of 2023 May 1. Orbital elements used to calculate C_1 and C_2 are extracted from the Minor Planet Center Orbit Database file as of 2023 May 1.

4.5. Summary of this chapter

We performed optical photometry and polarimetry of a small NEA 2010 XC_{15} in 2022 December. We found that the rotation period of 2010 XC_{15} is possibly a few to several dozen hours and color indices of 2010 XC_{15} are $g - r = 0.435 \pm 0.008$, $r - i = 0.158 \pm 0.017$, and $r - z = 0.186 \pm 0.009$ in the Pan-STARRS system. Additionally, we derived the linear polarization degrees of 2010 XC_{15} is a few percent at the phase angle range of 58° to 114°. We found that 2010 XC_{15} is a rare E-type NEA on the basis of its photometric and polarimetric properties. Taking the similarity of not only physical properties but also dynamical integrals and the rarity of E-type NEAs into account, we suppose that 2010 XC_{15} and 1998 WT_{24} are an E-type NEA pair. These two NEAs are the sixth NEA pair and first E-type NEA pair ever confirmed and were possibly formed by rotation fission. We conjecture that the parent body of 2010 XC_{15} and 1998 WT_{24} is from the main belt through the ν_6 resonance or the Hungaria region. The next observing windows of 2010 XC_{15} and 1998 WT_{24} will arrive in December 2027 with $V \leq 17$ mag and December 2029 with $V \leq 14$ mag, respectively. Additional spectroscopic observations in wide wavelength coverage are encouraged to further investigate the common origin of these two NEAs.

You can't connect the dots looking forward; you can only connect them looking backwards. So you have to trust that the dots will somehow connect in your future.
— Steve Jobs (1955–2011)

5. *Surface Properties and Interior Structures of Tiny Near-Earth Asteroids*

5.1. What we learned in this dissertation

We summarize the scope and our discoveries throughout this dissertation in Figure 5.1.

In Chapter 2, we have obtained the lightcurves of 108 tiny NEAs with the wide-field CMOS camera Tomo-e Gozen. We successfully derived the rotation periods of 52 samples. Compared with the literature, the distribution of the rotation periods of 52 objects shows a potential excess in shorter periods. Moreover, we discovered that the distribution of the tiny NEAs in the D-P diagram is truncated around a period of 10 s. We performed model calculations considering the YORP effect. A NEA smaller than 10 m is expected to rotate with a period shorter than 10 s assuming a constant acceleration by YORP, which is not consistent the present results. We found that the TYORP effect is a possible mechanism to produce the truncated distribution.

In Chapter 3, we have conducted optical multicolor photometry of the tiny NEA 2015 RN_{35} over twelve nights in 2022 December and 2023 January. We found that 2015 RN_{35} is in a non-principal axis spin state with two characteristic periods of 1149.7 ± 0.3 s and 896.01 ± 0.01 s. The visible reflectance spectrum of 2015 RN_{35} is as red as Justitia, one of the VROs in the main belt, which indicates that 2015 RN_{35} can be classified as an A- or Z-type asteroid. Together with the shallow slope of the phase curve, we suppose 2015 RN_{35} is a high-albedo A-type asteroid. However, the results can be explained by assuming that tiny NEA 2015 RN_{35} lacks the regolith on its surface.

In Chapter 4, we have conducted optical multicolor photometry and polarimetry of the small NEA 2010 XC_{15} during the close approach in 2022 December. We found similarities in the spectra and polarization degrees of two NEAs with similar orbits, 1998 WT_{24} and 2010 XC_{15}, although they are small asteroids with different sizes of about 400 m and 100 m for 1998 WT_{24} and 2010 XC_{15}, respectively. We suppose that 1998 WT_{24} and 2010 XC_{15} are an E-type NEA pair. Considering the small size of the parent body of 1998 WT_{24}–2010 XC_{15}, approximately 400 m in diameter, and the spherical shape, the YORP spin-up might lead to rotation fission.

We have expanded our knowledge about the formation mechanism and dynamical evolution of NEAs in Chapter 4 and 2, respectively. The TYORP is actually working on NEAs, and we showed that the rotation fission event could form an NEA of about 100 m in diameter. We discuss the surface properties and interior structures of NEAs in depth in the rest of this chapter.

5.2. Surface properties of tiny near-Earth asteroids

In Chapter 3, we found that 2015 RN_{35} is a fast-rotating NEA with a very red spectral slope and a very shallow phase slope. We conjecture that 2015 RN_{35} is an A-type NEA although the A-type is a very rare population with an abundance ratio of less than 1% (Marsset et al. 2022). Did we win the lottery with a probability of 1%? It is a hasty decision to conclude that 2015 RN_{35} is truly an A-type. As mentioned in Subsection 3.4.1, it is possible that the A-type classification is not correct due to the difference in the surface properties between large and tiny asteroids. This is possible evidence of the size dependence

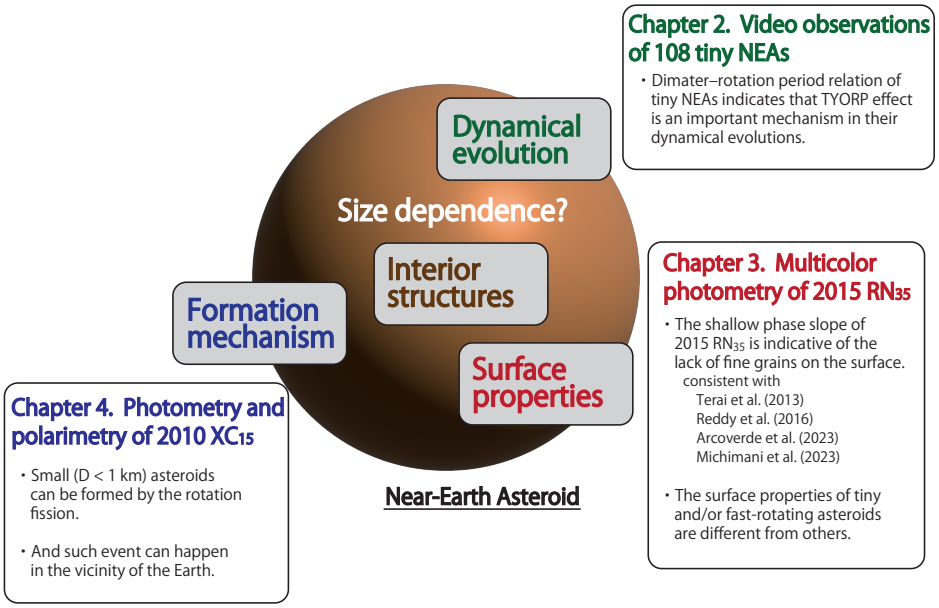

Figure 5.1. Scope and discoveries of this dissertation.

of the surface properties of NEAs. Smaller asteroids have fewer fine grains on their surface due to the weak gravity and strong centrifugal force arising from fast rotations. Our conclusion about the surface properties of NEAs in Chapter 3 is that **they may have size dependence owing to the difference of surface gravity as well as centrifugal force due to the fast rotation**. As Chapter 3 in the dissertation, Terai et al. (2013) also reported the shallow photometric phase slope of the tiny NEA Duende ($D \sim 50$ m). Duende is known to be a slow-rotating tumbling asteroid with a rotation and precession period of 23.67 hr and 8.71 hr, respectively (Moskovitz et al. 2020). This may indicate that **the surface of tiny asteroids might be free from fine grains regardless of the rotation state**.

In Chapter 4, we discovered the sixth NEA pair and the first E-type NEA pair 1998 WT_{24}–2010 XC_{15}. The formation mechanism of the pair is probably the rotation fission (Walsh et al. 2008). The result implies that there is no strong size dependence in the formation mechanism of NEA pairs; rotation fission is a common mechanism in a wide size range. It is also noteworthy that the distance between the Earth and the 1998 WT_{24}–2010 XC_{15} pair was only a few lunar distances during the close approach. Even under such an extreme condition, the asteroid pair can be formed and resulting bodies have similar surface properties. The similarities of the visible spectra and linear polarization degrees of 1998 WT_{24} and 2010 XC_{15} at a wide range of phase angles support the scenario that the two small NEAs have similar surface properties. Here, we focus on the small difference in their spectra in Figure 4.5. The slightly bluer spectrum of 2010 XC_{15} is indicative of a lack of fine grains on the surface as discussed in Reddy et al. (2016). Reddy et al. (2016) investigated properties of the tiny ($D \sim 2$ m) E-type NEA 2015 TC_{25} by ground-based observations and experimental approach. The interesting property of 2015 TC_{25} is its bluer spectrum compared to a typical E-type. They showed that increasing the grain size of the aubrite sample decreases the spectral slope of it, They interpreted the bluer slope of the tiny NEA 2015 TC_{25} in the visible wavelength with a lack of fine grains on the surface. Thus, we found direct evidence of the **size dependence of the surface properties of NEAs; small NEAs may lack fine grains on the surface**.

Our conclusion, tiny NEAs lack fine regolith on the surface, is consistent with a recent study about histories of surface regolith considering both removal and production of them (Delbo et al. 2014; Hsu et al. 2022). Delbo et al. (2014) showed that the thermal fatigue (also known as physical weathering

or thermal cracking, McFadden et al. 2005), which is rock weathering and fragmentation process due to diurnal temperature variation, makes regolith on the surface of asteroids by laboratory experiments. The regolith production of thermal fatigue does not depend on the size of the asteroid, but depends on its composition; more regolith is generated on the surface of silicaceous (S-type) asteroids rather than carbonaceous (C-type) asteroids since C-types experience more severe diurnal temperature variations than those of S-types. The existence of thermal fatigue on asteroids is recently indirectly indicated by the lack of low-albedo asteroids with small ($q \leq 0.6$ au) perihelion distances (Granvik et al. 2016). There are some interpretations for the lack of low-albedo asteroids with small perihelion distances. The one possibility is the super-catastrophic disruption by the thermal fatigue; other explanations are such as spin-up by the YORP effect and evaporation of volatile materials. Very recently, Hsu et al. (2022) investigated the history of surface regolith on sub-km asteroids by numerical modeling. They predict the lack of fine grains on the surface of small ($D < 1$ km) NEAs by model calculation considering the fragmentation of regolith by thermal fatigue (Delbo et al. 2014) and meteoroid impacts, escape of impact ejecta, and loss of grains by electrostatic dust transport. Despite the thermal fatigue is known to be a mechanism relevant to regolith production as discussed above, the net production rate is negative, i.e., **theoretically fine grains are removed on the surface of small NEAs**.

5.3. Interior structures of tiny near-Earth asteroids

In Chapter 2, we have explained the observed D-P diagram considering the TYORP effect, which was recently introduced by Golubov & Krugly (2012). The TYORP is caused by a recoil force parallel to the surface, which arises from the asymmetricity of scattered sunlight and thermal radiation from its surface. The TYORP predicts more spin acceleration rather than deceleration, which is consistent with the observational results that spin changes of twelve NEAs are all acceleration (see Section 1.4 and Figure 1.7). We succeeded in explaining the observed D-P relation in Chapter 2 assuming the tiny NEAs are monolithic asteroids. This may imply that our assumption is correct; **tiny asteroids are actually monolithic asteroids**.

Recently, Fenucci et al. (2021, 2023) estimated the thermal conductivities of the two tiny NEAs, (499998) 2011 PT ($D \sim 35$ m) and 2016 GE_1 ($D \sim 12$ m), as small as 0.1 W m^{-1} K^{-1} and 0.01 W m^{-1} K^{-1}, respectively by thermal modeling considering the Yarkovsky drift rates. It is possible that the two NEAs have fine regolith on their surface, or they are porous rocks (Avdellidou et al. 2020; Cambioni et al. 2021). Other studies on the Earth grazing tiny NEAs, 2009 BD, 2011 MD, and 2012 LA (Mommert et al. 2014a,b; Micheli et al. 2012, 2013, 2014), imply that the three tiny NEAs have low densities or high albedos. If tiny asteroids are *normal* monolithic asteroids as a rock with a density of that of a typical stony meteorite, its thermal conductivity is expected to be higher than the measurements in Fenucci et al. (2021, 2023). In conjunction with our conclusion about the surface properties of tiny NEAs summarized in the previous section, we conjecture that **tiny NEAs, at least 2011 PT, 2016 GE_1, 2009 BD, 2011 MD, and 2012 LA, might lack the regolith on their surface, and are porous rocks**.

The interpretation that tiny asteroids are porous rocks and free from fine grains agrees with an inverse correlation between the abundance of regolith and the porosity of rocks on the NEA Bennu (Cambioni et al. 2021), which was investigated by the OSIRIS-REx. They measured the surface abundance of regolith and porosity of 122 spots of about 40 m in diameter on Bennu observed by the OSIRIS-REx Thermal Emission Spectrometer, and found the tight inverse correlation between them. The origin of the correlation is explained as two regolith generation mechanisms, meteoroid impacts and thermal fatigue, are both less effective on porous rocks. Thus, the lack of regolith on the tiny NEAs implied in the previous section supports the porous interior structures of them.

A caveat to be noted is that some meteorites such as Almahata Sitta (also known as 2008 TC_3 Jenniskens et al. 2009) and Kaidun (Zolensky et al. 2003) were possible rubble-piles when they were asteroids or meteoroids before the atmospheric entries. It is known that Almahata Sitta meteorite contains

a large fraction of the variety of some meteorite types (Zolensky et al. 2010; DeMeo et al. 2015). The other caveat is estimates of mass density and albedo of the tiny NEA 2013 GH_{66} ($H_V \sim 28.1$, Micheli 2013). Marco Micheli interpreted that the estimated 2013 GH_{66}'s mass density of $\rho = 1100^{+600}_{-500}$ kg m^{-3} is a factor of two higher than the other four NEAs of his interests, 2009 BD, 2011 MD, 2012 LA, and 2006 RH_{120} ($D \sim 5$ m, Kwiatkowski et al. 2009). Marco Micheli concluded that 2013 GH_{66} is a *regular-density* object. However, the mass density is still low as the rubble-pile asteroid such as Ryugu ($\rho \sim 1200$ kg m^{-3}, Watanabe et al. 2019).

5.4. Implications

The conclusion of this dissertation, tiny asteroids lack fine regolith on the surface, helps the understanding of the current mysterious results of tiny NEAs as introduced in Subsection 1.7.3 such as the unusual spectrum of the tiny NEA 2022 AB (Licandro et al. 2023) and the empirical relation between the photometric phase slope and albedo of NEAs (Arcoverde et al. 2023). The different surface environments can lead to the different photometric trends (e.g., Terai et al. 2013; Reddy et al. 2016). More and more observations as this dissertation, i.e., statistical studies of phase curves of tiny NEAs (Chapter 3) and multicolor photometry of tiny NEAs (Chapter 3 and 4), are demanded to validate this interpretation.

The high porosity of tiny NEAs implies that they are more fragile than dense material (Lian et al. 2011). In terms of planetary defense, the effect of asteroid impact is qualitatively revised downward, although other properties such as size and composition are also keys to estimating the scale of the impact. Recently, observations of Earth impactors have been performed thanks to a large number of discoveries of NEAs by survey projects such as CSS and Pan-STARRS. To date, seven Earth impactors have been discovered before the impacts (Clark et al. 2023): 2008 TC_3, 2014 AA, 2018 LA, 2019 MO, 2022 EB_5, 2022 WJ_1, and 2023 CX_1. Only three of seven Earth impactors have been characterized by lightcurve and/or spectroscopic observations (Jenniskens et al. 2009, 2021; Kareta et al. 2023). The observations of Earth impactors give strong constraints on the interior structures of asteroids such as material strength in a different context from normal telescopic observations of them as this dissertation. Additional observations of Earth impactors are subjects of interest in the future using the next generation instruments.

A comparison of observational results of tiny NEAs and those of meteorite samples is worth doing. The typical porosity of ordinary chondrites and carbonaceous chondrites are $\leq 10\%$ and 10–30%, respectively (Consolmagno et al. 2008). These porosities are smaller than that of tiny NEAs, $\geq 45\%$ (Mommert et al. 2014a,b). A possible explanation for this discrepancy is the selection bias of the meteorite samples at the atmospheric entries. The deceleration of the orbital velocity of the meteoroid during the atmospheric entry leads to friction heating. The surface temperature of the meteoroid can reach 1500°C (Consolmagno et al. 2008), and a large meteoroid can be a small fragment during the entry. Thus, a porous fragile rock might not be able to survive at the entry. We note that the size of meteorites are smaller than the typical tiny NEAs ever observed, 1–100 m. Telescopic observations of sub-m asteroids are important future works for the direct comparison of meteorite samples and NEAs without size effect.

Our conclusion that tiny bodies are porous monolithic rocks expands our knowledge of the origin of tiny bodies. Recent impact experiments showed that tiny boulders on the asteroid could be ejected and become tiny asteroids by a cratering event (Okawa et al. 2022). They inferred that tiny boulders smaller than 64 m on Ryugu surface can be ejected by the impact event and become tiny asteroids. Meanwhile, recent spacecraft missions revealed that porous rocks exist on the surface of the NEA Bennu (Rozitis et al. 2020). Two types of porous boulders were found with porosities of about 30% and 50%. Combining these two facts, we suppose that to some extent the current tiny NEAs as our targets might be ejected from the surface of larger NEAs like Ryugu and Bennu, by cratering events. The rotation fission is also an important mechanism to make asteroids as shown in Chapter 3 and previous studies. The estimate of the ratio of these two mechanisms is worthy to study in the future. Assuming the tiny

monolithic asteroids are remnants of planetesimals without differentiation, observations of tiny asteroids are in turn the observations of planetesimals. Although it is difficult to observe tiny asteroids using current instruments as introduced in the introduction, measurements of bulk density, porosity, and composition of them inform us about planetesimals and planetary formation. The surface of NEAs can be refreshed by the frequent close encounters with inner planets (e.g., Binzel et al. 2010). Thus, NEAs and MBAs are in different environments in terms of surface refreshing. Observations of not only tiny NEAs but also tiny MBAs give more insights about planetesimals because MBAs do not experience the refresh much and preserve the primitive surface, although they might be affected by space weathering.

Stay hungry. Stay foolish.
— Steve Jobs (1955–2011)

6. Conclusions and Future Prospects

Conclusions

In this dissertation, we have presented the results of three observational studies of tiny asteroids. Tiny asteroids are the smallest limit among asteroids, and they are worthy of interest to investigate the formation mechanism, dynamical evolution, and surface properties as well as interior structures of the whole NEA population in a wide size range. Tiny asteroids in the main belt are too faint to observe even using 8 m class telescopes. Only NEAs during the close approaches and a few spacecraft mission targets give us knowledge about tiny bodies. However, it is not easy to characterize tiny NEAs; the number of targets is very limited for spacecraft missions, whereas ground-based observations are restricted by limited observational windows from hours to days, fast rotation sometimes less than a minute, and large apparent motion on the sky of about a few arcsec s^{-1} during the close approaches. Observations with exposure times sufficiently shorter than their rotation periods are essential to derive the short rotation period and suppress the trailing sensitivity loss effect. The previous surveys possibly undetected some very fast rotations due to a relatively long exposure time. Although characterizations of a handful of tiny NEAs have been conducted by campaign observations, most of tiny NEAs graze the Earth without being characterized even a little.

We have overcome the difficulties in observations of tiny asteroids by quick response or well-planned campaign observations using high-speed CMOS cameras. We obtained optical lightcurves of 108 tiny NEAs, and we conducted observation campaigns toward two NEAs: (i) optical multicolor photometry of the tiny NEA 2015 RN_{35} across a wide range of phase angles from 2° to 30° using two telescopes, and (ii) optical multicolor photometry and polarimetry of the NEA pair candidate 2010 XC_{15} using four telescopes. All observations were conducted during the close approaches of the NEAs.

We derived the rotation periods and axial ratios of 52 tiny NEAs including 23 fast rotators with rotation periods less than 60 s. The fastest rotator found during our survey is 2020 HS_7 with a rotation period of 2.99 s. We statistically confirmed that there is a certain number of tiny fast rotators in the NEA population, which have been missed with any previous surveys. Moreover, we discovered the critical rotation period of 10 s for tiny asteroids. The critical rotation period of 10 s could be explained by a nongravitational effect considering the TYORP effect, although further observational and theoretical studies are needed to reach a conclusion.

We found that 2015 RN_{35} is a non-principle axis rotator with two characteristic periods of 1149.7 ± 0.3 s and 896.01 ± 0.01 s. We showed that a slope of a visible spectrum of 2015 RN_{35} is as red as asteroid Justitia, one of the very red objects in the main belt, which indicates that 2015 RN_{35} could be classified as an A- or Z-type asteroid. In conjunction with the shallow slope of the phase curve, we suppose that 2015 RN_{35} is a high-albedo A-type asteroid. We demonstrated that the surface properties of tiny asteroids could be well constrained by intensive observations across a wide range of solar phase angles. 2015 RN_{35} is a possible mission accessible A-type NEA with a small Δv of 11.801 km s^{-1} in the launch window between 2030 and 2035. The other interpretation is that the shallow phase slope comes from the lack of fine grains on its surface due to weak gravity and strong centrifugal force.

We found that the rotation period of 2010 XC_{15} is possibly a few to several dozen hours, and color indices of 2010 XC_{15} are derived as $g - r = 0.435 \pm 0.008$, $r - i = 0.158 \pm 0.017$, and

$r - z = 0.186 \pm 0.009$ in the Pan-STARRS system. The linear polarization degrees of 2010 XC_{15} are a few percent at the phase angle range of 58° to 114°. We showed that 2010 XC_{15} is a rare E-type NEA on the basis of its photometric and polarimetric properties. Taking the similarity of not only physical properties but also dynamical integrals and the rarity of E-type NEAs into account, we suppose that 2010 XC_{15} and 1998 WT_{24} are of common origin. These two NEAs are the sixth NEA pair and the first E-type NEA pair ever confirmed, possibly formed by rotation fission. We conjecture that the parent body of 2010 XC_{15} and 1998 WT_{24} was transported from the main belt through the ν_6 resonance or Hungaria region.

Combining the parts into a whole, we revealed the nature of tiny NEAs. As for surface properties of tiny NEAs, we found that the tiny fast-rotating NEA 2015 RN_{35} may lack the regolith on its surface. This is explained with the lack of fine grains on its surface due to the weak gravity and/or strong centrifugal force caused by the fast rotation. We showed that asteroid pairs share similar surface properties even in the small size range (100–400 m in diameter). The slightly bluer spectrum of 2010 XC_{15} is indicative of a lack of fine grains on the surface. Thus, we found direct evidence of the size dependence of the surface properties of NEAs; small NEAs may lack fine grains on the surface. Our conclusion, tiny NEAs lack fine regolith on the surface, is supported by a recent study about histories of surface regolith considering both removal and production of them. As for interior structures, we succeeded in explaining the observed diameter and rotation period relation assuming the tiny NEAs are monolithic asteroids. This may imply that our assumption is correct; tiny asteroids are actually monolithic asteroids. In conjunction with the previous studies that imply some tiny asteroids are covered with fine grains or porous rocks, we suppose that the tiny asteroids might have porous structures. Throughout the dissertation, we conjecture that tiny asteroids are free from fine grains on the surface regardless of spin states, and possibly have porous interior structures.

The fact that tangential YORP is actually working on NEAs is an important implication to discuss the material transportation in our solar system. Our understanding of the formation mechanism of NEAs gives a strong constraint on the size frequency distribution of asteroids. Moreover, knowledge about the surface properties of tiny NEAs helps the understanding of the current mysterious results of tiny NEAs. The high porosity of tiny NEAs implies that they are more fragile than dense material. In terms of planetary defense, the effect of asteroid impact is qualitatively revised downward. Our conclusion that tiny bodies are porous monolithic rocks expands our knowledge of the origin of tiny bodies; the current tiny NEAs might be ejected from the surface of larger NEAs like Ryugu and Bennu, by cratering events. Assuming the tiny monolithic asteroids are remnants of planetesimals without differentiation, observations of tiny asteroids are in turn the observations of planetesimals. Measurements of bulk density, porosity, and composition of tiny asteroids may inform us about planetesimals and planetary formation. Our understanding of the formation mechanism, dynamical evolution, and surface properties as well as interior structures of whole NEA population were dramatically expanded in this dissertation.

Future prospects

Expand this dissertation We have characterized more than a hundred tiny asteroids using several medium-class telescopes for five years. First, more observations using the same or similar techniques are crucial to reach a consensus of the dynamical evolution, surface properties, and formation mechanism of NEAs discussed above.

In the near future, a bunch of new and lost asteroids will be discovered and recovered, respectively, by the Rubin Observatory Legacy Survey of Space and Time in Chile (LSST, Ivezić et al. 2019; Ivezić & Ivezić 2021). The LSST is expected to observe more than five million asteroids including 100000 NEAs during its ten-year survey using the Simonyi Survey Telescope with an effective aperture of 6.4 m. Furthermore, geometric albedos of a large number of NEAs would be derived by the NASA Near-Earth Object Surveyor (NEO Surveyor) mission (Mainzer et al. 2023), which is scheduled for launch in 2027.

NEO Surveyor will conduct survey observations at Channel NC1 (4–5.2 μm) and Channel NC2 (6–10 μm) with a 0.5 m infrared telescope. Since thermal observations are relatively unbiased with respect to albedo as described in Subsection 1.5.5, unbiased new asteroids will be discovered from the survey data. A significant number of discoveries of NEAs by LSST and NEO Surveyor before the close approaches of them give us opportunities for follow-up observations such as lightcurve observations of tiny NEAs as Chapter 2 and phase curve study of tiny NEAs as Chapter 3. These additional observations are essential to validate that tiny asteroids have different surface properties from large asteroids. Although geometric albedos of more than a hundred tiny NEAs were investigated in a previous study using WISE satellite (Mainzer et al. 2014), authors caution that there might be observational biases since their targets were optically selected samples. A number of NEAs with albedo estimates by NEO Surveyor enable us to find new asteroid pairs as Chapter 4 in this dissertation. The LSST and NEO Surveyor might discover more and more Earth impactors than current survey projects such as CSS and Pan-STARRS. Quick response follow-up observations are key to give strong constraints on the interior structures of tiny asteroids such as material strength in a different context by telescopic observations. In addition, characterizations of sub-m class asteroids discovered by LSST and NEO Surveyor are important future works for the direct comparison of meteorite samples and asteroids without size effect. The LSST can discover MBAs as small as $\sim$ 100 m in diameter (Ivezić et al. 2019). A future comparison of tiny NEAs and tiny MBAs is essential to discuss the effects of space weathering and its refresh.

The thermal observations using space telescopes such as NEO Surveyor, SST, and JWST are the best in terms of sensitivity without atmospheric absorption, but the observing window and opportunity are very limited. For instance, Mommert et al. (2014b) detected the tiny asteroid 2011 MD ($D \sim 10$ m) with a flux density of 0.60 ± 0.27 μJy at 4.5 μm. They used a total of 19.9 hr of observation time with IRAC on SST when the target was 0.14 au from SST. With the advent of JWST, many small MBAs and NEAs will be (sometimes serendipitously) observed, whereas the observing window is limited due to the restriction of the space telescope. The University of Tokyo Atacama Observatory (TAO) 6.5 m telescope is under construction in the Atacama Desert in Chile (Yoshii et al. 2010). In conjunction with its mid-infrared instrument Mid Infrared Multi-field Imager for gaZing at the UnKnown Universe (MIMIZUKU, Miyata et al. 2010) and capability of quick response observations at a high altitude of 5640 m on the summit of Co. Chajnantor, TAO 6.5 m telescope could also be used to derive the geometric albedo of tiny NEAs. Actually, the TAO's predecessor, miniTAO, and mid-IR camera MAX38 were used to characterize the small NEA (308635) 2005 YU_{55} ($D \sim 300$ m) in the thermal wavelength during its close approach (Müller et al. 2013).

Beyond this dissertation The understanding of the dynamical evolution of asteroids needs their thermal properties such as thermal inertia and roughness. These properties are rarely reported for tiny asteroids to date. Thermal observations as introduced in the paragraphs above are essential to derive the thermal properties, which are fundamental to updating the various models such as Yarkovsky and YORP.

Recently, Bolin et al. (2024) showed that the rotation periods and color indices of tiny fast-rotating asteroids can be constrained with a combination of long exposure time observations and streak photometry. This implies that the physical properties of tiny asteroids are also characterized even with CCD cameras. The multi-epoch lightcurves of asteroids might be useful to examine their shapes, interior structures, sense of rotation, and dynamical histories. The detailed analysis such as shape modeling using multi-epoch lightcurves with lightcurve inversion technique (Kaasalainen & Torppa 2001) is also an important future work. As for shape modeling, the pole orientation is also a quantity changed by the YORP effect, but the pole orientations of tiny asteroids are derived only for two NEAs: (54509) YORP (Taylor et al. 2007) and 2021 DW_1 (Kwiatkowski et al. 2021). Kwiatkowski et al. (2021) made the shape model of the tiny NEA 2021 DW_1 from one apparition. Only by utilizing NEAs, we could derive a pole solution of tiny asteroids even from one or a few apparitions. The comparison of observed pole directions (i.e., shape models) and theoretical predictions will deepen our understanding of dynamical histories of NEAs.

Synergy with spacecraft missions The upcoming spacecraft mission will also enlarge our understanding of the nature of tiny NEAs. The ESA Hera mission will conduct in situ measurements of the NEA Didymos–Dimorphos system (Michel et al. 2022), where recently DART mission visited and performed an impact on Dimorphos (Rivkin et al. 2021). The detailed investigation of surface properties of small satellite Dimorphos ($D \sim 170$ m, Pravec et al. 2022) will expand our knowledge of the surface status of small asteroids. The Hayabusa2 extended mission, or Hayabusa2♯ (SHARP: Small Hazardous Asteroid Reconnaissance Probe, Hirabayashi et al. 2021; Kikuchi et al. 2023), will perform flyby observations of 2001 CC_{21} ($D \sim 500$ m, Geem et al. 2023) in 2026 and rendezvous with the tiny asteroid 1998 KY_{26} ($D \sim 30$ m, Ostro et al. 1999) in 2031. A detailed image of the tiny asteroid will come for the first time, and our knowledge of the properties of tiny asteroids will be expanded. The serendipitous discovery of the small satellite of Dinkinesh ($D \sim 790$ m), Selam ($D \sim 220$ m), is also a valuable target to study [1]. Other flyby missions such examples as the Demonstration and Experiment of Space Technology for INterplanetary voYage, Phaethon fLyby and dUst Science (DESTINY$^+$, Arai et al. 2018) and the OSIRIS–Apophis Explorer (OSIRIS-APEX, DellaGiustina et al. 2023) will be also valuable for comparative purposes.

In summary, this dissertation is one small step to unveil the formation mechanism, dynamical evolution, and surface properties as well as interior structures of NEAs, one giant leap for the community.

[1] https://www.nasa.gov/image-article/nasas-lucy-spacecraft-discovers-2nd-asteroid-during-dinkinesh-flyby/

Appendices

A. Brightness corrections

In the photometric analysis of asteroids, the correction of distances is performed using the ephemerides provided by such as NASA JPL HORIZONS[1] with a following equation:

$$H(\alpha) = m_{\rm app} - 2.5\log_{10}(\Delta r_h)^2, \tag{A.1}$$

where $H(\alpha)$ is a reduced magnitude at a phase angle of α and $m_{\rm app}$ is an apparent magnitude. The $H(\alpha)$ is the corrected brightness at 1 au from both the Sun and observer. This correction compensates for the difference in distances at the time of observations.

The light-travel time correction should be performed to obtain a corrected lightcurve:

$$t_{\rm light} = \frac{\Delta}{c}, \tag{A.2}$$

$$t_{\rm ltcor} = t_{\rm obs} - t_{\rm light}, \tag{A.3}$$

$$\tag{A.4}$$

where $t_{\rm light}$ is a light traveling time, c is the speed of light, $t_{\rm ltcor}$ is a corrected time, and $t_{\rm obs}$ is an observation time.

The phase angle correction is performed using a following equation (Bowell et al. 1989):

$$H_{\rm cor} = H(\alpha) + 2.5\log_{10}\left[(1-G)\Phi_1(\alpha) + G\Phi_2(\alpha)\right], \tag{A.5}$$

where G is a slope parameter in the H-G model. Φ_1 and Φ_2 are magnitude phase functions (see the Appendix B). The G is an unknown parameter for a newly discovered asteroid, and conventionally G is assumed to be 0.15. It is known that the G parameter depends on the spectral type of the asteroid, and it is estimated by fitting observed magnitudes to Equation A.5 when the observations of a single asteroid at different phase angles are performed. This correction compensates for the difference in phase angles at the time of observations. The three parameter H-G_1-G_2 model is also proposed (Muinonen et al. 2010).

[1] https://ssd.jpl.nasa.gov/horizons

B. Phase curve models

Observationally, a tight correlation between the geometric albedo and slope of the photometric phase curve is seen, and this indicates that the geometric albedo plays a dominant role in the phase angle dependence of the brightness (Belskaya & Shevchenko 2000). In this appendix, we summarize two traditional phase curve models with phase functions, the H-G model and H-G_1-G_2 model.

H-G model In the H-G model, the phase angle dependence of the magnitude is expressed as follows (Bowell et al. 1989):

$$H(\alpha) = H - 2.5\log_{10}\left[(1-G)\Phi_1(\alpha) + G\Phi_2(\alpha)\right], \tag{B.1}$$

where H is an absolute magnitude and G is a slope parameter in the H-G model. Φ_1 and Φ_2 are magnitude phase functions written as follows with a basic function W:

$$\Phi_1(\alpha) = W\left(1 - \frac{0.986\sin\alpha}{0.119 + 1.341\sin\alpha - 0.754\sin^2\alpha}\right) + (1-W)\exp\left(-3.332\tan^{0.631}\frac{\alpha}{2}\right), \tag{B.2}$$

$$\Phi_2(\alpha) = W\left(1 - \frac{0.238\sin\alpha}{0.119 + 1.341\sin\alpha - 0.754\sin^2\alpha}\right) + (1-W)\exp\left(-1.862\tan^{1.218}\frac{\alpha}{2}\right), \tag{B.3}$$

$$W = \exp\left(-90.56\tan^2\frac{\alpha}{2}\right). \tag{B.4}$$

We present the phase functions $\Phi_1(\alpha)$ and $\Phi_2(\alpha)$ in upper left panel of Figure B.1. The magnitude phase curves with various G parameters are presented in lower left panel of Figure B.1.

H-G_1-G_2 model In the H-G_1-G_2 model, the phase angle dependence of the magnitude is expressed as follows (Muinonen et al. 2010):

$$H(\alpha) = H' - 2.5\log_{10}\left[G_1\Phi_1'(\alpha) + G_2\Phi_2'(\alpha) + (1-G_1-G_2)\Phi_3'(\alpha)\right], \tag{B.5}$$

where H' is an absolute magnitude in the H-G_1-G_2 model. G_1 and G_2 are slope parameters in the H-G_1-G_2 model. The $\Phi_1'(\alpha)$, $\Phi_2'(\alpha)$, and $\Phi_3'(\alpha)$ are phase functions written as follows:

$$\Phi_1'(\alpha) = 1 - \frac{6\alpha}{\pi}, \tag{B.6}$$

$$\Phi_2'(\alpha) = 1 - \frac{9\alpha}{5\pi}, \tag{B.7}$$

$$\Phi_3'(\alpha) = \exp\left(-4\pi\tan^{2/3}\frac{\alpha}{2}\right). \tag{B.8}$$

We present the phase functions $\Phi_1'(\alpha)$, $\Phi_2'(\alpha)$, and $\Phi_3'(\alpha)$ in upper right panel of Figure B.1. The magnitude phase curves with various G_1 and G_2 values with fixed G_3 of 0.2 are presented in lower right panel of Figure B.1.

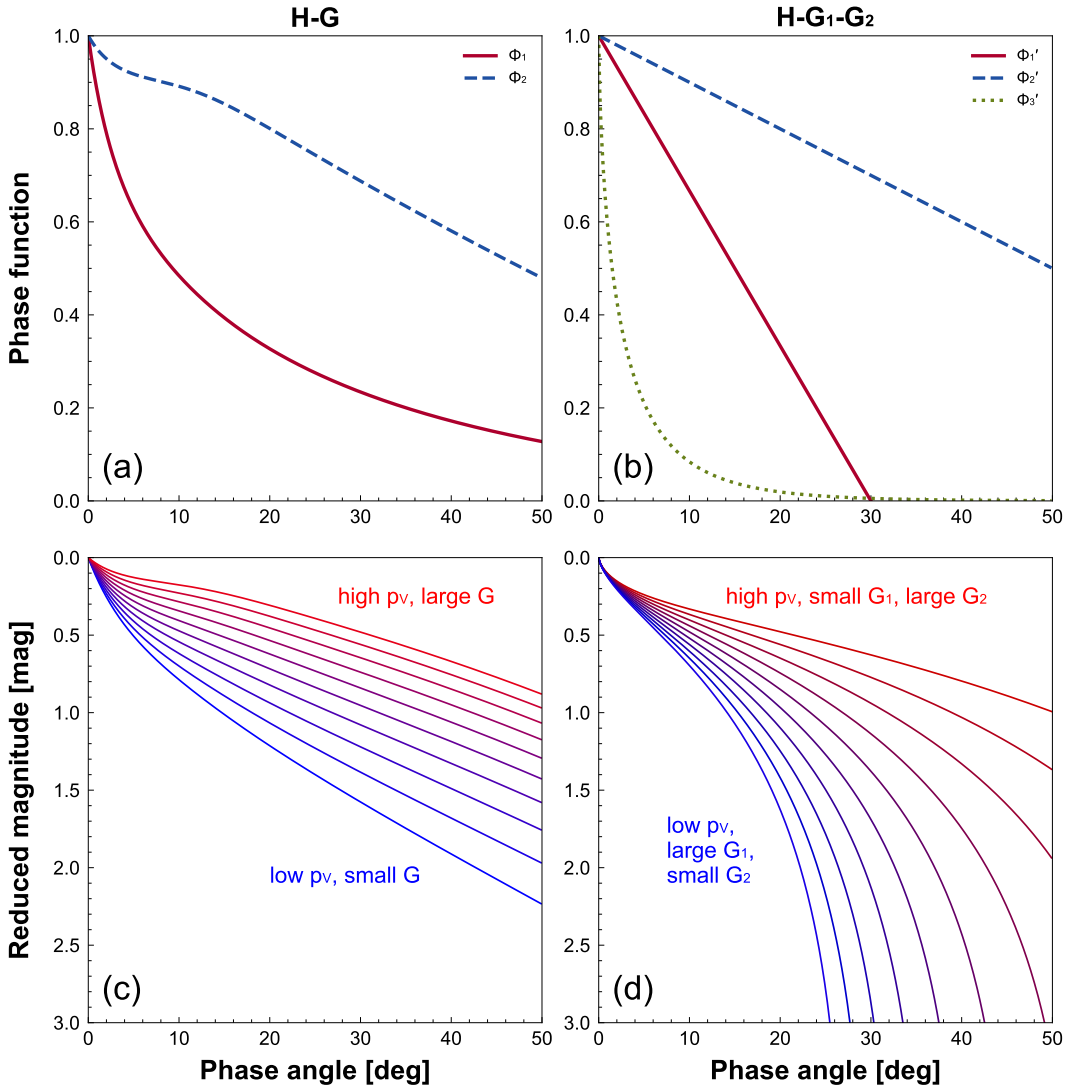

Figure B.1. Phase functions and phase angle dependence of reduced magnitude of the H-G model and H-G_1-G_2 model. (a) Phase functions of H-G model. (b) Phase functions of H-G_1-G_2 model. (c) Phase angle dependence of reduced magnitude of H-G model. Phase curves with various G parameters from 0 to 1 with a step size of 0.1 are shown. (d) Phase angle dependence of reduced magnitude of H-G_1-G_2 model. Phase curves with various G_1 parameters from 0 to 1 with a step size of 0.1 fixing G_3 as 0.2 are shown.

C. *Light curves, periodograms, and phased light curves (Beniyama et al. 2022)*

Light curves, Lomb-Scargle periodograms, and phased light curves of the Tomo-e NEOs are presented in Figures (C.1)–(C.3).

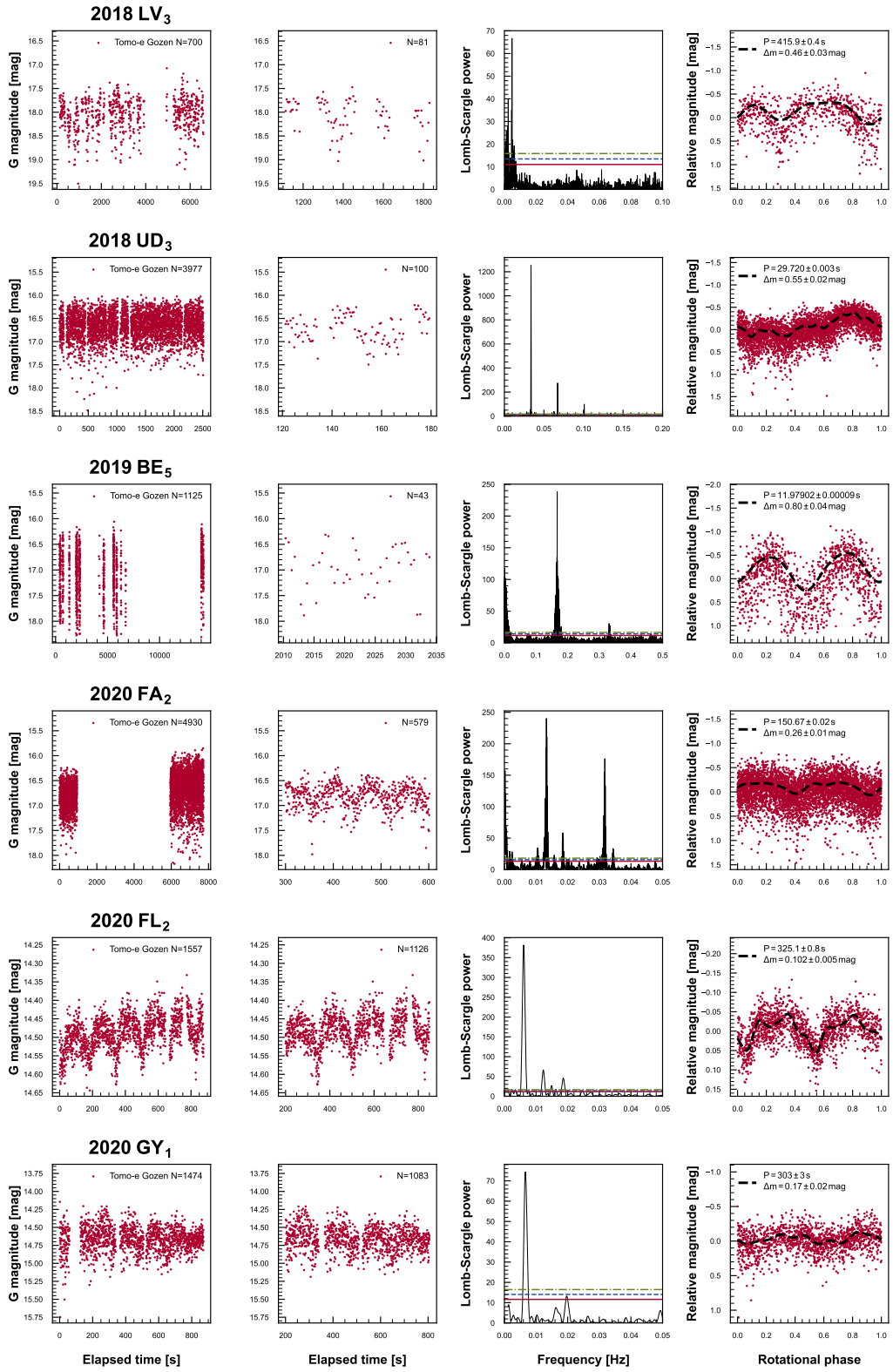

Figure C.1. From left to right, full light curves from the exposure starting time, partial light curves, Lomb-Scargle periodograms with n of 1, and phased light curves of the NEOs whose rotation periods are dirived with high reliability. Solid, dashed, and dot-dashed horizontal lines in the periodograms show 90.0, 99.0, and 99.9 % confidence levels, respectively. Confidence lines of some NEOs with strong peaks are hard to see due to scale effects. Dashed lines in the phased light curves show the model curves. Twice the rotation periods are adopted as time ranges of the partial light curves.

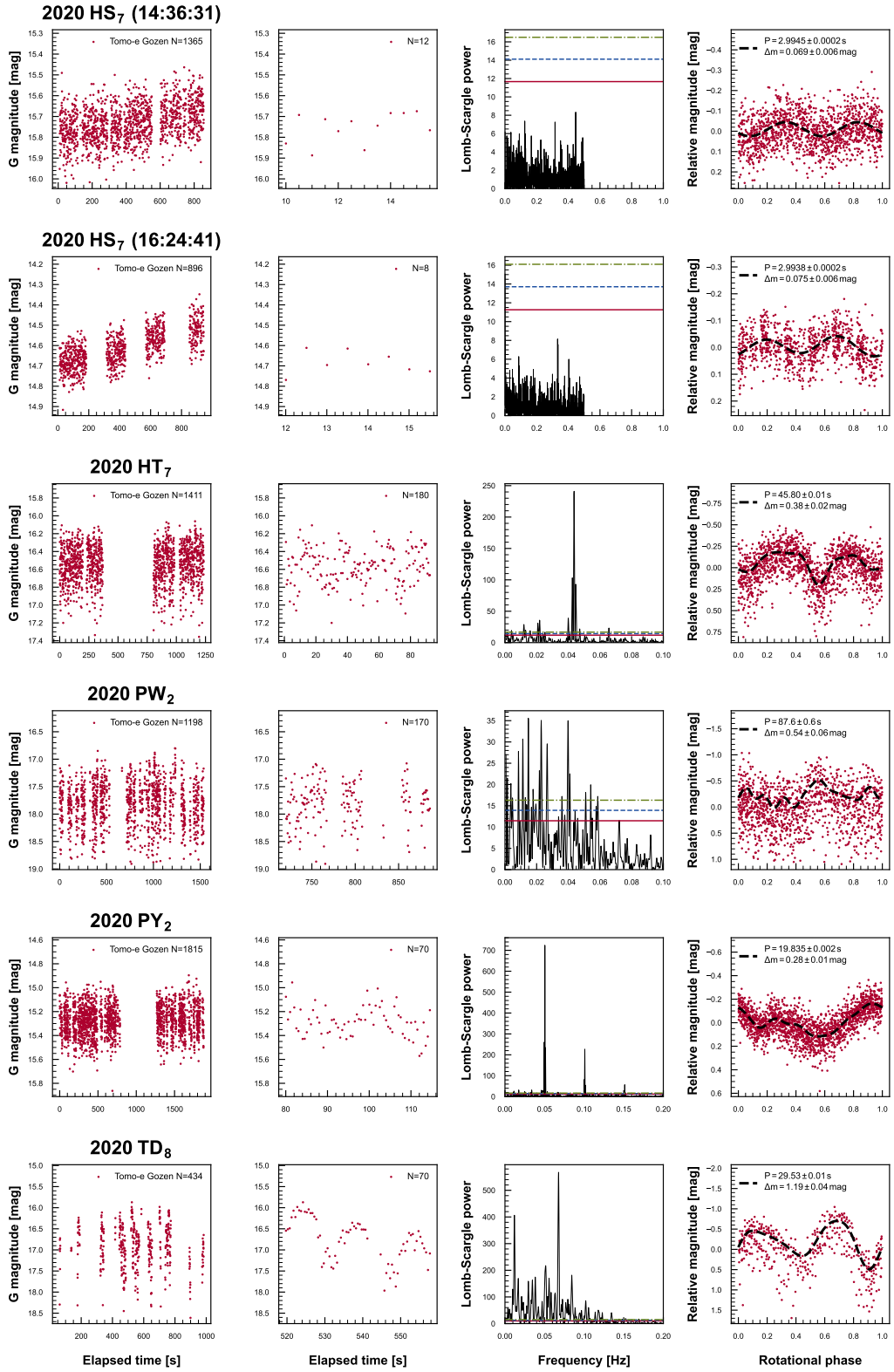

Figure C.1. (Continued)

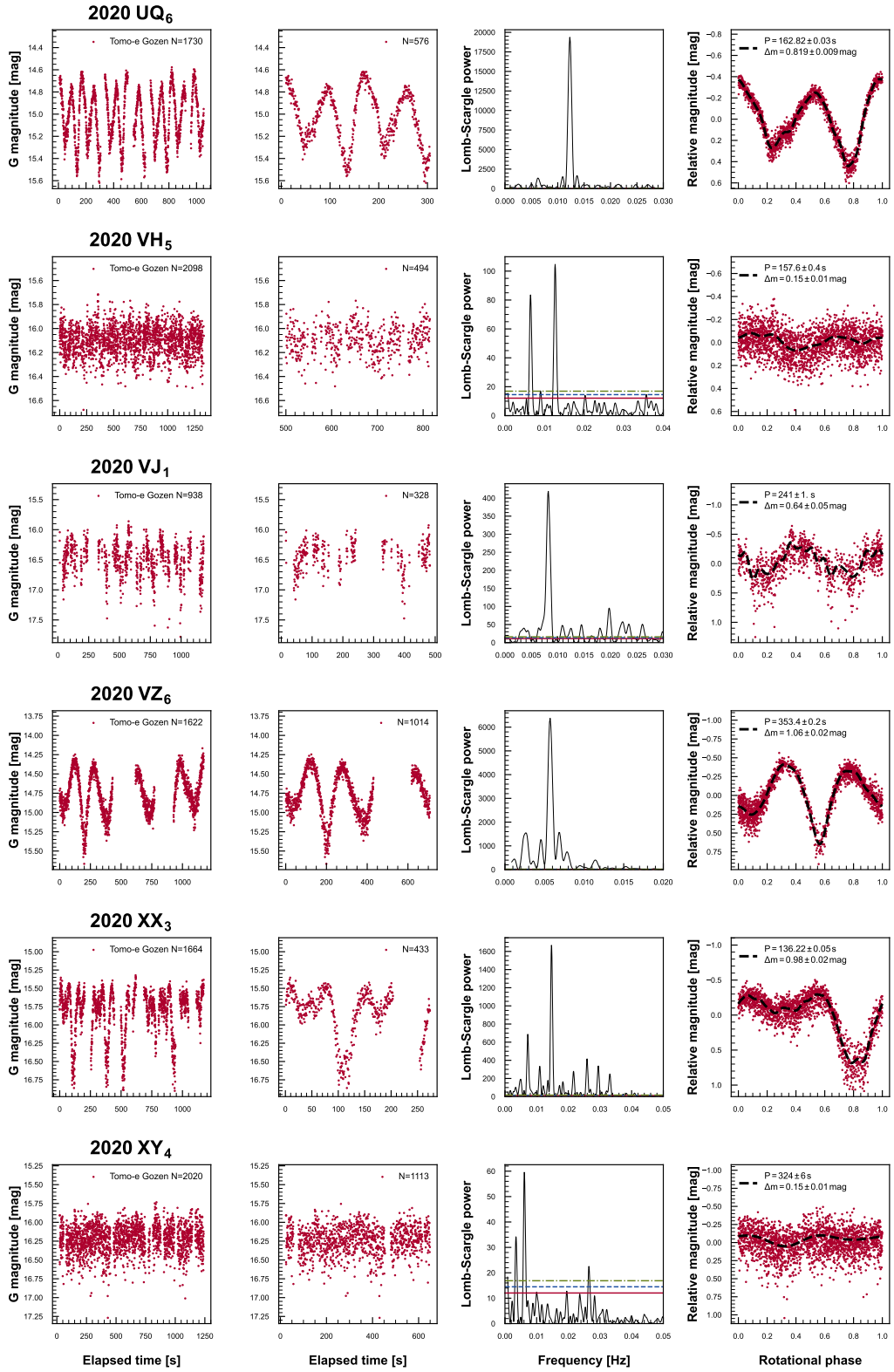

Figure C.1. (Continued)

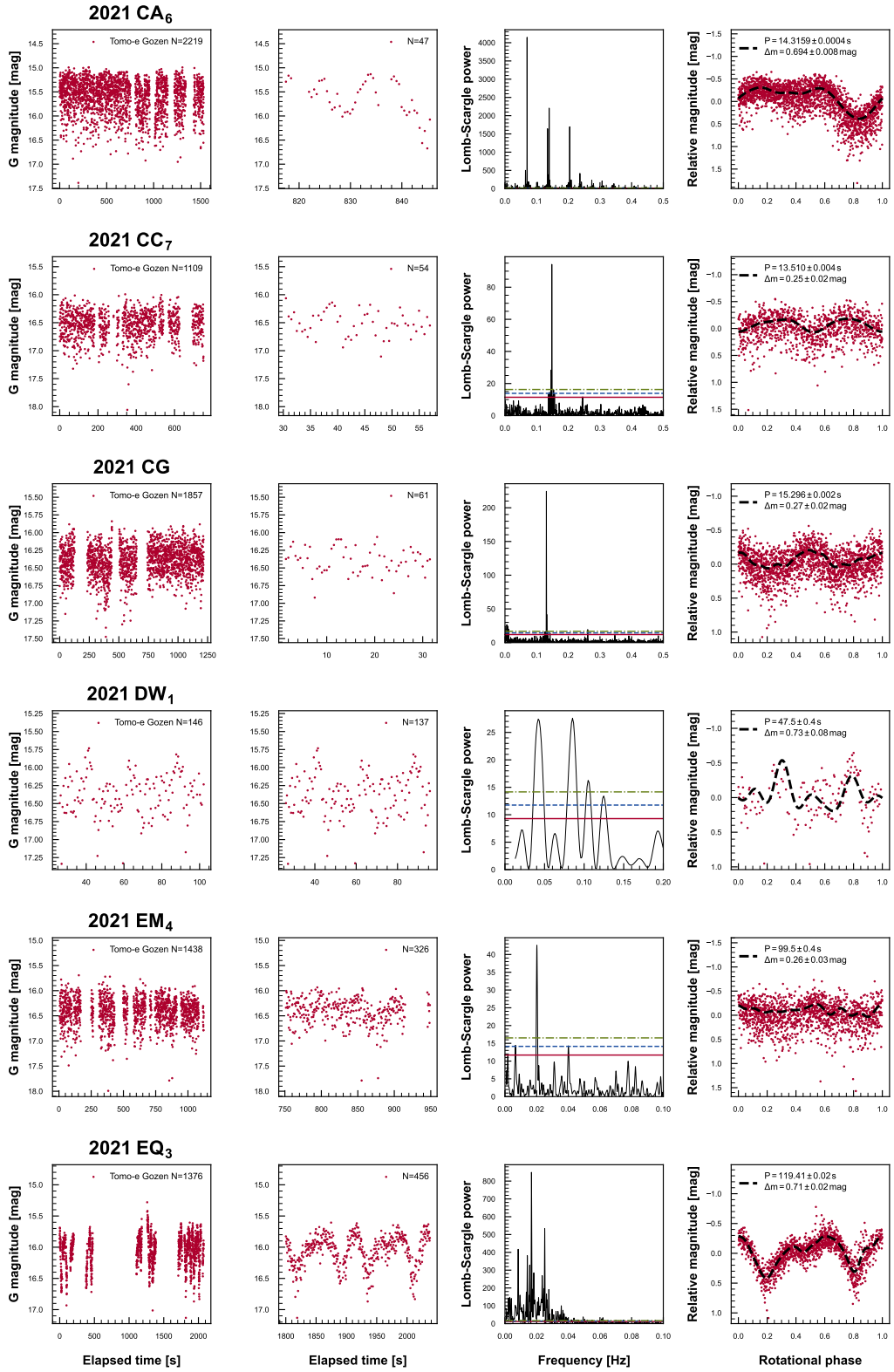

Figure C.1. (Continued)

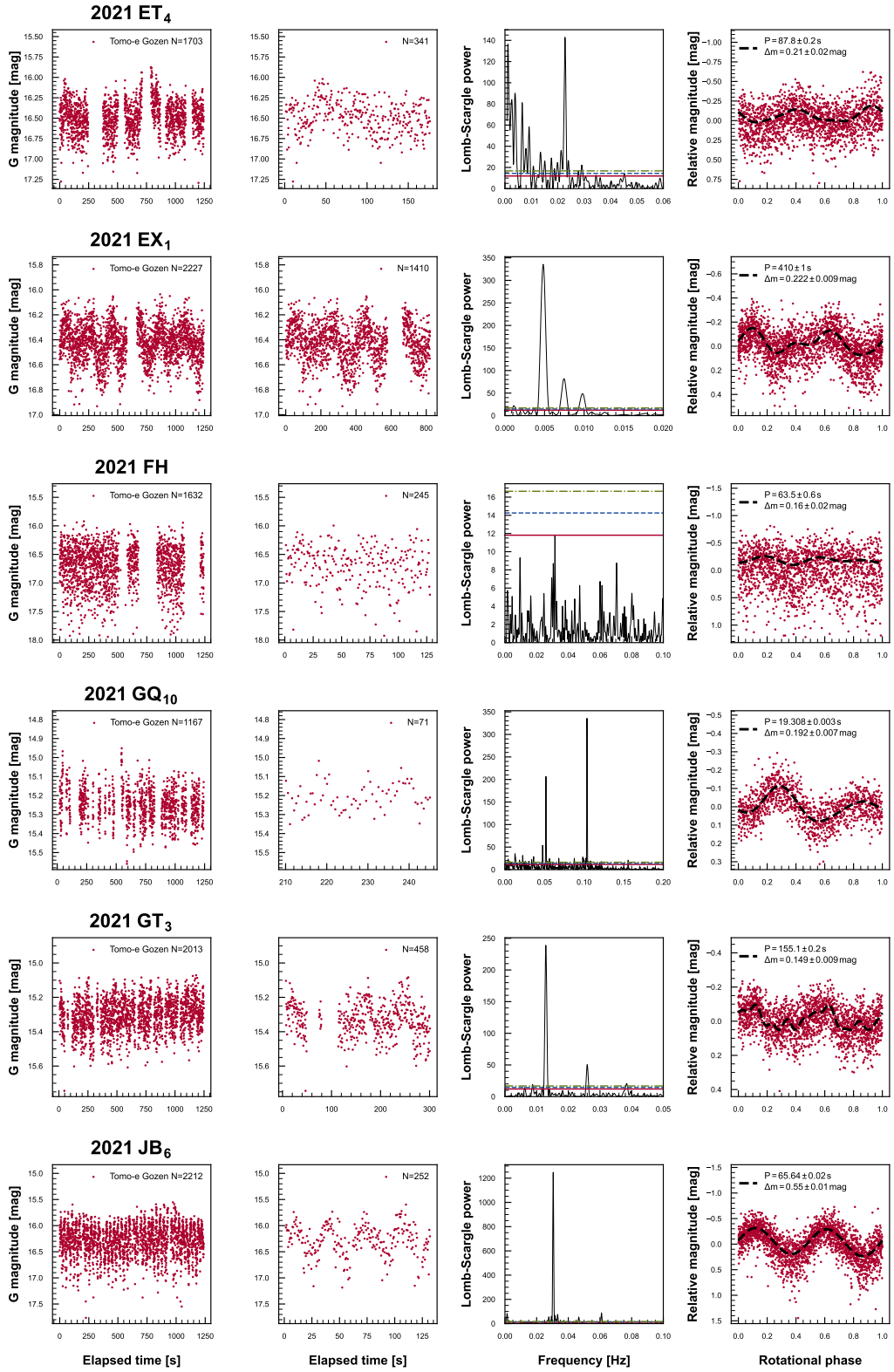

Figure C.1. (Continued)

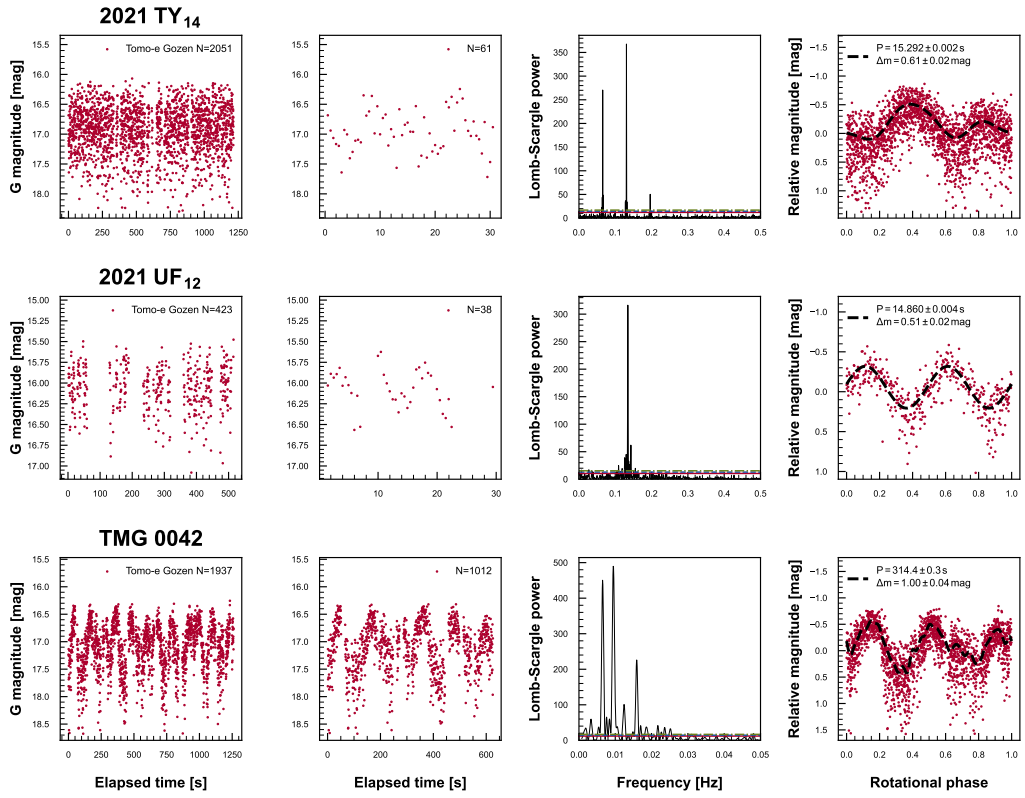

Figure C.1. (Continued)

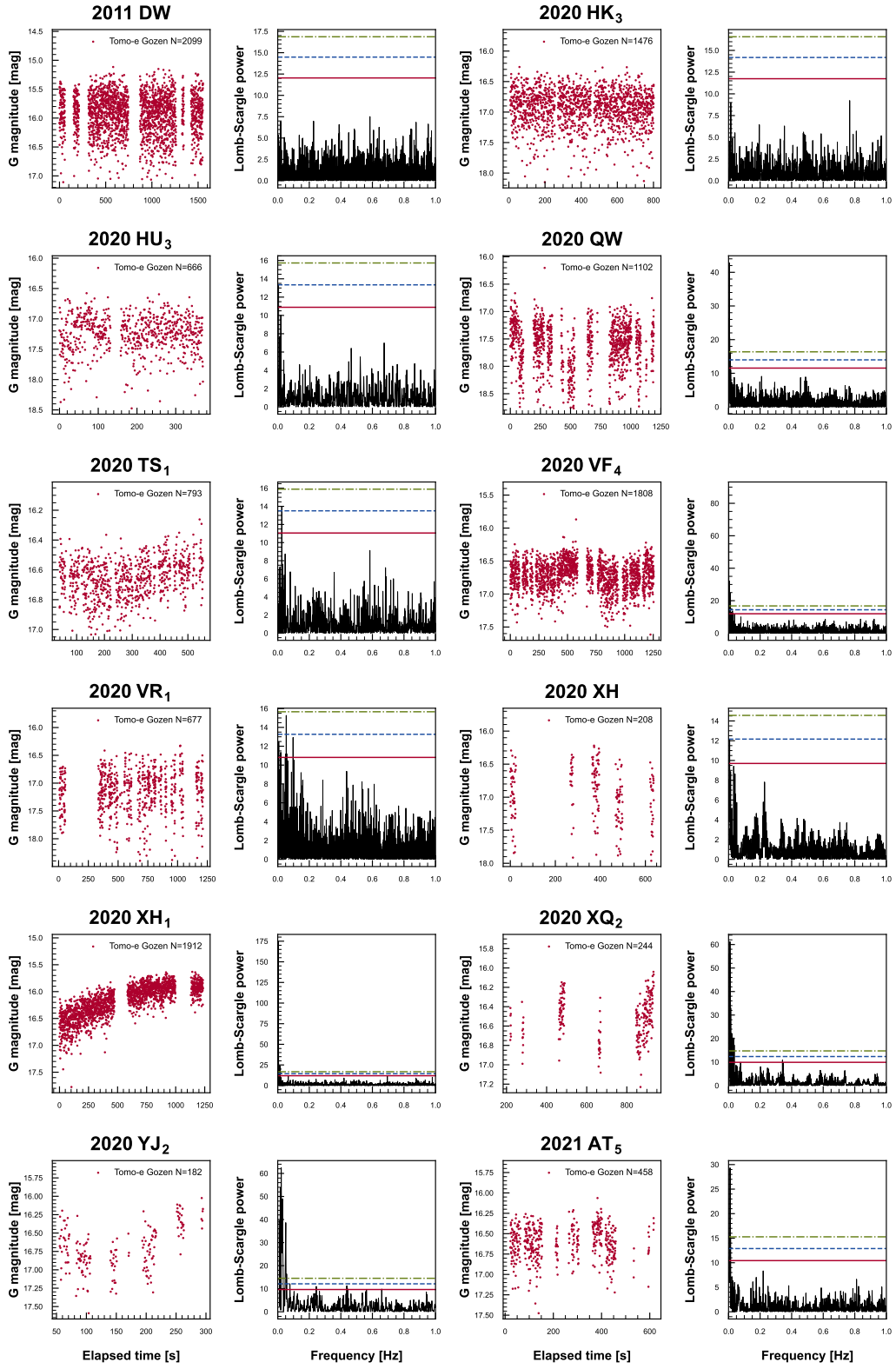

Figure C.2. Full light curves and Lomb-Scargle periodograms of the NEOs whose rotation periods are not derived. The same as the left 2 columns in Figure C.1.

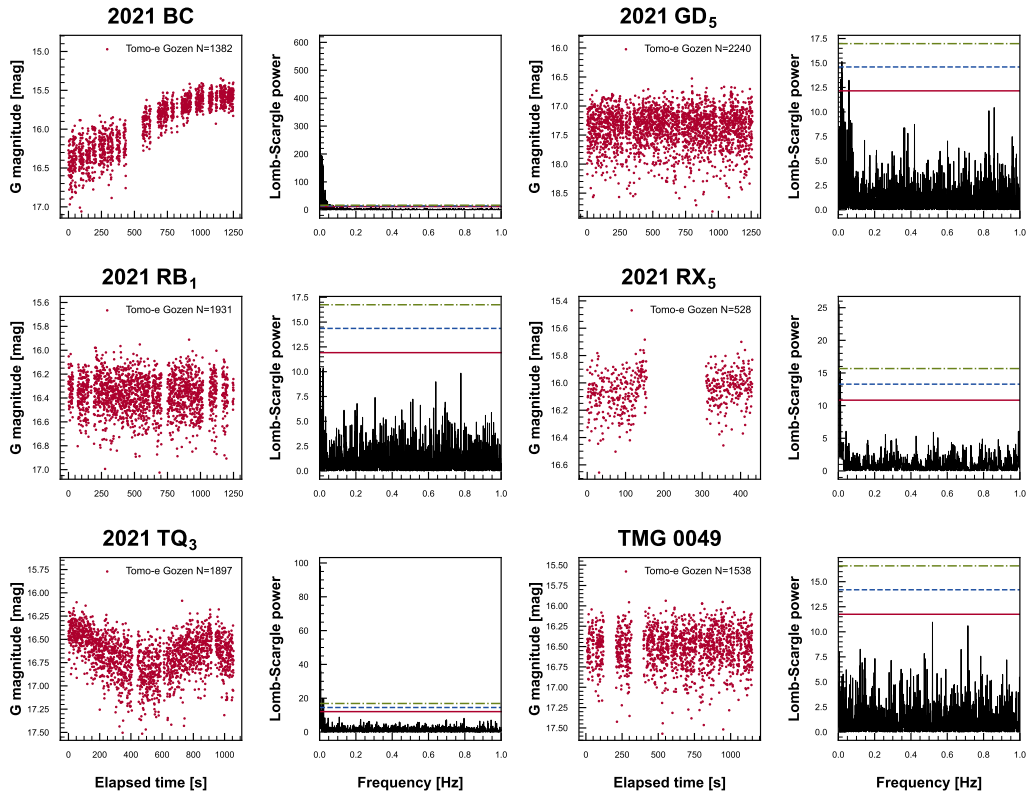

Figure C.2. (Continued)

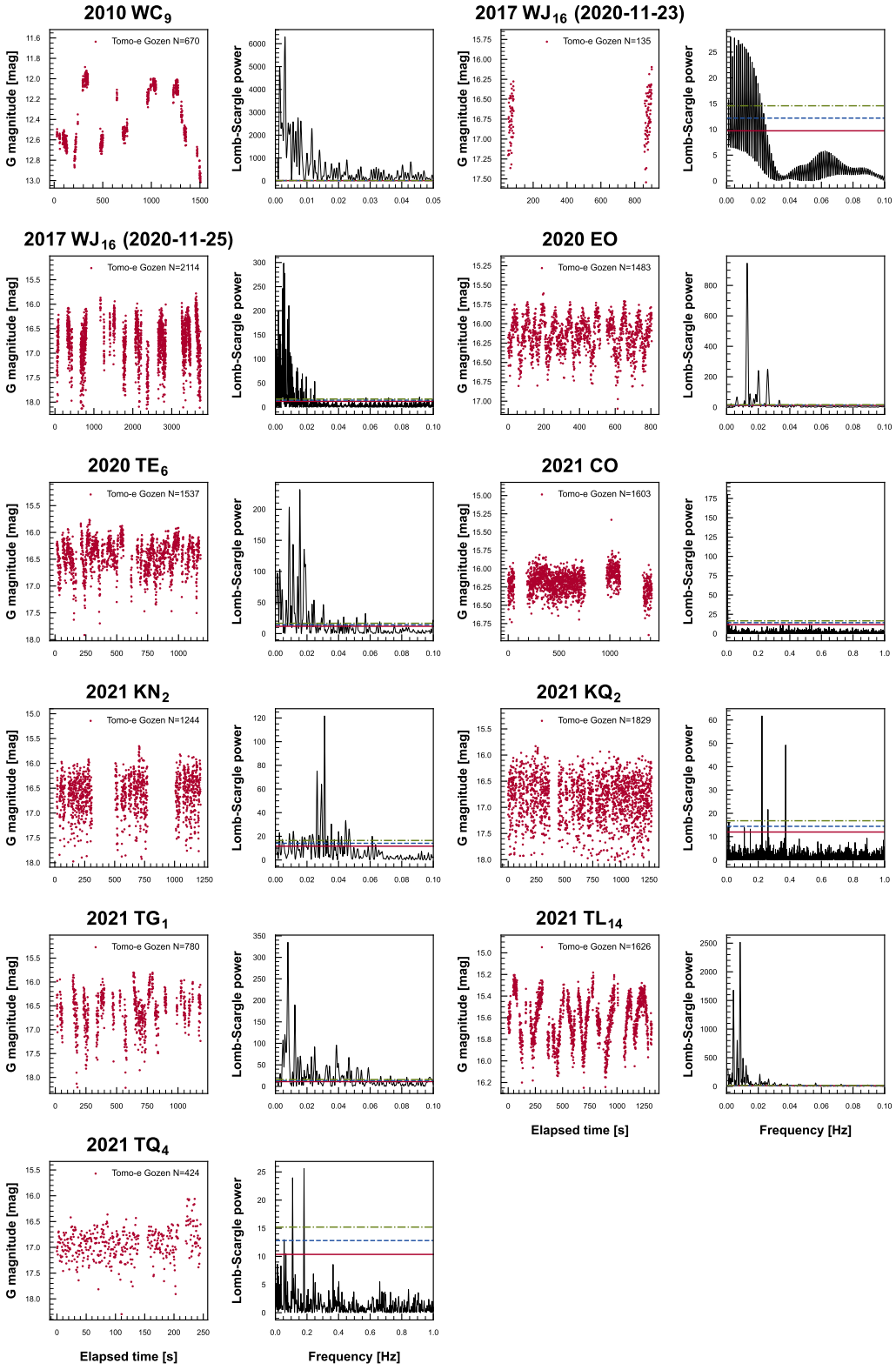

Figure C.3. Full light curves and Lomb-Scargle periodograms of the tumbler candidates. The same as the left 2 columns in Figure C.1.

D. Light curves, periodograms, and phased light curves (Beniyama et al. in prep.)

Light curves, Lomb-Scargle periodograms, and phased light curves of the Tomo-e NEOs are presented in Figures (D.1)–(D.3).

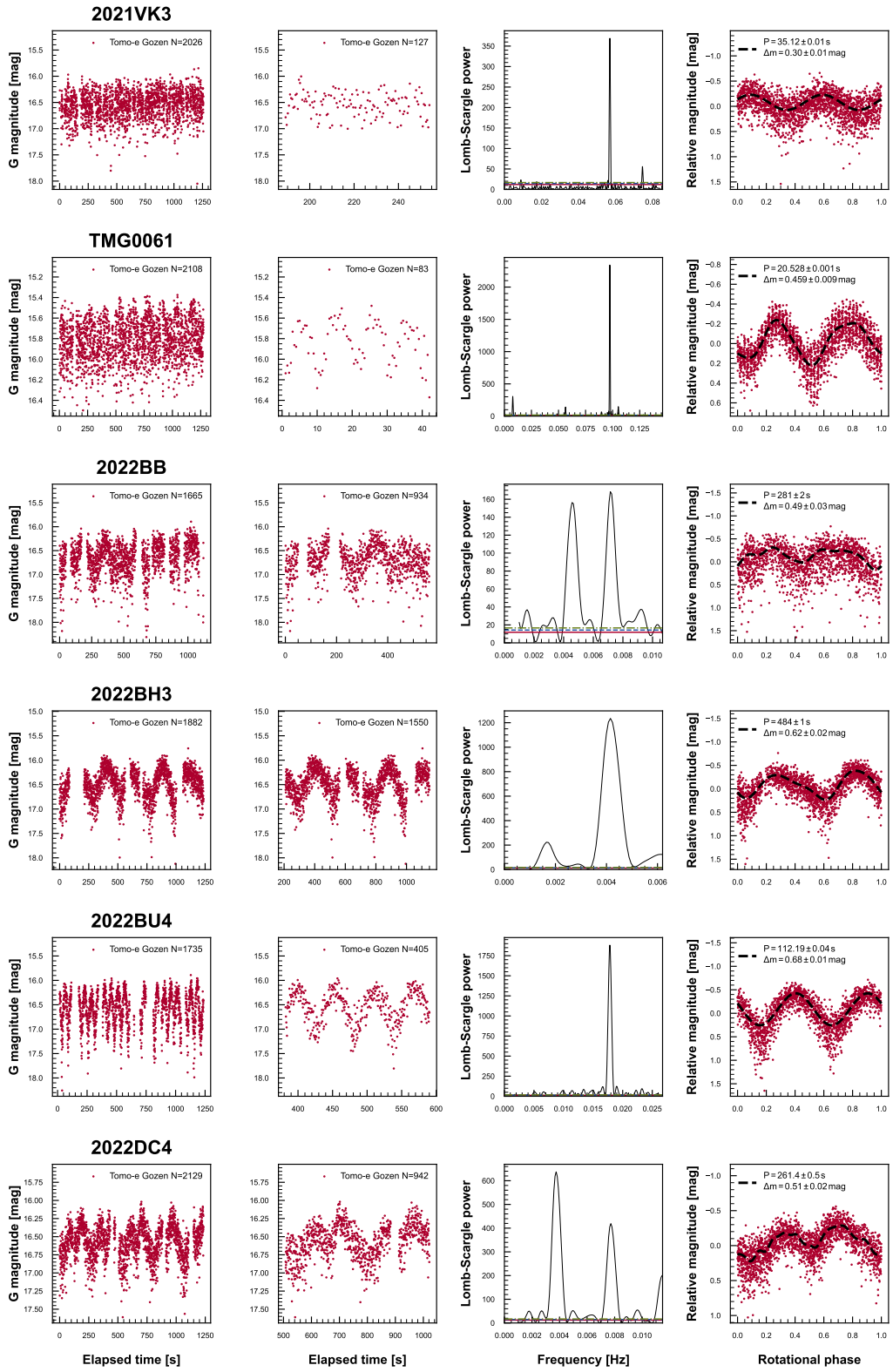

Figure D.1. From left to right, full light curves from the exposure starting time, partial light curves, Lomb-Scargle periodograms with n of 1, and phased light curves of the NEOs whose rotation periods are dirived with high reliability. Solid, dashed, and dot-dashed horizontal lines in the periodograms show 90.0, 99.0, and 99.9 % confidence levels, respectively. Confidence lines of some NEOs with strong peaks are hard to see due to scale effects. Dashed lines in the phased light curves show the model curves. Twice the rotation periods are adopted as time ranges of the partial light curves.

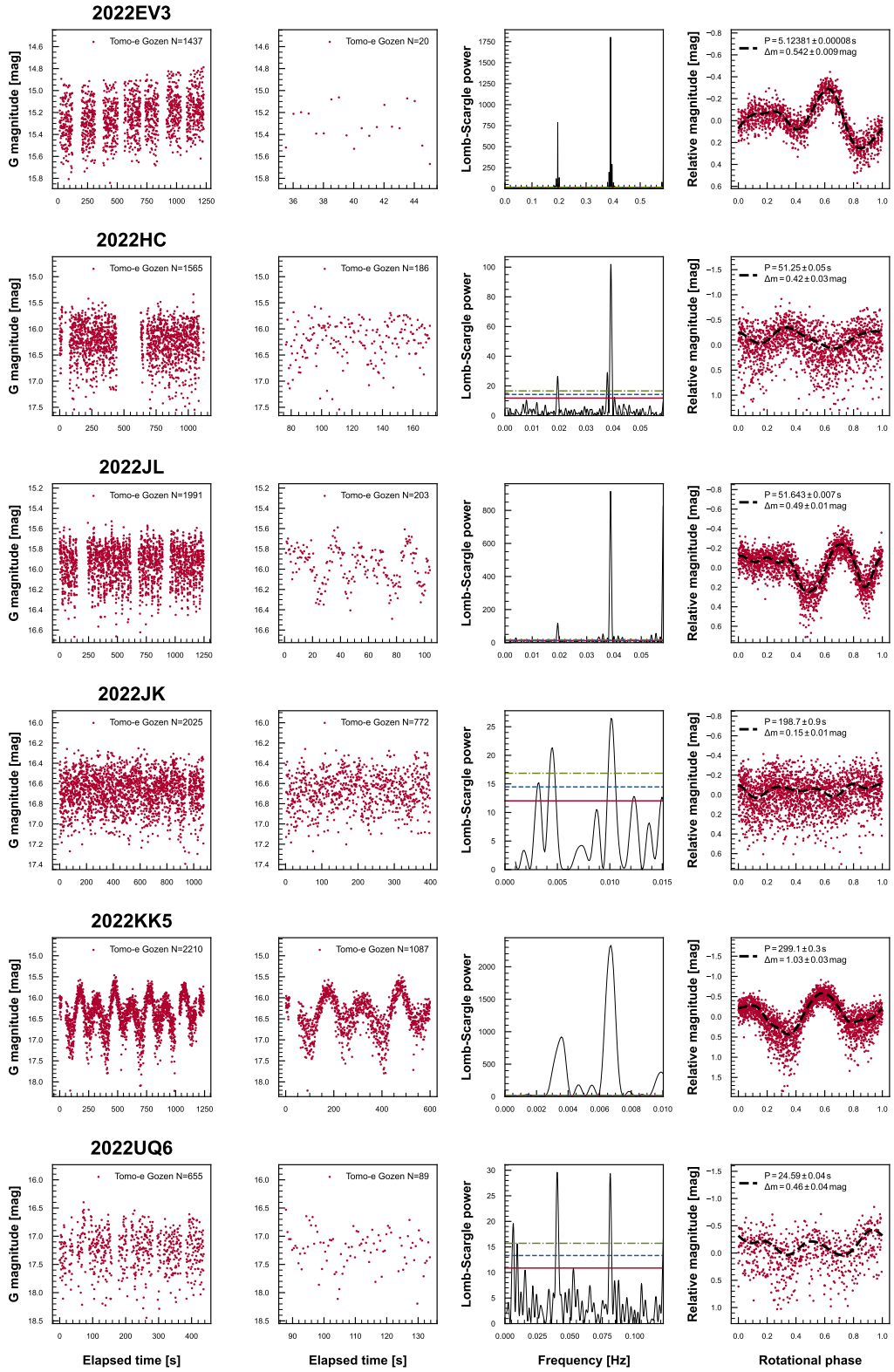

Figure D.1. (Continued)

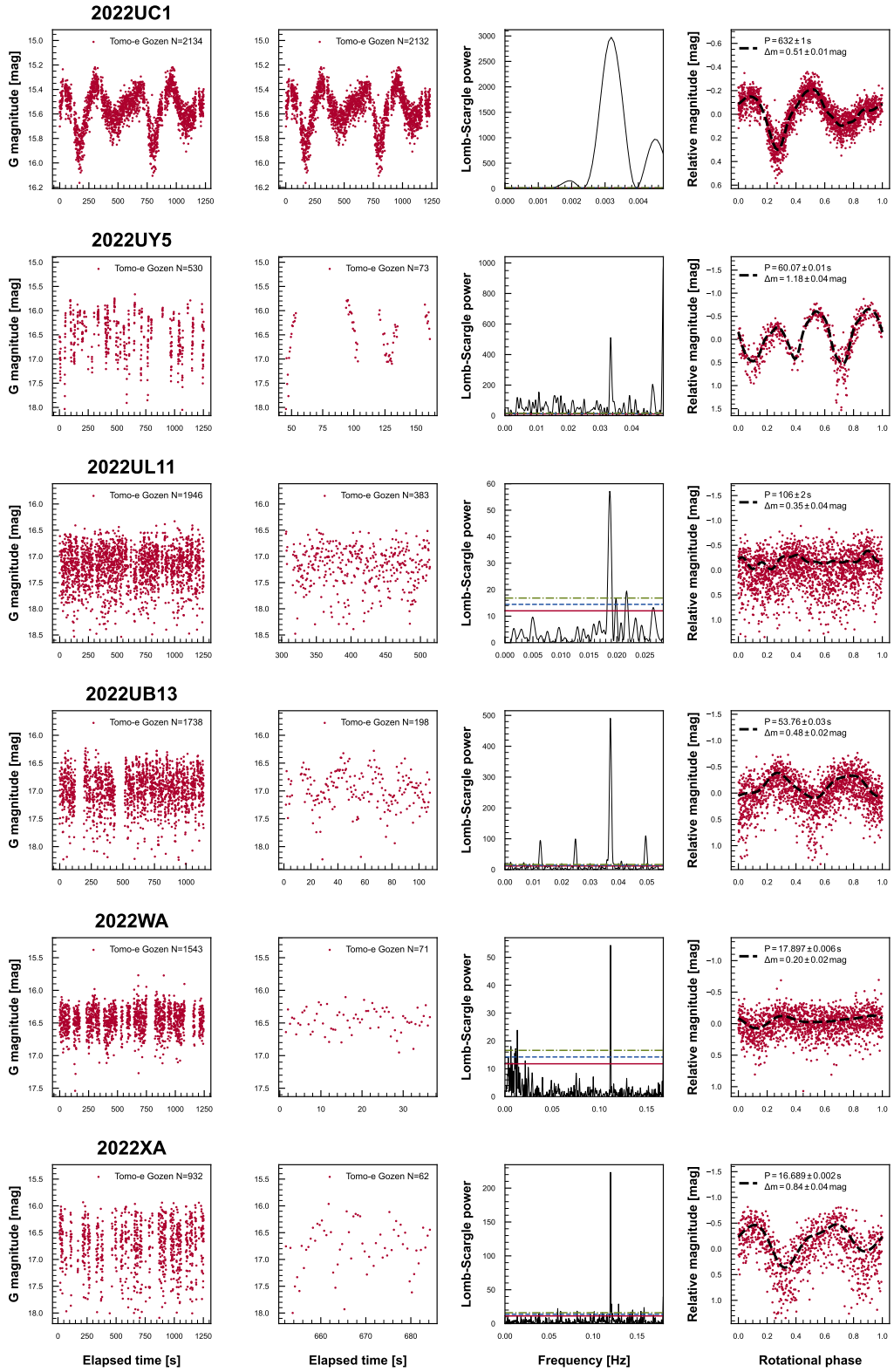

Figure D.1. (Continued)

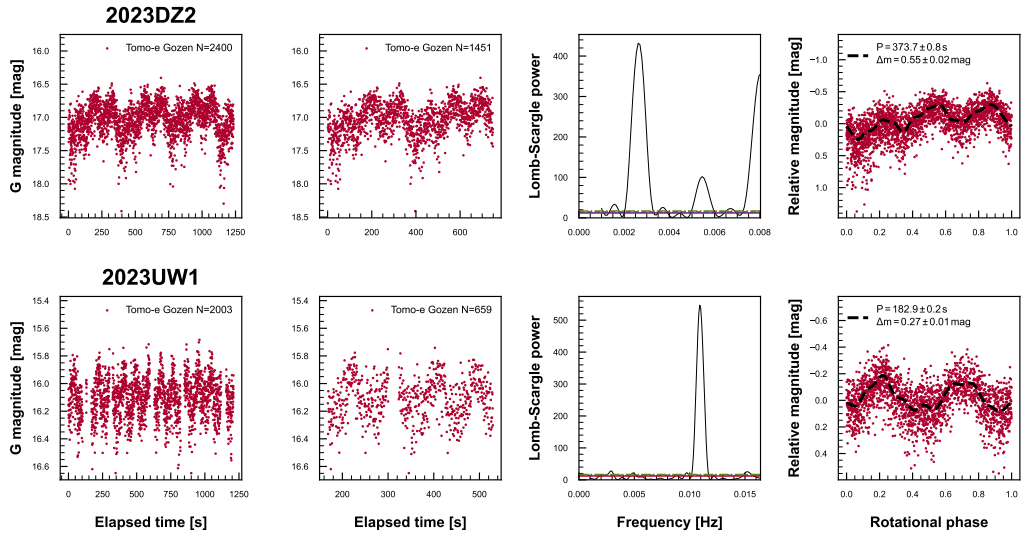

Figure D.1. (Continued)

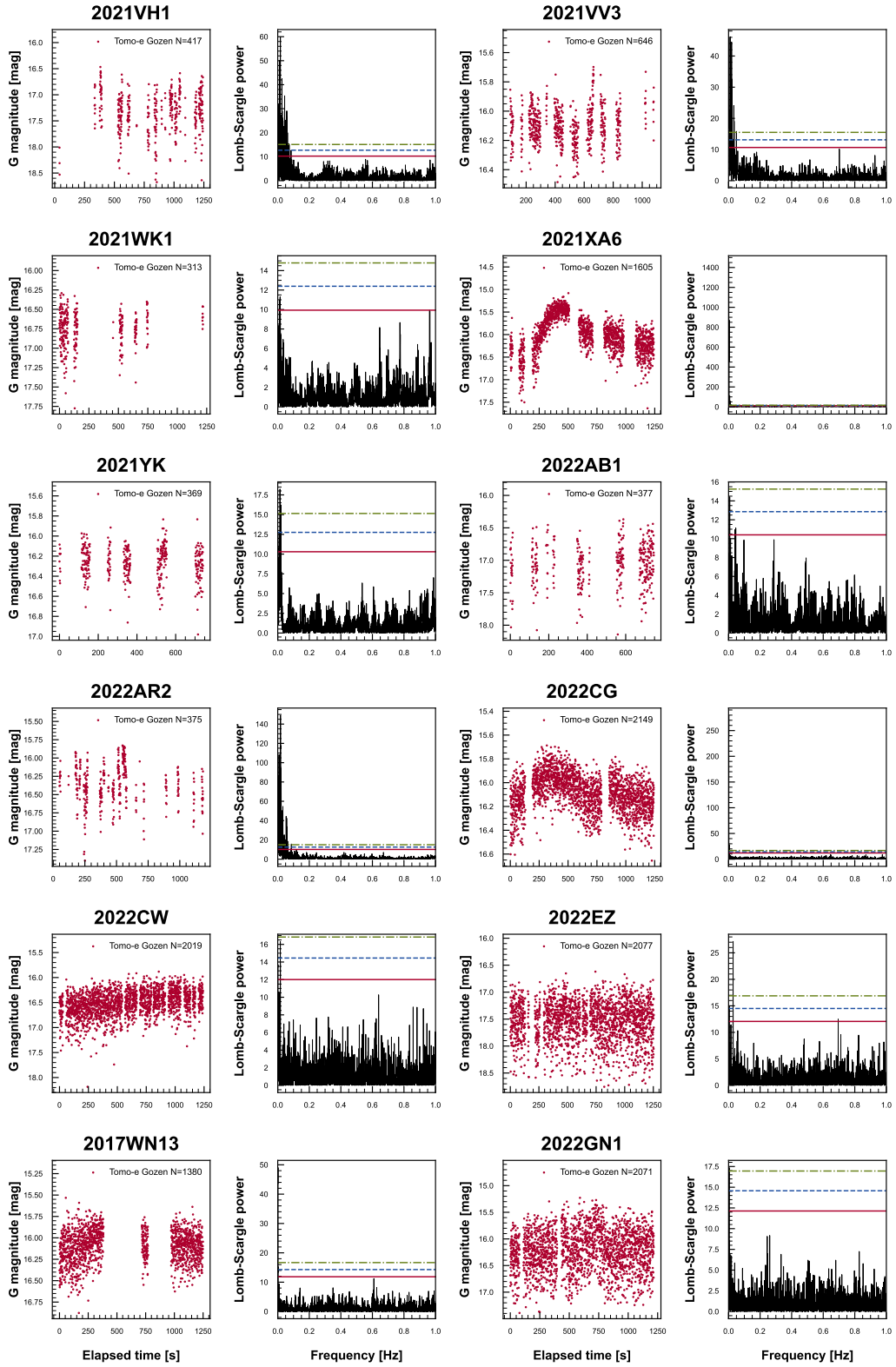

Figure D.2. Full light curves and Lomb-Scargle periodograms of the NEOs whose rotation periods are not derived. The same as the left 2 columns in Figure D.1.

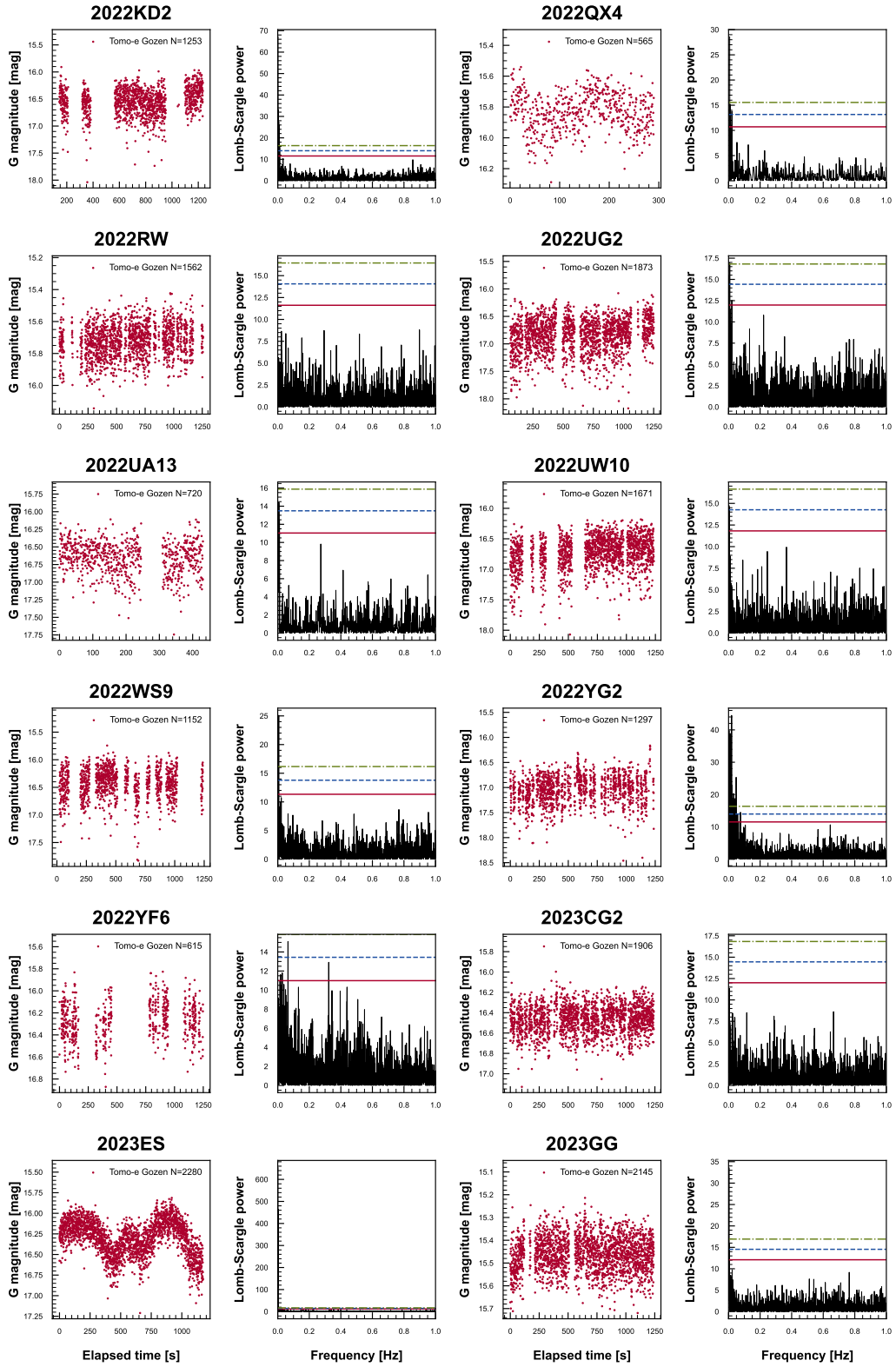

Figure D.2. (Continued)

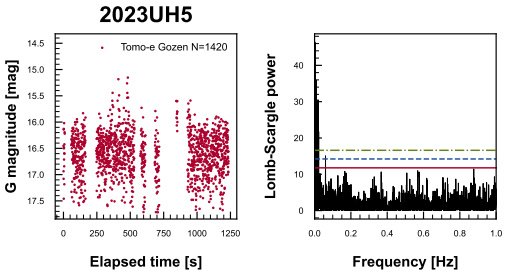

Figure D.2. (Continued)

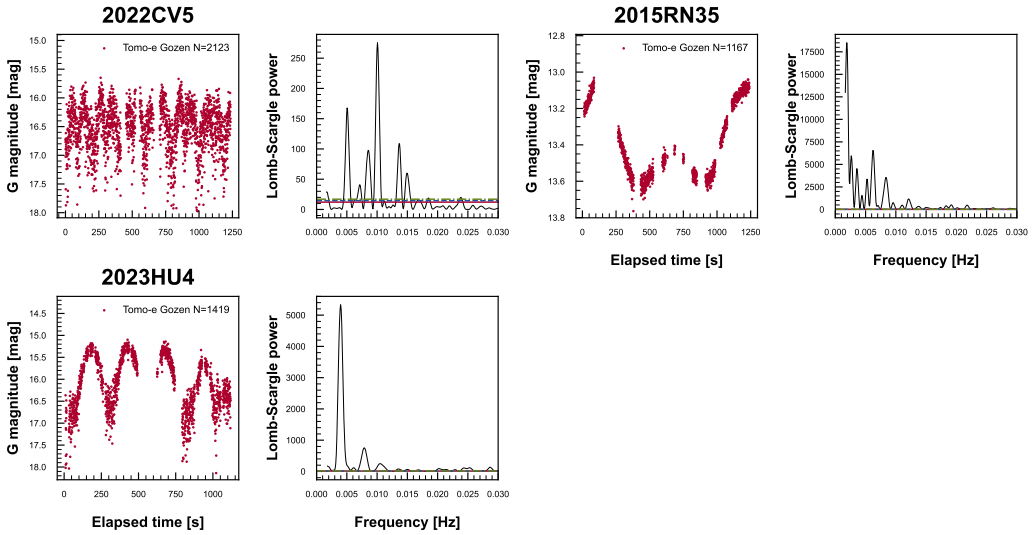

Figure D.3. Full light curves and Lomb-Scargle periodograms of the tumbler candidates. The same as the left 2 columns in Figure D.1.

E. Estimation of required cohesion

We estimate the required cohesion to keep asteroids from breaking apart following the previous works (Holsapple 2004, 2007). We use the Drucker-Prager model, which assumes that the shear stress is dependent linearly on the confining pressure (i.e., the cohesion is defined as shear strength at zero pressure). The pressure, p, is expressed with the three principal stresses, σ_1, σ_2, and σ_3, as follows:

$$p = \frac{\sigma_1 + \sigma_2 + \sigma_3}{3}. \tag{E.1}$$

The second invariant, J_2, is expressed as follows:

$$\sqrt{J_2} = \sqrt{\frac{(\sigma_1 - \sigma_2)^2 + (\sigma_2 - \sigma_3)^2 + (\sigma_3 - \sigma_1)^2}{6}}. \tag{E.2}$$

Then the Drucker–Prager failure criterion is given as follows:

$$\sqrt{J_2} < k - 3sp, \tag{E.3}$$

where k is a cohesion and s is a friction coefficient. The s is calculated as follows:

$$s = \frac{2\sin(\phi)}{\sqrt{3}(3 - \sin(\phi))}, \tag{E.4}$$

where ϕ is an angle of friction. We assume the asteroid is a triaxial ellipsoid with axial lengths of a, b, and c ($a > b > c$). For an ellipsoidal spinning body with self-gravity, the average of shear stress is exactly zero, and the normal stress components are, using a simpler notation, determined to be explicitly and simply given as follows (Holsapple 2004):

$$\sigma_x = \frac{(\rho\omega^2 - 2\pi\rho^2 G A_x)a^2}{5}, \tag{E.5}$$

$$\sigma_y = \frac{(\rho\omega^2 - 2\pi\rho^2 G A_y)b^2}{5}, \tag{E.6}$$

$$\sigma_z = \frac{(-2\pi\rho^2 G A_z)c^2}{5}, \tag{E.7}$$

where ρ is mass density, ω is an angular velocity of a body, G is the gravitational constant. Non-dimentional Shape related parameters, A_x, A_y, and A_z, are calculated as follows:

$$A_x = \alpha\beta \int \frac{1}{(x+1)^{3/2}(x+\beta^2)^{1/2}(x+\alpha^2)^{1/2}} dx, \tag{E.8}$$

$$A_y = \alpha\beta \int \frac{1}{(x+1)^{1/2}(x+\beta^2)^{3/2}(x+\alpha^2)^{1/2}} dx, \tag{E.9}$$

$$A_z = \alpha\beta \int \frac{1}{(x+1)^{1/2}(x+\beta^2)^{1/2}(x+\alpha^2)^{3/2}} dx, \tag{E.10}$$

where $\alpha = c/a$ and $\beta = b/a$. Throughout this paper, we adopt $\alpha = \beta = 1$, or $a = b = c$, and $\phi = 40°$ (Richardson et al. 2005). The spherical assumption means the derived required cohesions are minimum values. We numerically solved Equation E.4 for k using the `Python` package `SymPy` (Meurer et al. 2017), and derived the required cohesive strength.

F. Color and magnitude derivation

The contents of this appendix have been published in Beniyama et al. (2023c).

Derivation of colors Simultaneous multicolor observations are a reliable method to measure the accurate colors of asteroids. We derived the Phaethon's surface colors in the slightly different manner in Jackson et al. (2021)[1]. We used the linear relationship between instrumental colors and colors in the Pan-STARRS system as follows:

$$(g-r)^n_{\mathrm{PS},m} = \mathrm{CTG}_{g-r}(g-r)^n_{\mathrm{inst},m} + \mathrm{CTI}^n_{g-r}, \tag{F.1}$$
$$(r-i)^n_{\mathrm{PS},m} = \mathrm{CTG}_{r-i}(r-i)^n_{\mathrm{inst},m} + \mathrm{CTI}^n_{r-i}, \tag{F.2}$$

where m is the index of the object, n is the index of the frame, $(g-r)^n_{\mathrm{inst},m}$ and $(r-i)^n_{\mathrm{inst},m}$ are instrumental colors of m-th object on the n-th frame, CTG_{g-r} and CTG_{r-i} are color transformation gradients (CTGs) of the $g-r$ and $r-i$ colors, respectively, and CTI^n_{g-r} and CTI^n_{r-i} are color transformation intercepts (CTIs) of the $g-r$ and $r-i$ colors on the n-th frame, respectively. First, we derived the CTGs at the night by the linear fitting of the photometric results of the reference stars during the night. To determine the unique CTGs at the night, the photometric results were shifted frame by frame to cancel out the atmospheric variations in CTIs. After the derivation of CTGs, the CTIs in each frame were calculated with the derived CTGs with Equations F.1 and F.2. Phaethon's colors were derived from the instrumental colors, fixed CTGs, and CTIs. We computed the propagated uncertainties of $(g-r)_{\mathrm{PS}}$ and $(r-i)_{\mathrm{PS}}$ with the photometric errors and uncertainties of the CTGs and CTIs.

Derivation of magnitudes The same as color derivations, we used the linear relationship to derive the magnitudes as follows:

$$g^n_m = g^n_{\mathrm{inst},m} + \mathrm{CT}_g(g-r)^n_{\mathrm{PS},m} + \mathrm{Z}^n_g, \tag{F.3}$$
$$r^n_m = r^n_{\mathrm{inst},m} + \mathrm{CT}_r(g-r)^n_{\mathrm{PS},m} + \mathrm{Z}^n_r, \tag{F.4}$$
$$i^n_m = i^n_{\mathrm{inst},m} + \mathrm{CT}_i(g-r)^n_{\mathrm{PS},m} + \mathrm{Z}^n_i, \tag{F.5}$$

where g^n_m, r^n_m, and i^n_m are magnitudes in the Pan-STARRS system of m-th object on the n-th frame, $g^n_{\mathrm{inst},m}$, $r^n_{\mathrm{inst},m}$, and $i^n_{\mathrm{inst},m}$ are instrumental magnitudes of m-th object on the n-th frame, CT_g, CT_r, and CT_i, are color terms (CTs) of g, r, and i-band magnitudes, respectively, and Z^n_g, Z^n_r, and Z^n_i are zero points of g, r, and i-band magnitudes on the n-th frame, respectively. The same as colors, we firstly derived CTs at the night while shifting the photometric results of the reference stars during the night frame by frame so that the atmospheric variations in instrumental magnitudes and Zs were canceled out. Then, the Zs in each frame were calculated with the derived CTs with equations (F.3)–(F.5). We computed the propagated uncertainties of g, r, and i-band magnitudes with the photometric errors and uncertainties of $(g-r)_{\mathrm{PS}}$, CTs and Zs.

[1]The differences are filter bands and airmass dependences of first items Equations F.3–F.5. While our first items, instrumental magnitudes, depend on airmass, theirs do not.

G. Polarimetric analysis

The intrinsic Stokes vector $S = (I, Q, U, V)$ and observed Stokes vector $S' = (I', Q', U', V')$ are connected with Mueller matrix M (e.g., Kawabata et al. 1999):

$$S' = MS. \tag{G.1}$$

When a rotating angle of a rotatable half-wave plate (HWP) is θ, observed intensity, $I'(\theta)$, is expressed as follows:

$$I'(\theta) = \frac{I}{2}\left(1 + \frac{Q}{I}\cos(4\theta) + \frac{U}{I}\sin(4\theta)\right) k\eta(t), \tag{G.2}$$

where k is an efficiency of the instrument and $\eta(t)$ expresses atmospheric variation depends on time, t. We obtain the ordinary and extraordinary rays at once using the Wollaston prism. The observed ordinary and extraordinary intensities are written as follows:

$$I'_o(\theta) = \frac{I}{2}\left(1 + \frac{Q}{I}\cos(4\theta) + \frac{U}{I}\sin(4\theta)\right) k_o\eta(t), \tag{G.3}$$

$$I'_e(\theta) = \frac{I}{2}\left(1 - \frac{Q}{I}\cos(4\theta) - \frac{U}{I}\sin(4\theta)\right) k_e\eta(t), \tag{G.4}$$

where $I'_o(\theta)$ and $I'_e(\theta)$ are ordinary and extraordinary intensities when a rotating angle of a HWP is θ, respectively. And k_o and k_e are efficiencies of ordinary and extraordinary directions, respectively. We introduce the Stokes parameters Q and U normalized by the intensity I as follows:

$$q \equiv \frac{Q}{I}, \tag{G.5}$$

$$u \equiv \frac{U}{I}. \tag{G.6}$$

By observations of a target at θ =0.0, 22.5, 45.0, and 67.5°, we derive q and u as follows:

$$q = \frac{1 - R_q}{1 + R_q}, \tag{G.7}$$

$$u = \frac{1 - R_u}{1 + R_u}, \tag{G.8}$$

where

$$R_q = \sqrt{\frac{I_e(0.0)}{I_o(0.0)}\frac{I_o(45.0)}{I_e(45.0)}}, \tag{G.9}$$

$$R_u = \sqrt{\frac{I_e(22.5)}{I_o(22.5)}\frac{I_o(67.5)}{I_e(67.5)}}. \tag{G.10}$$

In this way, we could derive polarimetric parameters, q and u, canceling out the atmospheric variation $\eta(t)$. Then, we do three types of corrections for observed q and u to derive the linear polarization degree

and position angle of polarization: correction of polarization efficiency, correction of instrumental polarization, and correction of position angle offset. First, the correction of polarization efficiency is done using following equations:

$$q' = q/p_{\rm eff}, \tag{G.11}$$
$$u' = u/p_{\rm eff}, \tag{G.12}$$

where q' and u' are q and u after correction of polarization efficiency, respectively. And $p_{\rm eff}$ is a polarization efficiency. Next, the correction of instrumental polarization is performed using following equations

$$q'' = q' - \{\cos(2\theta_{\rm rot1})q_{\rm inst} - \sin(2\theta_{\rm rot1})u_{\rm inst}\}, \tag{G.13}$$
$$u'' = u' - \{\sin(2\theta_{\rm rot2})q_{\rm inst} + \cos(2\theta_{\rm rot2})u_{\rm inst}\}, \tag{G.14}$$

where q'' and u'' are q' and u' after the correction of instrumental polarization, respectively. The instrumental polarization generally depends on the angle of the instrumental rotator. $\theta_{\rm rot1}$ is an average position angle of instrumental rotator at θ =0.0, and 45.0°, and $\theta_{\rm rot2}$ is an average position angle of instrumental rotator at θ =22.5, and 67.5°. Finally, the correction of the position angle offset was done using equations below:

$$q''' = \cos(2\theta_{\rm off})q'' - \sin(2\theta_{\rm off})u'', \tag{G.15}$$
$$u''' = \sin(2\theta_{\rm off})q'' + \cos(2\theta_{\rm off})u'', \tag{G.16}$$
$$\theta_{\rm off} = \theta_{\rm lt} - \theta_{\rm obs}, \tag{G.17}$$

where q''' and u''' are q'' and u'' after the correction of position angle offset, respectively. Here, we note that $\theta_{\rm off}$ is defined as an excess of position angle in literature, $\theta_{\rm lt}$, to that in observation, $\theta_{\rm obs}$. This definition is different from those in previous papers (e.g., Ishiguro et al. 2017; Okazaki et al. 2020).

Finally, the linear polarization degree, P_0, and position angle of the polarization, θ_{P_0}, are derived as:

$$P_0 = \sqrt{q'''^2 + u'''^2}, \tag{G.18}$$
$$\theta_0 = \frac{1}{2}\arctan\left(\frac{u'''}{q'''}\right). \tag{G.19}$$

The uncertainty of P_0, σ_{P_0}, is estimated as follows:

$$\sigma_{P_0} = \sqrt{\sigma^2_{P_0,\rm ran} + \sigma^2_{P_0,\rm sys}} \tag{G.20}$$
$$\sigma_{\theta_0} = \sqrt{\sigma^2_{\theta_0,\rm ran} + \sigma^2_{\theta_0,\rm sys}}, \tag{G.21}$$
$$\tag{G.22}$$

where $\sigma_{P_0,\rm ran}$ and $\sigma_{P_0,\rm sys}$ are random error and systematic error of the polarization degree, respectively, and $\sigma_{\theta_0,\rm ran}$ and $\sigma_{\theta_0,\rm sys}$ are random error and systematic error of the position angle, respectively. We corrected polarization bias using the good approximation as follows (Wardle & Kronberg 1974):

$$P'_0 = \sqrt{P_0^2 - \sigma^2_{P_0}}, \tag{G.23}$$

where, P'_0 is the polarization degree after bias correction. Another approximation is investigated in Wang et al. (1997). When $P'_0 = 0$, the uncertainty of the position angle of polarization is set to $\theta_0 = 51.96°$ (Naghizadeh-Khouei & Clarke 1993).

The linear polarization degree of solar system objects, P_r, is defined as follows (e.g., Muinonen et al. 2002):

$$P_r = \frac{I_\perp - I_\parallel}{I_\perp + I_\parallel}, \tag{G.24}$$

where $I_\perp$ and $I_\parallel$ are intensities parallel and perpendicular to the scattering plane, respectively. P_0 is always positive by definition. On the other hand, P_r could be negative when $I_\perp$ is smaller than $I_\parallel$. This happens at small phase angles (so-called negative branch). We derived P_r from P_0' using the following equations (Zellner & Gradie 1976; Chernova et al. 1993):

$$P_r = P_0' \cos(2\theta_r), \tag{G.25}$$

$$\theta_r = \theta_0 - (\phi \pm 90^\circ), \tag{G.26}$$

where ϕ is the position angle of the scattering plane and θ_r is the position angle of the polarization plane relative to the perpendicular direction to the scattering plane. The sign in bracket is chosen to guarantee $0^\circ \leq \phi \pm 90^\circ \leq 180^\circ$.

H. Validation of polarimetric measurements

We present the polarimetric results of a polarimetric standard star HD 19820 (Schmidt et al. 1992) in Figure H.1 for validation purposes. We derived the linear polarization degrees, P, and position angles of polarization, θ, of HD 19820 with high accuracy. We considered the derivations between the photometric parameters in Schmidt et al. (1992) and those derived here as systematic uncertainties in the measurements of the polarimetric parameters of 2010 XC_{15}.

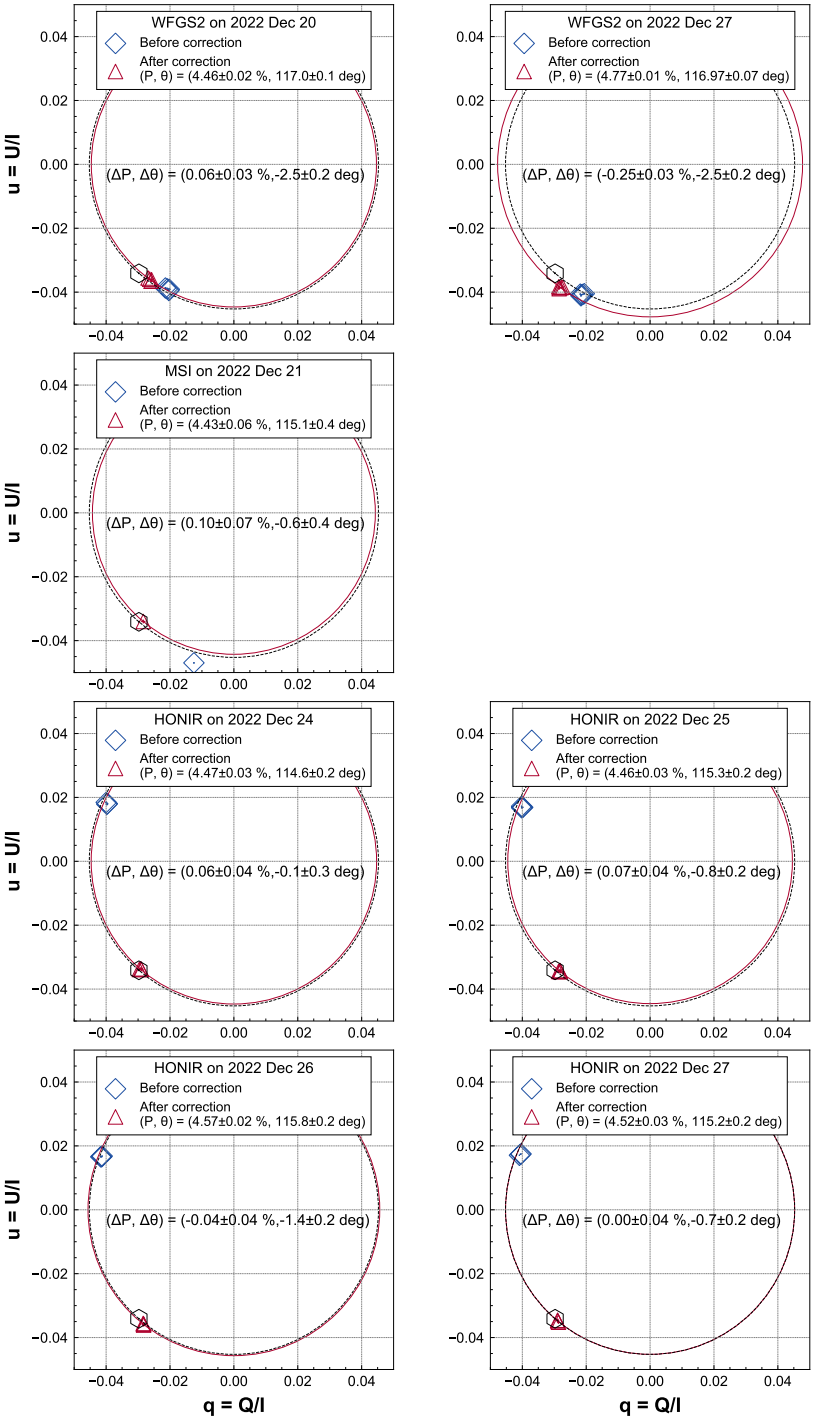

Figure H.1. Results of polarimetry of polarimetric standard star HD 19820 at each site on each day. The Stokes parameters Q and U normalized by the intensity I, $q \equiv Q/I$ and $u \equiv U/I$, before and after series of corrections are presented as diamonds and triangles, respectively. The q and u of HD 19920 calculated from P and θ in Schmidt et al. (1992) are shown by hexagons. Bars indicate the 1σ uncertainties. Polarization degrees of HD 19820 after series of corrections and those in Schmidt et al. (1992) are presented by large solid circles and dashed circles, respectively. The derivations ΔP, polarization degrees in Schmidt et al. (1992) - those derived here, and $\Delta\theta$, position angles of polarization in Schmidt et al. (1992) - those derived here, are shown.

References

Abell, P. A., Barbee, B. W., Mink, R. G., et al. 2012, in 43rd Annual Lunar and Planetary Science Conference, Lunar and Planetary Science Conference, 2842

Akaike, H. 1974, IEEE Transactions on Automatic Control, 19, 716

Akitaya, H., Moritani, Y., Ui, T., et al. 2014, in Society of Photo-Optical Instrumentation Engineers (SPIE) Conference Series, Vol. 9147, Ground-based and Airborne Instrumentation for Astronomy V, ed. S. K. Ramsay, I. S. McLean, & H. Takami, 91474O, doi: 10.1117/12.2054577

Alhameli, F. S., Parker, J. S., Caudill, M. T., et al. 2023, in Asteroids, Comets, and Meteors: ACM 2023

Alvarez, L. W., Alvarez, W., Asaro, F., & Michel, H. V. 1980, Science, 208, 1095, doi: 10.1126/science.208.4448.1095

Arai, T., Kobayashi, M., Ishibashi, K., et al. 2018, in 49th Annual Lunar and Planetary Science Conference, Lunar and Planetary Science Conference, 2570

Arcoverde, P., Rondón, E., Monteiro, F., et al. 2023, MNRAS, 523, 739, doi: 10.1093/mnras/stad1486

Ashton, E., Chang, C.-K., Chen, Y.-T., et al. 2023, ApJS, 267, 33, doi: 10.3847/1538-4365/acda1e

Avdellidou, C., Di Donna, A., Schultz, C., et al. 2020, Icar, 341, 113648, doi: 10.1016/j.icarus.2020.113648

Avdyushev, V. A., & Banshchikova, M. A. 2007, Solar System Research, 41, 413, doi: 10.1134/S0038094607050048

Bacci, P., & Maestripieri, M. 2023, Minor Planet Bulletin, 50, 206

Bagnulo, S., Gray, Z., Granvik, M., et al. 2023, ApJL, 945, L38, doi: 10.3847/2041-8213/acb261

Bannister, M. T., Gladman, B. J., Kavelaars, J. J., et al. 2018, ApJS, 236, 18, doi: 10.3847/1538-4365/aab77a

Barbary, K., Boone, K., Craig, M., Deil, C., & Rose, B. 2017, Kbarbary/Sep: V1.0.2, v1.0.2, Zenodo, Zenodo, doi: 10.5281/zenodo.896928

Barbary, K., Boone, K., & Deil, C. 2015, sep: v1.3.0, v1.3.0, Zenodo, doi: 10.5281/zenodo.15669

Barucci, M. A., Perna, D., Popescu, M., et al. 2018, MNRAS, 476, 4481, doi: 10.1093/mnras/sty532

Bell, J. F., Davis, D. R., Hartmann, W. K., & Gaffey, M. J. 1989, in Asteroids II, ed. R. P. Binzel, T. Gehrels, & M. S. Matthews, 921–945

Bellm, E. C., Kulkarni, S. R., Barlow, T., et al. 2019, PASP, 131, 068003, doi: 10.1088/1538-3873/ab0c2a

Belskaya, I., Cellino, A., Gil-Hutton, R., Muinonen, K., & Shkuratov, Y. 2015, in Asteroids IV, 151–163, doi: 10.2458/azu_uapress_9780816532131-ch008

Belskaya, I. N., & Shevchenko, V. G. 2000, Icarus, 147, 94, doi: 10.1006/icar.2000.6410

Belskaya, I. N., Shevchenko, V. G., Kiselev, N. N., et al. 2003, Icar, 166, 276, doi: 10.1016/j.icarus.2003.09.005

Belskaya, I. N., Fornasier, S., Tozzi, G. P., et al. 2017, Icar, 284, 30, doi: 10.1016/j.icarus.2016.11.003

Belton, M. J. S., Chapman, C. R., Thomas, P. C., et al. 1995, Natur, 374, 785, doi: 10.1038/374785a0

Beniyama, J., Sako, S., Ohsawa, R., et al. 2022, Publication of the Astronomical Society of Japan, 74, 877, doi: 10.1093/pasj/psac043

Beniyama, J., Ohsawa, R., Avdellidou, C., et al. 2023a, AJ, 166, 229, doi: 10.3847/1538-3881/ad0151

Beniyama, J., Sako, S., Ohtsuka, K., et al. 2023b, ApJ, 955, 143, doi: 10.3847/1538-4357/ace88f

Beniyama, J., Sekiguchi, T., Kuroda, D., et al. 2023c, Publication of the Astronomical Society of Japan, 75, 297, doi: 10.1093/pasj/psac109

Benner, L. A. M., Busch, M. W., Giorgini, J. D., Taylor, P. A., & Margot, J. L. 2015, in Asteroids IV, 165–182, doi: 10.2458/azu_uapress_9780816532131-ch009

Benson, C. J., Scheeres, D. J., & Moskovitz, N. A. 2020, Icarus, 340, 113518, doi: 10.1016/j.icarus.2019.113518

Berdeu, A., Langlois, M., & Vachier, F. 2022, A&A, 658, L4, doi: 10.1051/0004-6361/202142623

Bertin, E., & Arnouts, S. 1996, , 117, 393, doi: 10.1051/aas:1996164

Binzel, R. P., Morbidelli, A., Merouane, S., et al. 2010, Nature, 463, 331, doi: 10.1038/nature08709

Binzel, R. P., DeMeo, F. E., Turtelboom, E. V., et al. 2019, Icarus, 324, 41, doi: 10.1016/j.icarus.2018.12.035

Birtwhistle, P. 2022a, Minor Planet Bulletin, 49, 280

—. 2022b, Minor Planet Bulletin, 49, 169

—. 2023a, Minor Planet Bulletin, 50, 26

—. 2023b, Minor Planet Bulletin, 50, 295

—. 2021a, Minor Planet Bulletin, 48, 180

—. 2021b, Minor Planet Bulletin, 48, 286

—. 2021c, Minor Planet Bulletin, 48, 341

Bolin, B. T., Ghosal, M., & Jedicke, R. 2024, MNRAS, 527, 1633, doi: 10.1093/mnras/stad3227

Bolin, B. T., Ahumada, T., van Dokkum, P., et al. 2022, MNRAS, 517, L49, doi: 10.1093/mnrasl/slac089

Borisov, G., Christou, A. A., Colas, F., et al. 2018, A&A, 618, A178, doi: 10.1051/0004-6361/201732466

Bottke, W. F., Durda, D. D., Nesvorný, D., et al. 2005, Icar, 179, 63, doi: 10.1016/j.icarus.2005.05.017

Bottke, W. F., Jedicke, R., Morbidelli, A., Petit, J.-M., & Gladman, B. 2000, Science, 288, 2190, doi: 10.1126/science.288.5474.2190

Bottke, W. F., Vokrouhlický, D., Rubincam, D. P., & Nesvorný, D. 2006, Annual Review of Earth and Planetary Sciences, 34, 157, doi: 10.1146/annurev.earth.34.031405.125154

Bourdelle de Micas, J., Fornasier, S., Avdellidou, C., et al. 2022, A&A, 665, A83, doi: 10.1051/0004-6361/202244099

Bowell, E., Hapke, B., Domingue, D., et al. 1989, in Asteroids II, ed. R. P. Binzel, T. Gehrels, & M. S. Matthews (Tucson, AZ: Univ. Arizona Press), 524–556

Breiter, S., Rożek, A., & Vokrouhlický, D. 2011, MNRAS, 417, 2478, doi: 10.1111/j.1365-2966.2011.19411.x

Brož, M., Ďurech, J., Carry, B., et al. 2022, A&A, 657, A76, doi: 10.1051/0004-6361/202142055

Burns, J. A., Lamy, P. L., & Soter, S. 1979, Icar, 40, 1, doi: 10.1016/0019-1035(79)90050-2

Bus, S. J. 1999, PhD thesis, Massachusetts Institute of Technology

Bus, S. J., & Binzel, R. P. 2002, Icar, 158, 146, doi: 10.1006/icar.2002.6856

Busch, M. W., Benner, L. A. M., Ostro, S. J., et al. 2008, Icar, 195, 614, doi: 10.1016/j.icarus.2008.01.020

Cambioni, S., Delbo, M., Poggiali, G., et al. 2021, Natur, 598, 49, doi: 10.1038/s41586-021-03816-5

Campbell-Brown, M. D., & Braid, D. 2011, in Meteoroids: The Smallest Solar System Bodies, ed. W. J. Cooke, D. E. Moser, B. F. Hardin, & D. Janches, 304

Capaccioni, F., Coradini, A., Filacchione, G., et al. 2015, Science, 347, aaa0628, doi: 10.1126/science.aaa0628

Čapek, D., & Vokrouhlický, D. 2004, Icarus, 172, 526, doi: 10.1016/j.icarus.2004.07.003

Carry, B. 2012, , 73, 98, doi: 10.1016/j.pss.2012.03.009

Cellino, A., Bagnulo, S., Gil-Hutton, R., et al. 2015, MNRAS, 451, 3473, doi: 10.1093/mnras/stv1188

Chambers, J. E., & Migliorini, F. 1997, in AAS/Division for Planetary Sciences Meeting Abstracts, Vol. 29, AAS/Division for Planetary Sciences Meeting Abstracts #29, 27.06

Chambers, K. C., Magnier, E. A., Metcalfe, N., et al. 2016, arXiv:1612.05560, arXiv:1612.05560. https://arxiv.org/abs/1612.05560

Chang, C.-K., Chen, Y.-T., Fraser, W. C., et al. 2021, PSJ, 2, 191, doi: 10.3847/PSJ/ac13a4

—. 2022, ApJS, 259, 7, doi: 10.3847/1538-4365/ac50ac

Chapman, C. R., Morrison, D., & Zellner, B. 1975, Icar, 25, 104, doi: 10.1016/0019-1035(75)90191-8

Chapman, C. R., Veverka, J., Thomas, P. C., et al. 1995, Natur, 374, 783, doi: 10.1038/374783a0

Chernova, G. P., Kiselev, N. N., & Jockers, K. 1993, Icar, 103, 144, doi: 10.1006/icar.1993.1063

Cibulková, H., Nortunen, H., Ďurech, J., et al. 2018, A&A, 611, A86, doi: 10.1051/0004-6361/201731554

Clark, D. L., Wiegert, P. A., Brown, P. G., et al. 2023, PSJ, 4, 103, doi: 10.3847/PSJ/acc9b1

Colazo, M., Fornari, C., Ciancia, G., et al. 2023, Minor Planet Bulletin, 50, 235

Consolmagno, G., Britt, D., & Macke, R. 2008, Chemie der Erde / Geochemistry, 68, 1, doi: 10.1016/j.chemer.2008.01.003

Cordwell, A. J., Rattenbury, N. J., Bannister, M. T., et al. 2022, MNRAS, 514, 3098, doi: 10.1093/mnras/stac674

Cruikshank, D. P., & Hartmann, W. K. 1984, Science, 223, 281, doi: 10.1126/science.223.4633.281

de la Fuente Marcos, C., & de la Fuente Marcos, R. 2015, MNRAS, 453, 1288, doi: 10.1093/mnras/stv1725

—. 2019, MNRAS, 483, L37, doi: 10.1093/mnrasl/sly214

De Luise, F., Perna, D., Dotto, E., et al. 2007, Icar, 191, 628, doi: 10.1016/j.icarus.2007.05.018

Delbó, M., Harris, A. W., Binzel, R. P., Pravec, P., & Davies, J. K. 2003, Icar, 166, 116, doi: 10.1016/j.icarus.2003.07.002

Delbo', M., Walsh, K., Bolin, B., Avdellidou, C., & Morbidelli, A. 2017, Science, 357, 1026, doi: 10.1126/science.aam6036

Delbo, M., Libourel, G., Wilkerson, J., et al. 2014, Natur, 508, 233, doi: 10.1038/nature13153

DellaGiustina, D. N., Nolan, M. C., Polit, A. T., et al. 2023, PSJ, 4, 198, doi: 10.3847/PSJ/acf75e

DeMeo, F. E., Alexander, C. M. O., Walsh, K. J., Chapman, C. R., & Binzel, R. P. 2015, in Asteroids IV, 13–41, doi: 10.2458/azu_uapress_9780816532131-ch002

DeMeo, F. E., Binzel, R. P., Slivan, S. M., & Bus, S. J. 2009, Icar, 202, 160, doi: 10.1016/j.icarus.2009.02.005

DeMeo, F. E., & Carry, B. 2013, Icar, 226, 723, doi: 10.1016/j.icarus.2013.06.027

DeMeo, F. E., Polishook, D., Carry, B., et al. 2019, Icar, 322, 13, doi: 10.1016/j.icarus.2018.12.016

Devogèle, M., Moskovitz, N., Thirouin, A., et al. 2019, AJ, 158, 196, doi: 10.3847/1538-3881/ab43dd

Devogèle, M., MacLennan, E., Gustafsson, A., et al. 2020, PSJ, 1, 15, doi: 10.3847/PSJ/ab8e45

Drake, A. J., Djorgovski, S. G., Mahabal, A., et al. 2009, ApJ, 696, 870, doi: 10.1088/0004-637X/696/1/870

Drummond, J. D. 1991, Icar, 89, 14, doi: 10.1016/0019-1035(91)90084-7

Duddy, S. R., Lowry, S. C., Christou, A., et al. 2013, MNRAS, 429, 63, doi: 10.1093/mnras/sts309

Ďurech, J., Delbo', M., Carry, B., Hanuš, J., & Alí-Lagoa, V. 2017, A&A, 604, A27, doi: 10.1051/0004-6361/201730868

Ďurech, J., & Hanuš, J. 2018, A&A, 620, A91, doi: 10.1051/0004-6361/201834007

—. 2023, A&A, 675, A24, doi: 10.1051/0004-6361/202345889

Ďurech, J., Hanuš, J., & Alí-Lagoa, V. 2018a, A&A, 617, A57, doi: 10.1051/0004-6361/201833437

Ďurech, J., Hanuš, J., Oszkiewicz, D., & Vančo, R. 2016, A&A, 587, A48, doi: 10.1051/0004-6361/201527573

Ďurech, J., Hanuš, J., & Vančo, R. 2019, A&A, 631, A2, doi: 10.1051/0004-6361/201936341

Ďurech, J., Sidorin, V., & Kaasalainen, M. 2010, A&A, 513, A46, doi: 10.1051/0004-6361/200912693

Ďurech, J., Tonry, J., Erasmus, N., et al. 2020, A&A, 643, A59, doi: 10.1051/0004-6361/202037729

Ďurech, J., Vávra, M., Vančo, R., & Erasmus, N. 2022a, Frontiers in Astronomy and Space Sciences, 9, 809771, doi: 10.3389/fspas.2022.809771

Ďurech, J., Vokrouhlický, D., Kaasalainen, M., et al. 2008a, A&A, 488, 345, doi: 10.1051/0004-6361:200809663

—. 2008b, A&A, 489, L25, doi: 10.1051/0004-6361:200810672

Ďurech, J., Kaasalainen, M., Herald, D., et al. 2011, Icar, 214, 652, doi: 10.1016/j.icarus.2011.03.016

Ďurech, J., Vokrouhlický, D., Baransky, A. R., et al. 2012, A&A, 547, A10, doi: 10.1051/0004-6361/201219396

Ďurech, J., Vokrouhlický, D., Pravec, P., et al. 2018b, A&A, 609, A86, doi: 10.1051/0004-6361/201731465

—. 2022b, A&A, 657, A5, doi: 10.1051/0004-6361/202141844

—. 2023, arXiv e-prints, arXiv:2312.05157, doi: 10.48550/arXiv.2312.05157

Elkins-Tanton, L. T., Asphaug, E., Bell, J., et al. 2014, in 45th Annual Lunar and Planetary Science Conference, Lunar and Planetary Science Conference, 1253

Erasmus, N., McNeill, A., Mommert, M., et al. 2018, ApJS, 237, 19, doi: 10.3847/1538-4365/aac38f

Erasmus, N., Mommert, M., Trilling, D. E., et al. 2017, AJ, 154, 162, doi: 10.3847/1538-3881/aa88be

Eugster, O., Herzog, G. F., Marti, K., & Caffee, M. W. 2006, Irradiation Records, Cosmic-Ray Exposure Ages, and Transfer Times of Meteorites, ed. D. S. Lauretta & H. Y. McSween, 829

Farinella, P., Vokrouhlický, D., & Hartmann, W. K. 1998, Icarus, 132, 378, doi: 10.1006/icar.1997.5872

Farnocchia, D., Chesley, S. R., Vokrouhlický, D., et al. 2013, Icar, 224, 1, doi: 10.1016/j.icarus.2013.02.004

Fatka, P., Moskovitz, N. A., Pravec, P., et al. 2022, MNRAS, 510, 6033, doi: 10.1093/mnras/stab3719

Fenucci, M., Novaković, B., & Marčeta, D. 2023, A&A, 675, A134, doi: 10.1051/0004-6361/202346160

Fenucci, M., Novaković, B., Vokrouhlický, D., & Weryk, R. J. 2021, A&A, 647, A61, doi: 10.1051/0004-6361/202039628

Flewelling, H. A., Magnier, E. A., Chambers, K. C., et al. 2020, ApJS, 251, 7, doi: 10.3847/1538-4365/abb82d

Fowler, J. W., & Chillemi, J. R. 1992, Phillips Lab. Tech. Rep., 2049, 17

Franco, L., Marchini, A., Iozzi, M., et al. 2023, Minor Planet Bulletin, 50, 173

Fujiwara, A., Kawaguchi, J., Yeomans, D. K., et al. 2006, Science, 312, 1330, doi: 10.1126/science.1125841

Fukugita, M., Ichikawa, T., Gunn, J. E., et al. 1996, AJ, 111, 1748, doi: 10.1086/117915

Gaia Collaboration, et al. 2018, A&A, 616, A1, doi: 10.1051/0004-6361/201833051

Geake, J. E., & Dollfus, A. 1986, MNRAS, 218, 75, doi: 10.1093/mnras/218.1.75

Geem, J., Ishiguro, M., Granvik, M., et al. 2023, MNRAS, 525, L17, doi: 10.1093/mnrasl/slad073

Ginsburg, A., Sipőcz, B. M., Brasseur, C. E., et al. 2019, AJ, 157, 98, doi: 10.3847/1538-3881/aafc33

Gladman, B. J., Migliorini, F., Morbidelli, A., et al. 1997, Science, 277, 197, doi: 10.1126/science.277.5323.197

Golubov, O., & Krugly, Y. N. 2012, ApJL, 752, L11, doi: 10.1088/2041-8205/752/1/L11

Golubov, O., Scheeres, D. J., & Krugly, Y. N. 2014, ApJ, 794, 22, doi: 10.1088/0004-637X/794/1/22

Golubov, O., Unukovych, V., & Scheeres, D. J. 2021, AJ, 162, 8, doi: 10.3847/1538-3881/abfb64

Granvik, M., Vaubaillon, J., & Jedicke, R. 2012, Icar, 218, 262, doi: 10.1016/j.icarus.2011.12.003

Granvik, M., Morbidelli, A., Jedicke, R., et al. 2016, Natur, 530, 303, doi: 10.1038/nature16934

—. 2018, Icarus, 312, 181, doi: 10.1016/j.icarus.2018.04.018

Gray, Z., Bagnulo, S., Granvik, M., et al. 2023, arXiv e-prints, arXiv:2311.13483, doi: 10.48550/arXiv.2311.13483

Greenberg, A. H., Margot, J.-L., Verma, A. K., Taylor, P. A., & Hodge, S. E. 2020, AJ, 159, 92, doi: 10.3847/1538-3881/ab62a3

Greenberg, A. H., Margot, J.-L., Verma, A. K., et al. 2017, AJ, 153, 108, doi: 10.3847/1538-3881/153/3/108

Greenstreet, S., Ngo, H., & Gladman, B. 2012, Icar, 217, 355, doi: 10.1016/j.icarus.2011.11.010

Gronchi, G. F., & Milani, A. 2001, Icar, 152, 58, doi: 10.1006/icar.2001.6610

Gustafsson, A., Trilling, D. E., Mommert, M., et al. 2019, AJ, 158, 67, doi: 10.3847/1538-3881/ab29ea

Hadamcik, E., Renard, J. B., Lasue, J., Levasseur-Regourd, A. C., & Ishiguro, M. 2023, MNRAS, 520, 1963, doi: 10.1093/mnras/stac2749

Hanuš, J., Pejcha, O., Shappee, B. J., et al. 2021, A&A, 654, A48, doi: 10.1051/0004-6361/202140759

Hanuš, J., Ďurech, J., Oszkiewicz, D. A., et al. 2016a, A&A, 586, A108, doi: 10.1051/0004-6361/201527441

Hanuš, J., Delbo', M., Vokrouhlický, D., et al. 2016b, A&A, 592, A34, doi: 10.1051/0004-6361/201628666

Harris, A. W. 1998, Icarus, 131, 291, doi: 10.1006/icar.1997.5865

Harris, A. W., & Lupishko, D. F. 1989, in Asteroids II, ed. R. P. Binzel, T. Gehrels, & M. S. Matthews, 39–53

Harris, A. W., Mueller, M., Delbó, M., & Bus, S. J. 2007, Icar, 188, 414, doi: 10.1016/j.icarus.2006.12.003

Harris, A. W., Pravec, P., Galád, A., et al. 2014, Icar, 235, 55, doi: 10.1016/j.icarus.2014.03.004

Harris, C. R., Millman, K. J., van der Walt, S. J., et al. 2020, Natur, 585, 357, doi: 10.1038/s41586-020-2649-2

Hasegawa, S., Marsset, M., DeMeo, F. E., et al. 2021, ApJL, 916, L6, doi: 10.3847/2041-8213/ac0f05

Hatch, P., & Wiegert, P. A. 2015, , 111, 100, doi: 10.1016/j.pss.2015.03.019

Hergenrother, C. W., Nolan, M. C., Binzel, R. P., et al. 2013, Icar, 226, 663, doi: 10.1016/j.icarus.2013.05.044

Hergenrother, C. W., Maleszewski, C. K., Nolan, M. C., et al. 2019, Nature Communications, 10, 1291, doi: 10.1038/s41467-019-09213-x

Herschel, W. 1802, Philosophical Transactions of the Royal Society of London Series I, 92, 213

Hirabayashi, M., Mimasu, Y., Sakatani, N., et al. 2021, Advances in Space Research, 68, 1533, doi: 10.1016/j.asr.2021.03.030

Holsapple, K. A. 1993, Annual Review of Earth and Planetary Sciences, 21, 333, doi: 10.1146/annurev.ea.21.050193.002001

—. 2004, Icar, 172, 272, doi: 10.1016/j.icarus.2004.05.023

Holsapple, K. A. 2007, Icarus, 187, 500, doi: 10.1016/j.icarus.2006.08.012

Holsapple, K. A. 2020, arXiv:2012.15300, arXiv:2012.15300. https://arxiv.org/abs/2012.15300

Hora, J. L., Siraj, A., Mommert, M., et al. 2018, ApJS, 238, 22, doi: 10.3847/1538-4365/aadcf5

Hsu, H.-W., Wang, X., Carroll, A., Hood, N., & Horányi, M. 2022, Nature Astronomy, 6, 1043, doi: 10.1038/s41550-022-01717-9

Huang, J., Ji, J., Ye, P., et al. 2013, Scientific Reports, 3, 3411, doi: 10.1038/srep03411

Ieva, S., Arcoverde, P., Rondón, E., et al. 2022, MNRAS, 513, 3104, doi: 10.1093/mnras/stac1117

Ip, W.-H., Masci, F. J., Ye, Q., et al. 2022, ApJL, 935, L6, doi: 10.3847/2041-8213/ac8470

Ishiguro, M., Kuroda, D., Hasegawa, S., et al. 2014, ApJ, 792, 74, doi: 10.1088/0004-637X/792/1/74

Ishiguro, M., Kuroda, D., Watanabe, M., et al. 2017, AJ, 154, 180, doi: 10.3847/1538-3881/aa8b1a

Ishiguro, M., Bach, Y. P., Geem, J., et al. 2022, MNRAS, 509, 4128, doi: 10.1093/mnras/stab3198

Ito, T., & Ohtsuka, K. 2019, Monographs on Environment, Earth and Planets, 7, 1, doi: 10.5047/meep.2019.00701.0001

Ivezić, V., & Ivezić, Ž. 2021, Icar, 357, 114262, doi: 10.1016/j.icarus.2020.114262

Ivezić, Ž., Tabachnik, S., Rafikov, R., et al. 2001, AJ, 122, 2749, doi: 10.1086/323452

Ivezić, Ž., Kahn, S. M., Tyson, J. A., et al. 2019, ApJ, 873, 111, doi: 10.3847/1538-4357/ab042c

Jackson, S. L., Kolb, U. C., & Green, S. F. 2021, PASP, 133, 075003, doi: 10.1088/1538-3873/ac0f8c

Jacobson, S. A., Marzari, F., Rossi, A., & Scheeres, D. J. 2016, Icar, 277, 381, doi: 10.1016/j.icarus.2016.05.032

Jacobson, S. A., Marzari, F., Rossi, A., Scheeres, D. J., & Davis, D. R. 2014, MNRAS, 439, L95, doi: 10.1093/mnrasl/slu006

Jacobson, S. A., & Scheeres, D. J. 2011, Icar, 214, 161, doi: 10.1016/j.icarus.2011.04.009

Jedicke, R., Bolin, B. T., Bottke, W. F., et al. 2018, Frontiers in Astronomy and Space Sciences, 5, 13, doi: 10.3389/fspas.2018.00013

Jehin, E., Gillon, M., Queloz, D., et al. 2011, The Messenger, 145, 2

Jenniskens, P., Shaddad, M. H., Numan, D., et al. 2009, Natur, 458, 485, doi: 10.1038/nature07920

Jenniskens, P., Gabadirwe, M., Yin, Q.-Z., et al. 2021, , 56, 844, doi: 10.1111/maps.13653

Jurić, M., Ivezić, Ž., Lupton, R. H., et al. 2002, AJ, 124, 1776, doi: 10.1086/341950

Kaasalainen, M., & Torppa, J. 2001, Icar, 153, 24, doi: 10.1006/icar.2001.6673

Kaasalainen, M., Torppa, J., & Muinonen, K. 2001, Icar, 153, 37, doi: 10.1006/icar.2001.6674

Kaasalainen, M., Ďurech, J., Warner, B. D., Krugly, Y. N., & Gaftonyuk, N. M. 2007, Natur, 446, 420, doi: 10.1038/nature05614

Kadono, T., Arakawa, M., Ito, T., & Ohtsuki, K. 2009, Icarus, 200, 694 , doi: https://doi.org/10.1016/j.icarus.2008.11.021

Kalup, C. E., Molnár, L., Kiss, C., et al. 2021, ApJS, 254, 7, doi: 10.3847/1538-4365/abe76a

Kanamaru, M., Sasaki, S., Morota, T., et al. 2021, Journal of Geophysical Research (Planets), 126, e06863, doi: 10.1029/2021JE006863

Kareta, T., Reddy, V., Pearson, N., Sanchez, J. A., & Harris, W. M. 2021, PSJ, 2, 190, doi: 10.3847/PSJ/ac1bad

Kareta, T., Vida, D., Brown, P., et al. 2023, in AAS/Division for Planetary Sciences Meeting Abstracts, Vol. 55, AAS/Division for Planetary Sciences Meeting Abstracts, 510.02

Kasuga, T., & Jewitt, D. 2008, AJ, 136, 881, doi: 10.1088/0004-6256/136/2/881

Kawabata, K. S., Okazaki, A., Akitaya, H., et al. 1999, PASP, 111, 898, doi: 10.1086/316387

Kawakami, A., Itoh, Y., Takahashi, J., Tozuka, M., & Takayama, M. 2021, Stars and Galaxies, 4, 102

Kecskeméthy, V., Kiss, C., Szakáts, R., et al. 2023, ApJS, 264, 18, doi: 10.3847/1538-4365/ac9c67

Kikuchi, S., Mimasu, Y., Takei, Y., et al. 2023, Acta Astronautica, 211, 295, doi: 10.1016/j.actaastro.2023.06.010

Kirkwood, D. 1867, Meteoric astronomy: a treatise on shooting-stars, fireballs, and aerolites.

Kiselev, N. N., Rosenbush, V. K., Jockers, K., et al. 2002, in ESA Special Publication, Vol. 500, Asteroids, Comets, and Meteors: ACM 2002, ed. B. Warmbein, 887–890

Kitazato, K., Milliken, R. E., Iwata, T., et al. 2019, Science, 364, 272, doi: 10.1126/science.aav7432

Koehn, B. W., & Bowell, E. L. G. 2000, in AAS/Division for Planetary Sciences Meeting Abstracts, Vol. 32, AAS/Division for Planetary Sciences Meeting Abstracts #32, 14.03

Kojima, Y., Sako, S., Ohsawa, R., et al. 2018, Evaluation of large pixel CMOS image sensors for the Tomo-e Gozen wide field camera, doi: 10.1117/12.2311301

Kokubo, E., & Ida, S. 2000, Icar, 143, 15, doi: 10.1006/icar.1999.6237

Koleńczuk, P., Kwiatkowski, T., Kamińska, M., & Kaminski, K. 2023, in Asteroids, Comets, and Meteors: ACM 2023

Kozai, Y. 1962, AJ, 67, 591, doi: 10.1086/108790

Kurita, M., Kino, M., Iwamuro, F., et al. 2020, Publication of the Astronomical Society of Japan, 72, 48, doi: 10.1093/pasj/psaa036

Kuroda, D., Ishiguro, M., Naito, H., et al. 2021, A&A, 646, A51, doi: 10.1051/0004-6361/202039004

Kwiatkowski, T., Polinska, M., Loaring, N., et al. 2010, A&A, 511, A49, doi: 10.1051/0004-6361/200913468

Kwiatkowski, T., Kryszczyńska, A., Polińska, M., et al. 2009, A&A, 495, 967, doi: 10.1051/0004-6361:200810965

Kwiatkowski, T., Koleńczuk, P., Kryszczyńska, A., et al. 2021, A&A, 656, A126, doi: 10.1051/0004-6361/202142013

Lam, A. L. H., Margot, J.-L., Whittaker, E., & Myhrvold, N. 2023, PSJ, 4, 61, doi: 10.3847/PSJ/acc5e4

Lang, D., Hogg, D. W., Mierle, K., Blanton, M., & Roweis, S. 2010, AJ, 139, 1782, doi: 10.1088/0004-6256/139/5/1782

Lauretta, D. S., Balram-Knutson, S. S., Beshore, E., et al. 2017, , 212, 925, doi: 10.1007/s11214-017-0405-1

Lazzarin, M., Marchi, S., Barucci, M. A., Di Martino, M., & Barbieri, C. 2004, Icar, 169, 373, doi: 10.1016/j.icarus.2003.12.023

Lebofsky, L. A., & Spencer, J. R. 1989, in Asteroids II, ed. R. P. Binzel, T. Gehrels, & M. S. Matthews, 128–147

Lebofsky, L. A., Sykes, M. V., Tedesco, E. F., et al. 1986, Icar, 68, 239, doi: 10.1016/0019-1035(86)90021-7

Lee, H.-J., Moon, H.-K., Kim, M.-J., et al. 2017, Journal of Korean Astronomical Society, 50, 41, doi: 10.5303/JKAS.2017.50.3.41

Lee, H.-J., Ďurech, J., Vokrouhlický, D., et al. 2021, AJ, 161, 112, doi: 10.3847/1538-3881/abd4da

Lee, H. J., Kim, M. J., Marciniak, A., et al. 2022, A&A, 661, L3, doi: 10.1051/0004-6361/202243442

Lian, C., Zhuge, Y., & Beecham, S. 2011, Construction and Building Materials, 25, 4294, doi: https://doi.org/10.1016/j.conbuildmat.2011.05.005

Licandro, J., Popescu, M., Tatsumi, E., et al. 2023, MNRAS, 521, 3784, doi: 10.1093/mnras/stad708

Lidov, M. L. 1962, , 9, 719, doi: 10.1016/0032-0633(62)90129-0

Lomb, N. R. 1976, , 39, 447, doi: 10.1007/BF00648343

Lowry, S. C., Fitzsimmons, A., Pravec, P., et al. 2007, Science, 316, 272, doi: 10.1126/science.1139040

Lowry, S. C., Weissman, P. R., Duddy, S. R., et al. 2014, A&A, 562, A48, doi: 10.1051/0004-6361/201322602

Lumme, K., & Muinonen, K. O. 1993, in LPI Contributions, Vol. 810, Asteroids, Comets, Meteors 1993, 194

Maeda, N., Terai, T., Ohtsuki, K., et al. 2021, AJ, 162, 280, doi: 10.3847/1538-3881/ac2c6e

Mahlke, M., Carry, B., & Denneau, L. 2021, Icar, 354, 114094, doi: 10.1016/j.icarus.2020.114094

Mahlke, M., Carry, B., & Mattei, P. A. 2022, A&A, 665, A26, doi: 10.1051/0004-6361/202243587

Mainzer, A., Bauer, J., Grav, T., et al. 2011, ApJ, 731, 53, doi: 10.1088/0004-637X/731/1/53

—. 2014, ApJ, 784, 110, doi: 10.1088/0004-637X/784/2/110

Mainzer, A. K., Masiero, J. R., Abell, P. A., et al. 2023, arXiv e-prints, arXiv:2310.12918. https://arxiv.org/abs/2310.12918

Marchis, F., Descamps, P., Hestroffer, D., & Berthier, J. 2005, Natur, 436, 822, doi: 10.1038/nature04018

Margot, J. L., Nolan, M. C., Benner, L. A. M., et al. 2002, Science, 296, 1445, doi: 10.1126/science.1072094

Margot, J. L., Pravec, P., Taylor, P., Carry, B., & Jacobson, S. 2015, in Asteroids IV, 355–374, doi: 10.2458/azu_uapress_9780816532131-ch019

Marshall, S., Devogele, M., Taylor, P., et al. 2022, in AAS/Division for Planetary Sciences Meeting Abstracts, Vol. 54, AAS/Division for Planetary Sciences Meeting Abstracts, 514.07

Marsset, M., DeMeo, F. E., Burt, B., et al. 2022, AJ, 163, 165, doi: 10.3847/1538-3881/ac532f

Martikainen, J., Muinonen, K., Penttilä, A., Cellino, A., & Wang, X. B. 2021, A&A, 649, A98, doi: 10.1051/0004-6361/202039796

Masiero, J. R., Mainzer, A. K., Bauer, J. M., et al. 2021, PSJ, 2, 162, doi: 10.3847/PSJ/ac15fb

McCully, C., Crawford, S., Kovacs, G., et al. 2018, Astropy/Astroscrappy: V1.0.5 Zenodo Release, v1.0.5, Zenodo, Zenodo, doi: 10.5281/zenodo.1482019

McFadden, L. D., Eppes, M. C., Gillespie, A. R., & Hallet, B. 2005, Geological Society of America Bulletin, 117, 161, doi: 10.1130/B25508.1

McMillan, R. S., & Spacewatch Team. 2007, in Near Earth Objects, our Celestial Neighbors: Opportunity and Risk, ed. G. B. Valsecchi, D. Vokrouhlický, & A. Milani, Vol. 236, 329–340, doi: 10.1017/S1743921307003407

McNeill, A., Gowanlock, M., Mommert, M., et al. 2023, AJ, 166, 152, doi: 10.3847/1538-3881/acf194

McNeill, A., Mommert, M., Trilling, D. E., Llama, J., & Skiff, B. 2019, ApJS, 245, 29, doi: 10.3847/1538-4365/ab5223

Meech, K., & Raymond, S. N. 2020, in Planetary Astrobiology, ed. V. S. Meadows, G. N. Arney, B. E. Schmidt, & D. J. Des Marais, 325, doi: 10.2458/azu_uapress_9780816540068

Merline, W. J., Weidenschilling, S. J., Durda, D. D., et al. 2002, in Asteroids III, 289–312

Meurer, A., Smith, C. P., Paprocki, M., et al. 2017, PeerJ Computer Science, 3, e103, doi: 10.7717/peerj-cs.103

Michel, P., Küppers, M., Bagatin, A. C., et al. 2022, PSJ, 3, 160, doi: 10.3847/PSJ/ac6f52

Micheli, M. 2013, PhD thesis, University of Hawaii, Manoa

Micheli, M., Tholen, D. J., & Elliott, G. T. 2012, , 17, 446, doi: 10.1016/j.newast.2011.11.008

—. 2013, Icar, 226, 251, doi: 10.1016/j.icarus.2013.05.032

—. 2014, ApJL, 788, L1, doi: 10.1088/2041-8205/788/1/L1

Michikami, T., Nakamura, A. M., & Hirata, N. 2010, Icarus, 207, 277, doi: 10.1016/j.icarus.2009.10.008

Michikami, T., Honda, C., Miyamoto, H., et al. 2019, Icarus, 331, 179, doi: 10.1016/j.icarus.2019.05.019

Michimani, J., Rondón, E., Perna, D., et al. 2023, MNRAS, 526, 2067, doi: 10.1093/mnras/stad2883

Miyata, T., Sako, S., Nakamura, T., et al. 2010, in Society of Photo-Optical Instrumentation Engineers (SPIE) Conference Series, Vol. 7735, Ground-based and Airborne Instrumentation for Astronomy III, ed. I. S. McLean, S. K. Ramsay, & H. Takami, 77353P, doi: 10.1117/12.856744

Molnár, L., Pál, A., Sárneczky, K., et al. 2018, ApJS, 234, 37, doi: 10.3847/1538-4365/aaa1a1

Mommert, M. 2017, Astronomy and Computing, 18, 47, doi: 10.1016/j.ascom.2016.11.002

Mommert, M., Farnocchia, D., Hora, J. L., et al. 2014a, ApJL, 789, L22, doi: 10.1088/2041-8205/789/1/L22

Mommert, M., Hora, J. L., Farnocchia, D., et al. 2014b, ApJ, 786, 148, doi: 10.1088/0004-637X/786/2/148

Moskovitz, N. A., Fatka, P., Farnocchia, D., et al. 2019, Icar, 333, 165, doi: 10.1016/j.icarus.2019.05.030

Moskovitz, N. A., Benson, C. J., Scheeres, D., et al. 2020, Icar, 340, 113519, doi: 10.1016/j.icarus.2019.113519

Muinonen, K., Belskaya, I. N., Cellino, A., et al. 2010, Icar, 209, 542, doi: 10.1016/j.icarus.2010.04.003

Muinonen, K., Piironen, J., Shkuratov, Y. G., Ovcharenko, A., & Clark, B. E. 2002, in Asteroids III, 123–138

Müller, T. G., Micheli, M., Santana-Ros, T., et al. 2023, A&A, 670, A53, doi: 10.1051/0004-6361/202245304

Müller, T. G., Lellouch, E., Böhnhardt, H., et al. 2009, Earth Moon and Planets, 105, 209, doi: 10.1007/s11038-009-9307-x

Müller, T. G., Miyata, T., Kiss, C., et al. 2013, A&A, 558, A97, doi: 10.1051/0004-6361/201321664

Murakami, H., Baba, H., Barthel, P., et al. 2007, Publication of the Astronomical Society of Japan, 59, S369, doi: 10.1093/pasj/59.sp2.S369

Naghizadeh-Khouei, J., & Clarke, D. 1993, A&A, 274, 968

Neugebauer, G., Habing, H. J., van Duinen, R., et al. 1984, ApJL, 278, L1, doi: 10.1086/184209

Nolan, M. C., Howell, E. S., Scheeres, D. J., et al. 2019, GRL, 46, 1956, doi: 10.1029/2018GL080658

Ohsawa, R. 2022, Journal of Space Science Informatics Japan, 11, 1, doi: 10.20637/00048400

Ohtsuka, K., Arakida, H., Ito, T., Yoshikawa, M., & Asher, D. J. 2008, Meteoritics and Planetary Science Supplement, 43, 5055

Ohtsuka, K., Sekiguchi, T., Kinoshita, D., et al. 2006, A&A, 450, L25, doi: 10.1051/0004-6361:200600022

Ohtsuka, K., Arakida, H., Ito, T., et al. 2007, ApJL, 668, L71, doi: 10.1086/522589

Okawa, H., Arakawa, M., Yasui, M., et al. 2022, Icar, 387, 115212, doi: 10.1016/j.icarus.2022.115212

Okazaki, R., Sekiguchi, T., Ishiguro, M., et al. 2020, , 180, 104774, doi: 10.1016/j.pss.2019.104774

Oliphant, T. E. 2015, Guide to NumPy, 2nd edn. (North Charleston, SC, USA: CreateSpace Independent Publishing Platform)

Ostro, S. J., Connelly, R., & Belkora, L. 1988, Icar, 73, 15, doi: 10.1016/0019-1035(88)90083-8

Ostro, S. J., Pravec, P., Benner, L. A. M., et al. 1999, Science, 285, 557, doi: 10.1126/science.285.5427.557

Ostro, S. J., Margot, J.-L., Benner, L. A. M., et al. 2006, Science, 314, 1276, doi: 10.1126/science.1133622

Pál, A., Szakáts, R., Kiss, C., et al. 2020, ApJS, 247, 26, doi: 10.3847/1538-4365/ab64f0

Paolicchi, P., Burns, J. A., & Weidenschilling, S. J. 2002, Side Effects of Collisions: Spin Rate Changes, Tumbling Rotation States, and Binary Asteroids, ed. J. Bottke, W. F., A. Cellino, P. Paolicchi, & R. P. Binzel, 517–526

Penttilä, A., Lumme, K., Hadamcik, E., & Levasseur-Regourd, A. C. 2005, A&A, 432, 1081, doi: 10.1051/0004-6361:20042133

Perna, D., Barucci, M. A., Fulchignoni, M., et al. 2018, Planetary and Space Science, 157, 82, doi: 10.1016/j.pss.2018.03.008

Petrov, N. A., Vasil'ev, A. A., Kuteeva, G. A., & Sokolov, L. L. 2018, Solar System Research, 52, 326, doi: 10.1134/S0038094618040032

Podlewska-Gaca, E., Poleski, R., Bartczak, P., McDonald, I., & Pál, A. 2021, ApJS, 255, 4, doi: 10.3847/1538-4365/ac02c0

Polishook, D., Brosch, N., Prialnik, D., & Kaspi, S. 2009, , 44, 1955, doi: 10.1111/j.1945-5100.2009.tb02005.x

Polishook, D., Jacobson, S. A., Morbidelli, A., & Aharonson, O. 2017, Nature Astronomy, 1, 0179, doi: 10.1038/s41550-017-0179

Polishook, D., Moskovitz, N., Binzel, R. P., et al. 2014a, Icar, 233, 9, doi: 10.1016/j.icarus.2014.01.014

Polishook, D., Moskovitz, N., DeMeo, F. E., & Binzel, R. P. 2014b, Icar, 243, 222, doi: 10.1016/j.icarus.2014.08.010

Popescu, M., Birlan, M., & Nedelcu, D. A. 2012, A&A, 544, A130, doi: 10.1051/0004-6361/201219584

Popescu, M., de León, J., de la Fuente Marcos, C., et al. 2020, MNRAS, 496, 3572, doi: 10.1093/mnras/staa1728

Popescu, M. M., Văduvescu, O., de León, J., et al. 2023, A&A, 676, A126, doi: 10.1051/0004-6361/202346751

Popova, O. P., Jenniskens, P., Emel'yanenko, V., et al. 2013, Science, 342, 1069, doi: 10.1126/science.1242642

Poynting, J. H. 1904, Philosophical Transactions of the Royal Society of London Series A, 202, 525, doi: 10.1098/rsta.1904.0012

Pravdo, S. H., Rabinowitz, D. L., Helin, E. F., et al. 1999, AJ, 117, 1616, doi: 10.1086/300769

Pravec, P., & Harris, A. W. 2000, Icar, 148, 12, doi: 10.1006/icar.2000.6482

—. 2007, Icarus, 190, 250, doi: 10.1016/j.icarus.2007.02.023

Pravec, P., Harris, A. W., Kušnirák, P., Galád, A., & Hornoch, K. 2012, Icar, 221, 365, doi: 10.1016/j.icarus.2012.07.026

Pravec, P., Harris, A. W., Scheirich, P., et al. 2005, Icarus, 173, 108, doi: 10.1016/j.icarus.2004.07.021

Pravec, P., Scheirich, P., Kušnirák, P., et al. 2006, Icar, 181, 63, doi: 10.1016/j.icarus.2005.10.014

Pravec, P., Vokrouhlický, D., Polishook, D., et al. 2010, Natur, 466, 1085, doi: 10.1038/nature09315

Pravec, P., Scheirich, P., Ďurech, J., et al. 2014, Icar, 233, 48, doi: 10.1016/j.icarus.2014.01.026

Pravec, P., Fatka, P., Vokrouhlický, D., et al. 2019, Icar, 333, 429, doi: 10.1016/j.icarus.2019.05.014

Pravec, P., Thomas, C. A., Rivkin, A. S., et al. 2022, PSJ, 3, 175, doi: 10.3847/PSJ/ac7be1

Raymond, S. N., & Izidoro, A. 2017, Science Advances, 3, e1701138, doi: 10.1126/sciadv.1701138

Raymond, S. N., & Nesvorný, D. 2022, in Vesta and Ceres. Insights from the Dawn Mission for the Origin of the Solar System, 227, doi: 10.1017/9781108856324.019

Rayner, J. T., Toomey, D. W., Onaka, P. M., et al. 2003, PASP, 115, 362, doi: 10.1086/367745

Reddy, V., Gary, B. L., Sanchez, J. A., et al. 2015, ApJ, 811, 65, doi: 10.1088/0004-637X/811/1/65

Reddy, V., Sanchez, J. A., Bottke, W. F., et al. 2016, AJ, 152, 162, doi: 10.3847/0004-6256/152/6/162

Richardson, D. C., Bottke, W. F., & Love, S. G. 1998, Icar, 134, 47, doi: 10.1006/icar.1998.5954

Richardson, D. C., Elankumaran, P., & Sanderson, R. E. 2005, Icar, 173, 349, doi: 10.1016/j.icarus.2004.09.007

Rivkin, A. S., Chabot, N. L., Stickle, A. M., et al. 2021, PSJ, 2, 173, doi: 10.3847/PSJ/ac063e

Robertson, H. P. 1937, MNRAS, 97, 423, doi: 10.1093/mnras/97.6.423

Rojo, P., & Margot, J. L. 2011, ApJ, 727, 69, doi: 10.1088/0004-637X/727/2/69

Rondón, E., Arcoverde, P., Monteiro, F., et al. 2019, MNRAS, 484, 2499, doi: 10.1093/mnras/stz024

Rondón, E., Lazzaro, D., Carvano, J., et al. 2022, Icar, 372, 114723, doi: 10.1016/j.icarus.2021.114723

Rossi, A., Marzari, F., & Scheeres, D. J. 2009, Icarus, 202, 95, doi: 10.1016/j.icarus.2009.02.030

Rozitis, B., Ryan, A. J., Emery, J. P., et al. 2020, Science Advances, 6, eabc3699, doi: 10.1126/sciadv.abc3699

Rubincam, D. P. 2000, Icarus, 148, 2, doi: 10.1006/icar.2000.6485

Ryan, E. L., Sharkey, B. N. L., & Woodward, C. E. 2017, AJ, 153, 116, doi: 10.3847/1538-3881/153/3/116

Sako, S., Ohsawa, R., Takahashi, H., et al. 2018, Society of Photo-Optical Instrumentation Engineers (SPIE) Conference Series, 10702, 107020J, doi: 10.1117/12.2310049

Sanchez, J. A., Reddy, V., Nathues, A., et al. 2012, Icar, 220, 36, doi: 10.1016/j.icarus.2012.04.008

Scargle, J. D. 1982, ApJ, 263, 835, doi: 10.1086/160554

Scheeres, D. J. 2007, Icar, 189, 370, doi: 10.1016/j.icarus.2007.02.015

Scheeres, D. J., Ostro, S. J., Werner, R. A., Asphaug, E., & Hudson, R. S. 2000, Icar, 147, 106, doi: 10.1006/icar.2000.6443

Scheirich, P., & Pravec, P. 2009, Icar, 200, 531, doi: 10.1016/j.icarus.2008.12.001

Schmidt, G. D., Elston, R., & Lupie, O. L. 1992, AJ, 104, 1563, doi: 10.1086/116341

Scott, E. R. D., Keil, K., Goldstein, J. I., et al. 2015, in Asteroids IV, 573–595, doi: 10.2458/azu_uapress_9780816532131-ch030

Seligman, D. Z., Farnocchia, D., Micheli, M., et al. 2023, PSJ, 4, 35, doi: 10.3847/PSJ/acb697

Sergeyev, A. V., & Carry, B. 2021, A&A, 652, A59, doi: 10.1051/0004-6361/202140430

Shevchenko, V. G. 1996, in Lunar and Planetary Science Conference, Vol. 27, Lunar and Planetary Science Conference, 1193

Shevchenko, V. G., Belskaya, I. N., Muinonen, K., et al. 2016, , 123, 101, doi: 10.1016/j.pss.2015.11.007

Shevchenko, V. G., Belskaya, I. N., Mikhalchenko, O. I., et al. 2019, A&A, 626, A87, doi: 10.1051/0004-6361/201935588

Shoemaker, E. M., & Helin, E. F. 1978, in NASA Conference Publication, Vol. 2053, NASA Conference Publication, ed. D. Morrison & W. C. Wells, 245–256

Sioulas, N. 2023, Minor Planet Bulletin, 50, 238

Smith, B. A., & Terrile, R. J. 1984, Science, 226, 1421, doi: 10.1126/science.226.4681.1421

Sonka, A. B., Nedelcu, A., & Birlan, M. 2022, Minor Planet Bulletin, 49, 258

Southworth, R. B., & Hawkins, G. S. 1963, Smithsonian Contributions to Astrophysics, 7, 261

Statler, T. S. 2009, Icarus, 202, 502, doi: 10.1016/j.icarus.2009.03.003

Steckloff, J. K., & Jacobson, S. A. 2016, Icar, 264, 160, doi: 10.1016/j.icarus.2015.09.021

Stokes, G. H., Evans, J. B., Viggh, H. E. M., Shelly, F. C., & Pearce, E. C. 2000, Icar, 148, 21, doi: 10.1006/icar.2000.6493

Sugita, S., Honda, R., Morota, T., et al. 2019, Science, 364, eaaw0422, doi: 10.1126/science.aaw0422

Szabó, G. M., Pál, A., Kiss, C., et al. 2017, A&A, 599, A44, doi: 10.1051/0004-6361/201629401

Szabó, G. M., Kiss, C., Szakáts, R., et al. 2020, ApJS, 247, 34, doi: 10.3847/1538-4365/ab6b23

Szabó, G. M., Pál, A., Szigeti, L., et al. 2022, A&A, 661, A48, doi: 10.1051/0004-6361/202142223

Szabó, R., Pál, A., Sárneczky, K., et al. 2016, A&A, 596, A40, doi: 10.1051/0004-6361/201629059

Takahashi, J., Itoh, Y., & Takahashi, S. 2011, Publication of the Astronomical Society of Japan, 63, 499, doi: 10.1093/pasj/63.3.499

Tardivel, S., Sánchez, P., & Scheeres, D. J. 2018, Icar, 304, 192, doi: 10.1016/j.icarus.2017.06.037

Taylor, P. A., Margot, J.-L., Vokrouhlický, D., et al. 2007, Science, 316, 274, doi: 10.1126/science.1139038

Tedesco, E. F., Noah, P. V., Noah, M., & Price, S. D. 2002, AJ, 123, 1056, doi: 10.1086/338320

Terai, T., Urakawa, S., Takahashi, J., et al. 2013, A&A, 559, A106, doi: 10.1051/0004-6361/201322158

Terai, T., Yoshida, F., Ohtsuki, K., et al. 2018, Publication of the Astronomical Society of Japan, 70, S40, doi: 10.1093/pasj/psx105

Thirouin, A., Moskovitz, N., Binzel, R. P., et al. 2016, AJ, 152, 163, doi: 10.3847/0004-6256/152/6/163

Thirouin, A., Moskovitz, N. A., Binzel, R. P., et al. 2018, ApJS, 239, 4, doi: 10.3847/1538-4365/aae1b0

Tholen, D. J. 1984, PhD thesis, University of Arizona

Thomas, C. A., Trilling, D. E., Emery, J. P., et al. 2011, AJ, 142, 85, doi: 10.1088/0004-6256/142/3/85

Thomas, C. A., Naidu, S. P., Scheirich, P., et al. 2023, Natur, 616, 448, doi: 10.1038/s41586-023-05805-2

Tian, J., Zhao, H.-B., & Li, B. 2022, Research in Astronomy and Astrophysics, 22, 125004, doi: 10.1088/1674-4527/ac977d

Tonry, J. L. 2023, PASP, 135, 114502, doi: 10.1088/1538-3873/acff89

Tonry, J. L., Stubbs, C. W., Lykke, K. R., et al. 2012, ApJ, 750, 99, doi: 10.1088/0004-637X/750/2/99

Tonry, J. L., Denneau, L., Heinze, A. N., et al. 2018, PASP, 130, 064505, doi: 10.1088/1538-3873/aabadf

Tricarico, P. 2017, Icar, 284, 416, doi: 10.1016/j.icarus.2016.12.008

Trilling, D. E., Mueller, M., Hora, J. L., et al. 2010, AJ, 140, 770, doi: 10.1088/0004-6256/140/3/770

Trilling, D. E., Mommert, M., Hora, J., et al. 2016, AJ, 152, 172, doi: 10.3847/0004-6256/152/6/172

Uehara, M., Nagashima, C., Sugitani, K., et al. 2004, in Society of Photo-Optical Instrumentation Engineers (SPIE) Conference Series, Vol. 5492, Ground-based Instrumentation for Astronomy, ed. A. F. M. Moorwood & M. Iye, 661–668, doi: 10.1117/12.551055

Usui, F., Kasuga, T., Hasegawa, S., et al. 2013, ApJ, 762, 56, doi: 10.1088/0004-637X/762/1/56

Usui, F., Kuroda, D., Müller, T. G., et al. 2011, Publication of the Astronomical Society of Japan, 63, 1117, doi: 10.1093/pasj/63.5.1117

van Dokkum, P. G. 2001, PASP, 113, 1420, doi: 10.1086/323894

VanderPlas, J. T. 2018, ApJS, 236, 16, doi: 10.3847/1538-4365/aab766

Veeder, G. J., Matson, D. L., & Tedesco, E. F. 1983, Icar, 55, 177, doi: 10.1016/0019-1035(83)90058-1

Verbiscer, A., French, R., Showalter, M., & Helfenstein, P. 2007, Science, 315, 815, doi: 10.1126/science.1134681

Veverka, J., Farquhar, B., Robinson, M., et al. 2001, Natur, 413, 390, doi: 10.1038/35096507

Virkki, A. K., Marshall, S. E., Venditti, F. C. F., et al. 2022, PSJ, 3, 222, doi: 10.3847/PSJ/ac8b72

Virtanen, P., Gommers, R., Oliphant, T. E., et al. 2020, Nature Methods, 17, 261, doi: 10.1038/s41592-019-0686-2

Vokrouhlický, D. 1998, A&A, 335, 1093

Vokrouhlický, D., Bottke, W. F., Chesley, S. R., Scheeres, D. J., & Statler, T. S. 2015, in Asteroids IV, 509–531, doi: 10.2458/azu_uapress_9780816532131-ch027

Vokrouhlický, D., Breiter, S., Nesvorný, D., & Bottke, W. F. 2007, Icarus, 191, 636, doi: 10.1016/j.icarus.2007.06.002

Vokrouhlický, D., Milani, A., & Chesley, S. R. 2000, Icarus, 148, 118, doi: 10.1006/icar.2000.6469

Vokrouhlický, D., & Nesvorný, D. 2008, AJ, 136, 280, doi: 10.1088/0004-6256/136/1/280

Vokrouhlický, D., & Čapek, D. 2002, Icarus, 159, 449, doi: 10.1006/icar.2002.6918

Vokrouhlický, D., Čapek, D., Kaasalainen, M., & Ostro, S. J. 2004, A&A, 414, L21, doi: 10.1051/0004-6361:20031739

Wainscoat, R. J., Chambers, K., Weryk, R., et al. 2022, in 2022 IEEE Aerospace Conference (AERO), 1–6, doi: 10.1109/AERO53065.2022.9843625

Walsh, K. J., & Jacobson, S. A. 2015, in Asteroids IV, 375–393, doi: 10.2458/azu_uapress_9780816532131-ch020

Walsh, K. J., & Richardson, D. C. 2006, Icar, 180, 201, doi: 10.1016/j.icarus.2005.08.015

Walsh, K. J., Richardson, D. C., & Michel, P. 2008, Natur, 454, 188, doi: 10.1038/nature07078

Wang, L., Wheeler, J. C., & Höflich, P. 1997, ApJL, 476, L27, doi: 10.1086/310495

Wardle, J. F. C., & Kronberg, P. P. 1974, ApJ, 194, 249, doi: 10.1086/153240

Warner, B. D., Harris, A. W., & Pravec, P. 2009, Icarus, 202, 134, doi: 10.1016/j.icarus.2009.02.003

Watanabe, M., Takahashi, Y., Sato, M., et al. 2012, in Society of Photo-Optical Instrumentation Engineers (SPIE) Conference Series, Vol. 8446, Ground-based and Airborne Instrumentation for Astronomy IV, ed. I. S. McLean, S. K. Ramsay, & H. Takami, 84462O, doi: 10.1117/12.925292

Watanabe, S., Hirabayashi, M., Hirata, N., et al. 2019, Science, 364, 268, doi: 10.1126/science.aav8032

Werner, M. W., Roellig, T. L., Low, F. J., et al. 2004, ApJS, 154, 1, doi: 10.1086/422992

Wiegert, P. A. 2015, Icarus, 252, 22, doi: 10.1016/j.icarus.2014.12.022

Willmer, C. N. A. 2018, ApJS, 236, 47, doi: 10.3847/1538-4365/aabfdf

Wright, E. L., Eisenhardt, P. R. M., Mainzer, A. K., et al. 2010, AJ, 140, 1868, doi: 10.1088/0004-6256/140/6/1868

Wyatt, M. C. 2008, ARAA, 46, 339, doi: 10.1146/annurev.astro.45.051806.110525

Ye, Q., Masci, F. J., Ip, W.-H., et al. 2020, AJ, 159, 70, doi: 10.3847/1538-3881/ab629c

Yeomans, D. K., Antreasian, P. G., Barriot, J. P., et al. 2000, Science, 289, 2085, doi: 10.1126/science.289.5487.2085

York, D. G., Adelman, J., Anderson, John E., J., et al. 2000, AJ, 120, 1579, doi: 10.1086/301513

Yoshida, F., Hayamizu, T., Miyashita, K., et al. 2023, Publication of the Astronomical Society of Japan, 75, 153, doi: 10.1093/pasj/psac096

Yoshii, Y., Aoki, T., Doi, M., et al. 2010, in Society of Photo-Optical Instrumentation Engineers (SPIE) Conference Series, Vol. 7733, Ground-based and Airborne Telescopes III, ed. L. M. Stepp, R. Gilmozzi, & H. J. Hall, 773308, doi: 10.1117/12.856680

Yoshikawa, M., Froeschlé, C., & Michel, P. 2000, Advances in Space Research, 25, 273, doi: 10.1016/S0273-1177(99)00937-0

Zappala, V., Cellino, A., Barucci, A. M., Fulchignoni, M., & Lupishko, D. F. 1990, A&A, 231, 548

Zegmott, T. J., Lowry, S. C., Rożek, A., et al. 2021, MNRAS, 507, 4914, doi: 10.1093/mnras/stab2476

Zellner, B. 1975, ApJL, 198, 2, doi: 10.1086/181807

Zellner, B., & Gradie, J. 1976, AJ, 81, 262, doi: 10.1086/111882

Zellner, B., Leake, M., Morrison, D., & Williams, J. G. 1977, GCA, 41, 1759, doi: 10.1016/0016-7037(77)90208-3

Zellner, B., Thirunagari, A., & Bender, D. 1985a, Icar, 62, 505, doi: 10.1016/0019-1035(85)90190-3

Zellner, B., Tholen, D. J., & Tedesco, E. F. 1985b, Icar, 61, 355, doi: 10.1016/0019-1035(85)90133-2

Zhai, C., Shao, M., Nemati, B., et al. 2014, ApJ, 792, 60, doi: 10.1088/0004-637X/792/1/60

Zhou, W.-H., Zhang, Y., Yan, X., & Michel, P. 2022, A&A, 668, A70, doi: 10.1051/0004-6361/202244386

Zolensky, M., Nakamura, K., Weisberg, M. K., et al. 2003, , 38, 305, doi: 10.1111/j.1945-5100.2003.tb00266.x

Zolensky, M., Herrin, J., Mikouchi, T., et al. 2010, , 45, 1618, doi: 10.1111/j.1945-5100.2010.01128.x